



DEVELOPMENT AND *MASH* TL-4 EVALUATION OF TXDOT LARGE-SCUPPER MEDIAN BARRIER FOR FLOOD-PRONE AREAS



Crash testing performed at:
TTI Proving Ground
1254 Avenue A, Building 7091
Bryan, TX 77807

Test Report 0-6976-R1

Cooperative Research Program

TEXAS A&M TRANSPORTATION INSTITUTE
COLLEGE STATION, TEXAS

TEXAS DEPARTMENT OF TRANSPORTATION

in cooperation with the
Federal Highway Administration and the
Texas Department of Transportation
<http://tti.tamu.edu/documents/0-6976-R1.pdf>

1. Report No. FHWA/TX-21/0-6976-R1		2. Government Accession No.		3. Recipient's Catalog No.	
4. Title and Subtitle DEVELOPMENT AND <i>MASH</i> TL-4 EVALUATION OF TXDOT LARGE-SCUPPER MEDIAN BARRIER FOR FLOOD-PRONE AREAS				5. Report Date Published: June 2021 Revised: October 2021	
				6. Performing Organization Code	
7. Author(s) Chiara Silvestri Dobrovoly, James C. Kovar, Roger P. Bligh, Blair A. Johnson, Michael E. Barrett, Brandon Klenzendorf, Gregory Hendrickson, Wanda L. Menges, William Schroeder, and Darrell L. Kuhn				8. Performing Organization Report No. Report 0-6976-R1	
9. Performing Organization Name and Address Texas A&M Transportation Institute The Texas A&M University System College Station, Texas 77843-3135				10. Work Unit No. (TRAVIS)	
				11. Contract or Grant No. Project 0-6976	
12. Sponsoring Agency Name and Address Texas Department of Transportation Research and Technology Implementation Office 125 E. 11 th Street Austin, Texas 78701-2483				13. Type of Report and Period Covered Technical Report: August 2018–August 2020	
				14. Sponsoring Agency Code	
15. Supplementary Notes Project performed in cooperation with the Texas Department of Transportation and the Federal Highway Administration. Project Title: Development of Concrete Median Barrier for Flood-Prone Areas URL: http://tti.tamu.edu/documents/0-6976-R1.pdf					
16. Abstract <p>Concrete median barriers are designed to mitigate serious cross-median crashes by preventing penetration of errant vehicles into oncoming traffic. When implemented in flood-prone areas, however, solid concrete median barriers can act as a dam to floodwaters, as recently seen in Texas during Hurricane Harvey or in Louisiana and Pennsylvania following severe storms. These severe weather events raise the height of floodwaters and increase the severity of flooding on highways and surrounding roads and communities. In this study, new median barrier options with openings were investigated as a way to reduce flooding. Finite element simulations were used to aid investigation and evaluation of the designs, and laboratory testing was performed to evaluate the hydraulic efficiency of barrier designs in a variety of simulated flood conditions. A concrete single-slope profile median barrier with a large scupper was selected for crash testing following <i>Manual for Assessing Safety Hardware (MASH)</i> Test Level 4 impact conditions and evaluation criteria. The median barrier design was deemed <i>MASH</i> compliant and is ready for implementation in areas susceptible to flooding, with the goals of reducing flooding severity, decreasing associated risk to motorists, and reducing the level of flood damage to both highways and surrounding areas.</p>					
17. Key Words Longitudinal Barrier, Concrete Barrier, Single-Slope Concrete Barrier, Scuppers, Flood Prone, Crash Testing, Roadside Safety, Computer Simulations, Hydraulic Testing			18. Distribution Statement No restrictions. This document is available to the public through NTIS: National Technical Information Service Alexandria, Virginia http://www.ntis.gov		
19. Security Classif. (of this report) Unclassified		20. Security Classif. (of this page) Unclassified		21. No. of Pages 262	22. Price

DEVELOPMENT AND *MASH* TL-4 EVALUATION OF TXDOT LARGE-SCUPPER MEDIAN BARRIER FOR FLOOD-PRONE AREAS

by

Chiara Silvestri Dobrovolny, Ph.D.
Research Scientist
Texas A&M Transportation Institute

James C. Kovar
Assistant Research Scientist
Texas A&M Transportation Institute

Roger P. Bligh, Ph.D., P.E.
Research Engineer
Texas A&M Transportation Institute

Blair A. Johnson, Ph.D.
Assistant Professor
University of Texas at Austin

Michael E. Barrett, Ph.D., P.E.
Research Professor
University of Texas at Austin

Brandon Klenzendorf, Ph.D., P.E.
Lecturer
University of Texas at Austin

Gregory Hendrickson, M.S., E.I.T.
Graduate Student
University of Texas at Austin

Wanda L. Menges
Research Specialist
Texas A&M Transportation Institute

William Schroeder
Research Engineering Associate
Texas A&M Transportation Institute

Darrell L. Kuhn, P.E.
Research Specialist
Texas A&M Transportation Institute

Report 0-6976-R1
Project 0-6976

Project Title: Development of Concrete Median Barrier for Flood-Prone Areas

Performed in cooperation with the
Texas Department of Transportation
and the
Federal Highway Administration

Published: June 2021
Revised: October 2021

TEXAS A&M TRANSPORTATION INSTITUTE
College Station, Texas 77843-3135

DISCLAIMER

This research was performed in cooperation with the Texas Department of Transportation (TxDOT) and the Federal Highway Administration (FHWA). The contents of this report reflect the views of the authors, who are responsible for the facts and the accuracy of the data presented herein. The contents do not necessarily reflect the official view or policies of FHWA or TxDOT. This report does not constitute a standard, specification, or regulation.

This report is not intended for construction, bidding, or permit purposes. The engineer in charge of the project was Roger P. Bligh, P.E. Texas #78550.

The United States Government and the State of Texas do not endorse products or manufacturers. Trade or manufactures' names appear herein solely because they are considered essential to the object of this report.

TTI PROVING GROUND DISCLAIMER

The results of the crash testing reported herein apply only to the article tested.

REPORT AUTHORIZATION

DocuSigned by:

Bill Griffith

44A122CB271846B...

Bill L. Griffith, Research Specialist
Deputy Quality Manager

DocuSigned by:

Darrell L. Kuhn

D4CC23E85D5B4E7...

Darrell L. Kuhn, P.E., Research Specialist
Quality Manager

DocuSigned by:

Matt Robinson

EAA22BFA5BFD417...

Matthew N. Robinson, Research Specialist
Test Facility Manager & Technical Manager

DocuSigned by:

Chiara St. Dy

36EDAD98EFE94EC...

Chiara Silvestri Dobrovolny, Ph.D.
Research Scientist

ACKNOWLEDGMENTS

This project was conducted in cooperation with TxDOT and FHWA. The research team would like to thank Mr. Wade Odell, P.E. (TxDOT Project Manager), and the following project panel members for their valuable assistance and input on this project: Ken Mora, Rose Marie Klee, and Abderrahmane Maamar-Tayeb from the Design Division; Taya Retterer and Jon Ries from the Bridge Division; Adam Jack from the Beaumont District; and Prassana Chebbi from the Houston District. Portions of this research were conducted with high-performance research computing resources provided by Texas A&M University (<https://hprc.tamu.edu>).

TABLE OF CONTENTS

	Page
Chapter 1. Introduction	1
1.1 Background	1
1.2 Objective	1
1.3 Work Plan	2
1.3.1 Task 1. Conduct Project Management and Research Coordination	2
1.3.2 Task 2. Literature Review	2
1.3.3 Task 3. Develop and Evaluate Preliminary Design Concepts	3
1.3.4 Task 4. Conduct Large-Scale Hydraulic Testing	3
1.3.5 Task 5. Develop Detailed Design and Perform Engineering Analysis	3
1.3.6 Task 6. Construct Barrier System and Conduct Full-Scale Crash Testing	4
Chapter 2. Literature Review	7
2.1 Introduction	7
2.2 <i>MASH</i> Testing Standard Criteria	9
2.3 Literature Review	10
2.3.1 Cross-Highway Water Flow Requirements during Severe Weather Events Required to Prevent Significant Rise in Floodwater by Highway Barrier, Including Concrete Bridge Barriers	11
2.3.2 Weir Equation	13
2.3.3 Non-proprietary Concrete Barrier Systems, Either Existing or Under Development, for Implementation in Flood-Prone Areas, Including Concrete Bridge Barriers	23
2.3.4 Identification and Review of Testing Performance of Existing Compliance Rigid and Portable Concrete Barriers with Openings or Scuppers	32
2.4 Conclusions	33
Chapter 3. Preliminary Design Concepts	35
3.1 Introduction	35
3.2 Option A: 42-Inch-Tall Single-Slope Median Barrier	35
3.3 Options B1 and B2: Median Versions of the T223 TxDOT Post-and-Beam Bridge Rail	35
3.4 Option C: 42-Inch-Tall Median Concrete Post and Beam (Rectangular Posts)	39
3.5 Option D: 36-Inch or 42-Inch-Tall Median Concrete Post and Beam (Round Posts) ...	40
3.6 Option E: 36-Inch-Tall Median Version of the C1W TxDOT Bridge Rail	40
3.7 Conclusions	42
Chapter 4. Finite Element Analysis	47
4.1 Introduction	47
4.2 Model Calibration for Concrete Options	47
4.2.1 Full-Scale Crash Test	47
4.2.2 Computer Model Simulation	50
4.2.3 Conclusion	54
4.3 Model Calibration for Steel Option	54
4.3.1 Model Calibration	54
4.3.2 Available FE Computer Models	55

4.3.3	Full-Scale Crash Test.....	55
4.3.4	Test Article and Installation Details	56
4.3.5	<i>MASH</i> Test 5-10 (TTI Test 603911-1).....	57
4.3.6	<i>MASH</i> Test 5-11 (TTI Test 603911-2).....	61
4.3.7	Computer Model Simulation.....	64
4.3.8	<i>MASH</i> Test 5-10 Calibration (Test 603911-1).....	64
4.3.9	<i>MASH</i> Test 5-11 Calibration (Test 603911-2).....	66
4.3.10	<i>MASH</i> Test 5-11 (Driver-Side Impact) Calibration (Test 603911-2)	66
4.3.11	Conclusion	68
4.4	Simulations	69
4.4.1	Option A: 42-Inch-Tall Single-Slope Median Barrier	69
4.4.2	Option B: Median Version of the T223 TxDOT Post-and-Beam Bridge Rail	81
4.4.3	Option C: 38-Inch Open Steel Barrier	94
4.5	Conclusions.....	104
Chapter 5. Large-Scale Hydraulic Testing.....		105
5.1	Introduction.....	105
5.2	Experimental Setup.....	105
5.2.1	Physical Construction	106
5.2.2	Reservoir and Pipe Network	113
5.2.3	Test Channel	113
5.2.4	Upstream Water Depth	114
5.3	Experimental Procedure.....	118
5.3.1	Start-Up Procedure.....	118
5.3.2	Testing Procedure	119
5.3.3	Shut-Down Procedure.....	119
5.4	Test Cases	119
5.5	Hydraulic Testing Results and Analysis	120
5.5.1	Raw Data Rating Curves.....	120
5.5.2	Data Accuracy and Limitations	123
5.5.3	Model Fitting	124
5.5.4	Non-dimensional Values.....	124
5.5.5	Model Equations and Coefficients.....	124
5.5.6	Model Rating Curves	126
5.5.7	Model Discussion.....	129
5.5.8	Overlay Comparison	130
5.5.9	SSCB Alteration Example	130
5.6	Modeling Barriers in HEC-RAS.....	132
5.6.1	Introduction.....	132
5.6.2	Computation Methods.....	132
5.6.3	Example Details	132
5.6.4	Site Modifications	133
5.6.5	Data Integration Example	133
5.6.6	Weir Approximation	135
5.6.7	Discussion	138
5.7	Summary and Conclusions	139
5.7.1	Summary	139

5.7.2 Conclusions	140
Chapter 6. Barrier System Details	141
6.1 Test Article and Installation Details	141
6.2 Design Modifications during Tests	141
6.3 Material Specifications	141
Chapter 7. Test Requirements and Evaluation Criteria	145
7.1 Crash Test Performed/Matrix	145
7.2 Evaluation Criteria	146
Chapter 8. Test Conditions	149
8.1 Test Facility	149
8.2 Vehicle Tow and Guidance System	149
8.3 Data Acquisition Systems	149
8.3.1 Vehicle Instrumentation and Data Processing	149
8.3.2 Anthropomorphic Dummy Instrumentation	150
8.3.3 Photographic Instrumentation Data Processing	151
Chapter 9. MASH Test 4-10 (Crash Test No. 469760-06-1)	153
9.1 Test Designation and Actual Impact Conditions	153
9.2 Weather Conditions	153
9.3 Test Vehicle	153
9.4 Test Description	154
9.5 Damage to Test Installation	154
9.6 Damage to Test Vehicle	155
9.7 Occupant Risk Factors	156
Chapter 10. MASH Test 4-11 (Crash Test No. 469760-06-2)	159
10.1 Test Designation and Actual Impact Conditions	159
10.2 Weather Conditions	159
10.3 Test Vehicle	159
10.4 Test Description	160
10.5 Damage to Test Installation	160
10.6 Damage to Test Vehicle	162
10.7 Occupant Risk Factors	162
Chapter 11. MASH Test 4-12 (Crash Test No. 469760-06-3)	165
11.1 Test Designation and Actual Impact Conditions	165
11.2 Weather Conditions	165
11.3 Test Vehicle	165
11.4 Test Description	166
11.5 Damage to Test Installation	166
11.6 Damage to Test Vehicle	168
11.7 Vehicle Instrumentation	169
Chapter 12. Summary and Conclusions	171
12.1 Assessment of Test Results	171
12.2 Conclusions	171
Chapter 13. Implementation	177
References	179
Appendix A. Details of TxDOT Large-Scupper Median Barrier	183
Appendix B. Supporting Certification Documents	189

Appendix C. MASH Test 4-10 (Crash Test No. 469760-06-1)	201
C.1 Vehicle Properties and Information	201
C.2 Sequential Photographs.....	204
C.3 Vehicle Angular Displacements	207
C.4 Vehicle Accelerations	208
Appendix D. MASH Test 4-11 (Crash Test No. 469760-06-2)	211
D.1 Vehicle Properties and Information	211
D.2 Sequential Photographs.....	215
D.3 Vehicle Angular Displacements	218
D.4 Vehicle Accelerations	219
Appendix E. MASH Test 4-12 (Crash Test No. 469760-06-3)	223
E.1 Vehicle Properties and Information	223
E.2 Sequential Photographs.....	225
E.3 Vehicle Angular Displacements	228
E.4 Vehicle Accelerations	229
Appendix F. Details for Longer Segment Lengths and Cast-in-Place and Epoxy Rebar Anchor Options for TxDOT LSMB	235
Appendix G. Value of Research Estimate	239
G.1 Introduction.....	239
G.2 Qualitative Benefit Areas.....	239
G.2.1 Engineering Design Development/Improvement	239
G.2.2 Safety	240
G.3 Economic Benefits	240
G.4 Computed VoR	241
G.5 Discussion	243

LIST OF FIGURES

	Page
Figure 2.1. Examples of Flooding Scenarios Where Rigid, Solid Median Concrete Barriers Are Implemented.....	7
Figure 2.2. Examples of Flooding Scenarios Where Portable Concrete Median Barriers Are Installed as Permanent Applications.....	8
Figure 2.3. Drawing of Median Version of TxDOT T223 Concrete Barrier.....	9
Figure 2.4. Specific Energy Curve.....	12
Figure 2.5. Sharp-Crested Weir Diagram.....	13
Figure 2.6. Three Different Flows in Charbeneau Model.....	16
Figure 2.7. Experimental Setup for Bridge Rail in Rectangular Channel.....	18
Figure 2.8. Bridge Rail Rating Curves.....	19
Figure 2.9. Tested Bridge Rails.....	20
Figure 2.10. Different Curvatures Studied by Akiba et al.....	21
Figure 2.11. Different Curvatures Studied by Akiba et al.....	21
Figure 2.12. WSDOT Barrier Test 3-11.....	24
Figure 2.13. Revised WSDOT Barrier Test 3-11.....	25
Figure 2.14. Drawing for LaDOTD F-Shape Concrete Barrier.....	26
Figure 2.15. Side-View Comparison of LaDOTD F-Shape Barrier, TxDOT Wildlife Crossing Single-Slope Concrete Barrier (SSCB), and WSDOT Pin-and-Loop Barrier.....	27
Figure 2.16. Opening in Concrete Barrier to Allow for Rubber Block Installation.....	27
Figure 2.17. TxDOT SSCB (Wildlife Crossing).....	28
Figure 2.18. MassDOT F-Shape PCB.....	32
Figure 2.19. Concrete Crack after <i>MASH</i> Test 2-11.....	33
Figure 2.20. Concrete Crack after <i>MASH</i> Test 3-11 (Retrofit System).....	33
Figure 3.1. Option A Preliminary Drawing.....	36
Figure 3.2. Option B1 Preliminary Drawing.....	37
Figure 3.3. Option B2 Preliminary Drawing.....	38
Figure 3.4. Option C Preliminary Drawing.....	39
Figure 3.5. Option D Preliminary Drawing.....	41
Figure 3.6. Option E Preliminary Drawing.....	42
Figure 4.1. Available Finite Element Computer Models.....	47
Figure 4.2. Vehicle and Barrier System for FEA Calibration.....	48
Figure 4.3. Single-Slope Barrier System with and without Test Vehicle before Testing.....	48
Figure 4.4. Single-Slope Barrier System after Testing.....	48
Figure 4.5. Summary of Results for TxDOT Single-Slope Bridge Rail (Type SSTR) on Pan-Formed Bridge Deck System.....	49
Figure 4.6. LS-DYNA Calibration Barrier System Model.....	50
Figure 4.7. Available Finite Element Models of Vehicles.....	55
Figure 4.8. TBTA Bridge Rail.....	56
Figure 4.9. TBTA Bridge Rail/Test Vehicle Geometrics.....	58
Figure 4.10. Test Vehicle before Test.....	58
Figure 4.11. Test Vehicle after Test.....	58

Figure 4.12. Interior of Test Vehicle.....	59
Figure 4.13. Summary of <i>MASH</i> Test 5-10 on TBTA Bridge Rail.....	60
Figure 4.14. TBTA Bridge Rail/Test Vehicle Geometrics.....	61
Figure 4.15. Test Vehicle before Test.....	61
Figure 4.16. Test Vehicle after Test.....	61
Figure 4.17. Interior of Test Vehicle.....	62
Figure 4.18. Summary of <i>MASH</i> Test 5-11 on TBTA Bridge Rail.....	63
Figure 4.19. LS-DYNA Calibration Barrier System Model.....	64
Figure 4.20. CIPs Considered for Option A System.....	69
Figure 4.21. Developed FEA Model for Option A System.....	70
Figure 4.22. Computer Simulation Models for Option A with Different Vehicles.....	70
Figure 4.23. Computer Model for Option A with Passenger Car.....	71
Figure 4.24. Parametric Analysis Results for Option A with Passenger Car.....	72
Figure 4.25. Different Views of Computer Simulation Model for Option A with Pickup Truck.....	74
Figure 4.26. Parametric Analysis Results for Option A with Pickup Truck (without Tire Disengagement.).....	75
Figure 4.27. Parametric Analysis Results for Option A with Pickup Truck (with Tire Disengagement).....	77
Figure 4.28. Computer Simulation Model for Option A with SUT.....	79
Figure 4.29. Option B: Median Version of the T223 TxDOT Post-and-Beam Bridge Rail with Posts Sloped Laterally.....	81
Figure 4.30. Median Version of the T223 TxDOT Post-and-Beam Bridge Rail with Constant-Width Concrete Posts.....	82
Figure 4.31. Computer Simulation Models for Option B with Different Vehicles.....	83
Figure 4.32. Different Views of Computer Simulation Model for Option B with Passenger Car.....	83
Figure 4.33. Parametric Analysis Results for Option B with Passenger Car.....	84
Figure 4.34. Different Views of Computer Simulation Model for Option B with Pickup Truck (without Tire Disengagement).....	86
Figure 4.35. Parametric Analysis Results for Option B with Pickup Truck (without Tire Disengagement).....	87
Figure 4.36. Different Views of Computer Simulation Model for Option B with Pickup Truck (with Tire Disengagement).....	89
Figure 4.37. Parametric Analysis Results for Option B with Pickup Truck (with Tire Disengagement).....	90
Figure 4.38. Computer Simulation Model for Option B with SUT.....	92
Figure 4.39. Open Steel Barrier Model Developed as Option C.....	94
Figure 4.40. Computer Simulation Models for Option C with Different Vehicles.....	95
Figure 4.41. Different Views of Computer Simulation Model for Option C with Passenger Car.....	95
Figure 4.42. Maximum Deformation in Steel Barrier from Passenger Car.....	97
Figure 4.43. Energy Distribution History for Passenger Car.....	98
Figure 4.44. Different Views of Computer Simulation Model for Option C with Pickup Truck.....	98
Figure 4.45. Maximum Deformation in Steel Barrier from Pickup Truck.....	100

Figure 4.46. Energy Distribution History for Pickup Truck.....	101
Figure 4.47. Different Views of Computer Simulation Model for Option C with SUT.....	101
Figure 4.48. Maximum Deformation in Steel Barrier from SUT.	103
Figure 4.49. Energy Distribution History for SUT.....	104
Figure 5.1. Hydraulic Testing.....	105
Figure 5.2. Generalized Barrier.....	106
Figure 5.3. Weir Barrier.	107
Figure 5.4. SSCB.....	108
Figure 5.5. Post-and-Beam Barrier.....	108
Figure 5.6. Steel Barrier.	109
Figure 5.7. Initial Support Base Design.	110
Figure 5.8. (a) Weir Barrier Failure; (b) Hinged Connection Failure.	111
Figure 5.9. (a) Final Support Base Design; (b) Installation in Channel Barrier and Support Base Setup in Channel.....	112
Figure 5.10. Flume Layout.	113
Figure 5.11. Pump Outlets.....	114
Figure 5.12. Upstream Water Depth Measurement Locations.....	115
Figure 5.13. (a) ISCO 4230 Bubble Flow Meter; (b) Solar-Powered Housing Unit.	116
Figure 5.14. Discharge Weir and Gate.	117
Figure 5.15. Point Gauge.....	118
Figure 5.16. SSCB with Overlay.....	120
Figure 5.17. SSCB Rating Curves.....	121
Figure 5.18. Post-and-Beam Rating Curves.....	121
Figure 5.19. Steel Barrier Rating Curves.	122
Figure 5.20. Combined Rating Curves.	122
Figure 5.21. Curve Fitting Example.....	126
Figure 5.22. SSCB Model Rating Curves.	127
Figure 5.23. Post-and-Beam Model Rating Curves.	127
Figure 5.24. Steel Barrier Model Rating Curves.....	128
Figure 5.25. Combined Model Rating Curves.	128
Figure 5.26. Downstream Behavior Comparison.....	129
Figure 5.27. Steel Barrier Model Fit Comparison.....	130
Figure 5.28. SSCB Rating Curve Estimates—10 Percent Opening Reduction.....	131
Figure 5.29. SSCB Model Rating Curve.....	133
Figure 5.30. Steady-Flow Analysis Modifications.....	134
Figure 5.31. HEC-RAS Cross-Section.....	134
Figure 5.32. HEC-RAS Output Table.	135
Figure 5.33. Weir Approximation.	135
Figure 5.34. HEC-RAS Second Iteration Output.....	138
Figure 6.1. TxDOT LSMB Details.....	142
Figure 6.2. TxDOT LSMB prior to Testing.	143
Figure 7.1. Target CIP for <i>MASH</i> Test 4-10 on TxDOT LSMB.....	145
Figure 7.2. Target CIP for <i>MASH</i> Test 4-11 on TxDOT LSMB.....	146
Figure 7.3. Target CIP for <i>MASH</i> Test 4-12 on TxDOT LSMB.....	146
Figure 9.1. TxDOT LSMB/Test Vehicle Geometrics for Test No. 469760-06-1.....	153
Figure 9.2. Test Vehicle before Test No. 469760-06-1.....	154

Figure 9.3. TxDOT LSMB after Test No. 469760-06-1.	155
Figure 9.4. Test Vehicle after Test No. 469760-06-1.	156
Figure 9.5. Interior of Test Vehicle after Test No. 469760-06-1.	156
Figure 9.6. Summary of Results for <i>MASH</i> Test 4-10 on TxDOT LSMB.	158
Figure 10.1. TxDOT LSMB/Test Vehicle Geometrics for Test No. 469760-06-2.	159
Figure 10.2. Test Vehicle before Test No. 469760-06-2.	160
Figure 10.3. TxDOT LSMB after Test No. 469760-06-2.	161
Figure 10.4. Test Vehicle after Test No. 469760-06-2.	162
Figure 10.5. Interior of Test Vehicle after Test No. 469760-06-2.	162
Figure 10.6. Summary of Results for <i>MASH</i> Test 4-11 on TxDOT LSMB.	164
Figure 11.1. TxDOT LSMB/Test Vehicle Geometrics for Test No. 469760-06-3.	165
Figure 11.2. Test Vehicle before Test No. 469760-06-3.	166
Figure 11.3. TxDOT LSMB after Test No. 469760-06-3.	167
Figure 11.4. Movement of Barrier after Test No. 469760-06-3.	168
Figure 11.5. Field Side of Barrier after Test No. 469760-06-3.	168
Figure 11.6. Test Vehicle after Test No. 469760-06-3.	169
Figure 11.7. Interior of Test Vehicle after Test No. 469760-06-3.	169
Figure 11.8. Summary of Results for <i>MASH</i> Test 4-12 on TxDOT LSMB.	170

LIST OF TABLES

	Page
Table 2.1. TxDOT Bridge Rail Standards Summary Table.	29
Table 2.2. TxDOT Rigid-Barrier Summary Table (F-Shape).	31
Table 2.3. TxDOT Rigid-Barrier Summary Table (Single Slope).	31
Table 3.1. Option A Perceived Advantages and Disadvantages.	36
Table 3.2. Options B1 and B2 Perceived Advantages and Disadvantages.	38
Table 3.3. Option C Perceived Advantages and Disadvantages.	40
Table 3.4. Option D Perceived Advantages and Disadvantages.	41
Table 3.5. Option E Perceived Advantages and Disadvantages.	42
Table 3.6. Summary of Proposed Design Options for Median Barriers for Implementation in Flood-Prone Areas.	44
Table 4.1. Sequential Images of the Simulated Computer Model Impact Event.	51
Table 4.2. Comparison of Actual Crash Test and LS-DYNA Simulation.	52
Table 4.3. Comparison between Full-Scale Crash Test and Impact Event Computer Simulation.	54
Table 4.4. Comparison of Actual Crash Test and LS-DYNA Simulation.	65
Table 4.5. Comparison between Full-Scale Crash Test and Computer Simulation.	66
Table 4.6. Comparison of Actual Crash Test and LS-DYNA Simulation.	67
Table 4.7. Comparison between Full-Scale Crash Test and Computer Simulation.	68
Table 4.8. Comparison between Full-Scale Crash Test and Impact Event Computer Simulation.	68
Table 4.9. Sequential Images of the Simulated Computer Model Impact Events for Option A with Passenger Car.	73
Table 4.10. Sequential Images of the Simulated Computer Model Impact Events for Option A with Pickup Truck (without Tire Disengagement).	76
Table 4.11. Sequential Images of the Simulated Computer Model Impact Events for Option A with Pickup Truck (with Tire Disengagement).	78
Table 4.12. Sequential Images of the Simulated Computer Model Impact Events for Option A with SUT.	80
Table 4.13. Sequential Images of the Simulated Computer Model Impact Events for Option B with Passenger Car.	85
Table 4.14. Sequential Images of the Simulated Computer Model Impact Events for Option B with Pickup Truck (without Tire Disengagement).	88
Table 4.15. Sequential Images of the Simulated Computer Model Impact Events for Option B with Pickup Truck (with Tire Disengagement).	91
Table 4.16. Sequential Images of the Simulated Computer Model Impact Events for Option B with SUT.	93
Table 4.17. Sequential Images of the Simulated Computer Model Impact Events for Option C with Passenger Car.	96
Table 4.18. Occupant Risk and Vehicle Stability Information for Passenger Car.	97
Table 4.19. Sequential Images of the Simulated Computer Model Impact Events for Option C with Pickup Truck.	99
Table 4.20. Occupant Risk and Vehicle Stability Information for Pickup Truck.	100

Table 4.21. Sequential Images of the Simulated Computer Model Impact Events for Option C with SUT.....	102
Table 4.22. Occupant Risk and Vehicle Stability Information for SUT.....	103
Table 5.1. Barrier Dimensions.....	109
Table 7.1. Test Conditions and Evaluation Criteria Specified for <i>MASH</i> TL-4 Longitudinal Barriers.	145
Table 7.2. Evaluation Criteria Required for <i>MASH</i> TL-4 Longitudinal Barriers.....	147
Table 9.1. Events during Test No. 469760-06-1.	154
Table 9.2. Occupant Risk Factors for Test No. 469760-06-1.	157
Table 10.1. Events during Test No. 469760-06-2.	160
Table 10.2. Occupant Risk Factors for Test No. 469760-06-2.....	163
Table 11.1. Events during Test No. 469760-06-3.....	166
Table 12.1. Performance Evaluation Summary for <i>MASH</i> Test 4-10 on TxDOT LSMB.....	172
Table 12.2. Performance Evaluation Summary for <i>MASH</i> Test 4-11 on TxDOT LSMB.....	173
Table 12.3. Performance Evaluation Summary for <i>MASH</i> Test 4-12 on TxDOT LSMB.....	174
Table 12.4. Assessment Summary for <i>MASH</i> TL-4 Tests on TxDOT LSMB.	175

SI* (MODERN METRIC) CONVERSION FACTORS

APPROXIMATE CONVERSIONS TO SI UNITS

Symbol	When You Know	Multiply By	To Find	Symbol
LENGTH				
in	inches	25.4	millimeters	mm
ft	ft	0.305	meters	m
yd	yards	0.914	meters	m
mi	miles	1.61	kilometers	km
AREA				
in ²	square inches	645.2	square millimeters	mm ²
ft ²	square ft	0.093	square meters	m ²
yd ²	square yards	0.836	square meters	m ²
ac	acres	0.405	hectares	ha
mi ²	square miles	2.59	square kilometers	km ²
VOLUME				
fl oz	fluid ounces	29.57	milliliters	mL
gal	gallons	3.785	liters	L
ft ³	cubic ft	0.028	cubic meters	m ³
yd ³	cubic yards	0.765	cubic meters	m ³
NOTE: volumes greater than 1000L shall be shown in m ³				
MASS				
oz	ounces	28.35	grams	g
lb	pounds	0.454	kilograms	kg
T	short tons (2000 lb)	0.907	megagrams (or metric ton")	Mg (or "t")
TEMPERATURE (exact degrees)				
°F	Fahrenheit	5(F-32)/9 or (F-32)/1.8	Celsius	°C
FORCE and PRESSURE or STRESS				
lbf	poundforce	4.45	newtons	N
lbf/in ²	poundforce per square inch	6.89	kilopascals	kPa
APPROXIMATE CONVERSIONS FROM SI UNITS				
Symbol	When You Know	Multiply By	To Find	Symbol
LENGTH				
mm	millimeters	0.039	inches	in
m	meters	3.28	ft	ft
m	meters	1.09	yards	yd
km	kilometers	0.621	miles	mi
AREA				
mm ²	square millimeters	0.0016	square inches	in ²
m ²	square meters	10.764	square ft	ft ²
m ²	square meters	1.195	square yards	yd ²
ha	hectares	2.47	acres	ac
km ²	Square kilometers	0.386	square miles	mi ²
VOLUME				
mL	milliliters	0.034	fluid ounces	oz
L	liters	0.264	gallons	gal
m ³	cubic meters	35.314	cubic ft	ft ³
m ³	cubic meters	1.307	cubic yards	yd ³
MASS				
g	grams	0.035	ounces	oz
kg	kilograms	2.202	pounds	lb
Mg (or "t")	megagrams (or "metric ton")	1.103	short tons (2000lb)	T
TEMPERATURE (exact degrees)				
°C	Celsius	1.8C+32	Fahrenheit	°F
FORCE and PRESSURE or STRESS				
N	newtons	0.225	poundforce	lbf
kPa	kilopascals	0.145	poundforce per square inch	lb/in ²

*SI is the symbol for the International System of Units

CHAPTER 1. INTRODUCTION

1.1 BACKGROUND

Concrete median barriers are used to prevent serious cross-median crashes by preventing penetration of passenger vehicles and trucks into oncoming traffic. These solid concrete barriers are used on highways with high speeds and high traffic volumes not only to provide positive containment of vehicles but also to help reduce maintenance and repair needs.

When implemented in flood-prone areas, solid concrete median barriers can act as a dam for floodwaters, as recently occurred in the Houston and Beaumont areas during Hurricane Harvey or as occurs in Louisiana following a severe storm. These severe weather events raise the height of floodwaters and increase the severity of flooding on highways and surrounding roads and communities. Such flooding requires significant repair before highways can be reopened and the level of safety restored for motorists.

As a result, there was a need to develop and evaluate an appropriate median barrier in compliance with the American Association of State Highway and Transportation (AASHTO) *Manual for Assessing Safety Hardware (MASH)* Test Level 4 (TL-4) for implementation in flood-prone areas (1). To meet this objective, the Texas A&M Transportation Institute (TTI), in cooperation with the Texas Department of Transportation (TxDOT), designed a barrier to accommodate the passage of floodwater during severe weather events in order to reduce the severity of flooding, decrease risk to motorists and others in the area, and reduce the level of damage to the highway and surrounding area.

1.2 OBJECTIVE

The objective of this research was to develop and evaluate an appropriate median barrier for flood-prone areas that complies with AASHTO *MASH* TL-4. To satisfy this objective, researchers designed a barrier that allows floodwater to pass through it during severe weather events. This type of barrier can reduce the severity of flooding, risk to motorists and others, and level of damage to highways and surrounding areas.

The researchers designed and evaluated a new *MASH* TL-4 compliant concrete median barrier for implementation in flood-prone areas through engineering analyses, computer simulations, hydraulic large-scale testing, and full-scale vehicular crash testing. The researchers considered factors including but not limited to hydraulic and impact performance, maintenance, and cost.

The impact performances of roadside safety systems are judged on the basis of three factors: structural adequacy, occupant risk, and post-impact vehicle trajectory. The researchers tested the concrete median barrier based on *MASH* TL-4 criteria and utilized three types and specifications of vehicles for testing roadside safety systems: single-unit truck (SUT), quad-cab pickup, and passenger car.

For testing the structural adequacy of concrete traffic barriers at TL-4, the researchers used an SUT traveling at 56 mi/h at a 15-degree impact angle to verify the barrier capacity and ability to contain and redirect the SUT. The researchers also used a quad-cab pickup and passenger car to test the performance of a concrete barrier at TL-4 (traveling at 62 mi/h impact speed and a 25-degree impact angle). The researchers used these two tests to investigate the

ability of concrete traffic barriers to successfully contain and redirect light trucks, sport utility vehicles, and passenger cars. To achieve the objective, researchers proposed a work plan consisting of six tasks. Each task is summarized below.

1.3 WORK PLAN

1.3.1 Task 1. Conduct Project Management and Research Coordination

The researchers conducted project management activities and coordinated research activities including, but not limited to, project meetings between the Performing Agencies and the Receiving Agency, preparation of meeting notes, and documenting work efforts into monthly progress reports (MPRs).

The researchers conducted the following activities:

- Kick-off meeting.
- Progress meetings.
- Close-out meeting.
- MPRs.

The researchers conducted a Value of Research (VoR) assessment. In developing the VoR, the researchers identified sources for both qualitative and economic data, such as TxDOT construction bids (economic), material price lists from vendors (economic), pavement performance data (economic), and district personnel (qualitative).

The researchers completed the VoR Template, including the economic based calculations, the description of economic variables used within the calculations, and the qualitative values of the selected benefit areas.

The researchers evaluated the initial submission of the VoR Template and revised, if needed. TxDOT continued to identify qualitative and economic VoR data during the course of the research project. The researchers included this information within the resubmittal of the VoR Template at the end of the project within the project summary report and research report.

1.3.2 Task 2. Literature Review

The researchers performed a thorough literature search that was international in scope to assure a comprehensive review of relevant past or current research. Chapter 2 discusses what types of literature were explored.

Based on the results of the literature review, the researchers identified certain requirements or constraints, aspects of the testing, and evaluation criteria that needed to be considered for this project. The researchers analyzed, described, and critiqued relevant work from the literature review based on applicability and usefulness in developing barrier design options and a methodology for the hydraulic evaluation of the barrier systems. The researchers integrated any collected useful results into this project report.

1.3.3 Task 3. Develop and Evaluate Preliminary Design Concepts

The researchers developed concepts of a concrete median barrier for implementation in flood-prone areas. The design-preferred characteristics included profile shape and barrier height.

The researchers addressed basic requirements for the concrete median barrier system, including accommodation of service loads, to meet hydraulic and impact performance requirements. In addition, the researchers developed concrete median barrier design options with the primary intent to accommodate desired water flow and meet the AASHTO *MASH* requirements. The researchers considered placement of openings to reduce other hazards, such as hydroplaning, and to optimize driver safety by considering secondary effects of median barriers, including but not limited to glare shielding and passage of animals.

The researchers met with TxDOT representatives to present and discuss the concrete median system concepts. The researchers documented advantages and disadvantages for each design alternative, including any perceived performance benefits and application limitations. TxDOT then selected preferred design options for further evaluation in Task 3.

1.3.4 Task 4. Conduct Large-Scale Hydraulic Testing

The researchers conducted hydraulic testing of the selected preferred concrete median barrier designs to evaluate the passage of water through the openings to determine the most effective design from a hydraulic standpoint. The researchers conducted large-scale experiments on three preliminary designs that were based on theoretical rating curves from calculated head and discharge relationships.

Through these experiments, the researchers determined which of the barriers allowed adequate flows given varying flood conditions while still maintaining structural design elements necessary for strength and stability requirements.

Researchers performed laboratory tests to determine how the design—orientation, spacing, and location—of the openings affect:

- Flow of water through the barrier.
- Depth of flooding behind the barrier.
- Extent of backwater effects.

Upon determining the optimal hydraulic design of the concrete median barrier, the researchers provided guidance to TxDOT on how to use the measured relationships to estimate backwater effects during flood conditions and impact to upstream stakeholders.

1.3.5 Task 5. Develop Detailed Design and Perform Engineering Analysis

The researchers developed design details of the top three design options selected in Task 2 as candidates for detailed development and evaluation under vehicular impacts. The researchers performed detailed engineering analyses to determine (a) appropriate barrier reinforcement characteristics to resist vehicular impact loads per *MASH* TL-4 conditions, (b) proper barrier connections to the ground, and (c) appropriate dimensions and characteristics

of the openings and/or scuppers for each of the design concepts. The researchers verified whether each design could accommodate service load requirements.

Next, the researchers evaluated the ability of each design to meet impact performance requirements and provide desirable functional characteristics during flooding conditions. The researchers then used the results to assess the probability of each design concept to meet *MASH* TL-4 impact performance requirements and provide other desirable functional characteristics during flooding conditions.

At the end of each analysis, the researchers provided updated detailed drawings of the concrete median barrier systems to TxDOT. TxDOT reviewed the detailed design concepts and, based on the outcomes of Task 3 and Task 4, selected the preferred design option for further evaluation in Task 5.

1.3.6 Task 6. Construct Barrier System and Conduct Full-Scale Crash Testing

The researchers acquired the services of a subcontractor to construct the concrete median barrier system for testing. After construction of the concrete median barrier system, the researchers conducted *MASH* TL-4 full-scale crash tests following the approved test plan.

MASH provides guidance on the impact performance evaluation of roadside safety hardware. The test matrix recommended for the evaluation of longitudinal barriers under TL-4 consists of three tests:

1. ***MASH* Test 4-10:** An 1100C (2420-lb) passenger car impacting the critical impact point (CIP) along the length of need (LON) of the barrier at a nominal impact speed and angle of 62 mi/h and 25 degrees, respectively.
2. ***MASH* Test 4-11:** A 2270P (5000-lb) pickup truck impacting the CIP along the LON of the barrier at a nominal impact speed and angle of 62 mi/h and 25 degrees, respectively.
3. ***MASH* Test 4-12:** A 10000S (22,000-lb) SUT impacting the CIP along the LON of the barrier at a nominal impact speed and angle of 56 mi/h and 15 degrees, respectively.

MASH Tests 4-10 and 4-11 evaluate the barrier's ability to successfully contain and redirect passenger vehicles and determine occupant risk. *MASH* Test 4-12 evaluates the structural adequacy of the barrier system. Each of these tests is discussed in greater detail in future sections.

The researchers assessed the post-impact vehicle trajectory as part of *MASH* evaluation criteria to determine the potential for secondary impact of the impacting vehicle with other vehicles or fixed objects that can create further risk of injury to occupants of the impacting vehicle and risk of injury to occupants in other vehicles.

After construction of the concrete median barrier system, the researchers conducted the *MASH* TL-4 full-scale crash tests according to the approved test plan. *MASH* provides guidance on the impact performance evaluation of roadside safety hardware. The test matrix recommended for the evaluation of longitudinal concrete barriers under TL-4 consists of three tests, as listed in Section 1.3.5.

The researchers selected CIPs for the *MASH* testing by determining the location that maximizes pocketing and snagging of the vehicle against the tested system (*MASH* Tests 4-10 and 4-11) and maximizes the potential for failure of the concrete barrier (*MASH* Test 4-12). *MASH* provides information for the determination of CIPs for rigid and temporary barrier tests.

The researchers evaluated the vehicle crash tests in accordance with the criteria presented in *MASH* and judged the impact performance of the barrier based on three factors: structural adequacy, occupant risk, and post-impact vehicle trajectory. Structural adequacy is based upon the barriers' ability to contain and redirect the impacting vehicle. Occupant risk criteria rate the potential risk of hazard to occupants in the impacting vehicle, and to some extent, other traffic, pedestrians, or workers in construction zones, if applicable. The *MASH* occupant risk criteria include occupant impact velocity and ridedown acceleration, which are computed using the acceleration-time histories measured at the vehicle's center of gravity. These criteria are based on a flail space model that assumes an unrestrained occupant. The researchers also assessed the post-impact vehicle trajectory as part of the *MASH* evaluation criteria to determine the potential for secondary impact.

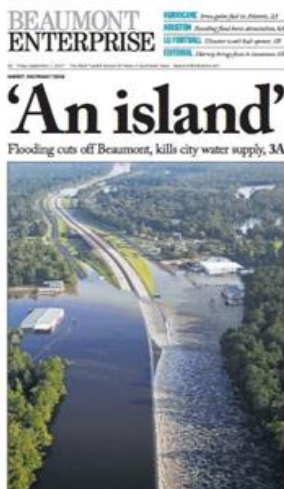
CHAPTER 2. LITERATURE REVIEW*

2.1 INTRODUCTION

Concrete median barriers are used to prevent serious cross-median crashes by preventing penetration of passenger vehicles and trucks into oncoming traffic. These solid concrete barriers are used on highways with high speeds and high traffic volume to not only provide positive containment of vehicles but also help reduce maintenance and repair needs. Any required barrier maintenance or repair increases risk to maintenance personnel and can result in significant congestion if a lane closure is required.

During Hurricane Harvey, it was observed that solid, rigid concrete median barriers can act as a dam for floodwaters. This situation raises the height of floodwaters and increases the severity of flooding on both the highway and the surrounding roads and community. This rise in floodwaters increases the risk to both motorists and others in the area and can also increase the level of flood damage to the road network and any nearby structures. Numerous highways in the Houston and Beaumont areas were severely affected by the damming of water caused by solid, rigid concrete median barriers, including Interstate Highway (IH) 10 and United States Highway (US) 59 in Houston, and US 96 in Beaumont. In the Beaumont area, several sections of median barrier were blown up to help mitigate the increased flooding being caused by the solid concrete barrier.

A recent severe storm in Louisiana on IH 12 resulted in a similar scenario to the one experienced in Texas as a result of Hurricane Harvey. A 19-mi length of rigid, solid concrete median barrier that was constructed to divide the eastbound and westbound lanes of IH 12 to prevent head-on crashes on the heavily traveled highway acted as a dam, causing greater flood damage to areas north of the highway. Figure 2.1 illustrates examples of flooding scenarios where rigid, solid concrete median barriers are implemented.



(a) In Beaumont, Texas, several sections of median barrier were exploded to help mitigate the increased flooding being caused by the solid concrete barrier (2).



(b) The flooded westbound lanes of Interstate 12 with a concrete barrier damming up the flow of water (Louisiana) (3).

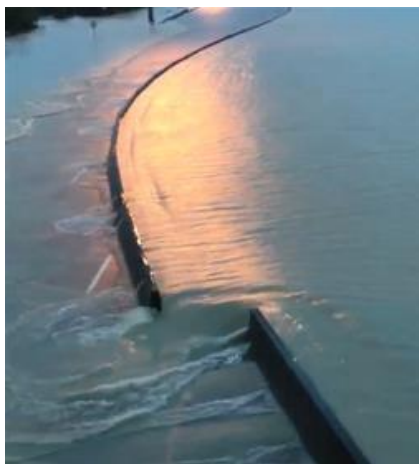
Figure 2.1. Examples of Flooding Scenarios Where Rigid, Solid Median Concrete Barriers Are Implemented.

* The opinions/interpretations identified/expressed in this chapter are outside the scope of TTI Proving Ground's A2LA Accreditation.

In the Houston area, large sections of portable, solid concrete barriers used as permanent median applications were displaced or broken by the floodwaters. These situations required significant repair before the highways could be reopened and a level of safety restored for motorists. Figure 2.2 illustrates examples of flooding scenarios where portable concrete median barriers were installed as permanent applications.



(a) Portable concrete median barrier on the Eastex Freeway was broken and thrust aside after Hurricane Harvey in Humble, Texas (left and above) (4).



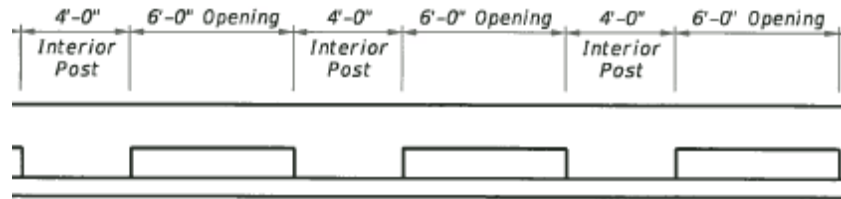
(b) Barrier pushed away from the roadway and finally split apart on Texas USHwy 59 (5).

Figure 2.2. Examples of Flooding Scenarios Where Portable Concrete Median Barriers Are Installed as Permanent Applications.

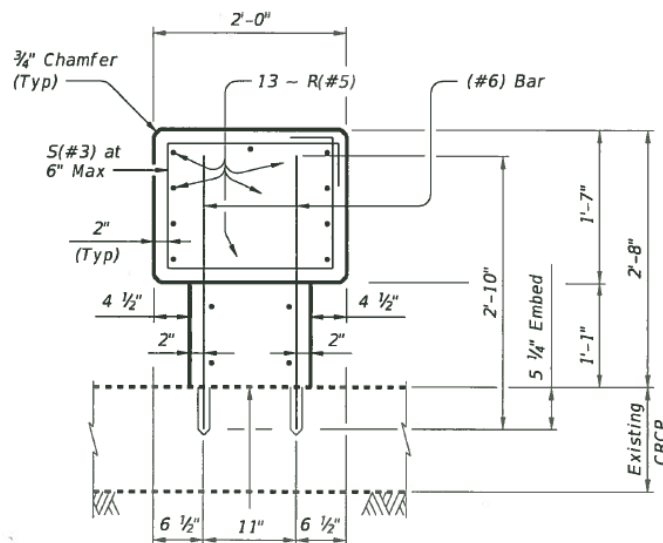
Because median barriers are an important safety feature that provide an increased level of safety for motorists, concrete median barriers cannot be removed. Consequently, a need exists for a crashworthy median barrier that is designed to accommodate the passage of floodwater during severe weather events. When implemented in flood-prone areas, such a barrier would reduce the severity of flooding, decrease risk to motorists and others in the area, and reduce the level of damage to the highway and surrounding area.

In some areas where severe flooding occurred, the existing concrete median barrier was replaced with a newly developed median barrier version of the existing TxDOT T223 bridge rail to allow for the water to drain through the barrier's openings (6). The median version of the

T223 bridge rail is a post-and-beam concrete barrier that consists of a 19-inch × 24-inch concrete beam supported by 13-inch × 15-inch concrete posts. The 4-ft-long interior concrete posts alternate with 6-ft-long × 13-inch-tall openings. The concrete barrier is 32 inches tall. Figure 2.3 illustrates the median version of the T223 concrete barrier.



(a) Elevation View



(b) Perpendicular View

Figure 2.3. Drawing of Median Version of TxDOT T223 Concrete Barrier.

2.2 MASH TESTING STANDARD CRITERIA

The AASHTO *MASH* roadside safety hardware testing and evaluation criteria, first published in 2009 and updated in 2016, were intended to be the latest in a series of documents to provide guidance on testing and evaluation of roadside safety features (1, 7). *MASH* standards contain comprehensive updates to crash test and evaluation procedures to reflect changes in the vehicle fleet, operating conditions, and roadside safety knowledge and technology. *MASH* supersedes National Cooperative Highway Research Program (NCHRP) Report 350, *Recommended Procedures for the Safety Performance Evaluation of Highway Features* (8).

The project described herein was designed to fit a TL-4 standard, and as such, *MASH* dictates use of the following three tests:

1. **MASH Test 4-10:** An 1100C (2420-lb) passenger car impacting the CIP along the LON of the barrier at a nominal impact speed and angle of 62 mi/h and 25 degrees, respectively. An uninstrumented, 50th-percentile male anthropomorphic test dummy

is required in this test by *MASH* guidelines to account for mass distribution and for visualization of occupant kinematics.

2. ***MASH* Test 4-11:** A 2270P (5000-lb) pickup truck impacting the CIP along the LON of the barrier at a nominal impact speed and angle of 62 mi/h and 25 degrees, respectively. In this test, a dummy is not required for inclusion in the vehicle unless a potential interaction is anticipated with the tested system and/or if the barrier being tested is taller than 32 inches.
3. ***MASH* Test 4-12:** A 10000S (22,000-lb) SUT impacting the CIP along the LON of the barrier at a nominal impact speed and angle of 56 mi/h and 15 degrees, respectively. In this test, a dummy is not required to be included in the vehicle.

In a previously conducted TxDOT research project, TTI researchers used impact simulations to calculate lateral impact loads for *MASH* TL-4 impact conditions for a rigid single-slope barrier with various heights (9). Results indicated that the lateral loads for *MASH* TL-4 were significantly greater than those loads specified for NCHRP Report 350 TL-4 impact conditions. Further, the lateral impact force varied with rail height. For a 36-inch-tall barrier, the design impact load was determined to be approximately 68 kip. As the height of the barrier increases, more of the cargo box of the SUT is engaged, and the lateral load on the barrier increases. For a barrier height of 42 inches, the lateral design impact load increases to approximately 80 kip.

Although the minimum rail height to achieve *MASH* TL-4 impact performance is 36 inches, some TL-4 rails are designed with a height greater than 36 inches to provide improved stability for heavy truck impacts and to accommodate future pavement overlays. Although not a specific *MASH* evaluation criterion, consideration should be given to the potential for occupant head excursion and contact with components of the rail system for these taller height barriers.

2.3 LITERATURE REVIEW

A thorough literature search was performed to assure a comprehensive review of relevant past or current research. Specific consideration was given to any identified research studies that addressed the following:

- Cross-highway water flow requirements during severe weather events required to prevent a significant rise in floodwater by a highway barrier, including concrete bridge barriers.
- Non-proprietary concrete barrier systems, either existing or under development, for implementation in flood-prone areas, including concrete bridge barriers.
- Identification and review of testing performance of existing compliant rigid and portable concrete barriers with openings or scuppers.

2.3.1 Cross-Highway Water Flow Requirements during Severe Weather Events Required to Prevent Significant Rise in Floodwater by Highway Barrier, Including Concrete Bridge Barriers

2.3.1.1 Floodway Encroachment

An *encroachment* is defined by the Federal Highway Administration (FHWA) as any action or development within the limits of the base floodplain that could impede flood flows (23 CFR § 650.105 [10]). The TxDOT *Hydraulic Design Manual (11)* states that for any TxDOT project with participation by FHWA that involves an encroachment on the 1 percent annual exceedance probability (AEP) (100-year event) floodplain, the location and design of the project must comply with FHWA Policy 23 CFR 650, Subpart A. Furthermore, this policy specifically designates the term *regulatory floodway* as a floodplain area that is reserved in an open manner by federal, state, or local requirements (i.e., unconfined or unobstructed either horizontally or vertically) to provide for the discharge of the base flood so the cumulative increase in water surface elevation is no more than a designated amount (not to exceed 1 ft, as established by the Federal Emergency Management Agency [FEMA]) (10). Any encroachment resulting in this increase of the water surface elevation by more than 1 ft requires that the FEMA floodplain maps be redrawn.

2.3.1.2 Energy in Open-Channel Flow

The general energy equation describes the energy head at two locations within an open channel (12). This form of the energy equation is normalized to the unit weight of the fluid; therefore, the terms shown in Equation 2.1 all have dimensions of length and represent the energy head due to various forces. This form of the energy equation, accounting for non-uniform flow distribution (α_1 , α_2) and energy lost from friction (h_L), is also known as Bernoulli's equation, which neglects head losses. The remaining terms z , h , and v represent the depth relative to a datum, total fluid depth, and velocity at Locations 1 and 2. The final term, g , represents the gravitational constant at all locations.

$$z_1 + h_1 + \alpha_1 \frac{v_1^2}{2g} = z_2 + h_2 + \alpha_2 \frac{v_2^2}{2g} + h_L \quad (2.1)$$

The following simplifications of Equation 2.1 were presented by Klenzendorf (13). The first simplification comes from the assumption of a small channel slope resulting in approximately equal z values, in which case they can be dropped from both sides of the equation. If the velocity is uniform, α_1 and α_2 are equal to a value of 1, allowing their omission from the equation. Finally, assuming that friction losses are negligible, the specific energy can be expressed according to Equation 2.2, where Q is the channel discharge (volumetric flow rate) and A is the flow cross-section area. The specific energy in a channel section is defined as the energy per unit weight of water at any section of a channel measured with respect to the channel bottom (12).

$$E = h + \frac{v^2}{2g} = h + \frac{Q^2}{2gA^2} \quad (2.2)$$

If the channel section is rectangular, the unit flow rate, q , may be defined as the volumetric flow rate per unit width of the channel (b).

$$q = \frac{Q}{b} = \frac{vA}{b} = \frac{vbh}{b} = vh \quad (2.3)$$

Equation 2.3 uses the flow rate equation $Q = vA$. The area is expanded into its height and width components, and the expression can be simplified to place the unit flow rate in terms of the fluid velocity and height. Plugging these expressions into Equation 2.2 yields the following:

$$E = h + \frac{q^2}{2gh^2} \quad (2.4)$$

This equation has three roots; however, one is a negative number with no physical meaning. The remaining two roots exist at every point greater than the value at the critical point.

Figure 2.4 shows the relationship between specific energy and water depth, where the horizontal peak represents the critical value.

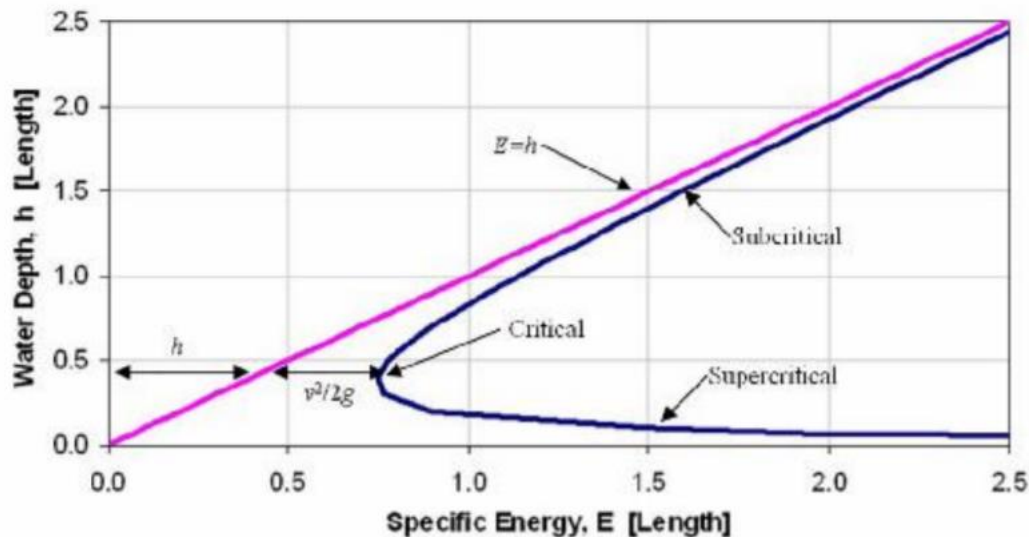


Figure 2.4. Specific Energy Curve.

Also plotted in Figure 2.4 is an $E = h$ line that represents the potential energy given a completely static fluid. The abscissa for this line is therefore equal to the water depth, and the difference between this value and the abscissa for the curve is equal to the kinetic energy. It follows that adding these two values together results in the total specific energy as plotted on the curve.

Taking the derivative of Equation 2.4 (dE/dh) yields the following:

$$h_c = \left(\frac{q^2}{g}\right)^{1/3} \quad (2.5)$$

Setting this equation equal to zero provides the critical energy—that is, the minimum specific energy. Flows at water depths above this point are known as subcritical flows and correspond to a lesser flow velocity, while water depths below this point are known as supercritical flows and correspond to a greater flow velocity.

By assuming that a highway median barrier causes a critical flow state at or near the obstruction location, Equation 2.5 generates the water depth at that location. As demonstrated by Bin-Shafique et al. (14), the energy equation can be rewritten to describe the critical depth as a function of the upstream water depth, assuming critical depth occurs further upstream:

$$h_c + \alpha_c \frac{v_c^2}{2g} = h_u + \alpha_u \frac{v_u^2}{2g} + h_L \quad (2.6)$$

where the subscript u represents the upstream location and c represents the critical location.

Equation 2.6 can be simplified further by assuming a subcritical state in the upstream flow due to the median barrier obstruction. As illustrated by Figure 2.4, an assumption of subcritical upstream flow will result in a negligible kinetic energy when compared to the potential energy ($\frac{v_u^2}{2g} \ll h_u$) at that point. Additionally, plugging in Equation 2.2 and assuming uniform flow and negligible friction losses, the specific energy can be expressed as follows:

$$h_c + \frac{q^2}{2gh_c^2} = h_u \quad (2.7)$$

Rearranging Equation 2.5 to solve for the unit flow rate gives the result $q = gh_c^3$. This result can then be inserted into Equation 2.7, and the resulting equation can be rearranged to solve for h_c .

$$h_c = \frac{2}{3} h_u \quad (2.8)$$

This equation describes the critical depth as a function of the upstream depth. Since the critical depth is not a parameter that can be directly measured, Equation 2.8 provides an estimation that can be used in mathematical models.

2.3.2 Weir Equation

A *weir* is defined as a device or overflow structure that is placed normal to the direction of flow. It serves the purpose of backing up water so that in flowing over the weir, the water goes through a critical depth (15). Sharp-crested weirs specifically have a sharp edge at the top that allows the nappe to separate from the weir and flow according to the principle of projectile motion (12). A sharp-crested weir diagram is included in Figure 2.5, where P_w is the weir height and H is the head above the weir crest, as shown in the next section.

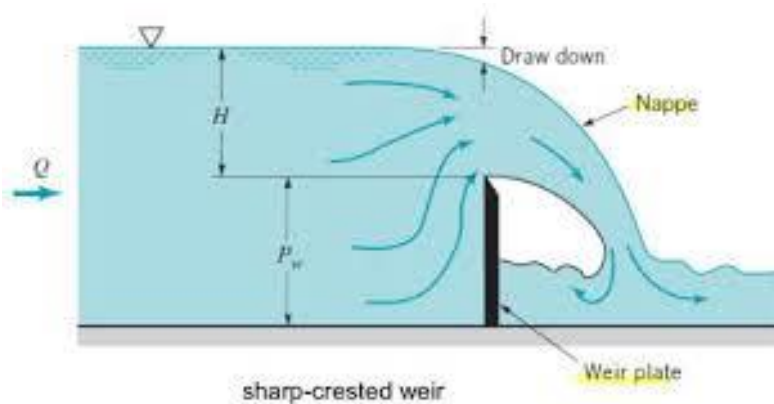


Figure 2.5. Sharp-Crested Weir Diagram.

This research utilized a sharp-crested weir for the purposes of average flow rate measurement across a rectangular channel. For a sharp-crested weir in a rectangular channel, the following equation is used, where Q = average channel volumetric flow rate, C_d = weir discharge coefficient, B = channel width, and H = head above the weir crest:

$$Q = C_d \frac{2}{3} \sqrt{2g} B H^{3/2} \quad (2.9)$$

The coefficient C_d accounts for the nonparallel streamlines seen in Equation 2.5 that are induced by the drawdown effect and crest contractions. This constant is approximately equal to 0.62 (15). The crest contraction forces the streamline immediately upstream to flow over the weir crest, creating the nappe on the downstream side (16). Equation 2.9 assumes a fully aerated nappe in which both the upper and lower nappe surfaces are subject to atmospheric pressure. Incomplete aeration reduces pressure beneath the nappe and has the consequences of (a) a change in shape of the nappe, (b) an increase in discharge that sometimes results in a pulsating nappe, and (c) unstable performance of the weir model (12). All three consequences introduce uncertainty into flow measurements.

Equation 2.9 simplifies the experimental flow rate measurement because only a single water depth measurement is required to quantify volumetric discharge. This measurement should be taken at a location where the flow is approximately even, and drawdown effects are negligible. In practice, this location is usually taken to be five times the depth of the drawdown away from the weir.

2.3.2.1 Physical Modeling and Scaling

Often in hydraulic engineering, physical models are used to study fluid flow phenomena under controlled laboratory conditions. Proper modeling takes into account modeling relationships designed to create hydraulic similitude between the physical model and its prototype. The prototype is the full-sized object being modeled. Similitude is accomplished through the use of dimensional analysis to ensure certain dimensionless parameters are the same for both the model and prototype. The Froude number is the most significant dimensionless number for open-channel models (17). It is defined in Equation 2.10:

$$Fr = \frac{v}{\sqrt{gL}} \quad (2.10)$$

where Fr is the Froude number, L is a characteristic length, and all other variables are as previously defined.

Froude number modeling is used when the inertial forces and gravitational forces are more important than surface tension or viscous forces because the Froude number represents the ratio of inertial forces to gravitational forces. Froude number modeling requires that $Fr_m = Fr_p$, where the subscripts m and p represent the model and prototype, respectively. In addition to hydraulic similitude between the model and prototype, constant geometric and kinematic similitude must be maintained (17). This process is accomplished through the geometric length ratio and velocity ratio, respectively. The length ratio is defined as follows:

$$L_r = \frac{L_m}{L_p} \quad (2.11)$$

where L_r is the length ratio, L_m is the model length scale, and L_p is the prototype length scale.

For this research, all length dimensions for individual bridge rails were scaled to half-size so that $L_r = 1/2$. Since this ratio is maintained for all dimensions, geometric similarity is maintained. To accomplish kinematic similarity, a velocity scale ratio is defined:

$$V_r = \frac{v_m}{v_p} \quad (2.12)$$

where V_r is the velocity scale ratio.

As previously mentioned, in Froude number modeling, the Froude numbers of the model and prototype are the same, as shown in Equation (2.13):

$$\frac{v_m}{\sqrt{gL_m}} = \frac{v_p}{\sqrt{gL_p}} \quad (2.13)$$

Rearranging Equation 2.13 and solving for the velocity scale ratio gives the following:

$$V_r = \sqrt{L_r} \quad (2.14)$$

Since the volumetric flow rate Q is defined as a velocity times an area, the following flow rate ratio, Q_r , can be determined as follows:

$$Q_r = V_r L_r^2 \quad (2.15)$$

Substituting Equation 2.14 into Equation 2.15 gives the following:

$$Q_r = L_r^{5/2} \quad (2.16)$$

Through this type of Froude number modeling, various characteristics and parameters between the model and prototype can be related. In addition to modeling scales, the Froude number can be used to determine when critical depth occurs. As previously mentioned, critical depth occurs at the minimum specific energy (shown in Figure 2.4). When the Froude number is equal to unity, critical depth occurs. When the Froude number is greater than unity, supercritical depth occurs, and when the Froude number is less than unity, subcritical depth occurs.

2.3.2.2 Charbeneau Model

The hydraulic performance of various bridge rail types was studied by Charbeneau et al. (18) in order to determine the hydraulic performance and the impact of different rails on the surrounding floodplains during different flood events. The result of this research is a three-parameter model that can be used to predict the free-flow rail rating curve. Using the energy equations detailed in the previous sections, this model can be used to estimate the flow through a bridge rail inlet given the upstream water depth.

The Charbeneau (18) model was expanded from the two-parameter model originally presented by Charbeneau et al. (19). In the earlier model, rating curves were created in order to define the hydraulic performance in inlet-controlled highway culverts. A third parameter was added to this model to define all potential flow scenarios through a bridge rail, as Figure 2.6 shows. The rail presented in this figure is TxDOT T203. This rail consists of a continuous concrete beam supported underneath by concrete posts.

Three different flow types, designated Type 1, Type 2, and Type 3, are explored in the Charbeneau (18) model. These flow conditions are shown in Figure 2.6. Type 1 flow describes the condition in which the water depth at the rail is less than the height of the bridge rail opening

($h_u < h_{rL}$). This unsubmerged flow condition is defined by the continuity equation $Q = vA$. Type 2 flow describes the submerged condition of the bridge rail opening in which the water depth at the rail is greater than the height of the opening but less than the total rail height ($h_{rL} < h_u < h_r$). This condition is governed by orifice flow equations. Type 3 flow describes the condition in which the water depth is greater than the total bridge rail depth ($h_u > h_r$). This condition is governed by both weir and orifice equations. Based on the input parameters, this model predicts which flow type governs as well as defines the transition points between each different condition.

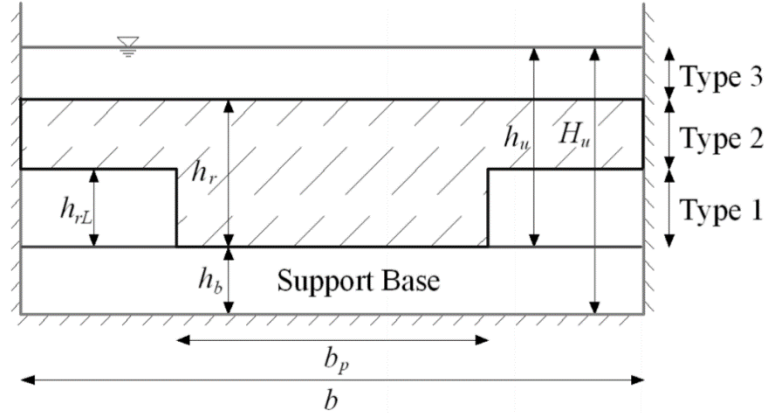


Figure 2.6. Three Different Flows in Charbeneau Model.

2.3.2.2.1 Type 1 Flow

For unsubmerged flow through the bridge rail opening, the model assumes the critical depth occurs at the obstruction due to choking from the rail (20). The base of the rail is selected as the model datum in order to separate the rail hydraulics from the overall bridge hydraulics. Choosing this datum removes the bridge height (H_u) from the model, leaving only the bridge rail height to calculate the specific energy. This flow is governed by the continuity equation, in which the area and velocity (v_c) are expanded to include the bridge rail parameters.

$$Q = Av_c = C_b(b - b_p)h_c\sqrt{gh_c} \quad (2.17)$$

In Equation 2.17, the critical velocity (v_c) is set equal to $\sqrt{gh_c}$ based on the assumption of an equal Froude number, as described in Equation 2.10 (21). In the critical flow through a rectangular opening, $h_c = \frac{2}{3}E_c$, where the critical energy, E_c , is assumed to be approximately equal to the upstream specific energy, E_u (22). The width of the bridge rail opening is described as the difference between the total rail width in the section and the rail support ($b - b_p$). The coefficient C_b represents energy losses between the upstream flow and the rail (19). The model applies this factor by creating a new effective width of the bridge rail opening that is reduced from the physical width.

Equation 2.17 can be rearranged to solve for the dimensionless flow rate, $\frac{Q}{A_r\sqrt{gh_f}}$. Substituting the critical depth into this new equation yields the following:

$$\frac{Q}{A_r\sqrt{gh_f}} = C_b F_o \left(\frac{h_f}{h_{rL}}\right) \left(\frac{2E_u}{3h_r}\right)^{1.5} \quad (2.18)$$

In Equation 2.18, F_0 equals the fractional open space in the bridge rail, and A_r equals the total rail area. The fractional open space represents the ratio of the rail opening area to the total rail area (A_0/A_r). This ratio can be expanded to include the model parameters:

$$F_0 = \frac{A_0}{A_r} = \frac{(b-b_p)h_{rL}}{bh_r} \quad (2.19)$$

2.3.2.2.2 Type 2 Flow

The water depth for Type 2 flow is greater than the opening height but less than the overall rail height, resulting in flow through the fully submerged opening. This flow can be modeled as flow through an orifice or sluice gate (19).

$$E_u \approx h_m + \frac{v_m^2}{2g} = C_c h_{rL} + \frac{v_m^2}{2g} \quad (2.20)$$

In Equation 2.20, v_m is the velocity at the rail, and h_m is the water depth at the point of least diameter of the stream. As shown, this value is equal to $C_c h_{rL}$, where C_c is the vertical contraction coefficient that is combined with h_{rL} to create a new effective height for the opening. Like C_b , the coefficient C_c represents energy losses between the upstream flow and the rail (20).

Plugging the continuity equation into Equation 2.20 and solving for the dimensionless flow rate, $\frac{Q}{A_r \sqrt{gh_r}}$, yields the following:

$$\frac{Q}{A_r \sqrt{gh_r}} = C_b C_c F_0 \sqrt{2 \left(\frac{E_u}{h_f} - C_c \frac{h_{rL}}{h_r} \right)} \quad (2.21)$$

In order to determine the transition point between Type 1 flow and Type 2 flow, Equation 2.5 and Equation 2.7 can be set equal to each other and solved for E_u . The result is a cubic function in which one root is negative with no physical meaning, while the remaining two roots are accounted for in the double root $3/2$. Using this root value, the specific energy at this point can be found by the following equation:

$$\frac{E_u}{h_r} = \frac{3}{2} C_c \frac{h_{rL}}{h_r} \quad (2.22)$$

In Equation 2.22, the specific energy is normalized to the rail height. At this transition point, both the rating curve and its slope are continuous, resulting in a smooth transition.

2.3.2.2.3 Type 3 Flow

The water depth for Type 3 flow is greater than the overall rail height, resulting in flow through the fully submerged opening as well as flow over the top of the rail. This flow can be modeled as a combination of orifice and weir flows. Flow over the rail was modeled as flow over a broad-crested weir based on the ratio of the difference between the upstream specific energy of the rail height to the thickness of the rail (23).

$$Q = C_d \frac{2}{3} b \sqrt{\frac{2}{3} g (E_u - h_r)^{1.5}} \quad (2.23)$$

In Equation 2.23, C_d is the weir discharge coefficient. This parameter differentiates the values calculated from different weir types since C_d is larger for a short-crested weir than for

broad-crested weirs (23). Rearranging Equation 2.23 to solve for the dimensionless flow rate and adding it to the Type 2 rating curve in Equation 2.21 yields the Type 3 rating curve:

$$\frac{Q}{A_r \sqrt{g h_r}} = C_b C_c F_o \sqrt{2 \left(\frac{E_u}{h_f} - C_c \frac{h_{rL}}{h_r} \right)} + C_d \left(\frac{2}{3} \right)^{1.5} \left(\frac{E_u}{h_r} - 1 \right)^{1.5} \quad (2.24)$$

The transition point between Type 2 and Type 3 flows occurs when the upstream specific energy is greater than the height of the rail.

$$\frac{E_u}{h_r} \geq 1 \quad (2.25)$$

The free-flow rating curve for a bridge rail can be determined based on the three flow types defined in Equations 2.18, 2.21, and 2.24, with transition points defined in Equations 2.22 and 2.25.

2.3.2.3 Experimental Methods for Charbeneau Model

The parameters for the Charbeneau model must be obtained experimentally (24). Experimental testing was conducted independently for multiple model bridge rails in a 150-cm (5-ft) rectangular channel with zero slope (Figure 2.7). The nine rails tested were the single-slope traffic rail (SSTR), T221, T501, T411, T203, T101, T101D, weir rail, and Wyoming rail. The data collected for this experiment were upstream and downstream water depths through the use of pitot tubes connected to an inclined manometer board. The model rails were scaled to half the size of standard TxDOT dimensions in most cases; however, certain adjustments had to be made to accommodate the space limitations within the channel. In these cases, the fractional open space was conserved. The primary construction material was wood, while specific rails such as the T101 and Wyoming rail were constructed out of metal. To mitigate any swelling in the wood, all surfaces were coated with waterproof primer. Since this experiment was not analyzing the hydraulic stability of the rails, the bases were anchored down to the channel.



Figure 2.7. Experimental Setup for Bridge Rail in Rectangular Channel.

To test the free-flow rating curve, the flow rate was set and allowed to reach steady state before any measurements were taken. Once steady state was achieved, the flow rate and upstream water depth were measured. Each time the flow rate was changed, it was allowed to reach steady state before further measurements were taken. For submergence testing, a tailwater gate was used to vary the downstream depth by means of a hydraulic jump while the flow rate

remained constant. Both the downstream and upstream water depths were measured each time the tailwater gate was adjusted.

The unknown parameter values in the mathematical models (C_b , C_c , C_d , m , and B) are used in the model equations and compared to the observed data in non-dimensional form. The standard error between the observed data and the predicted model results is minimized using the following equation in order to determine the appropriate values for each parameter:

$$S. E. = \sqrt{\frac{1}{N} \sum_{i=1}^N \left[\left(\frac{E_u}{h_r} \right)_d - \left(\frac{E_u}{h_r} \right)_m \right]^2} \quad (2.26)$$

In Equation 2.26, $S.E.$ is the standard error for N observed data points. The subscript d corresponds to the measured data for the dimensionless flow rate, and the subscript m represents the mathematical model results. Minimizing the standard error is accomplished by changing the model parameter values so that the model results closely match the observed data.

2.3.2.4 Charbeneau Results

In Charbeneau (18), the dimensionless upstream specific energy (E_u/h_r) was plotted (Figure 2.8) as a function of the dimensionless flow rate ($\frac{Q}{A_r \sqrt{gh_r}}$) to determine the free-flow rating curve for each of the tested bridge rails. The two most hydraulically efficient (least impact on upstream water depth) rails were the T101 and Wyoming rail, with the Wyoming rail performing better at higher flow rates. The second most hydraulically efficient rails were the T411 and T203, with the remaining rails all performing with appreciably less efficiency.

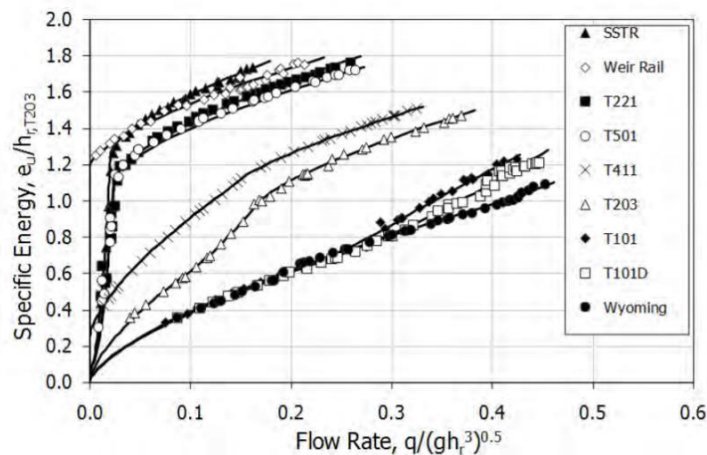


Figure 2.8. Bridge Rail Rating Curves. (Charbeneau, 2008)

The primary factor for hydraulic efficiency is the fractional open space, as can be seen by comparing the data in Figure 2.8 with the physical barriers in Figure 2.9. The rails not presented in Figure 2.8 are all solid rails with minimal openings, resulting in a much lower hydraulic efficiency. Although the fractional open space between the rails T203 and T411 is similar, the location of the opening at the base combined with the greater opening width results in a greater hydraulic efficiency for T203. This factor is especially true at low flow rates.



(a) T101



(b) Wyoming Rail



(c) T203



(d) T411

Figure 2.9. Tested Bridge Rails.

2.3.2.5 Streamlined Barrier Openings

2.3.2.5.1 Flow Separation

In a viscous fluid, the velocity at the surface of a solid boundary is zero, while the free-stream velocity away from the interface is non-zero. In between these two flow conditions lies the boundary layer, where velocity changes from zero to the free-stream velocity. Flow around obstructions can result in flow separation—the separation of a fluid from the boundary layer followed by the subsequent recirculatory flows known as turbulent eddies (16). Over time, these eddies can wear down the concrete corners, potentially diminishing the structural integrity of the median barrier and decreasing its life span.

Flow separation is primarily a function of obstruction shape, roughness, and a non-dimensional parameter known as the Reynolds number:

$$Re = \frac{VD}{\nu} = \frac{VR_h}{\nu} \quad (2.27)$$

where V is the fluid velocity, D is the diameter or width of the barrier opening, ν is the kinematic viscosity, and R_h is the hydraulic radius of the channel. The Reynolds number is an important parameter in open-channel flow characterization, with values less than 500 indicating laminar flow and values greater than 750 indicating turbulent flow. In terms of flow separation, there are negligible effects at Re less than 50 and increasing effects as Re increases from that point.

2.3.2.5.2 Drag Coefficients

A second important parameter affecting the wear of concrete median barriers is the drag coefficient. Streamlining a square corner can greatly reduce the drag coefficient for flow through an orifice, thereby reducing wear along the barrier opening. Akiba et al. (25) explored the effect of different orifice shapes (Figure 2.10) on the overall drag coefficient. It was determined that as the orifice edge curvature of the corners increased, their respective drag coefficients decreased.

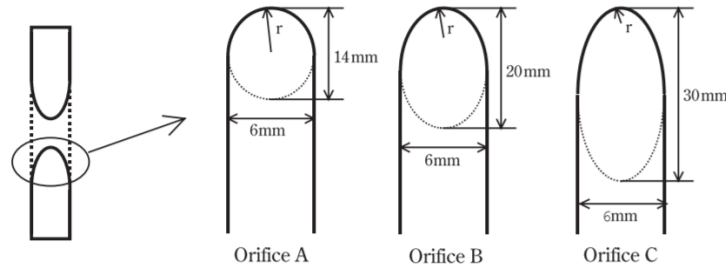


Figure 2.10. Different Curvatures Studied by Akiba et al.

2.3.2.6 Stability of Concrete Barrier

Two of the primary failure modes for concrete barriers during flooding events are overtopping and sliding (26). Bin-Shafique et al. (14) detailed the process for examining the forces behind these two failure modes.

Based on the principle of mechanics (27), the factor of safety (FS) against overturning about Point C in Figure 2.11 may be expressed by the equation shown immediately following the figure.

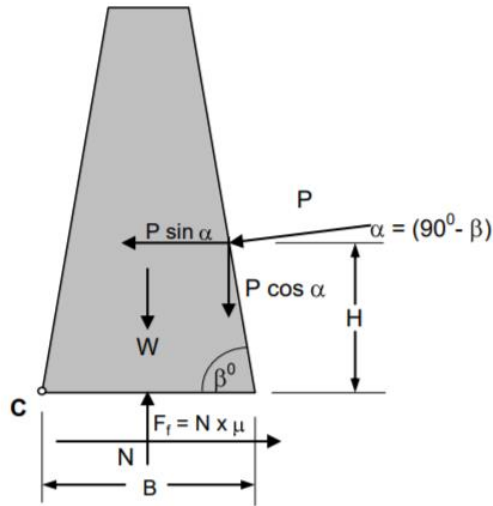


Figure 2.11. Free Body Diagram for Typical Median Barrier (Bin-Shafique, 2011)

$$FS_{\text{overturning}} = \frac{\sum M_R}{\sum M_0} \quad (2.28)$$

where,

$\sum M_R$ = sum of the moments of forces tending to resist overturning.
 $\sum M_0$ = sum of the moments of forces tending to overturn about Point C.

In Figure 2.11:

$$\sum M_R = W \times 0.5B + [P \cos(\alpha)] \times [B - H \cot(\beta)] \quad (2.29)$$

where,

W = weight of the temporary concrete traffic barrier (TCTB).

B = width of the TCTB at base.

P = hydrodynamic force per unit length of the TCTB, which acts perpendicular to the surface and can be calculated from the specific energy.

H = vertical distance of the resultant force, which can be determined from the pressure diagram.

Also:

$$\sum M_0 = P \sin(\alpha) \times H \quad (2.30)$$

Additionally, buoyant forces from the displacement fluid add to the overturning moment (16).

$$F_b = \gamma V_b \quad (2.31)$$

where,

F_b = buoyant force acting upward on the bottom of the median barrier.

γ = specific weight of water.

V_b = volume of displaced fluid.

Similarly, the FS against sliding may be expressed with this equation:

$$FS_{\text{overturning}} = \frac{\sum F_R}{\sum F_d} \quad (2.32)$$

where,

$\sum F_R$ = sum of horizontal resisting forces.

$\sum F_d$ = sum of horizontal driving forces.

In Figure 2.11:

$$\sum F_R = N\mu = \mu[W + P \cos(\alpha)] \quad (2.33)$$

where,

μ = coefficient of static friction, which is a function of two friction surfaces.

In addition:

$$\sum F_d = P \sin(\alpha) \quad (2.34)$$

Bin-Shafique et al. (14) explored the effects of buoyancy and friction loss on the stability of TCTBs. For various upstream and downstream water depths, including fully submerged conditions, the buoyant force acting on the median barrier varied from 45 percent to 48 percent of the opposing gravitational force. The coefficient of friction was highly affected by the roadway surface type and presence of sand or silt particles underneath the barrier. It is expected that permanent concrete median barriers will be appreciably more resilient against these two hydraulic phenomena.

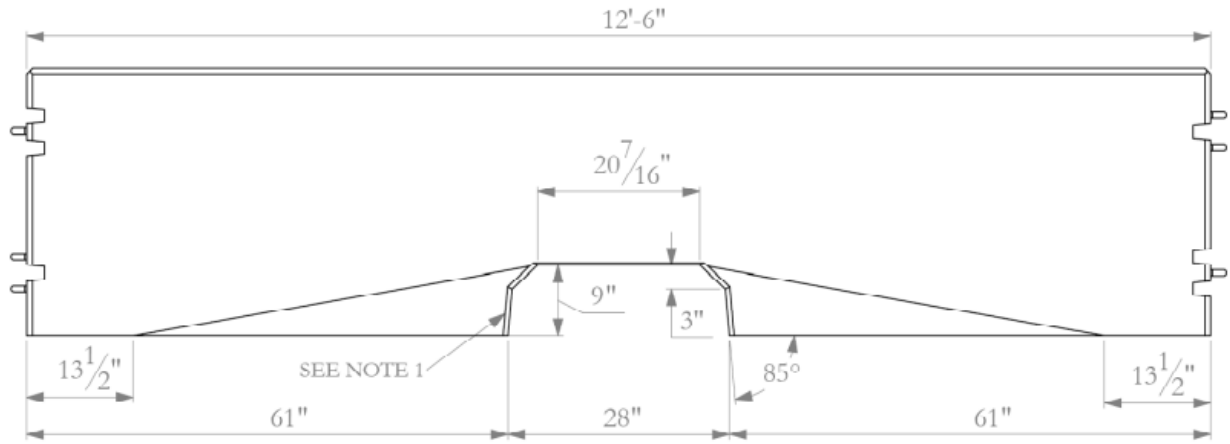
2.3.3 Non-proprietary Concrete Barrier Systems, Either Existing or Under Development, for Implementation in Flood-Prone Areas, Including Concrete Bridge Barriers

In 2010, Williams et al. completed a research study that tested and evaluated the Washington State Department of Transportation (WSDOT) pin-and-loop concrete barrier with drainage slots per *MASH* Test 3-11 (28). The barrier had a height of 34 inches and consisted of 12-ft 6-inch long segments. The barrier was a uniform single-slope barrier with a 21-inch base width and an 8-inch top width. Each barrier segment presented a rectangular drainage scupper opening at the center of the barrier length. This opening had a height of 9 inches and a length of 28 inches. Barrier segments' pin-and-loop connections consisted of ¾-inch A36 steel loops and 1-inch-diameter AISI 4142 pins. A finite element model (FEM) analysis revealed a maximum lateral barrier deflection of 53 inches and displayed noticeable deformation of the pin-and-loop connection as well. Additional FEM analysis showed no risk of wheel snagging against the drainage scupper.

A 2004 Dodge RAM 1500 quad-cab truck was used for the completion of *MASH* Test 3-11. The truck, traveling at 60.2 mi/h, impacted the barrier at an angle of 26.2 degrees at the critical point of impact—51.2 inches upstream of the segment joint. During the impact event, the test vehicle lost its stability and rolled on its side. The truck began rotating after being successfully redirected and contained by the barrier, causing the test to fail by *MASH* standards. Although the barrier did not pass the *MASH* testing evaluation criteria, it was concluded that the “drainage slots and scupper opening did not appear in any way to adversely affect the crash performance of the barrier system” (28). Figure 2.12 illustrates representative photos of this 2010 WSDOT Test 3-11.

In 2011, a variation of the Washington pin-and-loop barrier was retested. In this second crash test scenario, the 1-inch-diameter AISI 4142 pins were replaced with 1¼-inch diameter F1554-grade 105 steel rods. The steel rods and the pins were the same length. The vehicle appeared to perform better than in the previous test; however, vehicle overturning still occurred after barrier contact. After being contained and redirected, the truck landed on its left side and remained that way as it eventually slid to a stop. Therefore, the barrier still did not pass *MASH* TL-3 standards. Figure 2.13 illustrates representative photos of the 2011 WSDOT Test 3-11 (29).

In 2010, an evaluation was performed on the Louisiana Department of Transportation and Development (LaDOTD) concrete F-shape barrier, which was designed with drainage slots to accommodate drainage through the bridge rail into scuppers or off the sides of the bridge (Figure 2.14) (30). The purpose of this evaluation was to investigate and compare the LaDOTD barrier strength to other existing barriers with similar openings. The barrier was 32 inches high, with a base width of 13.25 inches. The openings for the LaDOTD F-shape barrier were 6 inches high and 24 inches long. The potential for vehicles snagging the barrier during interaction with the openings was determined to be low. When compared to the TxDOT wildlife crossing barrier and the Washington pin-and-loop barrier, the openings of the LaDOTD barrier had a lower height (Figure 2.15). The LaDOTD F-shape barrier with drainage slots was considered acceptable per NCHRP Report 350 TL-4 standards.



(a) Barrier Drawing

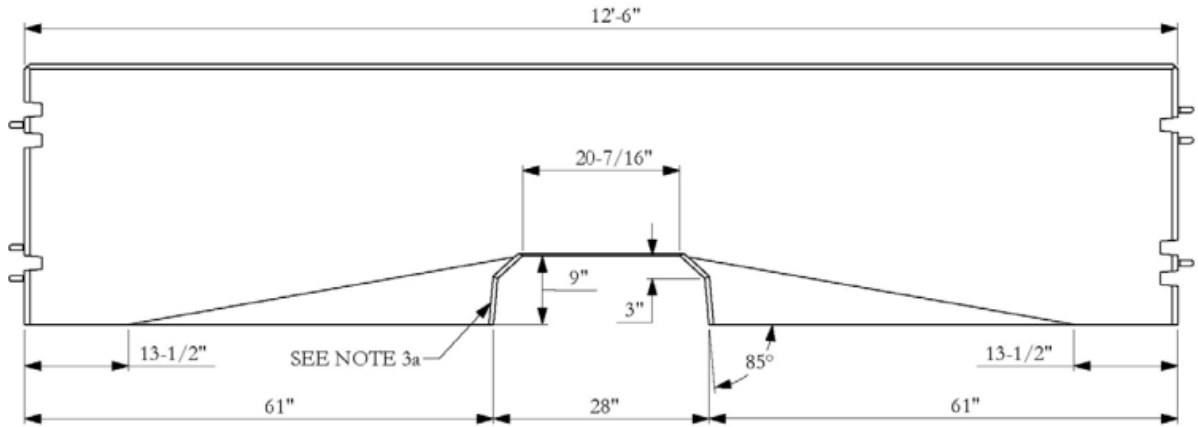


(b) Test Article before Impact



(c) Test Article after Impact

Figure 2.12. WSDOT Barrier Test 3-11.



(a) Barrier Drawing



(b) Test Article before Impact



(c) Test Article after Impact

Figure 2.13. Revised WSDOT Barrier Test 3-11.

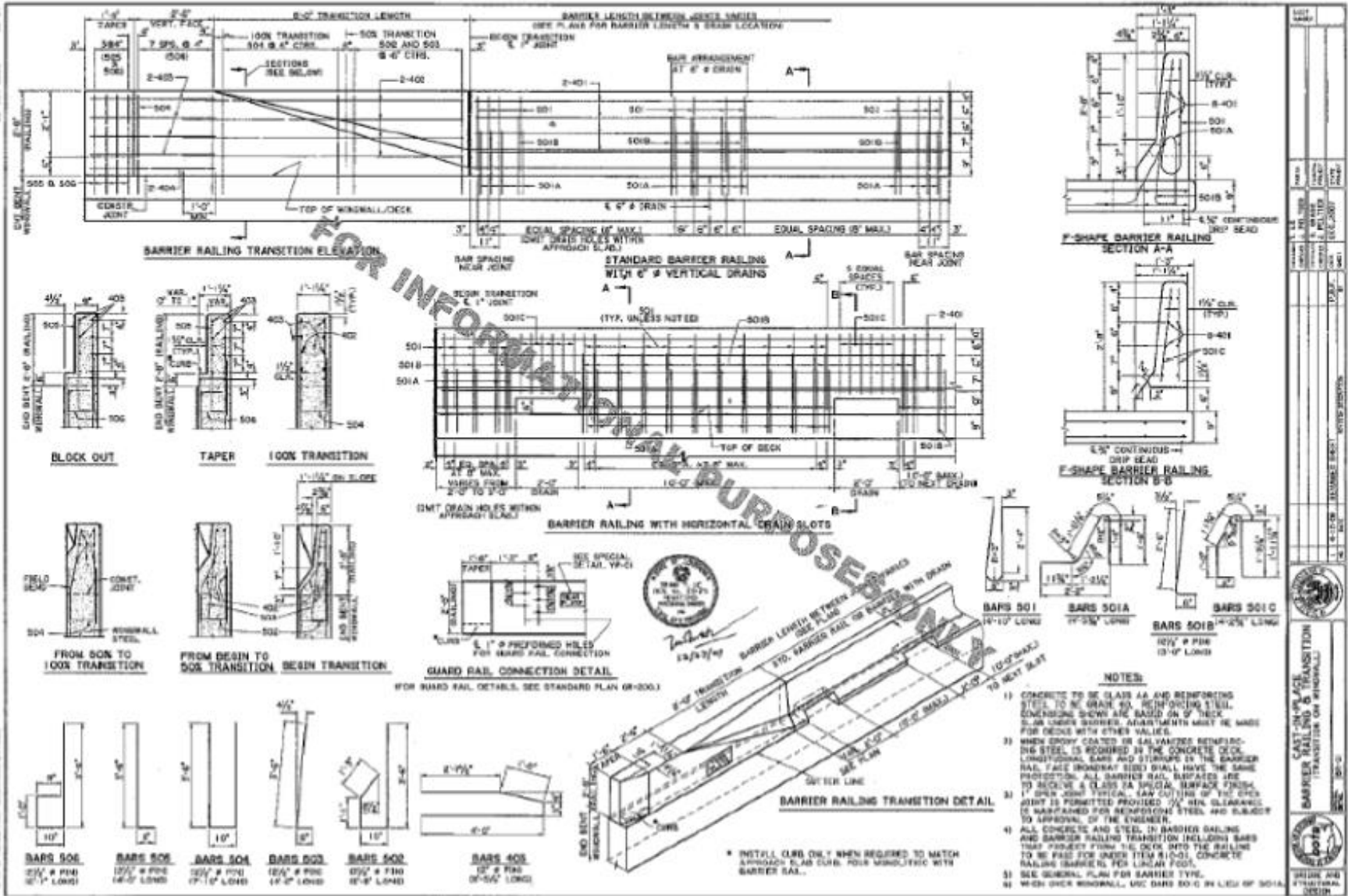


Figure 2.14. Drawing for LaDOTD F-Shape Concrete Barrier.

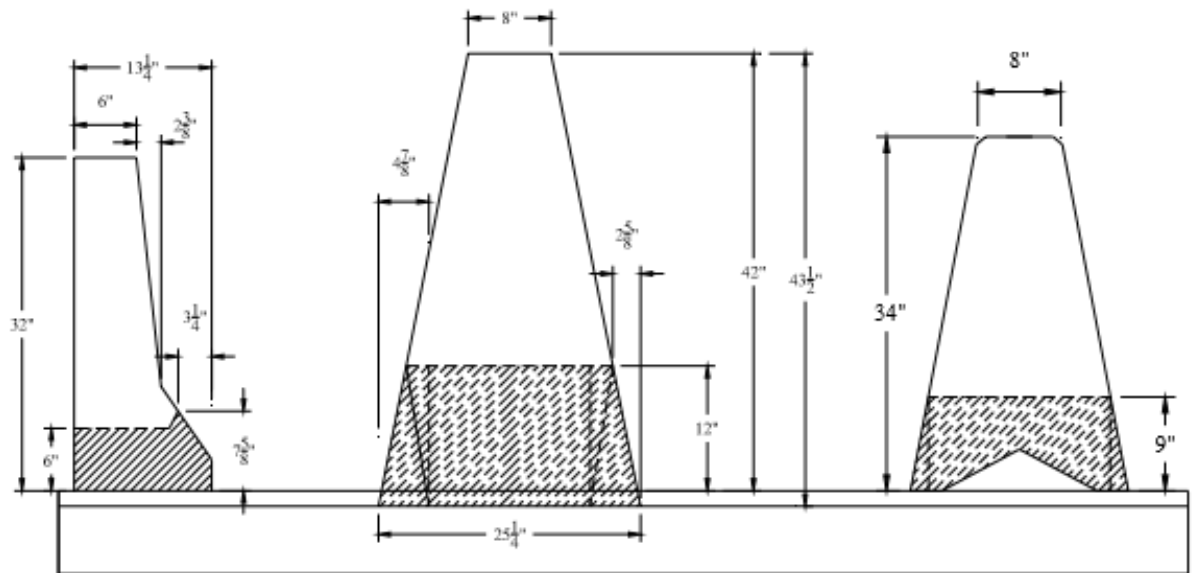


Figure 2.15. Side-View Comparison of LaDOTD F-Shape Barrier, TxDOT Wildlife Crossing Single-Slope Concrete Barrier (SSCB), and WSDOT Pin-and-Loop Barrier.

TTI researchers recently completed a project with TxDOT in which a new low-maintenance median barrier was developed (31). The barrier was thoroughly analyzed using extensive computer simulation and full-scale crash testing efforts. The final design includes anchoring a 42-inch-tall SSCB with a set of rubber anchor blocks that are bolted to the ground. Typically, the rigid SSCBs are anchored with the use of steel rebar connecting the concrete pavement to the barrier. This process prevents any significant deflection of the barrier from occurring, but the new design with rubber blocks allows the barrier to rotate upon impact. Figure 2.16 shows an opening in the barrier with the installed rubber block.



Figure 2.16. Opening in Concrete Barrier to Allow for Rubber Block Installation.

These large openings create stress concentrations in the barrier and limit the available section in terms of strength calculations. When the system was tested with a *MASH* 3-11 pickup truck, large cracks originated from the corners of these openings. Therefore, TTI researchers reinforced these areas with additional steel rebar to ensure that cracking would be prevented in

the future. This project provided TTI researchers with much knowledge on the effects of large openings in concrete barriers during impact that proved applicable when designing openings for water drainage during flooding.

While drainage slots will provide relief from flooding in stricken areas, these openings may also provide another safety benefit. Vehicular impacts with animals are becoming more common today as development further encroaches into wilderness. Thus, vehicle and animal interactions will also increase. When animals enter the roadway, they are often trapped by the concrete median barrier. As vehicles approach, they will often sprint back to the roadside. If the animals have another exit path through the barrier, they may not choose to retreat in the path of oncoming traffic. This alternative route might also protect occupants of the vehicle. If an animal sprints across the road, a driver may swerve his or her vehicle to avoid impact, which could cause vehicle instability and loss of control at high speeds. Therefore, providing animals an alternative escape path might prevent vehicle accidents and collisions. The TxDOT wildlife crossing barrier was designed with this specific intent (30).

The TxDOT wildlife crossing barrier is 42 inches in height and has openings for wildlife access through the barrier (Figure 2.17) (30). Each unit is 30 ft in length and contains two openings that are 12 inches high and 5 ft in length. Based on a review of the geometric features of this barrier, it was determined that the TxDOT wildlife crossing barrier was crashworthy with respect to NCHRP Report 350 TL-3 criteria.



Figure 2.17. TxDOT SSCB (Wildlife Crossing).

The researchers investigated TxDOT standards to identify concrete barriers for bridge rail and rigid applications currently in use within the state (Table 2.1 through Table 2.3) (32, 33). Specifically, the researchers investigated whether concrete barriers currently meeting TxDOT standards might potentially be modified to integrate large openings in their design, with the dual objective of allowing relief to flooding areas and maintaining barrier structural adequacy and crashworthiness when impacted by errant vehicles at high speed.

Table 2.1. TxDOT Bridge Rail Standards Summary Table.


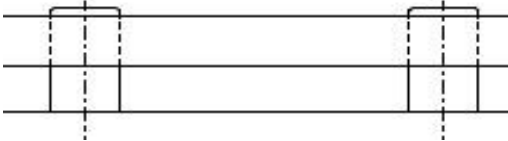


Barrier Name	Test Evaluation	Barrier			Drainage			TxDOT Standard Link	Corresponding Images
		Height (in)	Width (Top) (in)	Width (Base) (in)	Drainage Length (ft)	Curb (in)	Drainage Height (in)		
T552	MASH TL-3	30.5	5.5	12.25	2	N/A	2	rlstd010-18.pdf	
T66	NCHRP REPORT 350 TL-3	32	17.5	19	5.25	N/A	11	rlstd012-18.pdf	
T223	MASH TL-3	32	15.5	9.5	6	N/A	13	rlstd005-18.pdf	
T224	MASH TL-5	42	16.5	10	9	12	rlstd042-18.pdf		

Table 2.1. TxDOT Bridge Rail Standards Summary Table (Continued).

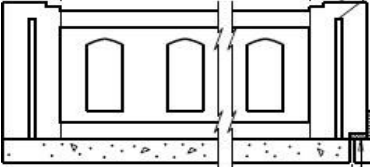


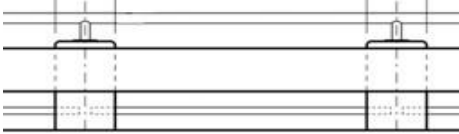
Barrier Name	Test Evaluation	Barrier			Drainage			TxDOT Standard Link	Corresponding Images
		Height (in)	Width (Top) (in)	Width (Base) (in)	Drainage Length (ft)	Curb (in)	Drainage Height (in)		
T411	NCHRP Report 350 TL-2	32	14	14	0.5	7	18	rlstd008-18.pdf	
C411	MASH TL-2	44	12	12	0.5	9	24	rlstd021-18.pdf	
C412	MASH TL-5	42	17.5	17.5	0.479	26	13	rlstd033-18.pdf	Note: Optional Drainage 3" x 2" Slots 
C66	NCHRP Report 350 TL-3	42	17.5	12	5.25	9	11	rlstd036-18.pdf	

Table 2.2. TxDOT Rigid-Barrier Summary Table (F-Shape).

Barrier Description	Barrier			Drainage Slots		TxDOT Standard Link
	Height (in)	Width (Top) (in)	Width (Base) (in)	Length (ft)	Height (in)	
F-Shape CSB(1)-10	33	9.5	24	3	3	csb110.pdf
F-Shape CSB(2)-13	33	9.5	24	3	3	csb213.pdf
F-Shape CSB(3)-16	32	9.5	24	3	3	csb316.pdf
F-Shape CSB(4)-10	33	6	21			csb410.pdf
F-Shape CSB(6)-10	30.25	9.5–14	24–33.25			csb610.pdf

Table 2.3. TxDOT Rigid-Barrier Summary Table (Single Slope).

Barrier Description	Barrier			Drainage Slots		TxDOT Standard Link
	Height (in)	Width (Top) (in)	Width (Base) (in)	Length (ft)	Height (in)	
Single-Slope SSCB(1)-16	42–54	8	24–28.5	3	3	sscb116.pdf
Single-Slope SSCB(1F)-10	42–54	8	24–28.5	3	3	sscb1f10.pdf
Single-Slope SSCB(2)-10	42	8	24	3	3	sscb210.pdf
Single-Slope SSCB(3)-10	42–54	8–14	24/30–28.5/34.5			sscb310.pdf
Single-Slope SSCB(4)-10	42–54	6	20.5–25.0625			sscb410.pdf
Single-Slope SSCB(5)-10	42		24			sscb510.pdf

Some TxDOT concrete bridge rails do present large openings. In fact, some of these barrier designs were already previously evaluated from a hydraulic perspective to determine their capability to allow considerable passage of water. Examples of such barriers with large openings are the T66/C66 or the T223 (Table 2.1). Other examples are the T224, C411/T411, and C412 (Table 2.1). These last barriers, however, also include a curb in their current design, which is not an ideal design detail since it will block initial passage of water. In addition, consideration was given to the test-level criteria for which these barriers were designed and tested. Some of them are designed for low-speed vehicular impact. Consideration of such barriers for application to this project would have required appropriate barrier design modification to adapt their current roadside design to median applications.

As for those rigid barriers currently on TxDOT standard drawings, not all of them presented considerable-sized openings of interest for a large quantity of water drainage (Table 2.2 and Table 2.3). The reviewed rigid barriers for roadside application either did not account for openings in their designs or, at most, only included limited-sized scuppers. Although scuppers might serve other purposes, it was anticipated that a 3-inch-tall scupper would not provide adequate opening to allow relief to flooding areas.

2.3.4 Identification and Review of Testing Performance of Existing Compliance Rigid and Portable Concrete Barriers with Openings or Scuppers

The primary concern with concrete barriers containing scuppers is that they can become a location for high stress concentration during an impact event. It is not infrequent for under-reinforced barriers or for high load impacts to have cracks propagating from scupper locations through the barrier during an impact event. The Massachusetts Department of Transportation (MassDOT) Highway Division developed a 32-inch-tall, precast F-shape portable concrete barrier (PCB) system for use as a temporary installation for construction projects requiring positive protection (Figure 2.18) (34). The 10-ft-long barrier segment had a single drainage relief/forklift slot (3 ft 4 inches long \times 3 inches high) precast and symmetrically centered in the bottom of each barrier segment. The barrier was crash tested and performed acceptably for *MASH* TL-2 impact conditions. However, it was noted that the impact segment cracked completely through near the center of the segment after *MASH* Test 2-11 (Figure 2.19).



Figure 2.18. MassDOT F-Shape PCB.



Figure 2.19. Concrete Crack after *MASH* Test 2-11.

This barrier was then retrofitted and tested in accordance with *MASH* TL-3. Because of the crack on the barrier segment, TTI researchers developed a 9-ft-long 6-inch \times 4-inch \times ½-inch steel angle that was secured to the back (field) side of each barrier segment with six screw anchors. Although the MassDOT PCB with this newly applied angle rail stiffener performed acceptably for *MASH* TL-3 impact conditions, the barrier segment fractured vertically near the center of the segment on the impact side. Concrete spalling also occurred at the base of the segment on the traffic side (Figure 2.20).



Figure 2.20. Concrete Crack after *MASH* Test 3-11 (Retrofit System).

The researchers also scrutinized available concrete barriers available through the *MASH* database, which contains known roadside safety hardware devices tested per *MASH* standards throughout the country. The objective was to verify whether other barriers of interest were recently tested and evaluated per *MASH* standards requirements. Unfortunately, all known *MASH*-tested concrete barriers (besides the already discussed TxDOT ones) did not present considerable-sized openings that would accommodate a large quantity of water drainage. In fact, barriers are usually limited to include drainage scuppers only 3 inches in height and a maximum 3 ft in length.

2.4 CONCLUSIONS

Based on the collected information, a few concluding observations are reported below. The hydraulic literature review portion of this research revealed the following:

- Fractional open space is the primary parameter affecting hydraulic efficiency.
- Hydraulic efficiency increases as barrier opening width increases and the opening gets closer to the road surface.

- The Charbeneau model using experimentally determined parameters accurately predicts flow characteristics. Adjusting the fractional open space parameter can simulate flow obstructions in barrier openings.
- Streamlining barrier openings can effectively reduce drag coefficient and the degree of flow separation, thereby reducing wear on concrete. This element has the potential to extend the concrete barrier's lifespan.

The barrier design and crashworthiness literature review portion of this research pointed to the following conclusions:

- The researchers found no evidence of the existence of a roadside safety, rigid concrete median barrier that passed *MASH* TL-4 evaluation criteria and can be implemented in flood-prone zones to allow relief from flooding.
- Very limited research and testing studies have investigated the structural adequacy and crashworthiness of concrete barriers with large openings. The investigated concrete barriers were for bridge or roadside applications. However, no studies with similar objectives were conducted on concrete barriers for median application.
- A few concrete barrier designs were identified for consideration in this project. Barrier design modifications, however, would be required to adapt those barriers to a roadside median application.
- From a structural and crashworthiness perspective, when designing a new barrier or applying design modification to an existing concrete barrier to account for properly sized openings, two specific considerations need to be taken into account:
 - The structural capacity of the barrier needs to be carefully evaluated because openings in the barriers have been proven to become high concentrations of stresses during impact events, thereby allowing for crack formation and propagation.
 - The opening size and design characteristics can create snagging potential for vehicles during an impact event, creating a chance for high occupant risk and vehicle instability.

CHAPTER 3. PRELIMINARY DESIGN CONCEPTS*

3.1 INTRODUCTION

The purpose of this chapter is to provide preliminary design options of a median barrier for implementation in flood-prone areas. Included are five design options, as well as anticipated advantages and disadvantages for each design alternative, including any perceived performance benefits and application limitations. The designs have been tailored to account for *MASH* TL-4 median barrier design requirements, as requested by TxDOT.

Each option is centered on having a large scupper present across the span length to allow for water passage while still maintaining adequate barrier strength for potential vehicle impact events. Each option is presented with a description of the barrier design concept, preliminary drawing, and perceived barrier advantages, disadvantages, performance benefits, and application limitations.

3.2 OPTION A: 42-INCH-TALL SINGLE-SLOPE MEDIAN BARRIER

Figure 3.1 shows the single-slope (SS) median barrier as a 42-inch-tall barrier. The base is 24 inches wide, and the barrier is 8 inches wide at the top. Openings are 13 inches tall. The length of the proposed openings is to be defined (TBD). Results from large-scale hydraulic testing and finite element computer simulations to be developed in future tasks will guide the determination of appropriate opening size. The opening would be sloped laterally to limit risk of vehicle snagging during a potential impact event. Table 3.1 lists the advantages and disadvantages of Option A.

3.3 OPTIONS B1 AND B2: MEDIAN VERSIONS OF THE T223 TXDOT POST-AND-BEAM BRIDGE RAIL

Options B1 and B2 represent two possible variations of a proposed median version of the existing T223 TxDOT post-and-beam bridge rail. In both cases, the concrete beam is 23 inches high and 24 inches wide, with concrete posts that are 13 inches tall. For both options, the posts would be sloped laterally to limit risk of vehicle snagging during a potential impact event.

In Option B1, the post configuration extrudes to the full width of the barrier (Figure 3.2, Detail E). In Option B2, the post reaches a maximum width of 19 inches (Figure 3.3, Detail I). Minimum post width would need to be determined through computer simulations to verify that the narrower width does not constitute risk for potential vehicle snagging while still maintaining required post strength. System height needs to be at least 36 inches for *MASH* TL-4 requirements; however, an alternative system height of 42 inches is also proposed.

Results from large-scale hydraulic testing and finite element computer simulations to be developed in future tasks will guide the determination of appropriate opening size. The openings would be sloped laterally to limit risk of vehicle snagging during a potential impact event. Table 3.2 lists the advantages and disadvantages of Options B1 and B2.

* The opinions/interpretations identified/expressed in this chapter are outside the scope of TTI Proving Ground's A2LA Accreditation.

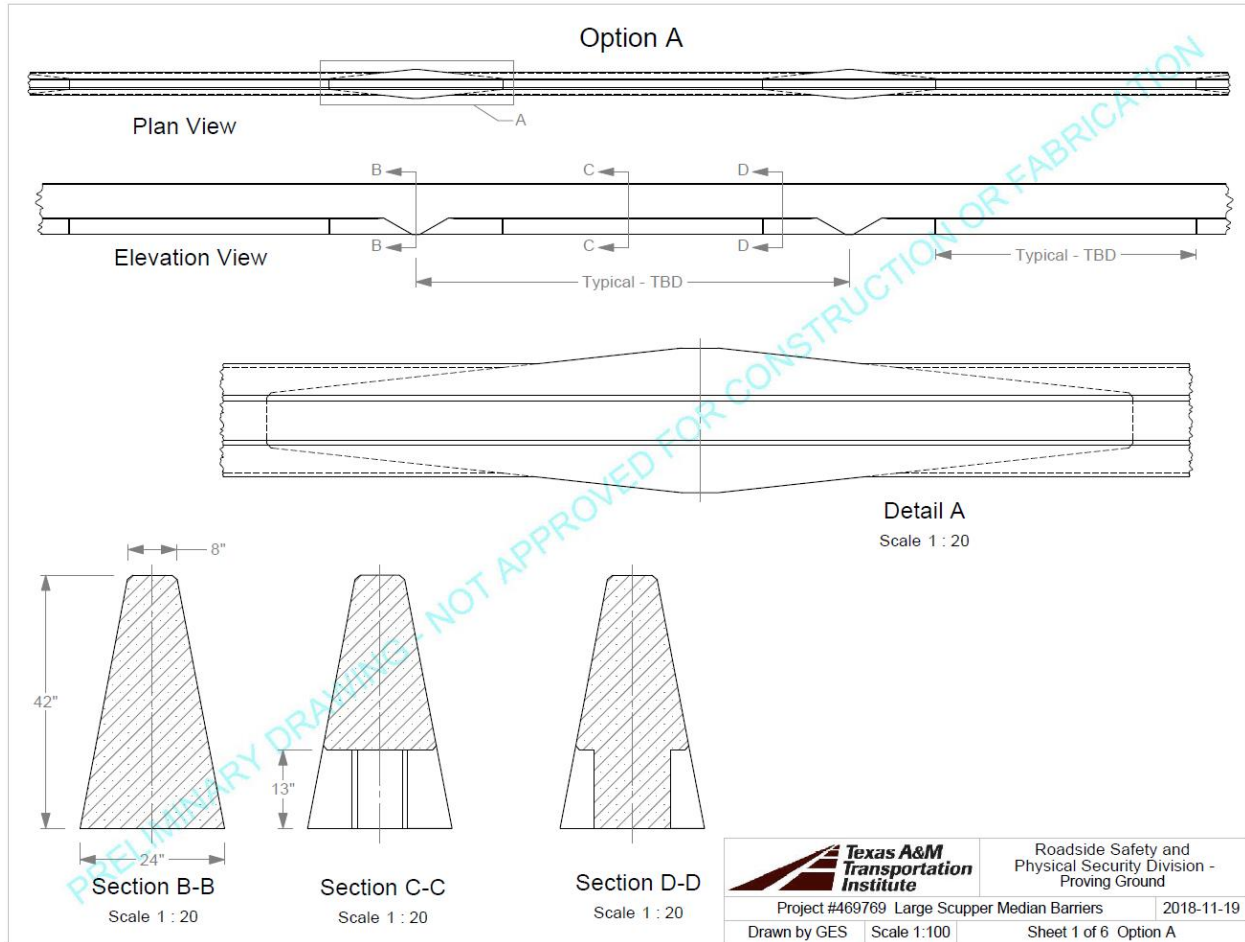


Figure 3.1. Option A Preliminary Drawing.

Table 3.1. Option A Perceived Advantages and Disadvantages.

Advantages	Disadvantages
<ul style="list-style-type: none"> • Openings sloped laterally to limit risk of vehicle snagging • Minimal transition to standard SS median barrier • Simple implementation within existing median SS barrier 	<ul style="list-style-type: none"> • Shy distance concern • Potential for more vehicle climbing • Sloping post combined with SS profile creates constructability difficulties • Cast in place (on-site construction)

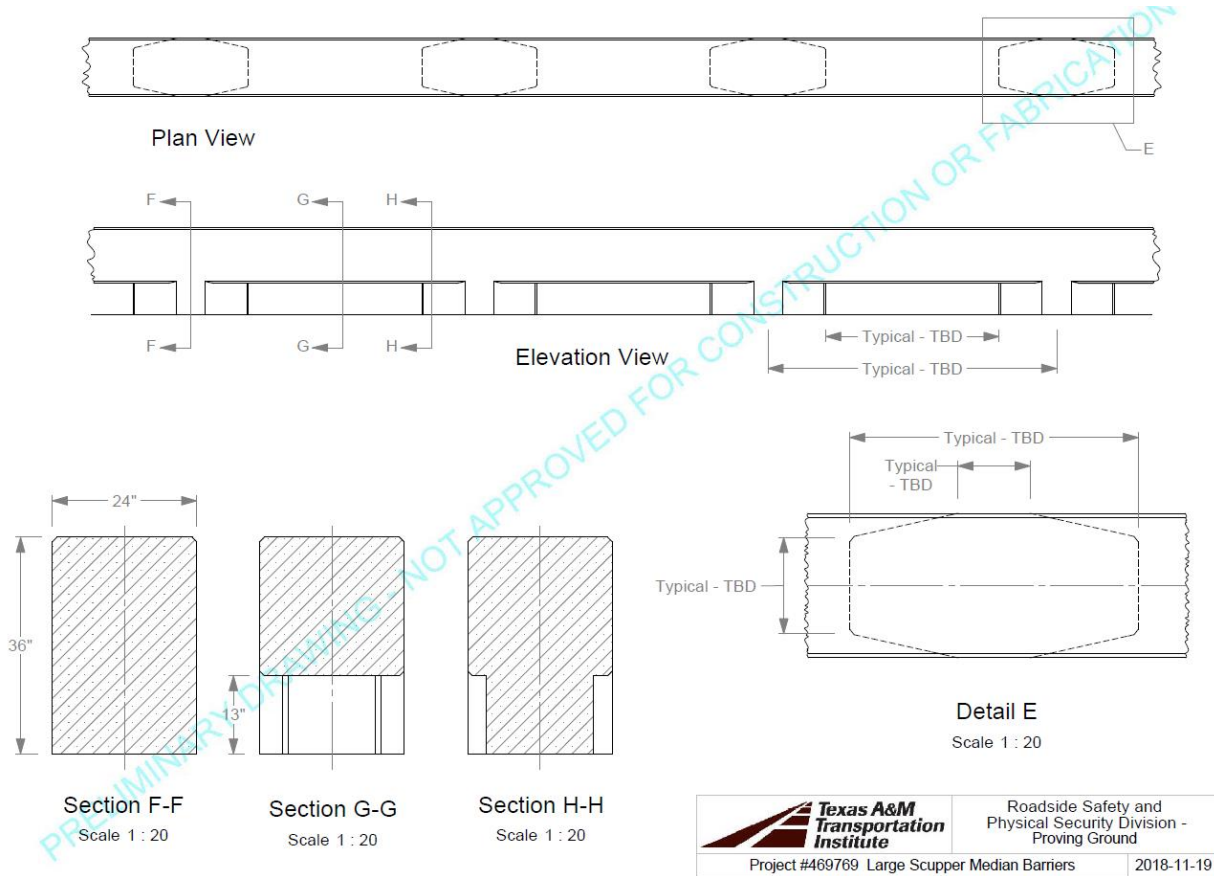


Figure 3.2. Option B1 Preliminary Drawing.

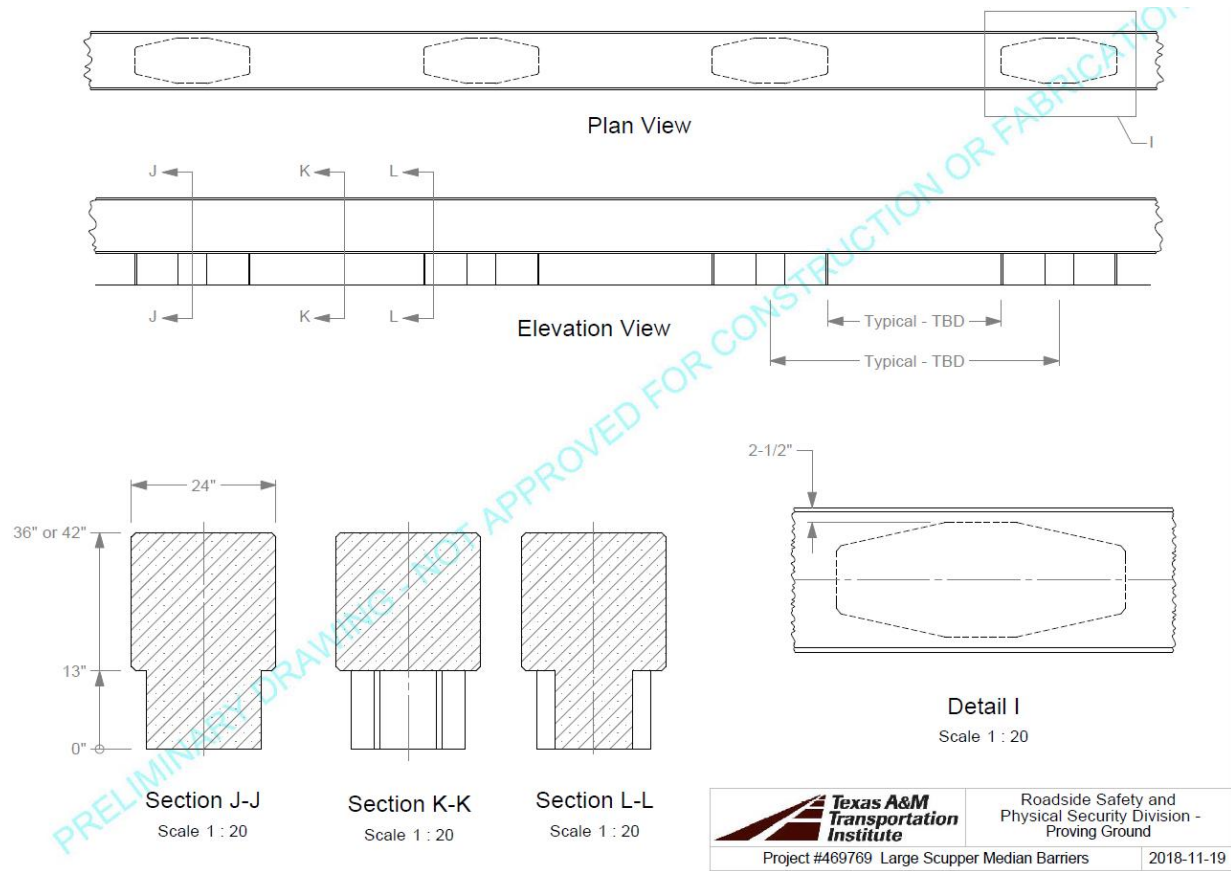


Figure 3.3. Option B2 Preliminary Drawing.

Table 3.2. Options B1 and B2 Perceived Advantages and Disadvantages.

Advantages	Disadvantages
<ul style="list-style-type: none"> • Tapered geometry might allow greater water passage • Potential for less vehicle climb 	<ul style="list-style-type: none"> • Large concrete beam near driver eye level • Shy distance concern • Difficulties transitioning profile to new and existing safety shapes • Cast in place (on-site construction)

3.4 OPTION C: 42-INCH-TALL MEDIAN CONCRETE POST AND BEAM (RECTANGULAR POSTS)

Option C represents a possible variation of the proposed median version of the existing TxDOT T223 concrete post-and-beam bridge rail (Figure 3.4). The concrete beam is 29 inches high and 24 inches wide, with concrete posts that are 13 inches tall. Concrete posts are 48 inches long and 15 inches wide. Detailed engineering analysis, results from large-scale hydraulic testing, and finite element computer simulations to be developed in future tasks can guide the optimization of post dimensions, which also translates into determination of appropriate opening size. Table 3.3 shows the advantages and disadvantages of Option C.

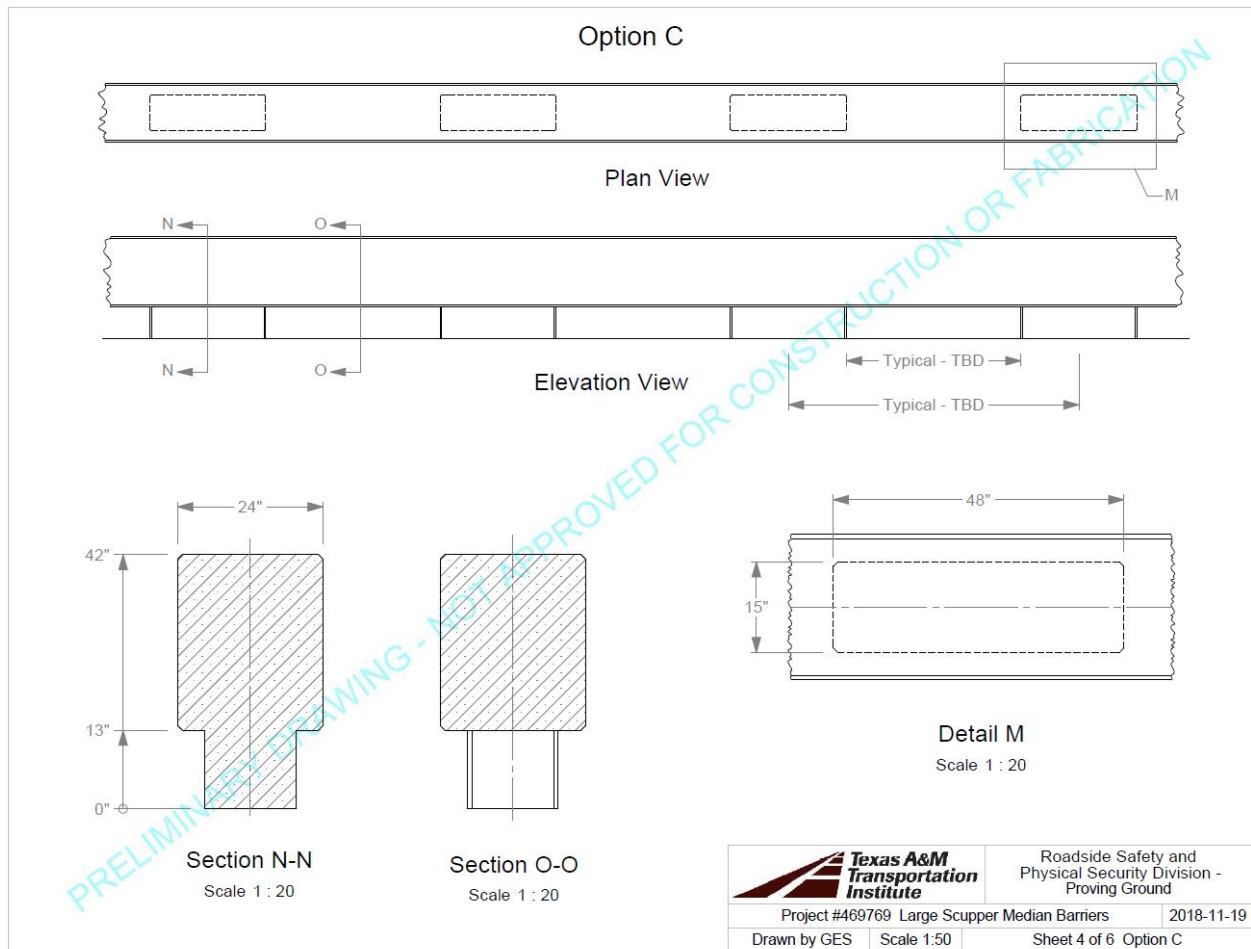


Figure 3.4. Option C Preliminary Drawing.

Table 3.3. Option C Perceived Advantages and Disadvantages.

Advantages	Disadvantages
<ul style="list-style-type: none"> • Wall post sections could allow for variability in length/spacing • Design is based off TL-5 design (could likely pass TL-4) 	<ul style="list-style-type: none"> • Large concrete beam near driver eye level • Risk of vehicle snagging • Cast in place (on-site construction)

3.5 OPTION D: 36-INCH OR 42-INCH-TALL MEDIAN CONCRETE POST AND BEAM (ROUND POSTS)

Figure 3.5 shows Option D, which represents a possible variation of the proposed median version of the existing TxDOT T223 concrete post-and-beam bridge rail. The concrete beam is 23 or 29 inches high and 24 inches wide. Concrete round posts are 13 inches tall. Detailed engineering analysis, results from large-scale hydraulic testing, and finite element computer simulations to be developed in future tasks can guide the optimization of post dimensions, specifically post diameter, which also translates into determination of appropriate opening size. Table 3.4 provides the advantages and disadvantages of Option D.

3.6 OPTION E: 36-INCH-TALL MEDIAN VERSION OF THE C1W TxDOT BRIDGE RAIL

Option E represents a proposed median version of the existing TxDOT C1W bridge rail (Figure 3.6). Option E is a 36-inch-tall full metal rail. This option consists of four passing hollow structural sections (HSSs) on each side of the barrier with a center-center spacing of 7.5 inches. The HSS plates would pass through metal posts with a center-center spacing of 9 inches. The rail is bolted directly to the deck/concrete piers.

Table 3.5 lists advantages and disadvantages of Option E. The primary advantage of this design is that it has the highest possible water pass-through of all options presented, and the design has the potential for alterations to make it more easily manufactured. In order to maintain a system construction cost comparable to that of the concrete barrier options proposed above, this system represents the rail option with potentially the highest deflections due to vehicular impacts. This system represents the option with most likely the highest maintenance needs and costs after severe vehicular impacts. In addition, a specific transition design would need to be constructed from and to existing median barriers upstream and downstream of Option E.

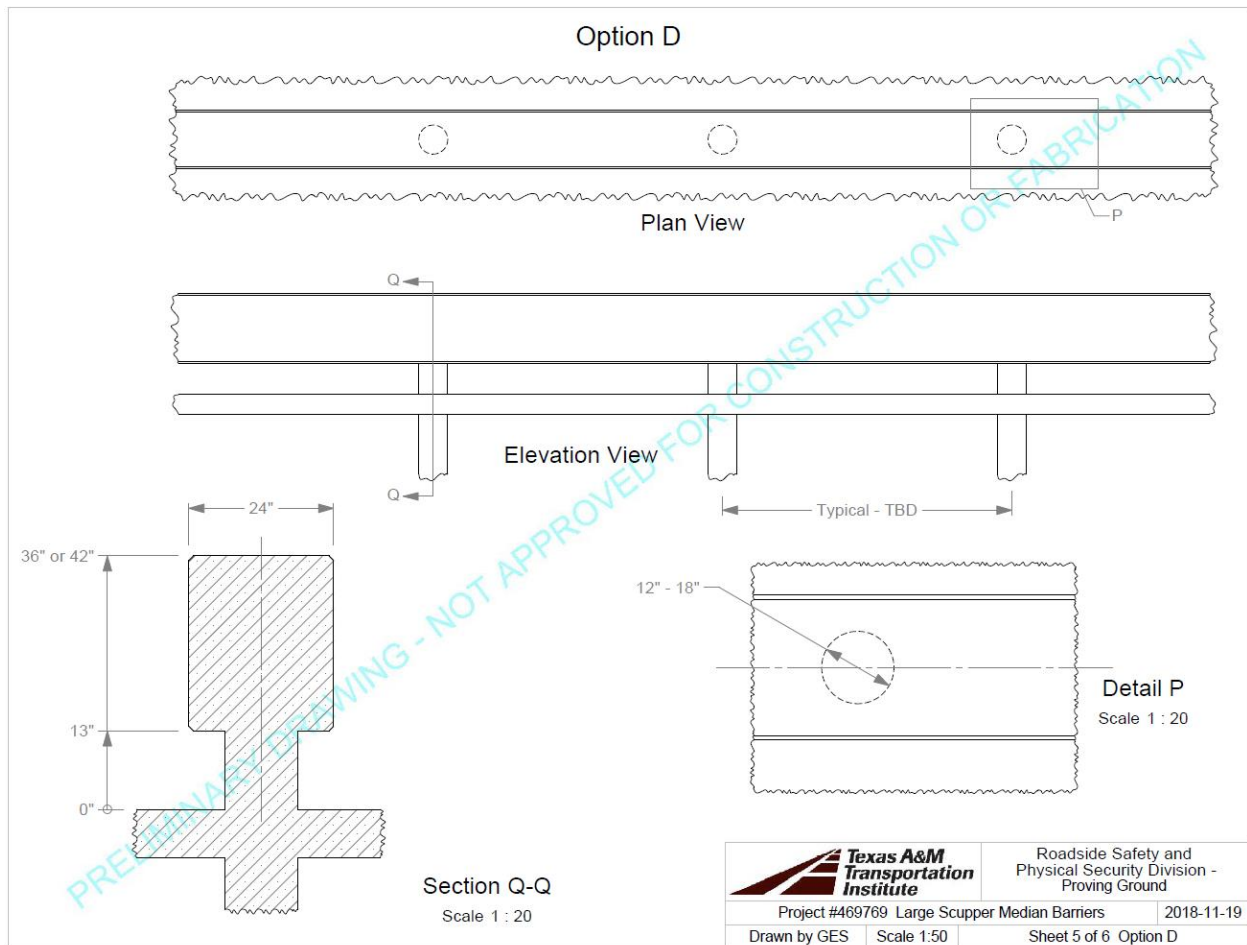


Figure 3.5. Option D Preliminary Drawing.

Table 3.4. Option D Perceived Advantages and Disadvantages.

Advantages	Disadvantages
<ul style="list-style-type: none"> • Potential lower risk for vehicle snagging • Round posts might allow greater water passage 	<ul style="list-style-type: none"> • Large concrete beam near driver eye level • Pier size is limited by the post width • Cast in place (on-site construction)

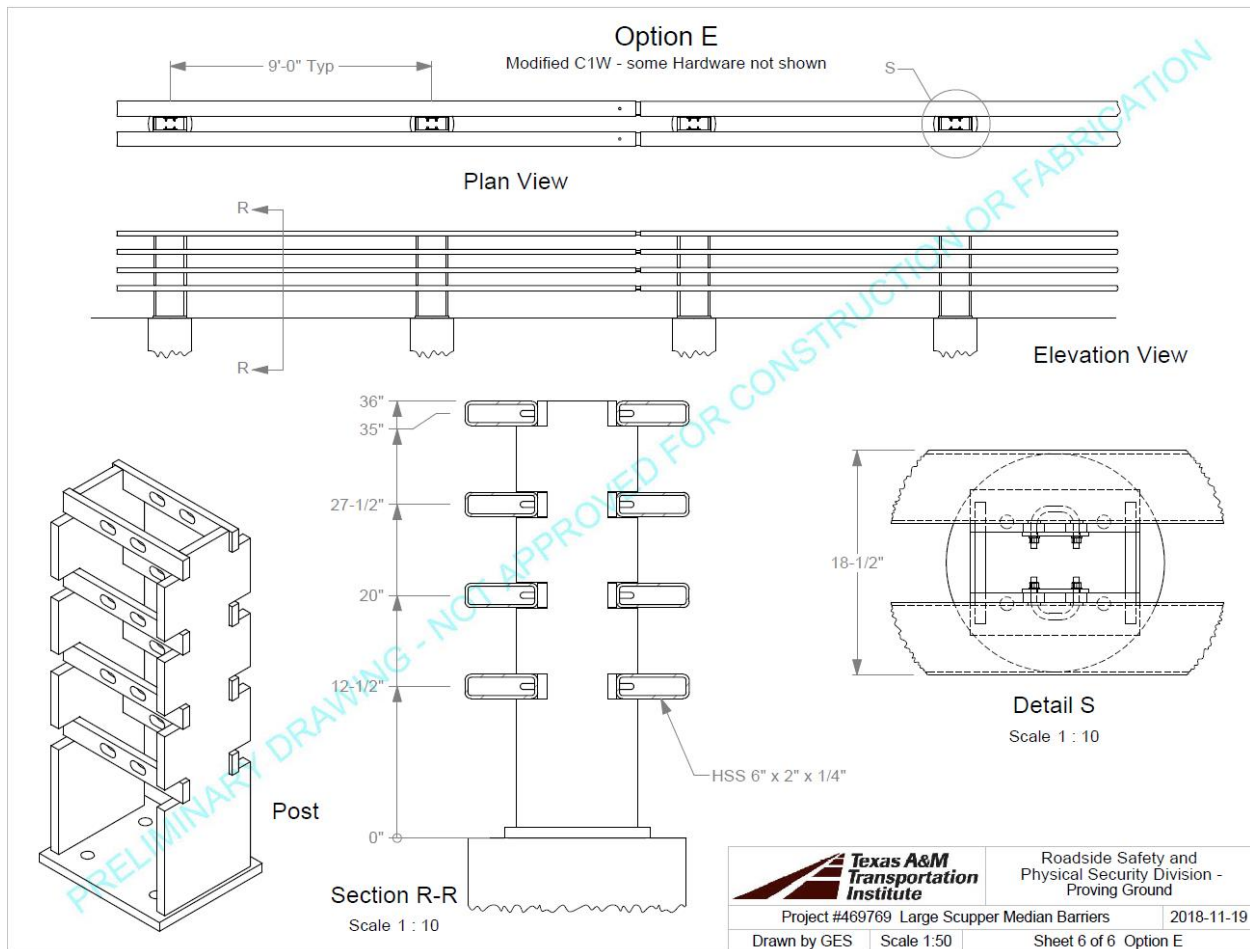


Figure 3.6. Option E Preliminary Drawing.

Table 3.5. Option E Perceived Advantages and Disadvantages.

Advantages	Disadvantages
<ul style="list-style-type: none"> • Anticipated greatest amount of water passage • Variation of an existing system that passed <i>MASH</i> TL-4 testing • Off-site rail and post fabrication • Anticipated minimal amount of wind turbulence 	<ul style="list-style-type: none"> • Highest deflections during severe vehicular impact • Highest maintenance and repair cost after severe vehicular impact • More complex transition to existing median barriers upstream and downstream • Risk for vehicle snagging

3.7 CONCLUSIONS

The objective of the task described in this chapter was to provide preliminary design options of a median barrier for implementation in flood-prone areas. The designs were tailored to account for *MASH* TL-4 median barrier design requirements. The researchers identified five design options, as well as anticipated advantages and disadvantages for each design alternative,

including any perceived performance benefits and application limitations. Table 3.6 summarizes the proposed design options.

Three median barrier options were approved for further investigation through computer simulations and hydraulic testing:

- Option A: 42-inch-tall single-slope median barrier.
- Option B: 38-inch median version of the T223 TxDOT post-and-beam bridge rail.
- Option C: 38-inch open steel barrier.

Table 3.6. Summary of Proposed Design Options for Median Barriers for Implementation in Flood-Prone Areas.

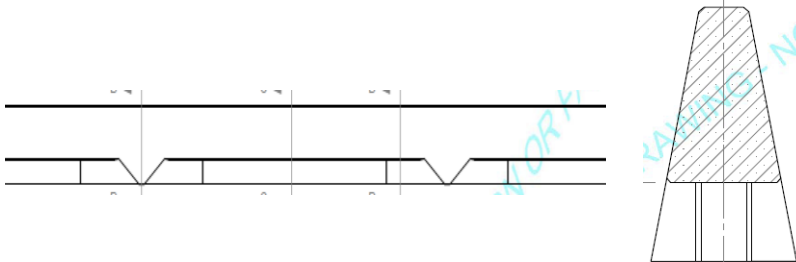
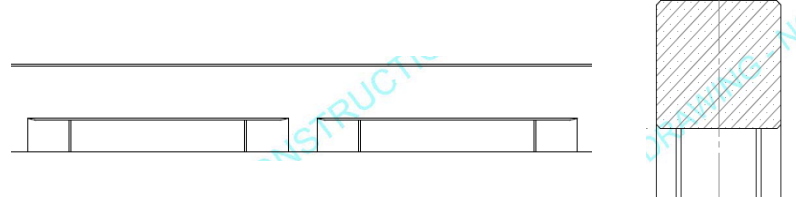
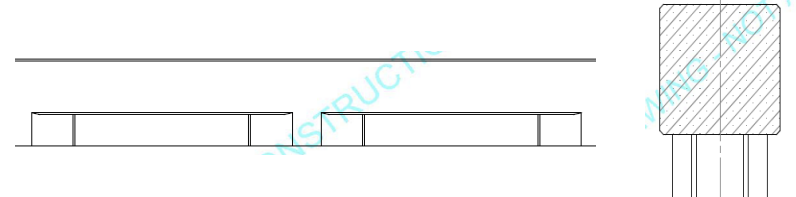
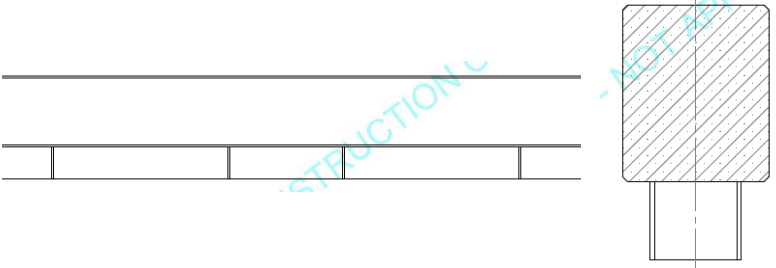
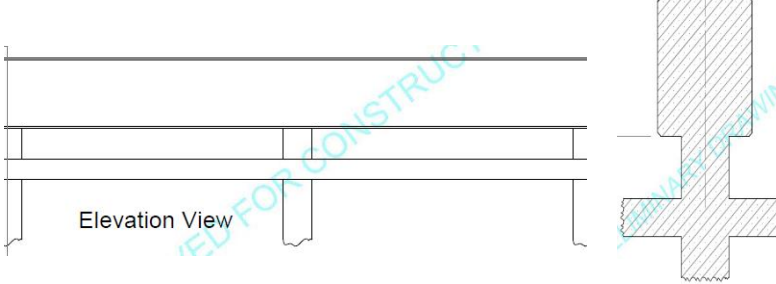
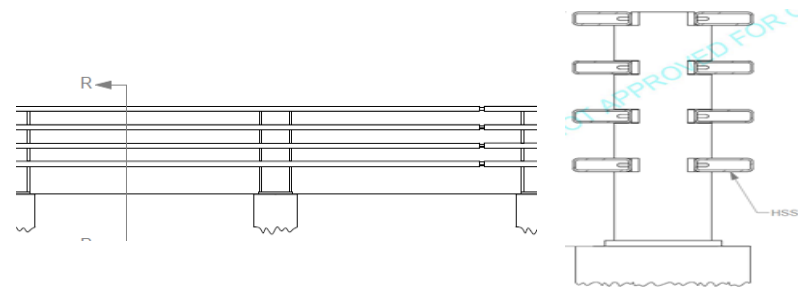
Barrier Option	Barrier Height (in)	Barrier Width (Top) (in)	Barrier Width (Base) (in)	Images
Option A	42	8	24	
Option B1	36	24	TBD-24	
Option B2	36-42	24	TBD-19	

Table 3.6. Summary of Proposed Design Options for Median Barriers for Implementation in Flood-Prone Areas (Continued).

Barrier Option	Barrier Height (in)	Barrier Width (Top) (in)	Barrier Width (Base) (in)	Images
Option C	42	24	15	
Option D	36-42	24	12-18 (post diameter)	 <p>Elevation View</p>
Option E	36	18.5	TBD	

CHAPTER 4. FINITE ELEMENT ANALYSIS*

4.1 INTRODUCTION

The purpose of this chapter is to inform the developed design details of the top three design options selected in Chapter 3 as candidates for detailed development and evaluation under vehicular impacts. The researchers performed detailed engineering analyses to determine appropriate barrier characteristics to resist vehicular impact loads per *MASH* TL-4 conditions, as well as appropriate dimensions and characteristics of the openings and/or scuppers for each of the design concepts. The ability of each design to meet impact performance requirements was evaluated. The evaluation involved the use of finite element analysis (FEA) model development and impact simulations. A detailed FEA model was developed for each of the selected design concepts.

The explicit FEA code LS-DYNA was used to perform critical impact simulations using the developed barrier model and available vehicles models, as shown in Figure 4.1. These models include (a) Toyota Yaris model representing a 2420-lb (1100C) *MASH* small car test vehicle; (b) Chevrolet Silverado model representing a 5000-lb (2270P) *MASH* pickup truck test vehicle; and (c) SUT model representing a 22,000-lb (10000S) heavy truck test vehicle.

The researchers used the results to assess the probability of each design concept to meet *MASH* TL-4 impact performance requirements while providing other desirable functional characteristics during flooding conditions.

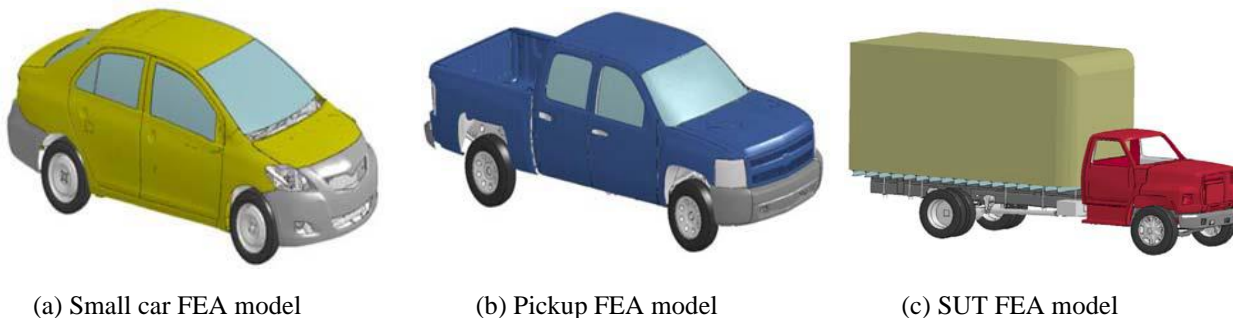


Figure 4.1. Available Finite Element Computer Models.

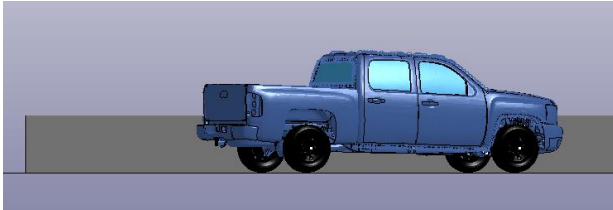
4.2 MODEL CALIBRATION FOR CONCRETE OPTIONS

4.2.1 Full-Scale Crash Test

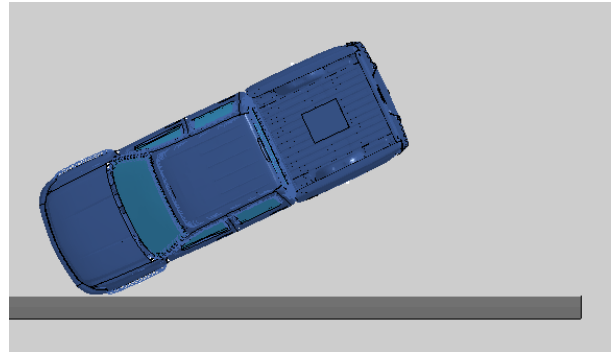
The researchers used a *MASH*-compliant TxDOT single-slope bridge rail (Type SSTR) on a pan-formed bridge deck tested by TxDOT for calibrating the LS-DYNA FEA model. The researchers conducted *MASH* Test 3-11 on this single-slope bridge rail and used the results to calibrate the developed concrete barrier computer model system by comparing vehicle impact behavior and stability, as well as occupant risk and barrier system performance upon vehicle impact.

* The opinions/interpretations identified/expressed in this chapter are outside the scope of TTI Proving Ground's A2LA Accreditation.

The 2013 RAM 1500 pickup truck used in the test weighed 5036 lb. Actual impact speed and angle were 63.8 mi/h and 24.8 degrees, respectively. Figure 4.2 illustrates the vehicle and barrier system FEA model from the side and top views.



(a) Perspective View



(b) Top View

Figure 4.2. Vehicle and Barrier System for FEA Calibration.

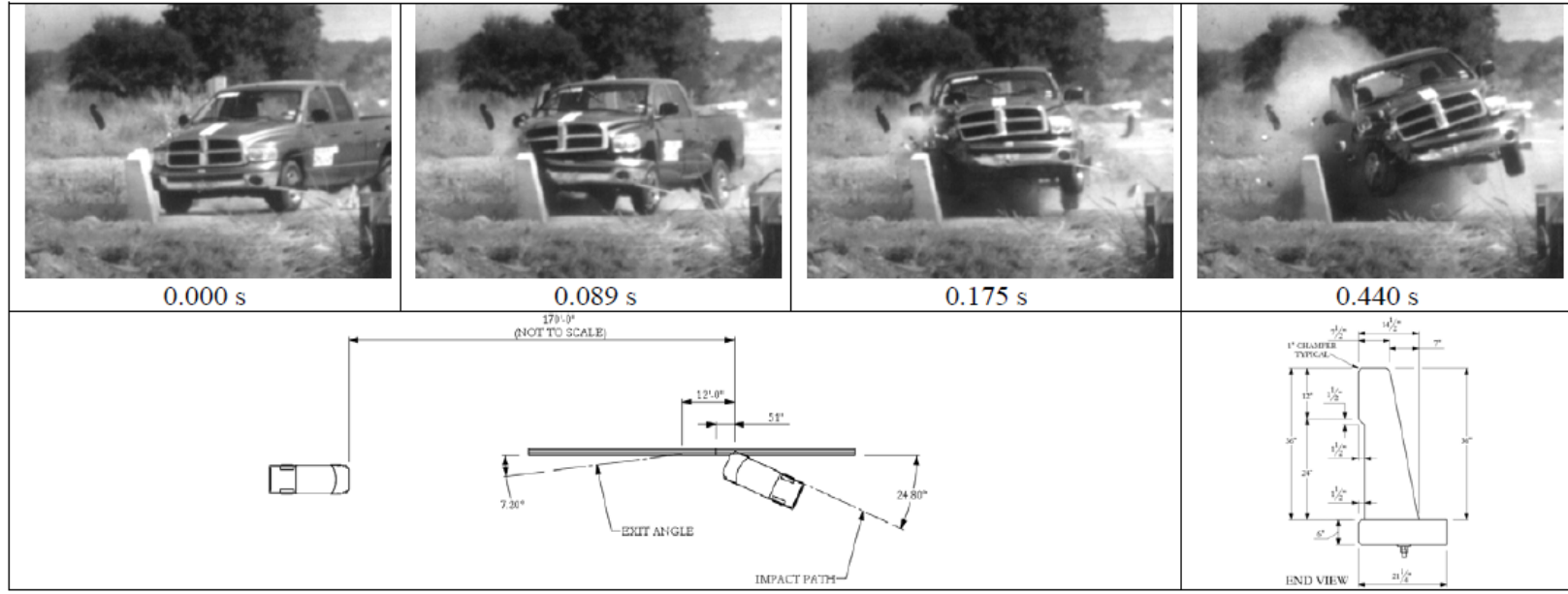
Figure 4.3 shows the barrier and vehicle before testing, and Figure 4.4 illustrates the barrier system after testing. Figure 4.5 summarizes the full-scale crash test results.



Figure 4.3. Single-Slope Barrier System with and without Test Vehicle before Testing.



Figure 4.4. Single-Slope Barrier System after Testing.



General Information

Test Agency..... Texas Transportation Institute (TTI)
 Test Standard Test No. MASH Test 3-11
 TTI Test No. 420020-3
 Date..... 2010-08-03

Test Article

Type..... Bridge Rail
 Name..... TxDOT Pan-Formed Bridge Rail
 Installation Length..... 75 ft
 Material or Key Elements..... TxDOT Single Slope Traffic Rail (Type SSTR) anchored to top of 6-inch thick reinforced concrete deck cantilever
 Concrete Bridge Deck, Dry

Soil Type and Condition.....

Test Vehicle

Type/Designation..... 2270P
 Make and Model..... 2005 Dodge Ram 1500
 Curb..... 4723 lb
 Test Inertial..... 5036 lb
 Dummy..... No dummy
 Gross Static..... 5036 lb

Impact Conditions

Speed..... 63.8 mi/h
 Angle..... 24.8 degrees
 Location/Orientation..... 5.2 ft upstream of

Exit Conditions

Speed..... 49.5 mi/h
 Angle..... 7.2 degrees

Occupant Risk Values

Impact Velocity
 Longitudinal..... 22.0 ft/s
 Lateral..... 29.9 ft/s
 Ridedown Accelerations
 Longitudinal..... -5.3 G
 Lateral..... -11.7 G
 THIV..... 40.6 km/h
 PHD..... 11.7 G
 ASI..... 2.02
 Max. 0.050-s Average
 Longitudinal..... -10.9 G
 Lateral..... -15.5 G
 Vertical..... -6.1 G

Post-Impact Trajectory

Stopping Distance..... 170 ft dnwstrm
 6.0 ft twd traffic

Vehicle Stability

Maximum Yaw Angle..... -34 degrees
 Maximum Pitch Angle..... 8 degrees
 Maximum Roll Angle..... 26 degrees
 Vehicle Snagging..... No
 Vehicle Pocketing..... No

Test Article Deflections

Dynamic..... Nil
 Permanent..... Nil
 Working Width..... 10 inches

Vehicle Damage

VDS..... 01RFQ5
 CDC..... 01RDEW4
 Max. Exterior Deformation..... 18.0 inches
 OCDI..... RF0020000
 Max. Occupant Compartment
 Deformation..... 2.75 inches
 Impact Severity..... 3881 kip-ft (+5%)

Figure 4.5. Summary of Results for TxDOT Single-Slope Bridge Rail (Type SSTR) on Pan-Formed Bridge Deck System.

4.2.2 Computer Model Simulation

The researchers used LS Pre-Post to develop an SSCB with rigid concrete material properties. Figure 4.6 shows the LS-DYNA model of the single-slope barrier used for calibration.

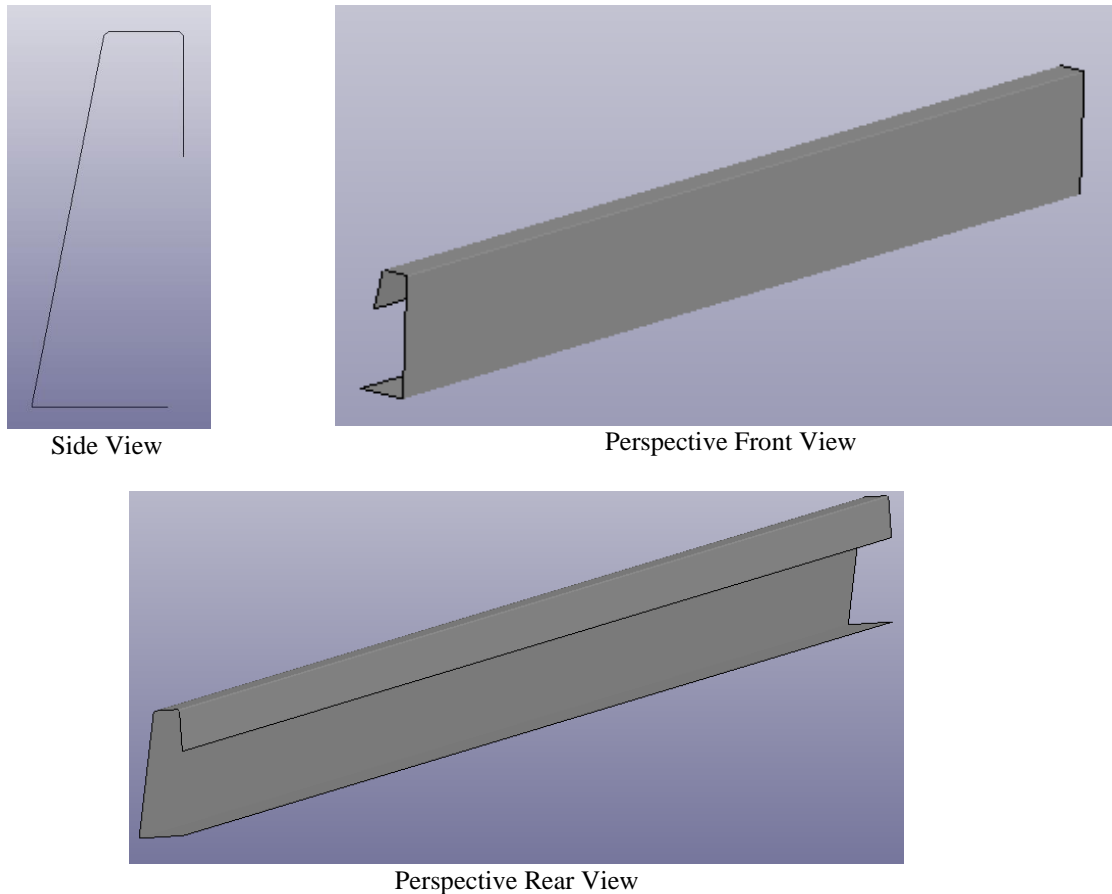
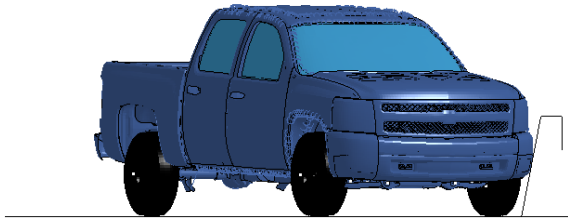


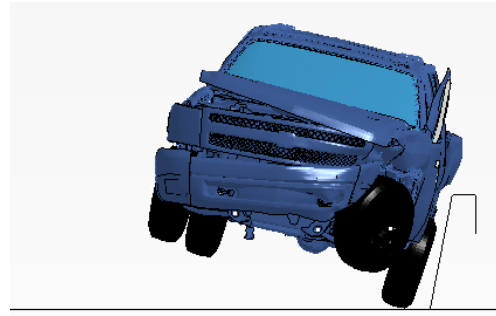
Figure 4.6. LS-DYNA Calibration Barrier System Model.

The researchers used a validated Silverado pickup truck model with similar weight as the actual crash test RAM model as the test vehicle. The test vehicle's actual impact speed and angle orientation were implemented in the computer simulation. Table 4.1 shows sequential illustrations of the simulated computer model impact event. Table 4.2 compares frames from the actual full-scale crash test and the calibrated computer model impact simulation.

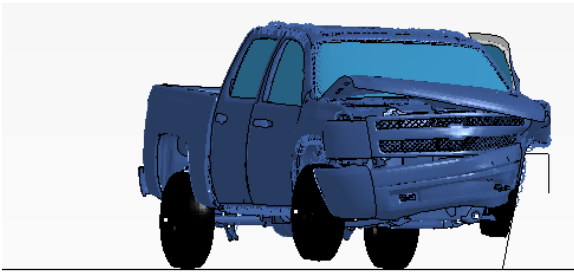
Table 4.1. Sequential Images of the Simulated Computer Model Impact Event.



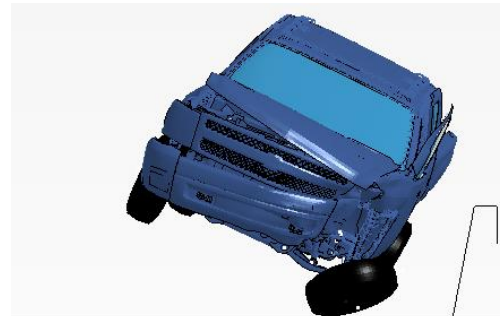
0.0 s



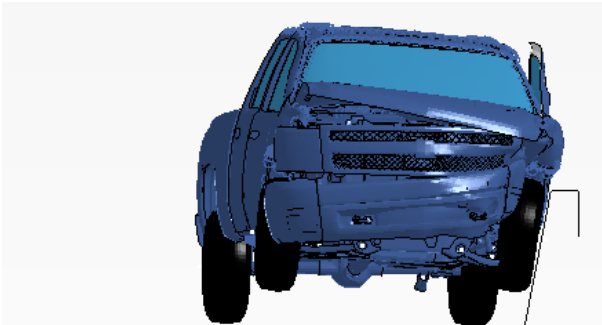
0.25 s



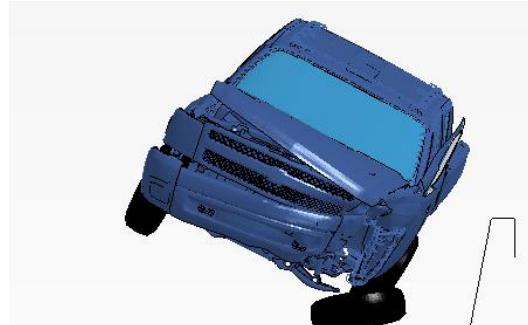
0.08 s



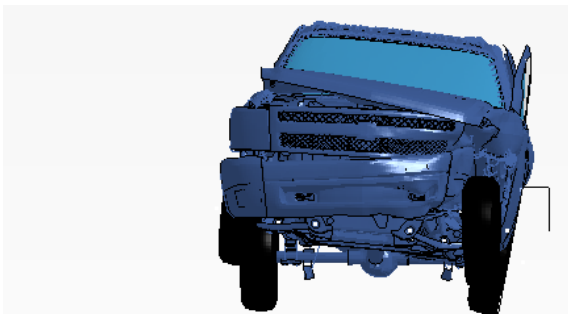
0.4 s



0.13 s



0.42 s



0.17 s

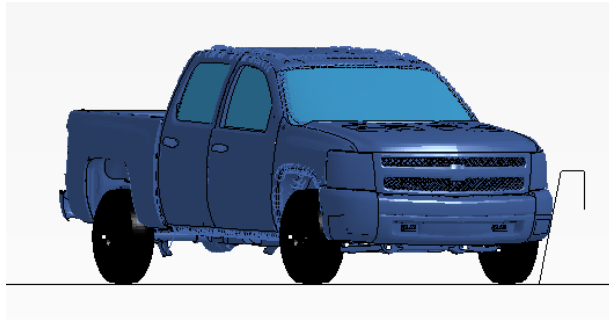


0.65 s

Table 4.2. Comparison of Actual Crash Test and LS-DYNA Simulation.



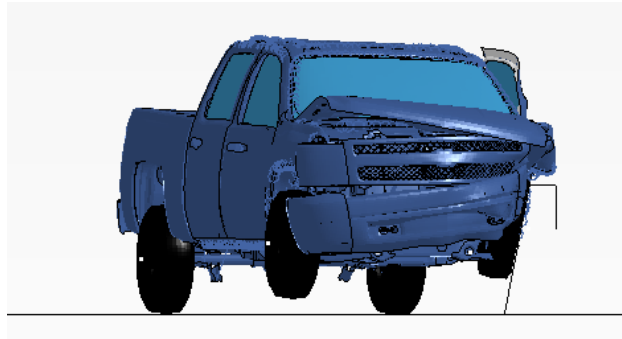
0.0 s



0.0 s



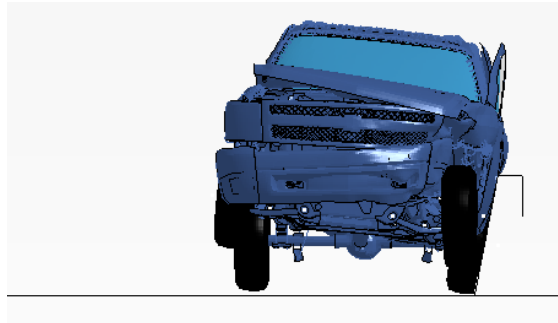
0.089 s



0.089 s



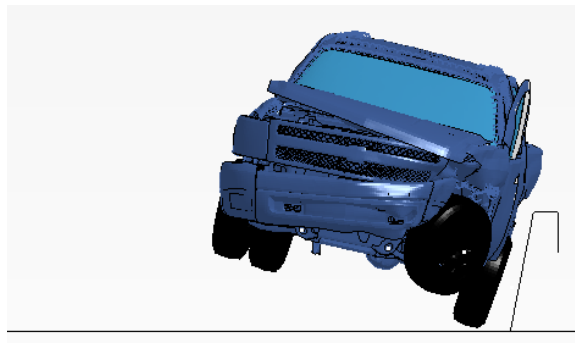
0.175 s



0.175 s



0.263 s

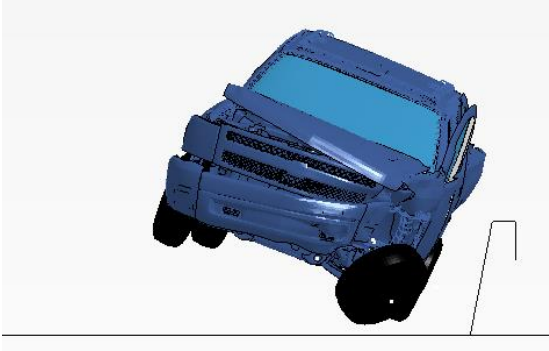


0.263 s

Table 4.2. Comparison of Actual Crash Test and LS-DYNA Simulation (Continued).



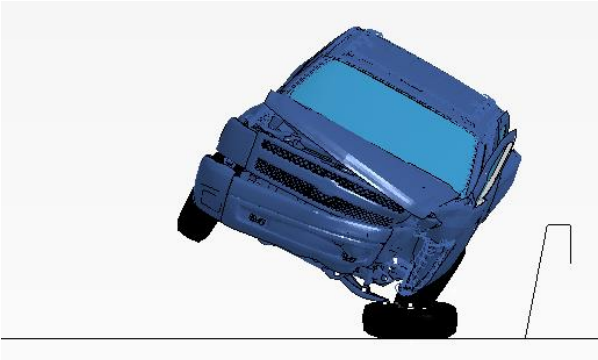
0.352 s



0.352 s



0.440 s



0.440 s



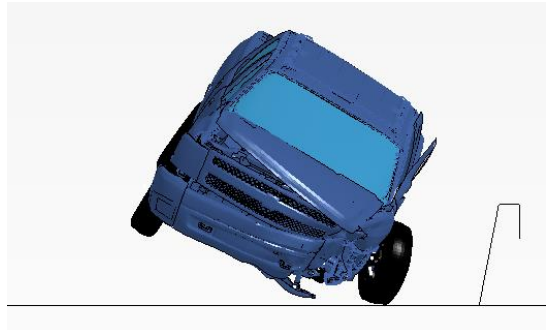
0.526 s



0.526 s



0.615 s



0.615 s

Table 4.3 summarizes occupant risk, vehicle stability information, and system deflection values from the comparison between the actual crash test values and the simulated impact event.

Table 4.3. Comparison between Full-Scale Crash Test and Impact Event Computer Simulation.

Impact Severity Index	Actual Crash Test Values	FEA Simulation Values
Longitudinal OIV	22 ft/s	15.09 ft/s
Lateral OIV	29.9 ft/s	26.57 ft/s
Longitudinal Ridedown	5.3 g	5.5 g
Lateral Ridedown	11.7 g	18.5 g
THIV	37.003 ft/s	30.83 ft/s
PHD	11.7 g	18.8 g
ASI	2.02	2.04
Max 0.050-s Average		
 Longitudinal	-10.9 g	-8.6 g
 Lateral	-15.5 g	-15.7 g
 Vertical	-6.1 g	-4.7 g
Maximum Roll	26°	38.8°
Maximum Pitch	8°	14.3°
Maximum Yaw	34°	32.9°

Note: OIV = occupant impact velocity; THIV = theoretical head impact velocity; PHD = post-impact head deceleration; ASI = acceleration severity index.

4.2.3 Conclusion

Comparison of LS-DYNA simulation results and actual crash test values revealed that the computer models (system and vehicle) could be considered calibrated with respect to the actual crash test. The simulated impact event closely matched the actual crash test events. The ridedown acceleration value was slightly overpredicted in the computer model with respect to the actual result obtained through the full-scale crash test. Generally, however, the FEA model closely replicated the testing outcomes in terms of vehicle stability and general behavior during impact event.

4.3 MODEL CALIBRATION FOR STEEL OPTION

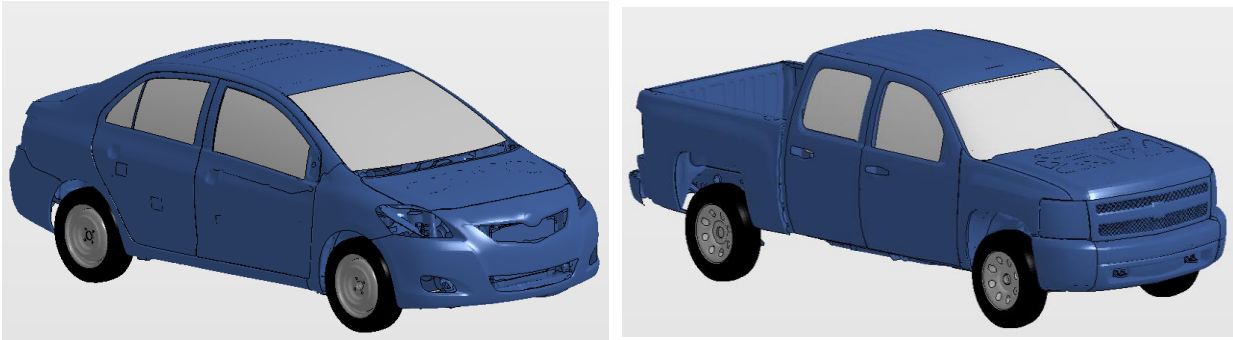
4.3.1 Model Calibration

LS-DYNA was used to simulate the behavior of vehicular impacts with a steel median barrier system. LS-DYNA is an all-purpose, explicit FEA code. It is extensively used to simulate the nonlinear, dynamic response of three-dimensional problems and for capturing intricate interactions of the vehicle with a Triborough Bridge and Tunnel Authority (TBTA) steel bridge rail system. LS-DYNA is also capable of producing dynamic load-time history responses for any impact. Before modeling the actual system, the researchers used earlier studies by TTI for

calibrating the LS-DYNA FEA model. LS-DYNA was used to perform critical impact simulations using the developed sign support system and available vehicle model.

4.3.2 Available FE Computer Models

Figure 4.7 illustrates the available FE models of the vehicles. These models include (a) Toyota Yaris model representing a 2420-lb (1100C) *MASH* small car test vehicle, and (b) Chevrolet Silverado model representing a 5000-lb (2270P) *MASH* pickup truck test vehicle.



Toyota Yaris FE Model

Chevrolet Silverado FE Model

Figure 4.7. Available Finite Element Models of Vehicles.

4.3.3 Full-Scale Crash Test

The researchers used a TBTA steel bridge rail tested for HNTB New York Engineering and Architecture, P.C. under the TTI project for calibrating the LS-DYNA FEA model. The researchers at TTI conducted *MASH* Test 5-10 and 5-11 on this TBTA steel bridge rail system to calibrate the results of the developed system in LS-DYNA by comparing vehicle impact behavior and stability, as well as occupant risk and sign support performance upon vehicle impact.

Vehicle stability, occupant risk, and structural adequacy were evaluated using the Test Risk Assessment Program (TRAP). Vehicle angular velocities, also known as roll, pitch, and yaw angles, were used to evaluate vehicle stability. *MASH* specifies that the maximum roll and pitch angles should not exceed 75 degrees. Occupant risk describes the risk of hazard to occupants. It was evaluated from the data collected by the accelerometer located at the center of gravity in the vehicle. Two factors were mainly analyzed in preliminary simulations through the acceleration data: occupant impact velocity (OIV) and occupant ridedown acceleration (ORA). OIV and ORA are the change in velocity that the hypothetical occupant feels at impact and the acceleration from the collision just after impact. *MASH* requires the OIV to be lower than 40 ft/s and ORA to be smaller than 20.49 g in the longitudinal and lateral directions.

A 2010 Kia Rio passenger car and 2010 Dodge RAM 1500 pickup truck were used in the full-scale crash test. The nominal impact speed and angle for both tests were 62 mi/h and 25 degrees, respectively.

Figure 4.8 illustrates the actual constructed TBTA bridge rail.



Figure 4.8. TBTA Bridge Rail.

4.3.4 Test Article and Installation Details

The test installation was a 132-ft-long (post to post) steel bridge rail with four rail tubes mounted on 17 posts. The bridge rail measured 3 ft 6 inches in height above the bridge deck, and the posts were equally spaced at 8 ft 3 inches along the length of the installation. The centerlines of the rails were located 40½ inches, 30 inches, 18 inches, and 7½ inches above the paved surface of the bridge deck.

The top rail element was comprised of 5×3×½-inch HSSs. Two horizontal ⅞-inch × 7-inch button head bolts with a spring lock washer, flat washer, and hex nut secured the rail to each post through holes located 1¾ inches from the centerline of each post. The upper middle rail element was comprised of 6×6×⅜-inch HSSs. Two horizontal ⅞-inch × 8½-inch button head bolts with a spring lock washer, flat washer, and hex nut secured the rail to each post through staggered holes located 1¾ inches from the centerline of each post. The lower middle rail element was comprised of 6×6×⅜-inch HSSs. Two vertical ¾-inch × 8-inch hex head bolts with a spring lock washer, flat washer, and hex nut secured the rail to a 6½-inch-long 5×5×⅜-inch railing shelf angle.

The shelf angle was secured to the face of the post with two horizontal ¾-inch × 2½-inch hex head bolts with a spring lock washer, flat washer, and hex nut. All bolts and holes were located 1¾ inches from the centerline of each post. The bottom rail element was comprised of 5×3×½-inch HSSs. Two horizontal ⅞-inch × 7-inch button head bolts with a spring lock washer, flat washer, and hex nut secured the rail to each post through holes located 1¾ inches from the centerline of each post.

The test installation had three splices. The center of the first rail splice joint was located 30 ft from the right end of the installation. The second joint was 40 ft ⅞ inches from the first joint. The third joint was 40 ft ⅞ inches from the second joint.

The rail sections were connected with a bolted splice connection. Each HSS rail contained four 1-inch-wide × 2-inch-long slots, two in the top and two in the bottom. These slots were centered 5⁷/₁₆ inches and 11⁷/₁₆ inches from the end of the rail. The top and bottom rails utilized a 1½-inch-thick × 3½-inch-wide × 30¼-inch-long internal steel bar. The middle two rails utilized a 5×5×⅜-inch HSS × 30¼-inch-long internal tube. Each splice was connected with four ¾-inch × 4-inch-long (or 7-inch-long) button head bolts with two flat washers and heavy hex nut, which was finger tightened. Rail splice end gaps measured ⅞ inches.

Seventeen fabricated steel posts, every 3 ft 7¾ inches in overall height (including the base plate), supported the four rails at equal post spacing of 8 ft 3 inches along the test installation. Each railing post was a built-up welded structure that was comprised of a W8×28 beam, 3 ft 6 inches tall that was beveled at the top 1¾ inches downward to the field side. The pseudo-trapezoidal base plate was 14 inches × 7¾ inches wide × 12¾ inches long × 1¾ inches thick and was welded to the W8×28 beam with continuous fillet welds. The base plate contained eight 1⁵/₁₆-inch diameter holes to accommodate either ⅞-inch diameter HS bolts to the supporting bridge span steel (Posts 3–9) or ¾-inch diameter expansion anchors into the concrete foundation (Posts 1–2 and 10–17), as required. The traffic-side flange of each post contained 1-inch diameter holes as necessary to attach the railings or shelf angles. The traffic-side face of each post was located 6 inches behind the vertical traffic face of the ⅝-inch-thick × 5-inch-tall curb plate on the bridge deck. The posts were supported by and bolted to the bridge deck lateral sub-floor beams, longitudinal stringer extensions, and railing connection extensions.

4.3.5 MASH Test 5-10 (TTI Test 603911-1)

Figure 4.9 shows the bridge rail and test vehicle geometrics. Figure 4.10 and Figure 4.11 show the test vehicle before and after the test. Figure 4.12 shows the interior of the test vehicle before and after the test. Figure 4.13 summarizes the full-scale crash test results.



Figure 4.9. TBTA Bridge Rail/Test Vehicle Geometrics.



Figure 4.10. Test Vehicle before Test.



Figure 4.11. Test Vehicle after Test.

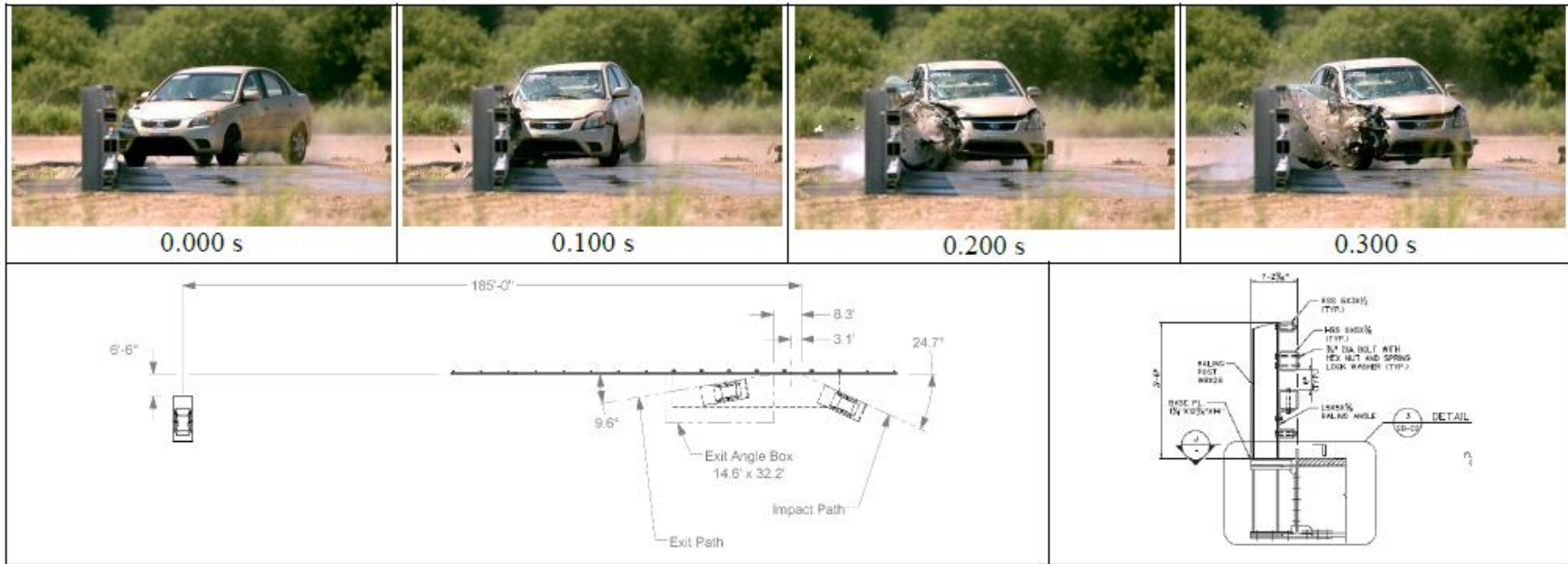


Before Test



After Test

Figure 4.12. Interior of Test Vehicle.



General Information

Test Agency..... Texas A&M Transportation Institute (TTI)
 Test Standard Test No..... MASH Test 5-10
 TTI Test No. 603911-1
 Test Date..... 2016-06-07

Test Article

Type Bridge Rail
 Name..... TBTA Bridge Rail
 Installation Length..... 132 ft long (post to post)
 Material or Key Elements... Quadruple rail steel bridge rail 3 ft-6 inches in height mounted on 17 posts attached either to a 49 ft-6 inch bridge span (posts 3-9), or to a concrete foundation up to the bridge span and beyond the bridge span

Soil Type and Condition

Concrete Bridge Deck

Test Vehicle

Type/Designation..... 1100C
 Make and Model 2010 Kia Rio
 Curb..... 2478 lb
 Test Inertial..... 2425 lb
 Dummy 165 lb
 Gross Static..... 2590 lb

Impact Conditions

Speed 62.5 mi/h
 Angle 24.7 degrees
 Location/Orientation 3.1 ft upstrm of splice btw 4 & 5

Impact Severity

55 kip-ft

Exit Conditions

Speed 48.3 mi/h
 Angle 9.6 degrees

Occupant Risk Values

Longitudinal OIV 22.0 ft/s
 Lateral OIV 34.8 ft/s
 Longitudinal Ridedown 4.1 g
 Lateral Ridedown 10.9 g
 THIV 44.8 km/h
 PHD 10.9 g
 ASI 2.82

Max. 0.050-s Average

Longitudinal -13.1 g
 Lateral..... -21.2 g
 Vertical..... -3.2 g

Post-Impact Trajectory

Stopping Distance..... 185 ft downstrm
 6.5 ft twd traffic

Vehicle Stability

Maximum Yaw Angle 74 degrees
 Maximum Pitch Angle 8 degrees
 Maximum Roll Angle 9 degrees
 Vehicle Snagging No
 Vehicle Pocketing No

Test Article Deflections

Dynamic..... 1.5 inches
 Permanent 0.5 inch
 Working Width..... 15.5 inches

Vehicle Damage

VDS..... 01RFQ4
 CDC..... 01FREW3
 Max. Exterior Deformation..... 10.5 inches
 OCDI..... RF0013000
 Max. Occupant Compartment Deformation 2.25 inches

Figure 4.13. Summary of MASH Test 5-10 on TBTA Bridge Rail.

4.3.6 MASH Test 5-11 (TTI Test 603911-2)

Figure 4.14 shows the bridge rail and test vehicle geometrics. Figure 4.15 and Figure 4.16 show the test vehicle before and after the test. Figure 4.17 shows the interior of the test vehicle before and after the test. Figure 4.18 summarizes the full-scale crash test results.



Figure 4.14. TBTA Bridge Rail/Test Vehicle Geometrics.



Figure 4.15. Test Vehicle before Test.



Figure 4.16. Test Vehicle after Test.

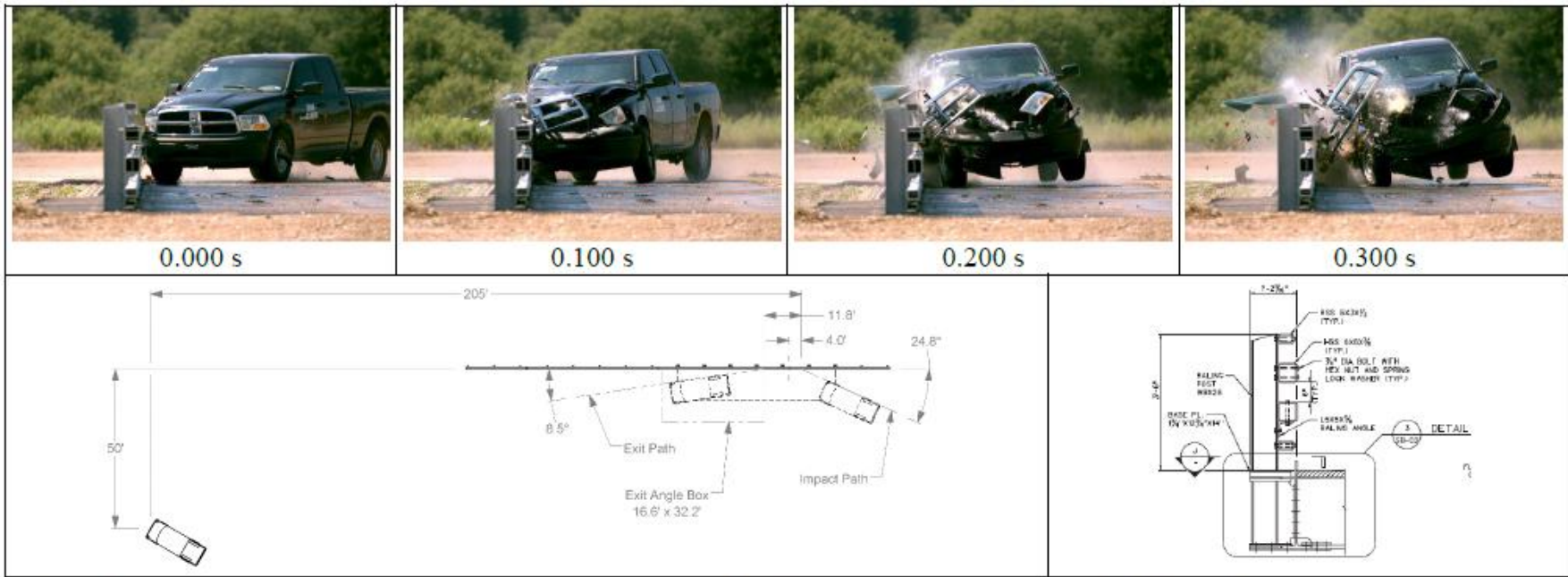


Before Test



After Test

Figure 4.17. Interior of Test Vehicle.



General Information

Test Agency..... Texas A&M Transportation Institute (TTI)
 Test Standard Test No. MASH Test 5-11
 TTI Test No. 603911-2
 Test Date 2016-06-09

Test Article

Type Bridge Rail
 Name TBTA Bridge Rail
 Installation Length 132 ft long (post to post)
 Material or Key Elements ... Quadruple rail steel bridge rail 3 ft-6 inches in height mounted on 17 posts attached either to a 49 ft-6 inch bridge span (posts 3-9), or to a concrete foundation up to the bridge span and beyond the bridge span

Soil Type and Condition

Concrete Bridge Deck

Test Vehicle

Type/Designation 2270P
 Make and Model 2010 Dodge RAM 1500 Pickup Truck
 Curb 5009 lb
 Test Inertial 5052 lb
 Dummy 165 lb
 Gross Static 5217 lb

Impact Conditions

Speed 64.3 mi/h
 Angle 24.8 degrees
 Location/Orientation 4.0 ft upstream of splice btw 4 and 5

Impact Severity.....

123 kip-ft

Exit Conditions

Speed 51.9 mi/h
 Angle 8.5 degrees

Occupant Risk Values

Longitudinal OIV 17.4 ft/s
 Lateral OIV 28.5 ft/s
 Longitudinal Ridedown 6.0 g
 Lateral Ridedown 10.7 g
 THIV 37.1 km/h
 PHD 10.8 g
 ASI 1.92

Max. 0.050-s Average

Longitudinal -8.5 g
 Lateral -15.2 g
 Vertical 2.8 g

Post-Impact Trajectory

Stopping Distance 205 ft downstrm
 50 ft twd traffic

Vehicle Stability

Maximum Yaw Angle 43 degrees
 Maximum Pitch Angle 4 degrees
 Maximum Roll Angle 10 degrees
 Vehicle Snagging No
 Vehicle Pocketing No

Test Article Deflections

Dynamic 2.0 inches
 Permanent 0.75 inch
 Working Width 15.8 inches

Vehicle Damage

VDS 01RFQ4
 CDC 01FREW4
 Max. Exterior Deformation 16.0 inches
 OCDI RF0030000
 Max. Occupant Compartment Deformation 5.0 inches

Figure 4.18. Summary of MASH Test 5-11 on TBTA Bridge Rail.

4.3.7 Computer Model Simulation

LS Pre-Post was used to develop a TBTA steel bridge rail. A steel bridge rail was developed with multiple different material and section properties. W-sections were modeled with MAT024—Piecewise Linear Plasticity to define steel post material properties. MAT024 was also used to define the material properties of base plates and both HSSs. Nodal rigid body constrained connections were used to connect base plates to W-sections and HSSs to W-sections. Figure 4.19 shows the LS-DYNA model of the TBTA steel bridge rail system used for calibration.

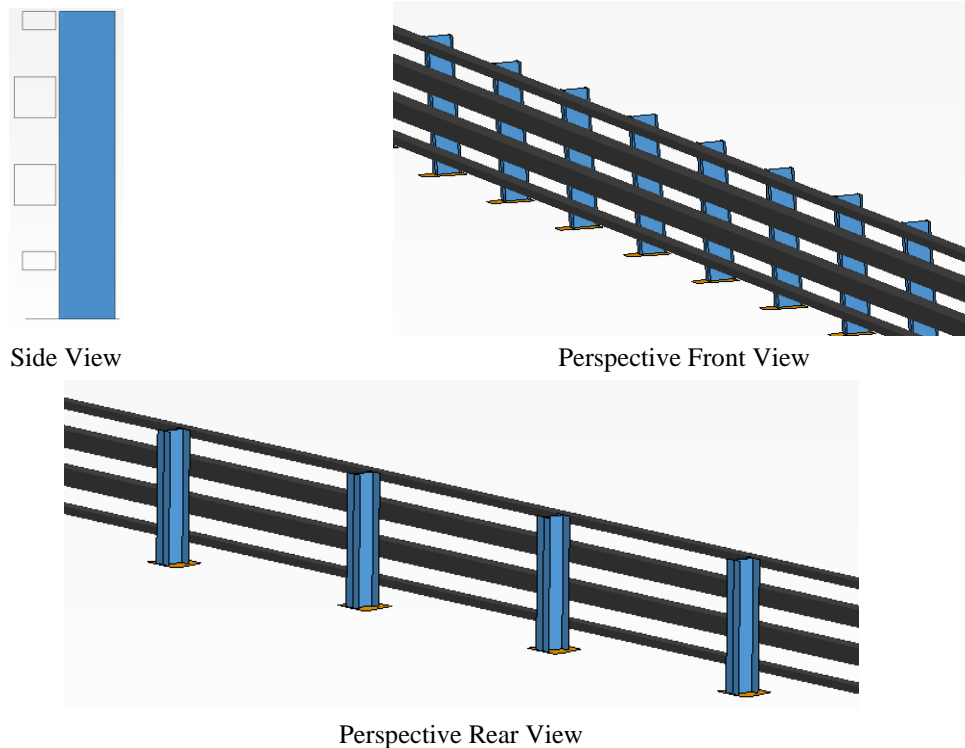


Figure 4.19. LS-DYNA Calibration Barrier System Model.

4.3.8 MASH Test 5-10 Calibration (Test 603911-1)

The researchers used a validated Toyota Yaris model with a similar weight as the actual crash test Kia Rio model as the test vehicle. The test vehicle's actual impact speed and angle orientation were implemented in the computer simulation. Table 4.4 shows the sequential illustration of the simulated computer model impact event. Table 4.4 compares frames from the actual full-scale crash test and the calibrated computer model impact simulation.

Table 4.4. Comparison of Actual Crash Test and LS-DYNA Simulation.


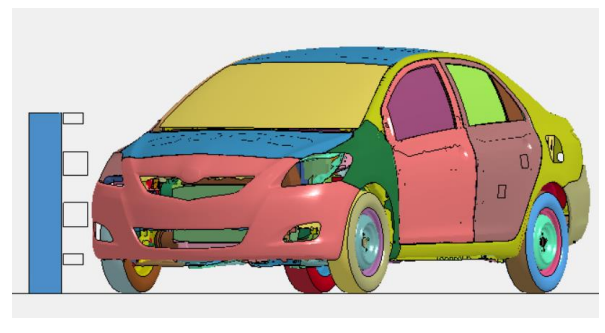

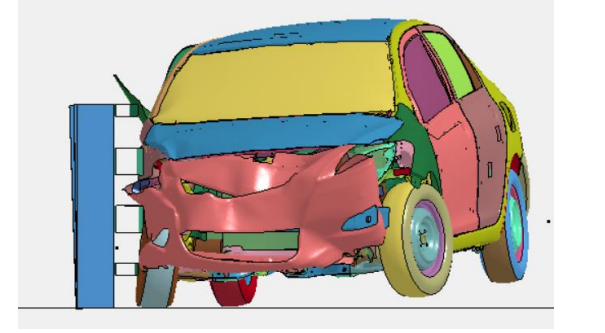

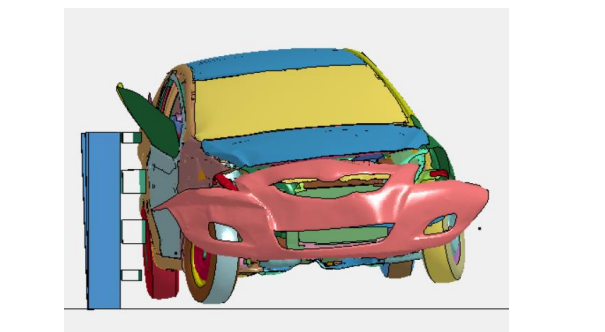

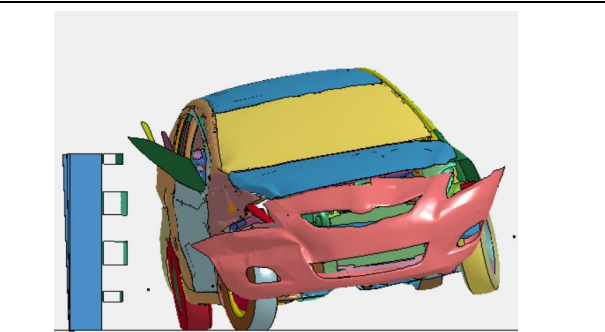
	
<p>0.0 s</p>	
	
<p>0.1 s</p>	
	
<p>0.2 s</p>	
	
<p>0.3 s</p>	

Table 4.5 summarizes occupant risk, vehicle stability information, and system deflection values from the comparison between the actual crash test values and the simulated impact event.

Table 4.5. Comparison between Full-Scale Crash Test and Computer Simulation.

	Actual Crash Test	FEA Simulation
Longitudinal OIV	22.0 ft/s	20.59 ft/s
Lateral OIV	34.8 ft/s	-30.43 ft/s
Longitudinal Ridedown	4.1 g	-4.3 g
Lateral Ridedown	10.9 g	21.9 g
THIV	44.8 km/h	42.7 km/h
PHD	10.9	21.9
ASI	2.82	2.6
Max 0.050-s Average		
Longitudinal	-13.1 g	-13.3 g
Lateral	21.2 g	20.2 g
Vertical	3.2 g	4.8 g
Maximum Roll	9°	11.5°
Maximum Pitch	8°	2.2°
Maximum Yaw	74°	35.7°

4.3.9 MASH Test 5-11 Calibration (Test 603911-2)

The researchers used a validated Silverado model with a similar weight as the actual crash test Dodge RAM model as the test vehicle. The test vehicle’s actual impact speed and angle orientation were implemented in the computer simulation. Table 4.6 compares frames from the actual full-scale crash test and the calibrated computer model impact simulation. Table 4.7 summarizes occupant risk, vehicle stability information, and system deflection values from the comparison between the actual crash test values and the simulated impact event.

4.3.10 MASH Test 5-11 (Driver-Side Impact) Calibration (Test 603911-2)

For more accurate calibration, researchers also validated the driver side of the pickup truck for MASH Test 5-11. The test vehicle’s actual impact speed and angle orientation were implemented in the computer simulation. Table 4.6 compares frames from the actual full-scale crash test and the calibrated computer model impact simulation. Table 4.7 summarizes occupant risk, vehicle stability information, and system deflection values from the comparison between the actual crash test values and the simulated impact event.

Table 4.6. Comparison of Actual Crash Test and LS-DYNA Simulation.


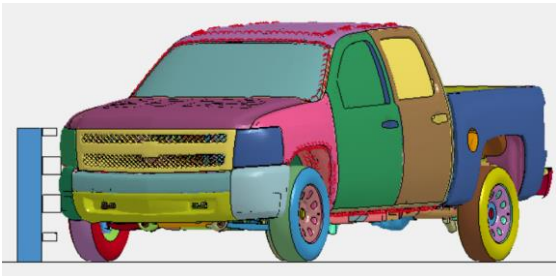

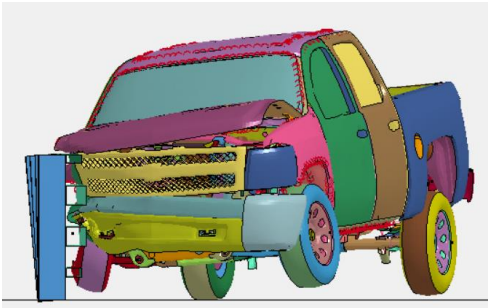

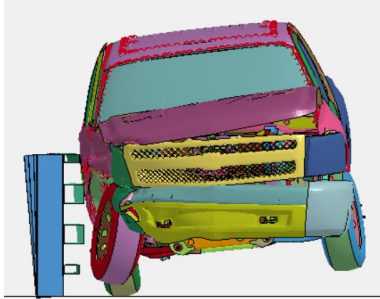

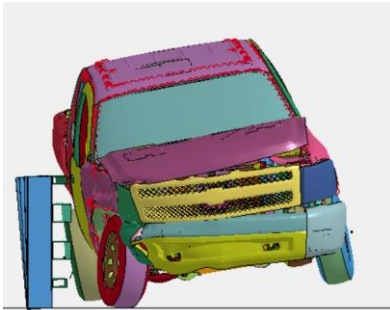
	
0.0 s	
	
0.1 s	
	
0.2 s	
	
0.3 s	

Table 4.7. Comparison between Full-Scale Crash Test and Computer Simulation.

	Actual Crash Test	FEA Simulation
Longitudinal OIV	17.4 ft/s	28.2 ft/s
Lateral OIV	28.5 ft/s	-28.2 ft/s
Longitudinal Ridedown	6.0 g	-15.9 g
Lateral Ridedown	10.7 g	14.7 g
THIV	37.1 km/h	43.1 km/h
PHD	10.8	19.7
ASI	1.92	2.08
Max 0.050-s Average		
Longitudinal	-8.5 g	-13.3 g
Lateral	-15.2 g	14.2 g
Vertical	2.8 g	3.8 g
Maximum Roll	10°	11.3°
Maximum Pitch	4°	6.9°
Maximum Yaw	43°	30.3°

Table 4.8. Comparison between Full-Scale Crash Test and Impact Event Computer Simulation.

	Actual Crash Test	FEA Simulation
Longitudinal OIV	17.4 ft/s	21.648 ft/s
Lateral OIV	28.5 ft/s	29.192 ft/s
Longitudinal Ridedown	6.0 g	-5.7 g
Lateral Ridedown	10.7 g	-16.9 g
THIV	37.1 km/h	39.8 km/h
PHD	10.8	16.9
ASI	1.92	1.94
Max 0.050-s Average		
Longitudinal	-8.5 g	-11.6 g
Lateral	-15.2 g	-15 g
Vertical	2.8 g	2.9 g
Maximum Roll	10°	-12.8°
Maximum Pitch	4°	9°
Maximum Yaw	43°	-31.5°

4.3.11 Conclusion

A comparison of LS-DYNA simulation results and actual crash test values revealed that the computer models (system and vehicle) could be considered calibrated concerning the actual crash test. The simulated impact event closely matched the actual crash test events. The ridedown acceleration value was slightly overpredicted in the computer model versus the actual result obtained through the full-scale crash test. Generally, however, the FEA model closely replicated the testing outcomes in terms of vehicle stability and general behavior during the impact event.

4.4 SIMULATIONS

Multiple options were developed for possible barrier systems to prevent cross-median crashes of passenger vehicles and trucks. The options were also developed with the specific need to accommodate the passage of floodwater during severe weather events in mind. Therefore, the proposed options would serve the multiple objectives of reducing flooding severity, decreasing risk to motorists and others in the area, and reducing the level of damage to the highway and surrounding area.

The following options were approved for further consideration:

- Option A: 42-inch-tall single-slope median barrier.
- Option B: 38-inch median version of the T223 TxDOT post-and-beam bridge rail.
- Option C: 38-inch open steel barrier.

For Options A and B, an FE parametric study was conducted to investigate potential CIP for vehicular impacts.

4.4.1 Option A: 42-Inch-Tall Single-Slope Median Barrier

Figure 3.1 shows preliminary drawings of the proposed 42-inch single-slope median barrier. The barrier base is 24 inches wide, and the barrier is 8 inches wide at the top. Openings are 13 inches tall. The length of the proposed openings is 18 ft. The openings are sloped laterally to limit risk of vehicle snagging during a potential vehicle impact event.

Figure 4.20 shows the different CIPs considered for the parametric study for Option A.

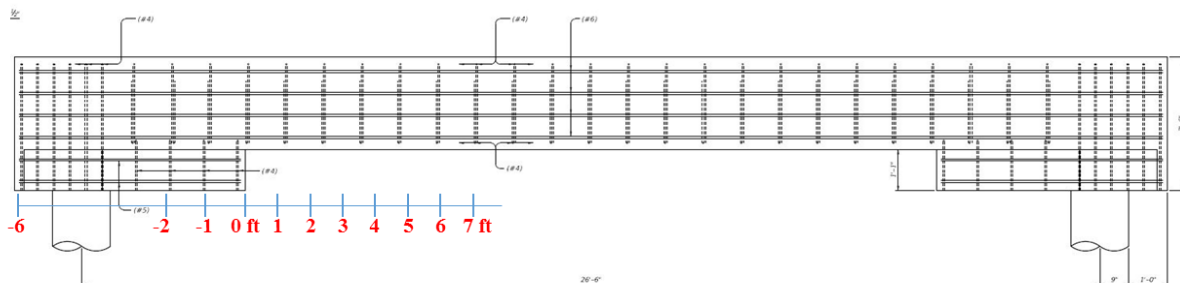


Figure 4.20. CIPs Considered for Option A System.

Figure 4.21 shows the different views of the developed FEA model for the Option A system. Analysis was performed with all three vehicles (passenger car, pickup truck, and large SUT truck). Shell elements were used for developing the 42-inch single-slope barrier system. RIGID-020 material properties were used to define concrete properties. In other words, FEAs were conducted to specifically investigate the vehicle stability and the potential for vehicle underriding at opening locations during an impact event. Steel reinforcement details and related barrier strength were investigated through engineering analysis, as detailed at the end of this section.

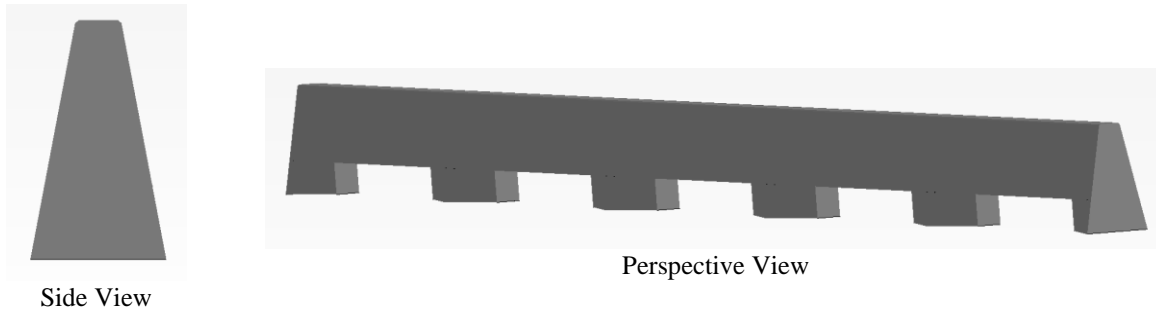


Figure 4.21. Developed FEA Model for Option A System.

The developed computer model was used to perform simulations with vehicle models. Figure 4.22 shows the view of the developed barrier model with inclusion of the three vehicles needed for *MASH* TL-4 evaluation.

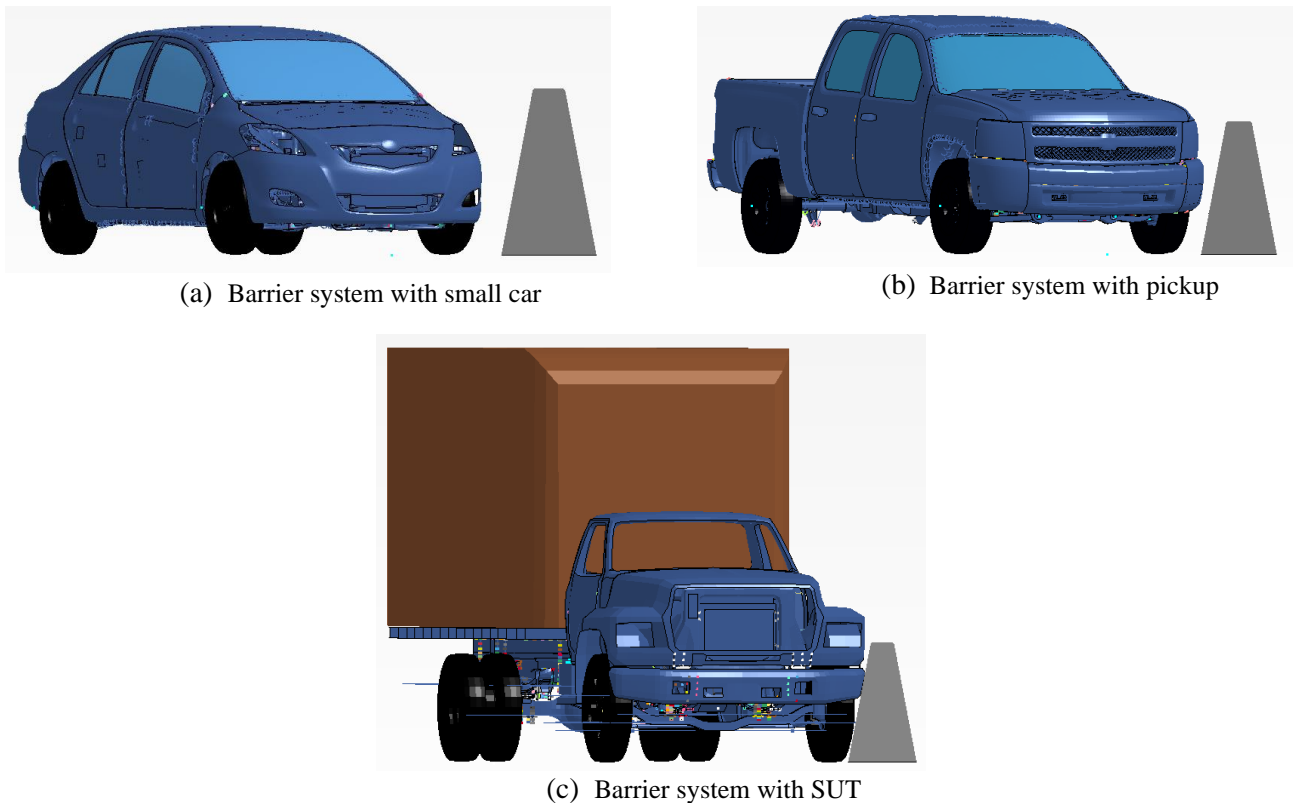
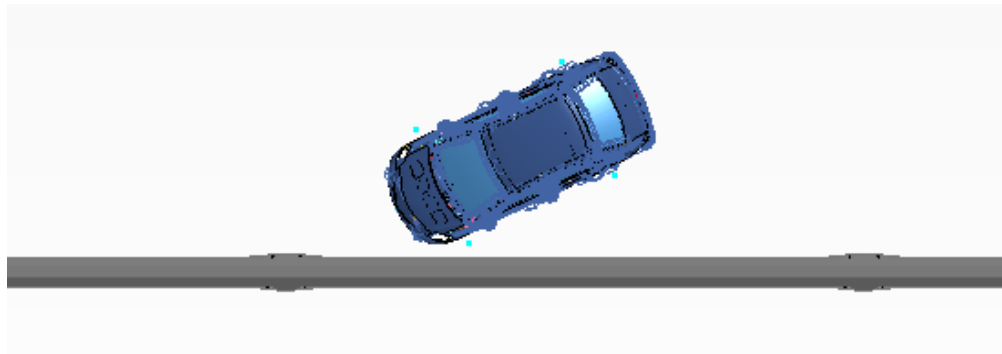


Figure 4.22. Computer Simulation Models for Option A with Different Vehicles.

4.4.1.1 42-Inch-Tall Single-Slope Median Barrier with Passenger Car

AUTOMATIC_SURFACE_TO_SURFACE and AUTOMATIC_SURFACE_TO_SURFACE contact keyword cards were used to define contact between the vehicle and the barrier. The vehicle impact speed and angle were 62 mi/h and 25 degrees, respectively. Figure 4.23 illustrates different views of the Option A barrier system with the passenger car (*MASH* 1100C vehicle).



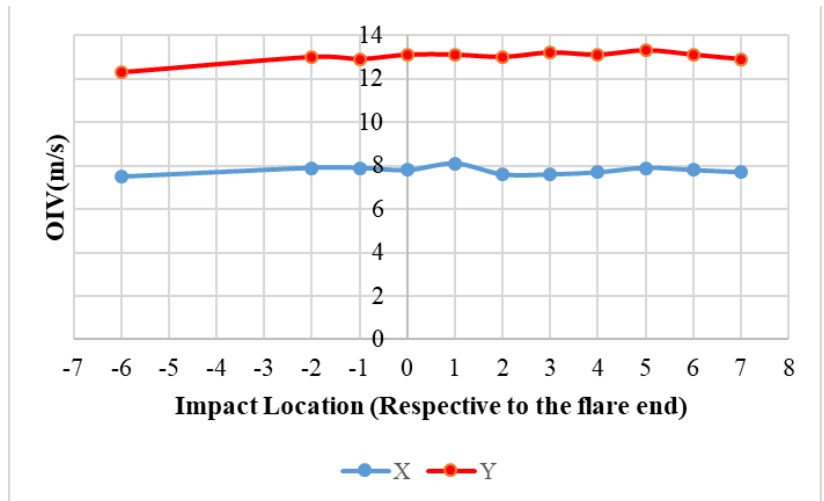
(a) Top View



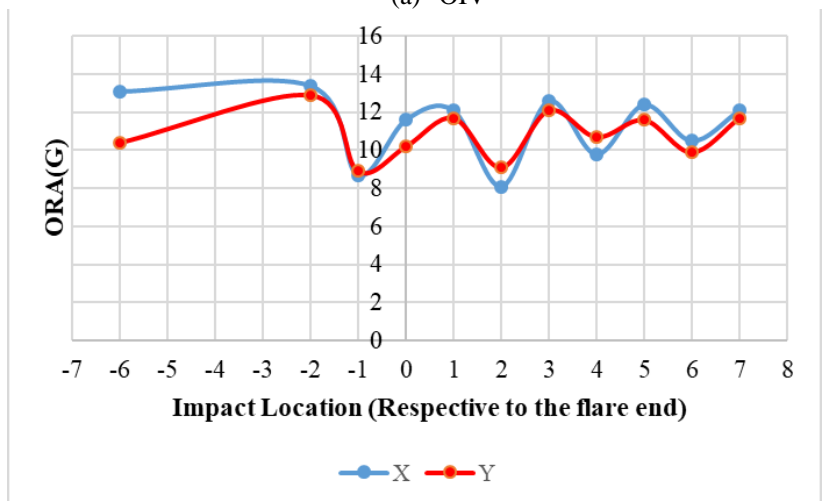
(b) Perspective View

Figure 4.23 Computer Model for Option A with Passenger Car.

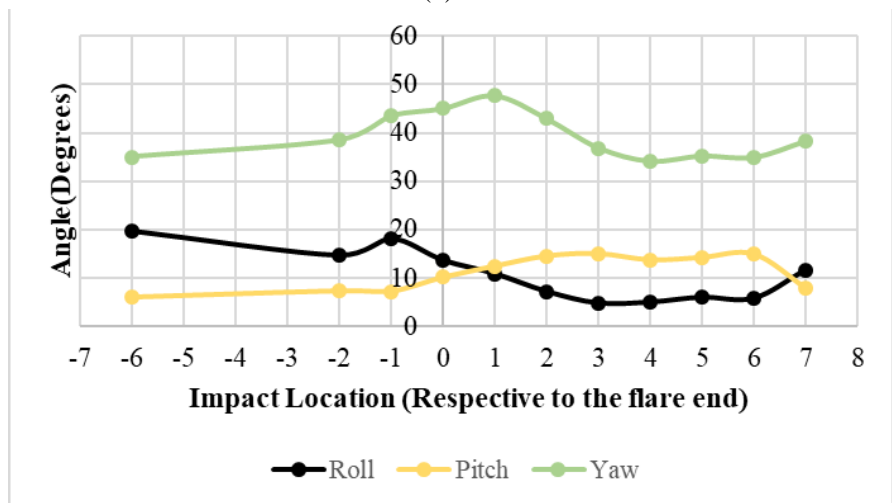
Figure 4.24 shows occupant risk and vehicle stability results from the performed CIP parametric analysis with the passenger car. Table 4. illustrates sequential images of the simulation results from the performed FEA computer simulations for 4-ft CIP respective to the flare end.



(a) OIV



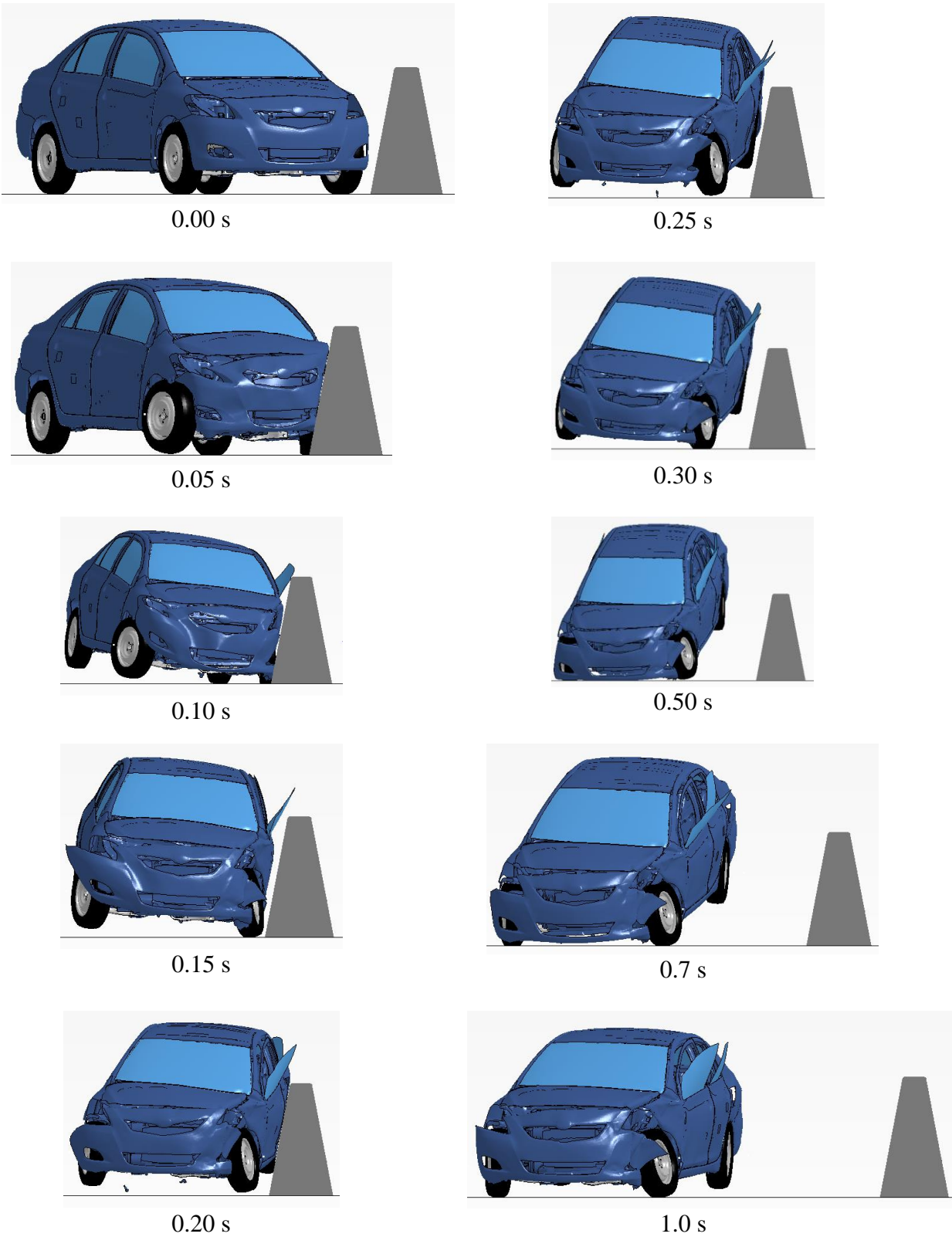
(b) ORA



(c) Vehicular Displacement

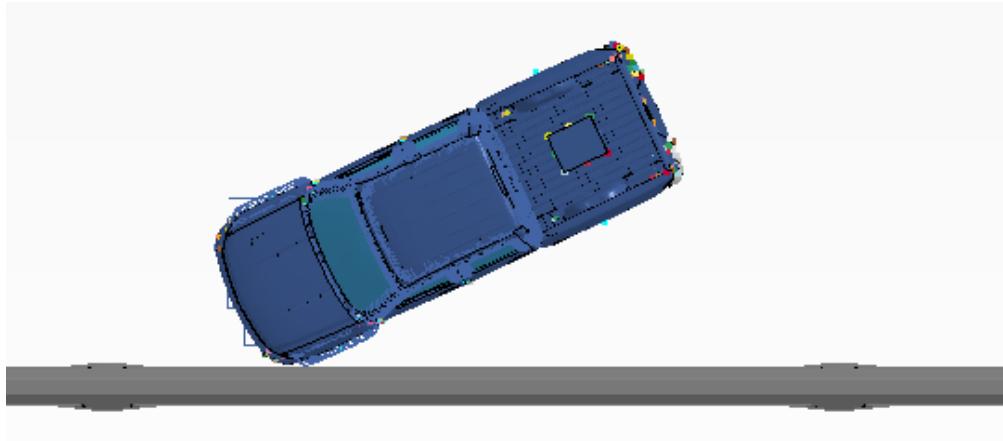
Figure 4.24. Parametric Analysis Results for Option A with Passenger Car.

Table 4.9. Sequential Images of the Simulated Computer Model Impact Events for Option A with Passenger Car.



4.4.1.2 42-Inch-Tall Single-Slope Median Barrier with Pickup Truck (without Tire Disengagement)

For the pickup truck, two different simulations were performed: with and without tire disengagement. The vehicle impact speed and angle were 62 mi/h and 25 degrees, respectively. Figure illustrates the different views of the Option A barrier system with the pickup truck (*MASH 2270P* vehicle).



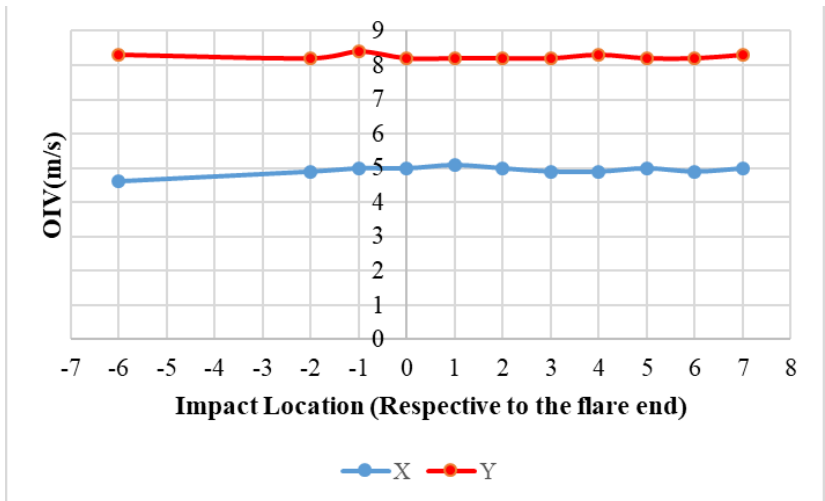
(a) Top View



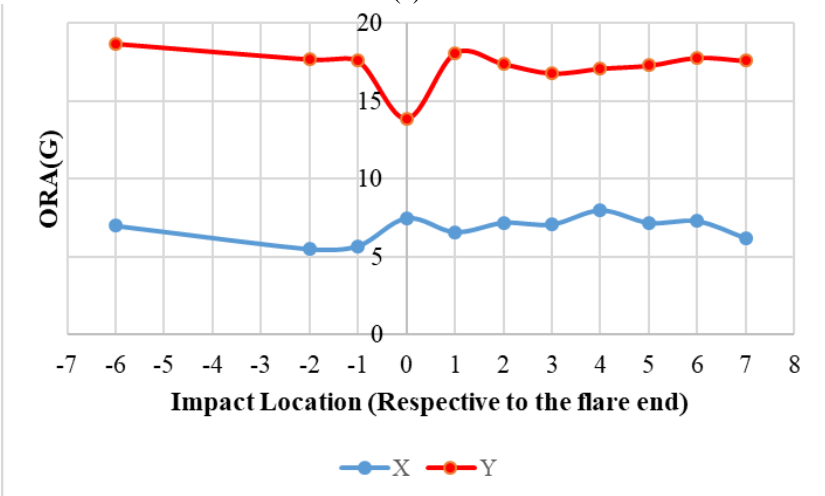
(b) Perspective View

Figure 4.25. Different Views of Computer Simulation Model for Option A with Pickup Truck.

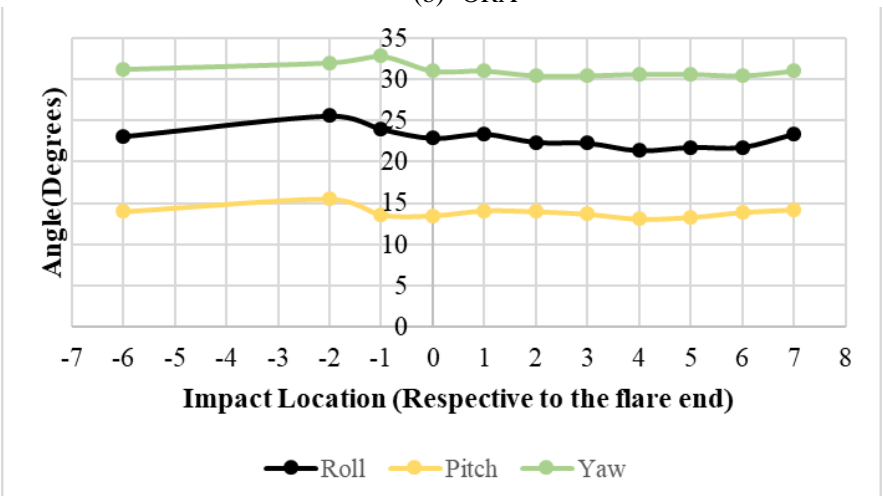
Figure 4.26 shows occupant risk and vehicle stability results from the performed CIP parametric analysis with the pickup truck. Table 4.10 illustrates sequential images of the simulation results from the performed FEA computer simulations for 4-ft CIP upstream of the flared end of the barrier opening.



(a) OIV



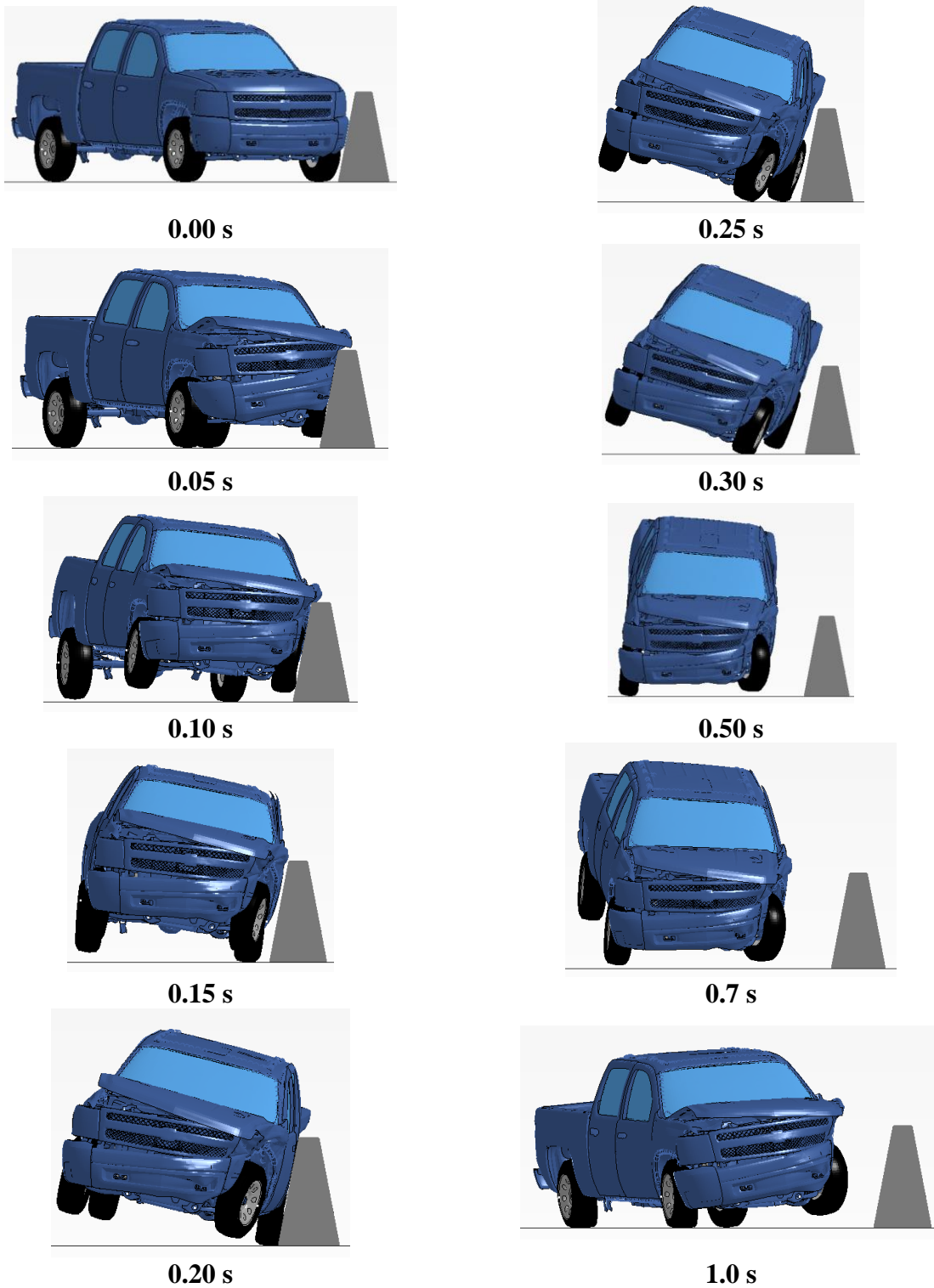
(b) ORA



(c) Vehicular Displacement

Figure 4.26. Parametric Analysis Results for Option A with Pickup Truck (without Tire Disengagement.)

Table 4.10. Sequential Images of the Simulated Computer Model Impact Events for Option A with Pickup Truck (without Tire Disengagement).



4.4.1.3 42-Inch-Tall Single-Slope Median Barrier with Pickup Truck (with Tire Disengagement)

Figure 4.27 shows occupant risk and vehicle stability results from the performed CIP parametric analysis with the pickup truck.

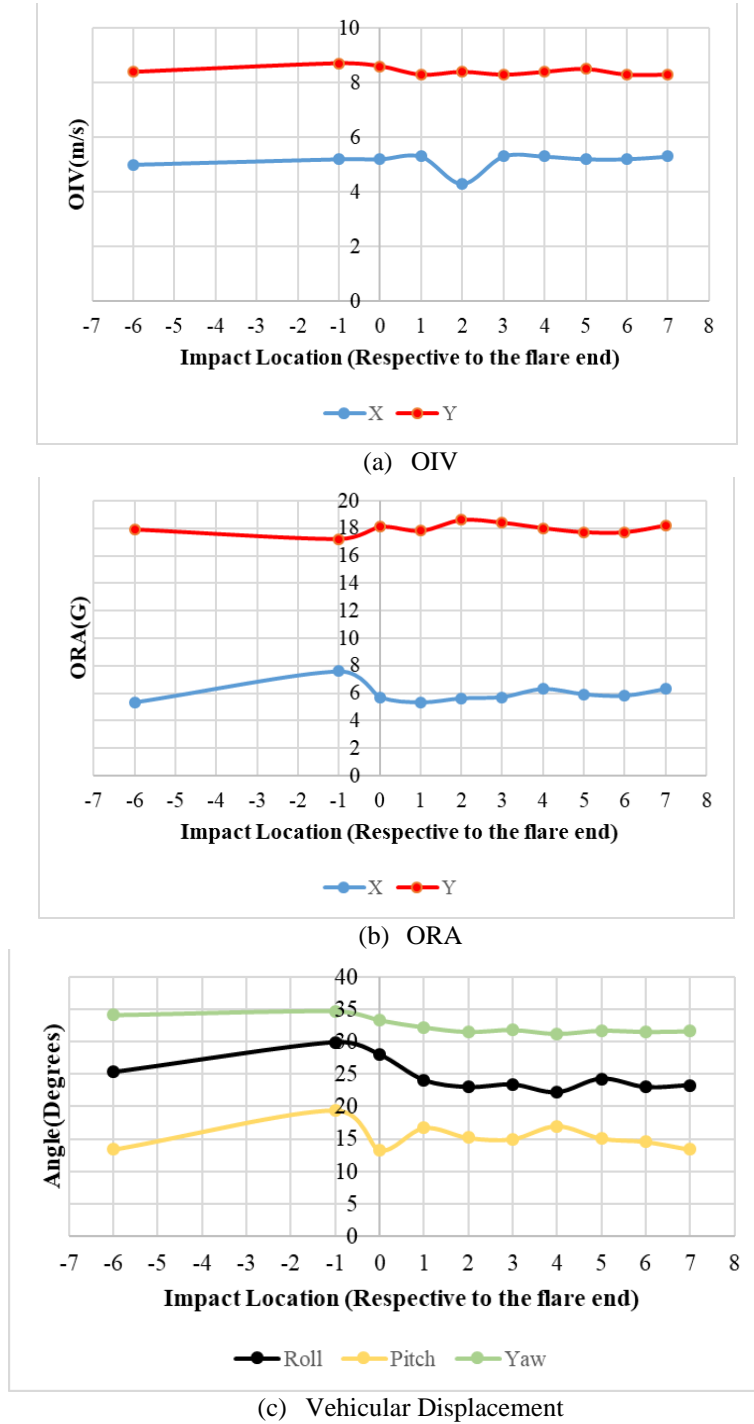
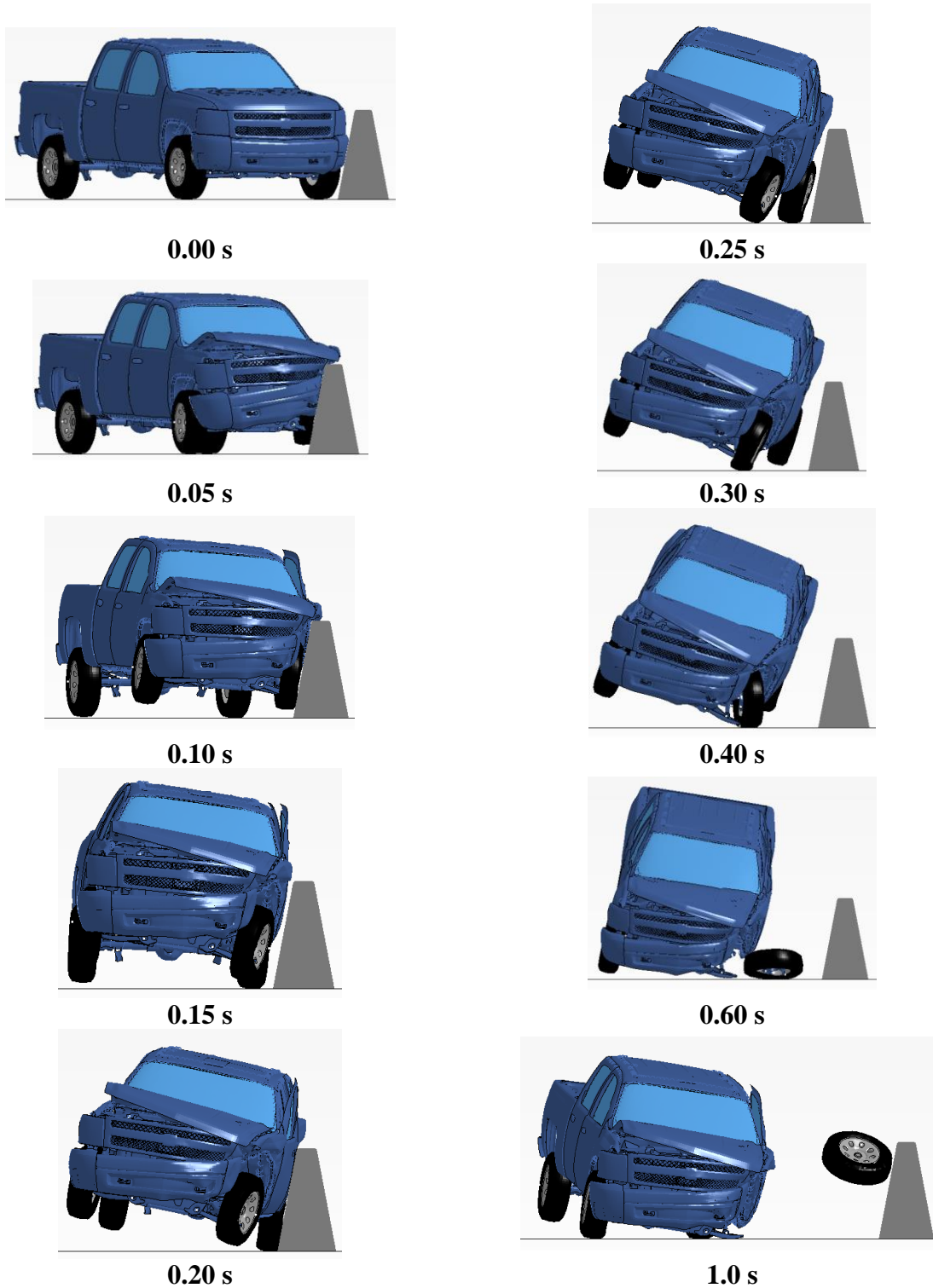


Figure 4.27. Parametric Analysis Results for Option A with Pickup Truck (with Tire Disengagement).

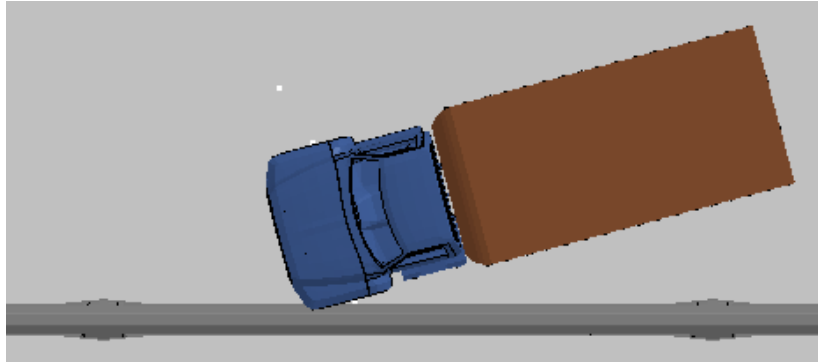
Table 4.11 illustrates sequential images of the simulation results from the performed FEA computer simulations for 4-ft CIP upstream of the flared end of the barrier opening.

Table 4.11. Sequential Images of the Simulated Computer Model Impact Events for Option A with Pickup Truck (with Tire Disengagement).



4.4.1.4 42-Inch-Tall Single-Slope Median Barrier with Single-Unit Truck

For the SUT vehicle impact, a simulation was performed with the CIP being 5 ft upstream of the flared end of the barrier opening. The vehicle impact speed and angle were 56 mi/h and 15 degrees, respectively. Figure 4.28 illustrates different views of the Option A barrier system with the SUT (*MASH 1000S* vehicle).



(a) Top View

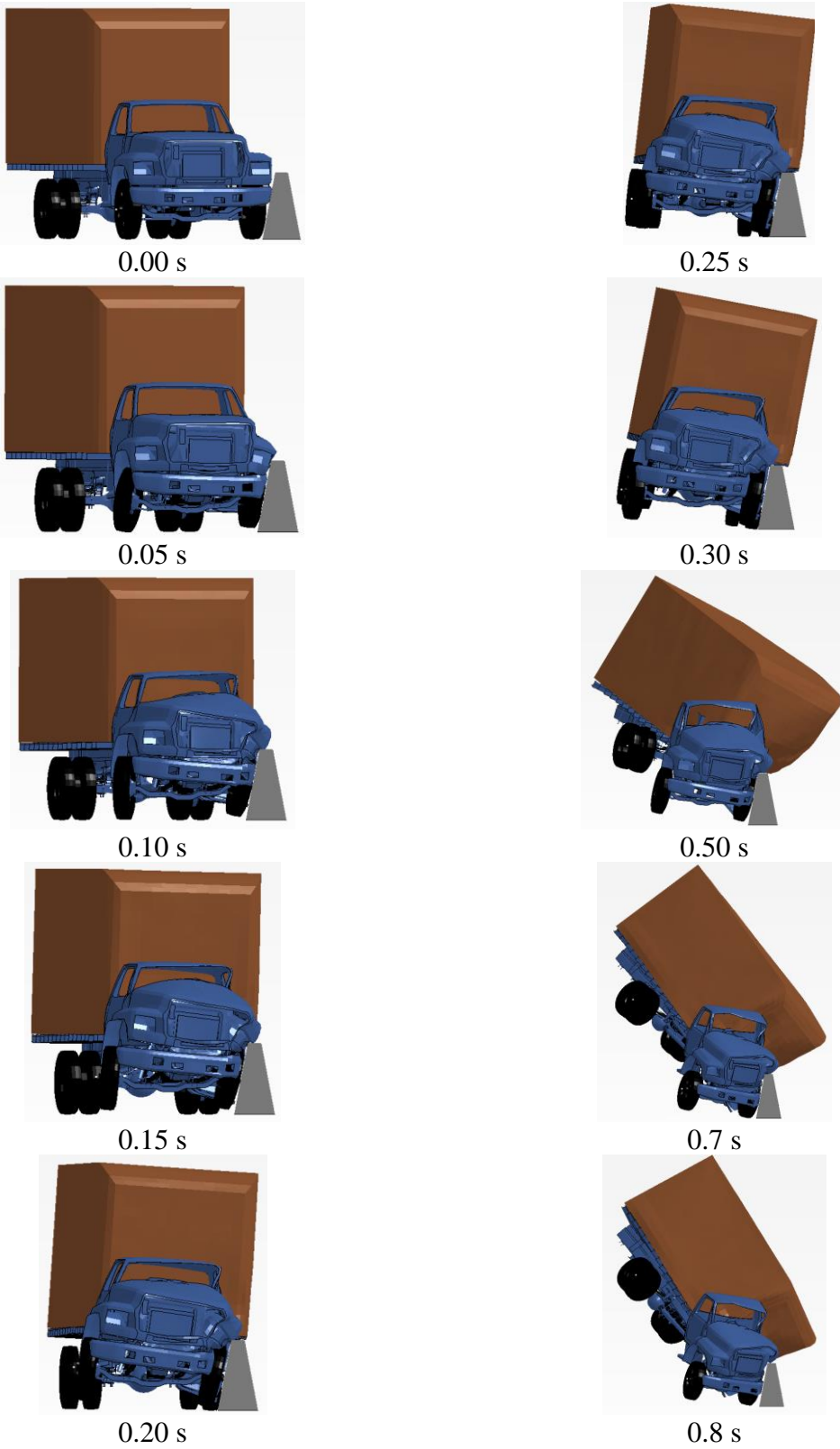


(b) Perspective View

Figure 4.28. Computer Simulation Model for Option A with SUT.

Table 4.12. illustrates sequential images of the simulation results from the performed FEA computer simulations.

Table 4.12. Sequential Images of the Simulated Computer Model Impact Events for Option A with SUT.



4.4.2 Option B: Median Version of the T223 TxDOT Post-and-Beam Bridge Rail

Option B represents a proposed median version of the existing T223 TxDOT concrete post-and-beam bridge rail. The concrete beam is 25 inches high and 24 inches wide, with concrete posts that are 13 inches tall. Two configurations were considered for computer simulations: (a) with concrete posts sloped laterally, as depicted in Figure 4.29; and (b) with constant-width concrete posts, as depicted in Figure 4.30. For simplicity, only frames from simulations considering constant-width concrete posts are reported in this chapter. No significant differences were noted while comparing the performances of these two barrier designs during vehicular impacts.

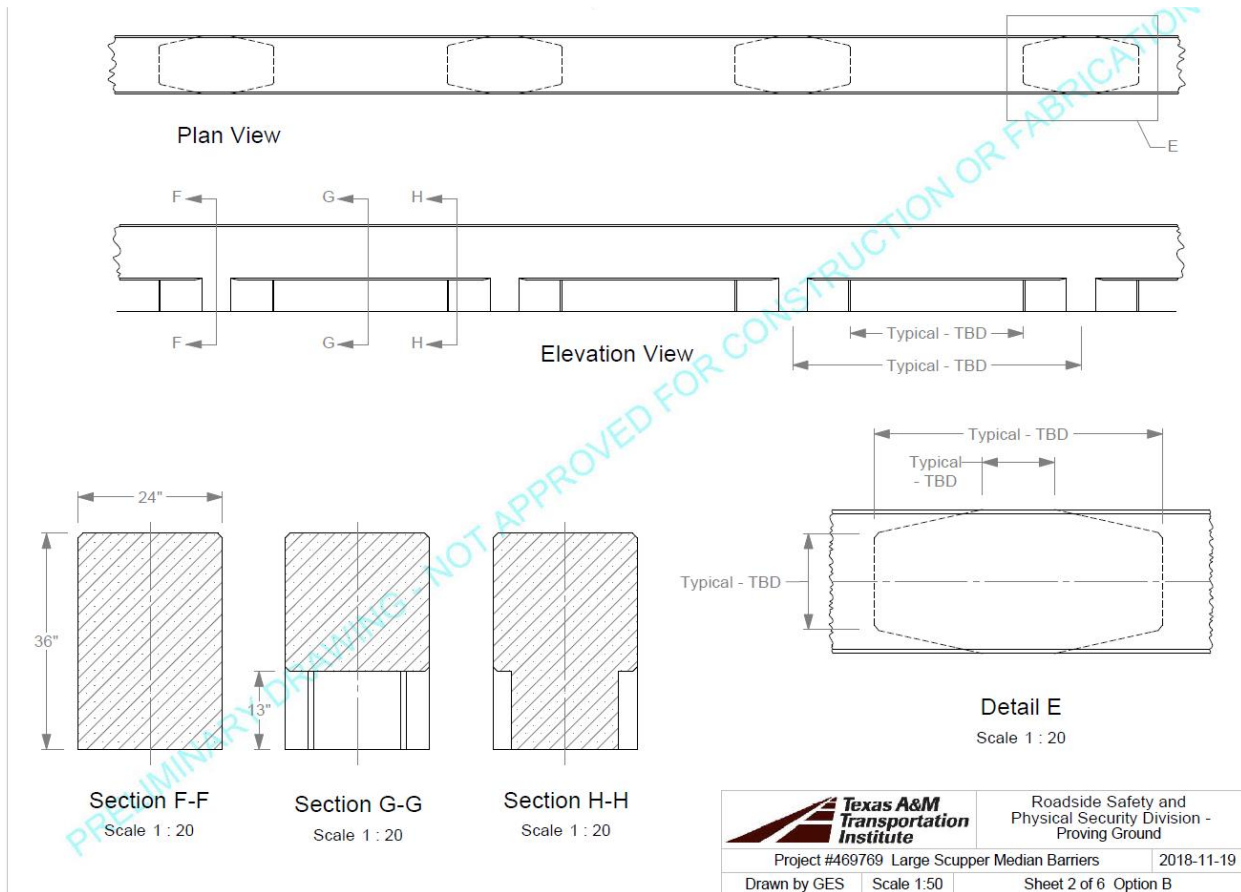


Figure 4.29. Option B: Median Version of the T223 TxDOT Post-and-Beam Bridge Rail with Posts Sloped Laterally.

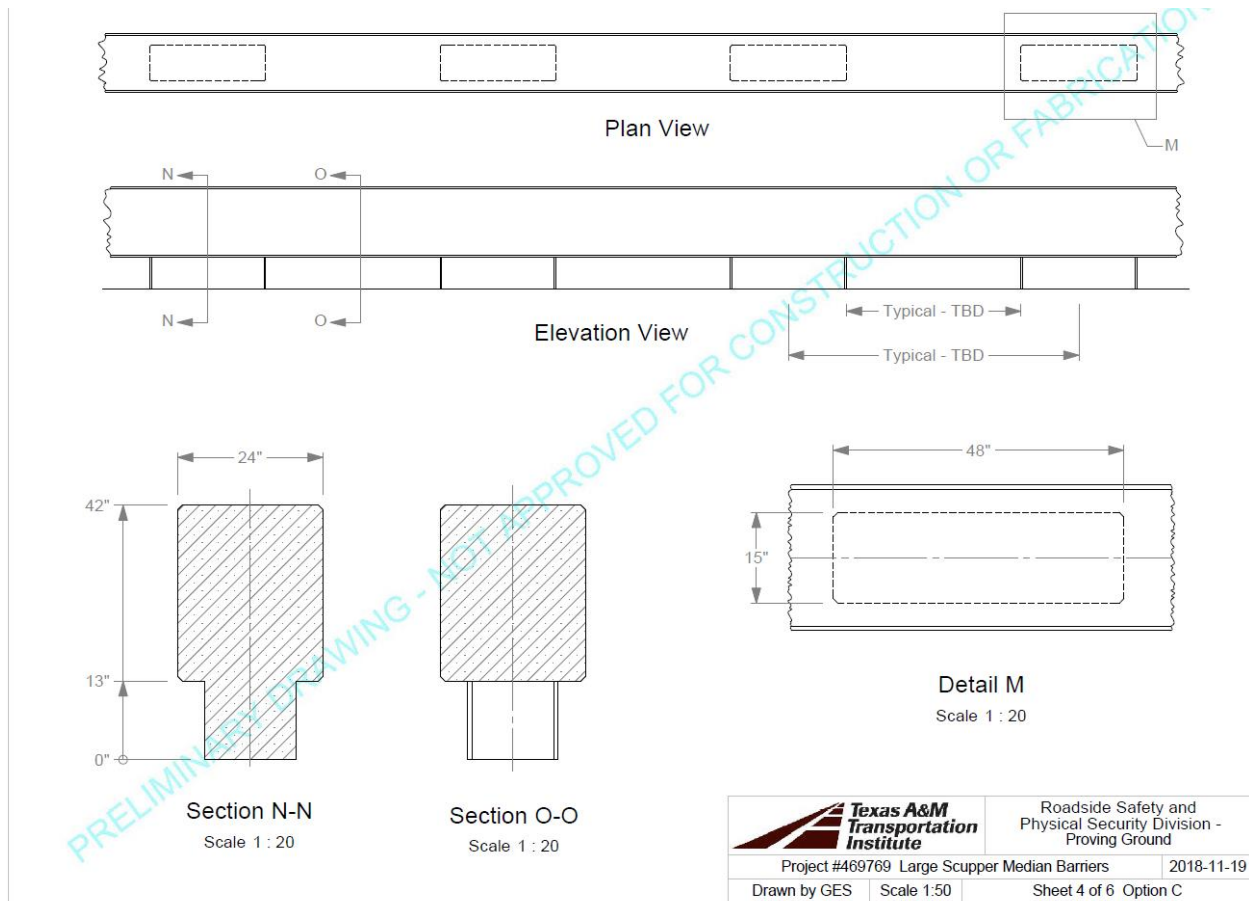


Figure 4.30. Median Version of the T223 TxDOT Post-and-Beam Bridge Rail with Constant-Width Concrete Posts.

Figure 4.31 shows the different views of the developed FEA model for the Option B system. Analysis was performed with all three vehicles (passenger car, pickup truck, and large SUT truck). Shell elements were used for developing the 38-inch-high post-and-beam system. The concrete beam is 25 inches high and 24 inches wide. Concrete posts are 48 inches long and 15 inches wide. Rigid material properties were used to define concrete properties since the purpose of these simulations was mainly to investigate vehicle stability and vehicle interaction with the rigid system during the impact event.

4.4.2.1 T223 TxDOT Post-and-Beam Bridge Rail with Passenger Car

The vehicle impact speed and angle were 62 mi/h and 25 degrees, respectively. Figure 4.32 illustrates different views of the Option B barrier system with the passenger car. Figure 4.33 shows occupant risk and vehicle stability results from the performed CIP parametric analysis with the passenger car. Table 4.13 illustrates sequential images of a representative simulation with the passenger car.

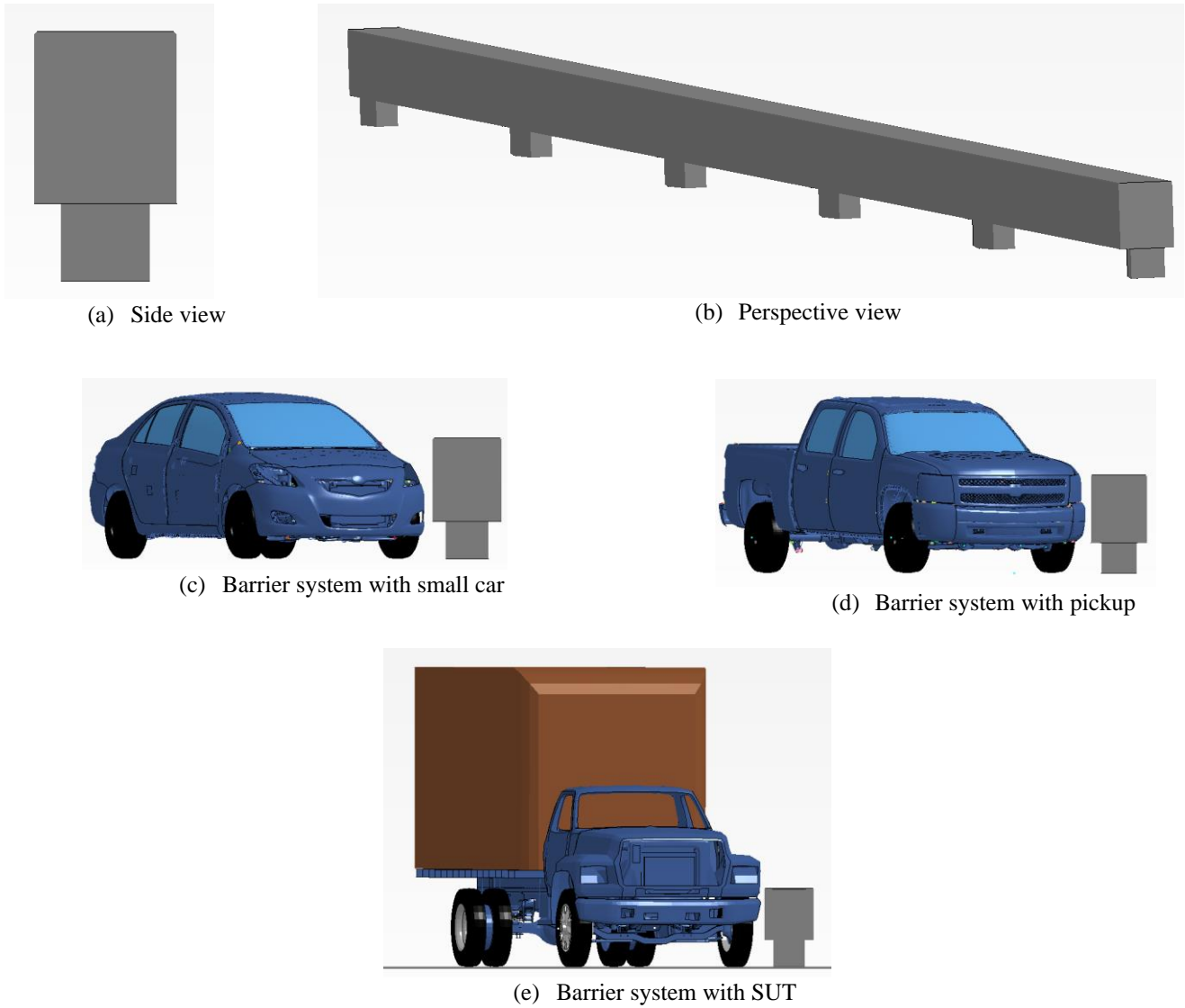


Figure 4.31 Computer Simulation Models for Option B with Different Vehicles.

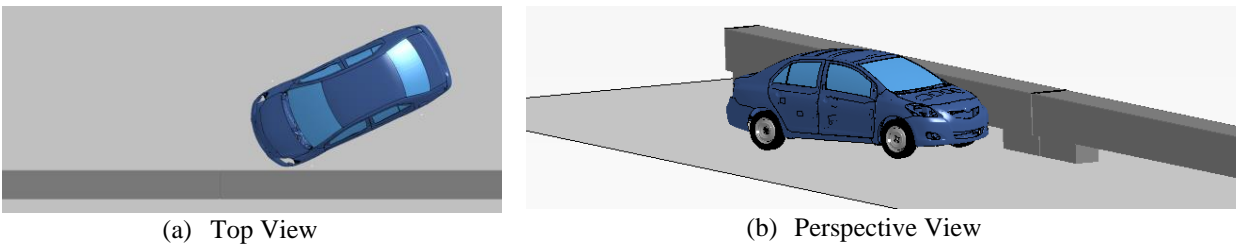
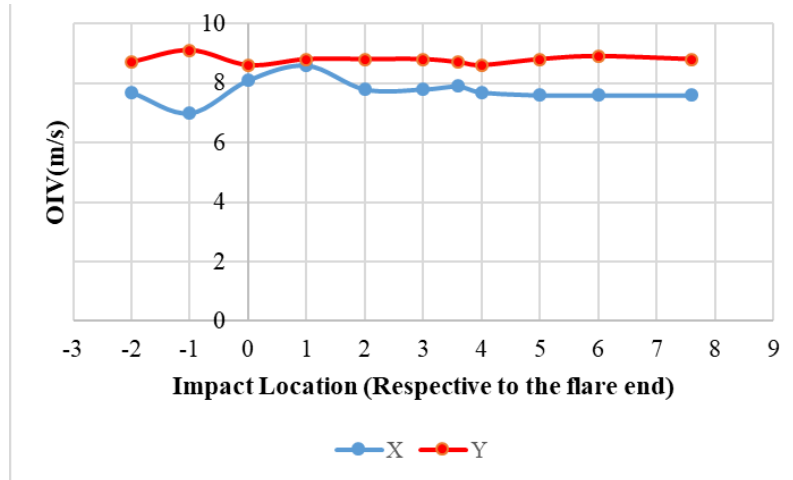
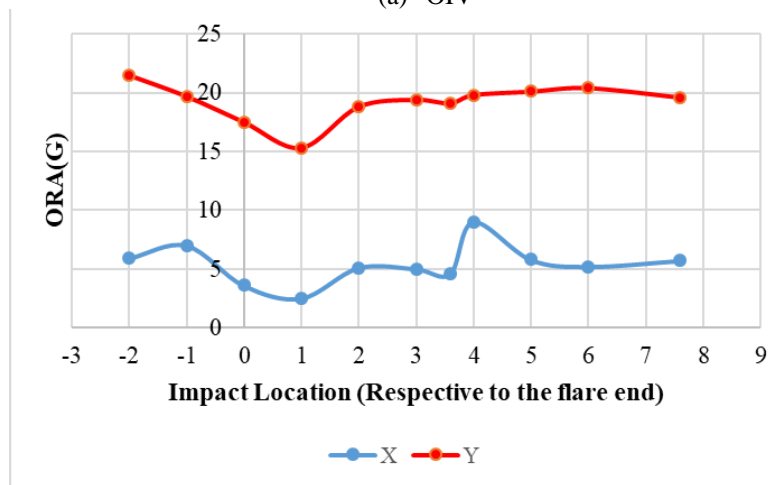


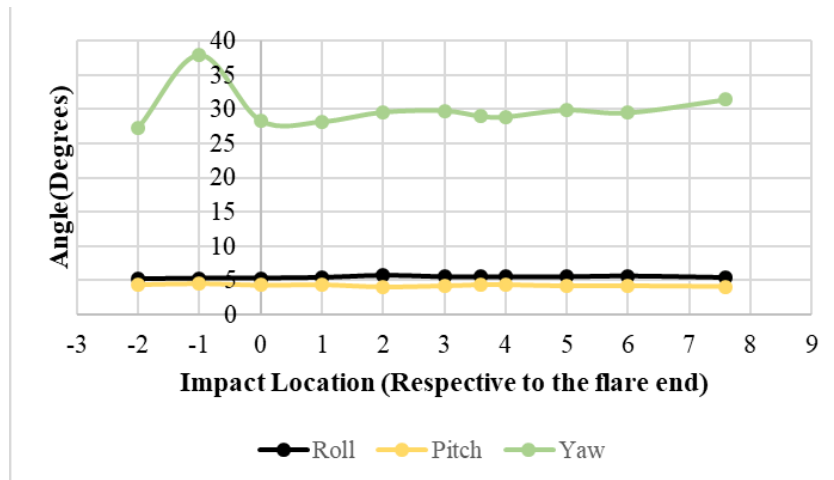
Figure 4.32. Different Views of Computer Simulation Model for Option B with Passenger Car.



(a) OIV



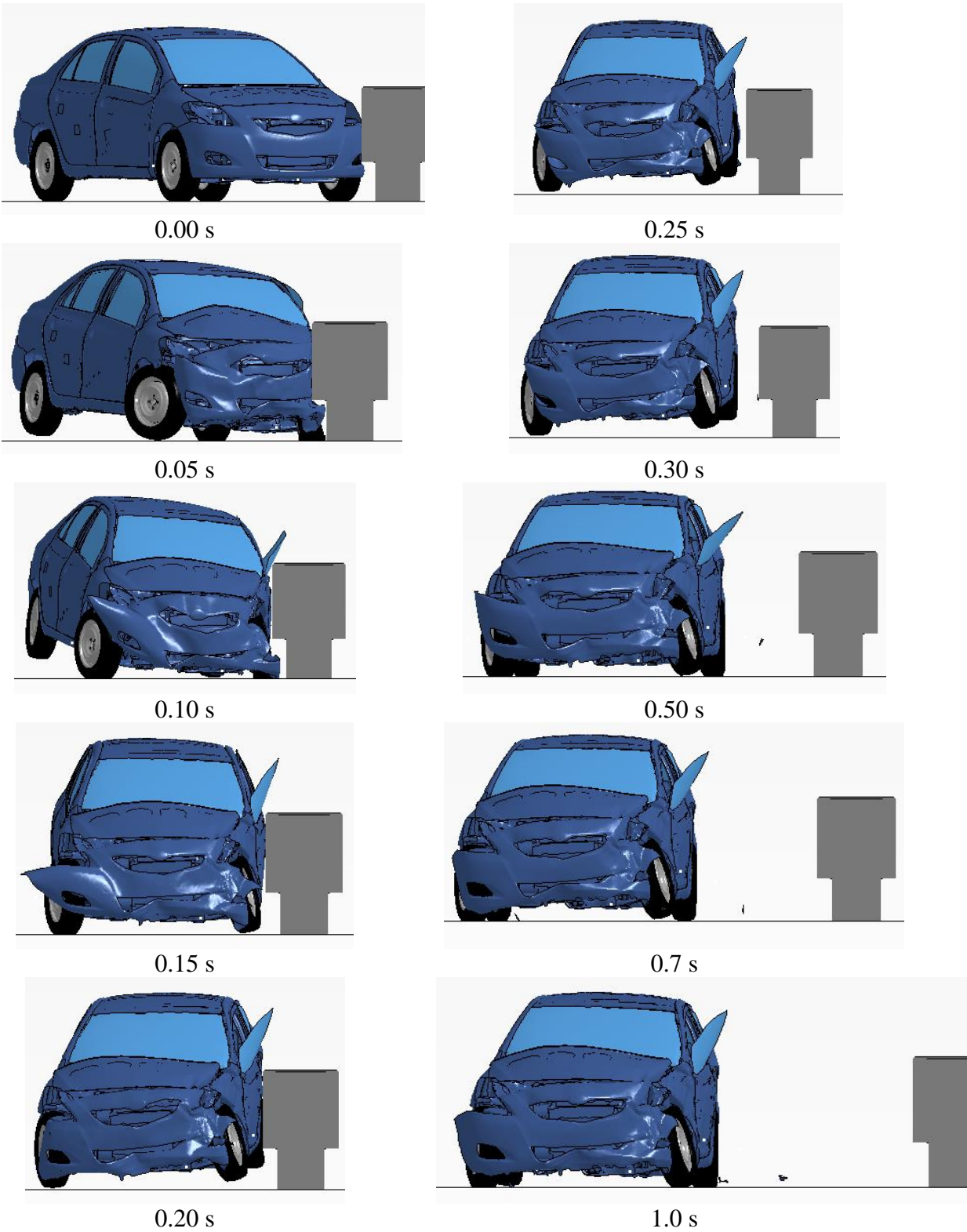
(b) ORA



(c) Vehicular Displacement

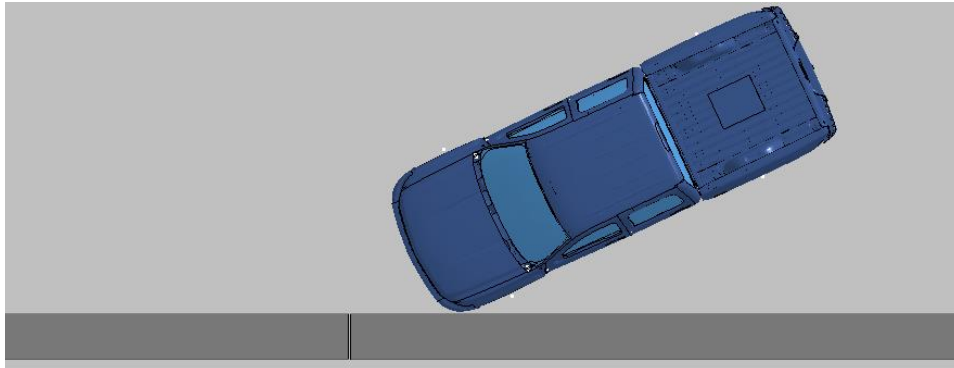
Figure 4.33. Parametric Analysis Results for Option B with Passenger Car.

Table 4.13. Sequential Images of the Simulated Computer Model Impact Events for Option B with Passenger Car.

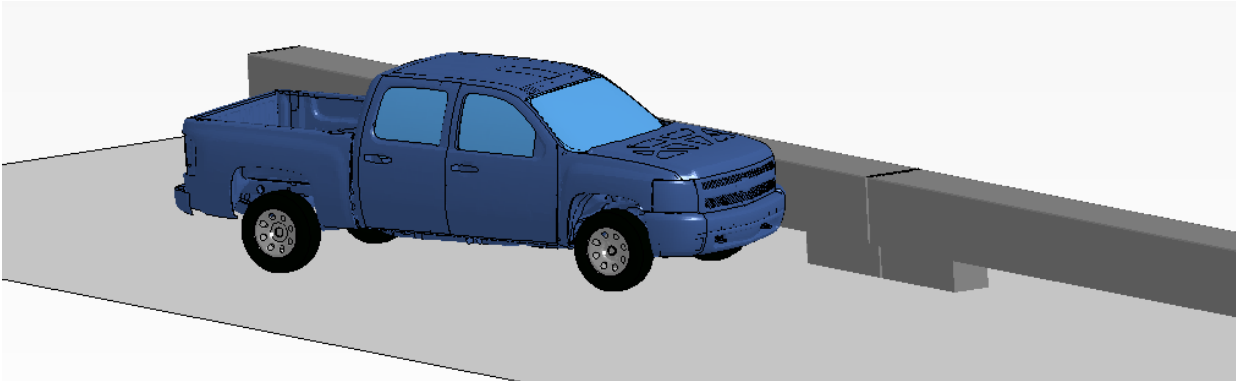


4.4.2.2 T223 TxDOT Post-and-Beam Bridge Rail with Pickup Truck (without Tire Disengagement)

For the pickup truck, two different categories of simulations were performed: one with vehicle tire disengagement and one without tire disengagement. The vehicle impact speed and angle were 62 mi/h and 25 degrees, respectively. Figure 4.34 illustrates different views of the Option B barrier system with the pickup truck.



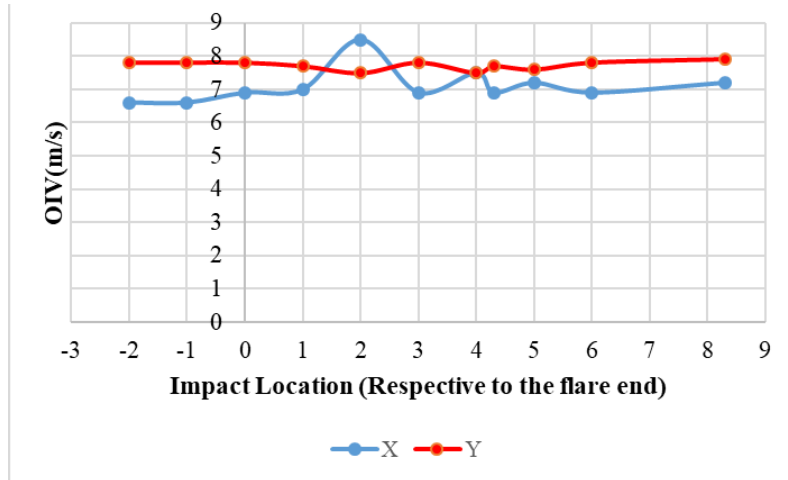
(a) Top View



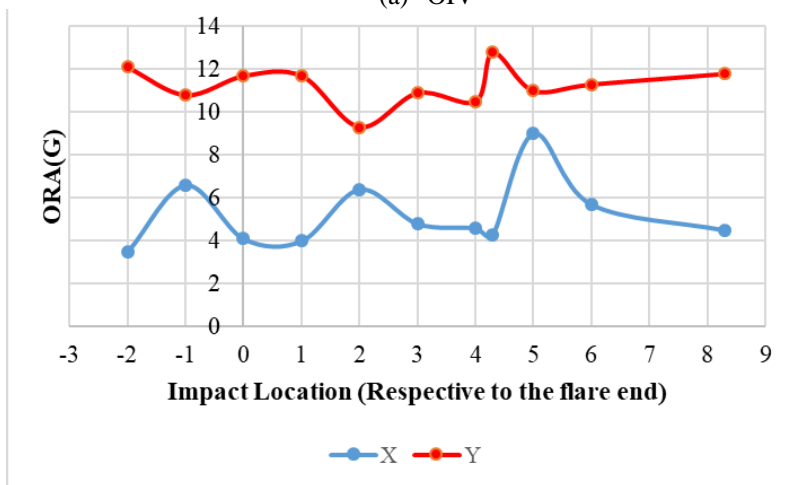
(b) Perspective View

Figure 4.34. Different Views of Computer Simulation Model for Option B with Pickup Truck (without Tire Disengagement).

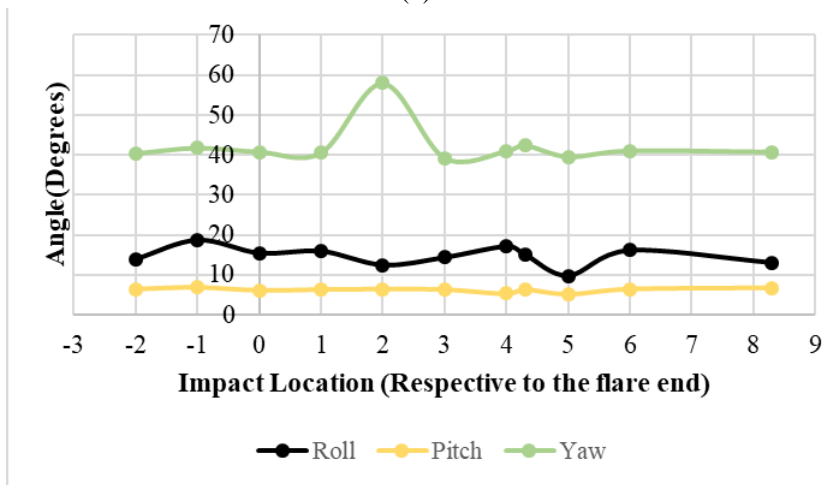
Figure 4.35 shows occupant risk and vehicle stability results from the performed CIP parametric analysis with the pickup truck. Table 4.13 illustrates sequential images of a representative simulation with the pickup truck.



(a) OIV



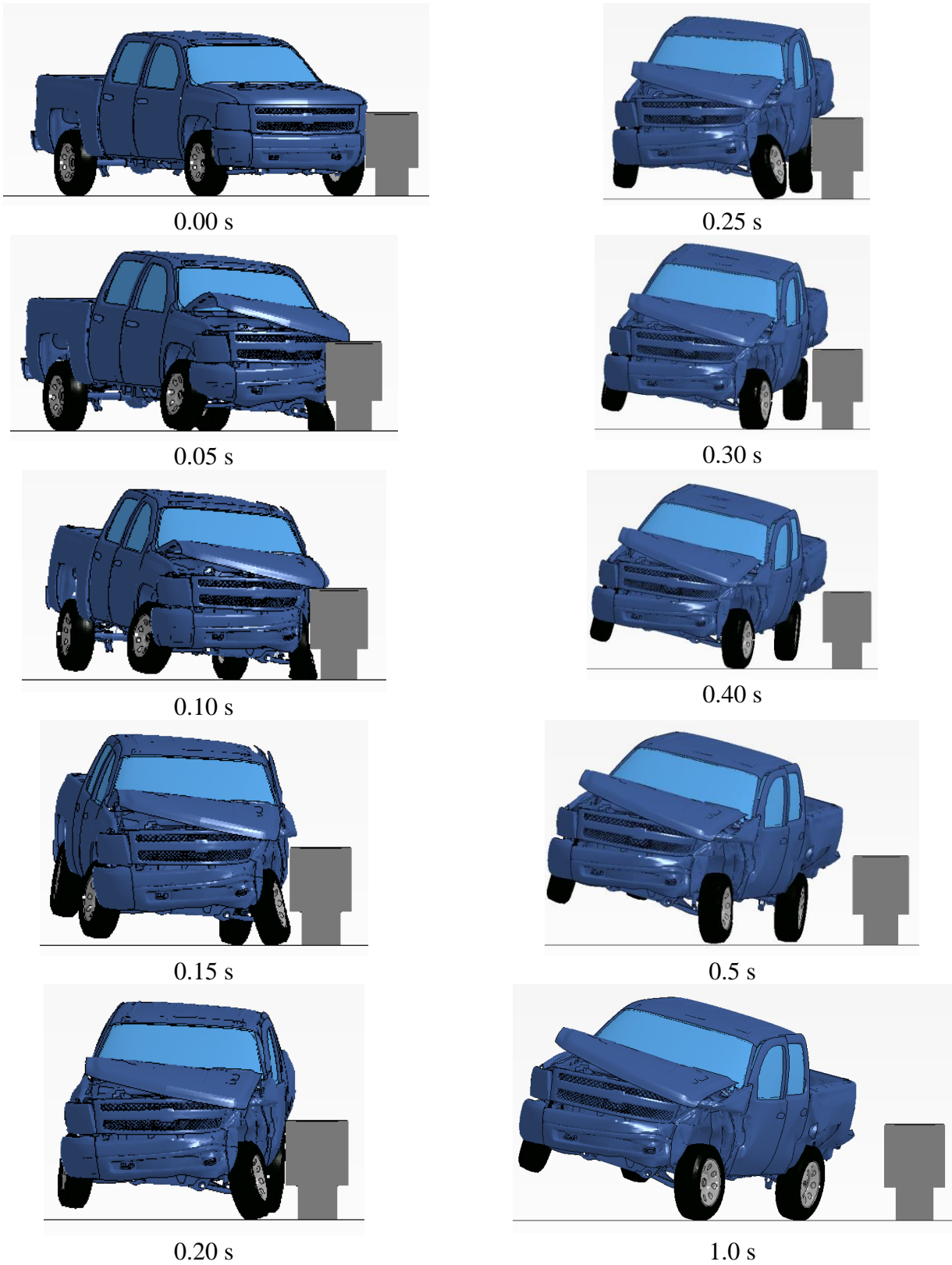
(b) ORA



(c) Vehicular Displacement

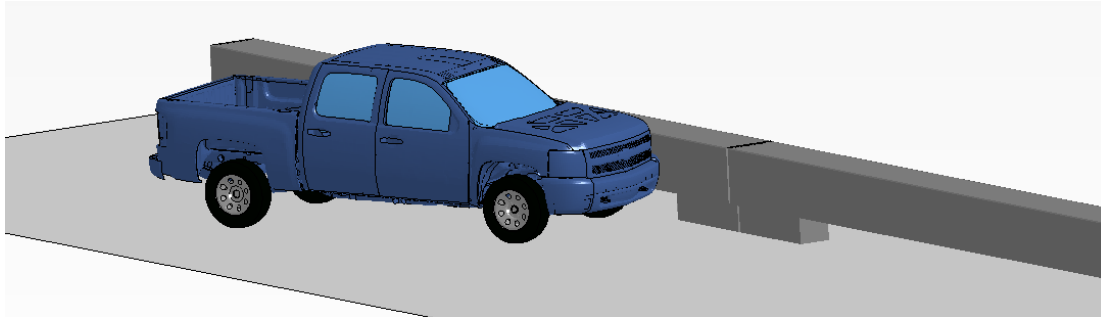
Figure 4.35. Parametric Analysis Results for Option B with Pickup Truck (without Tire Disengagement).

Table 4.14. Sequential Images of the Simulated Computer Model Impact Events for Option B with Pickup Truck (without Tire Disengagement).

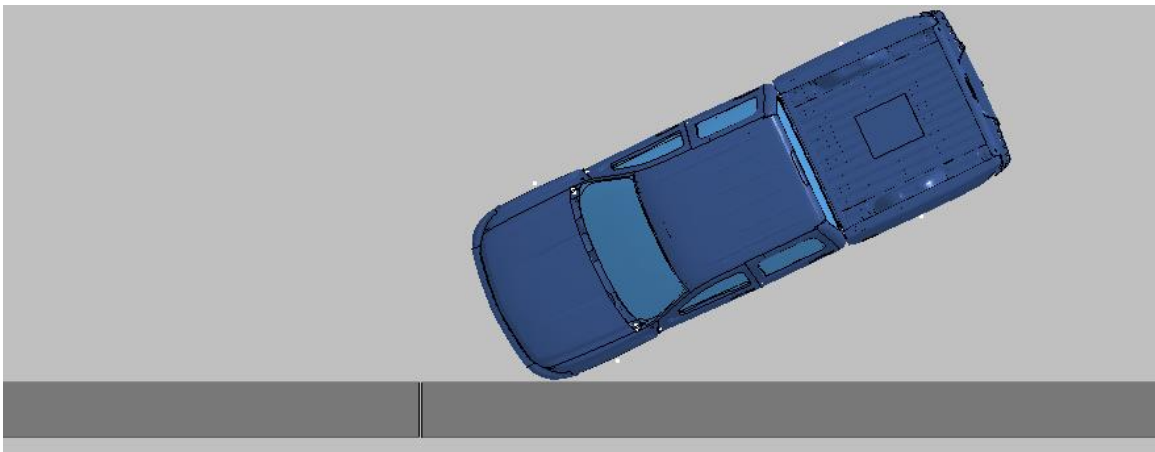


4.4.2.3 T223 TxDOT Post-and-Beam Bridge Rail with Pickup Truck (with Tire Disengagement)

The vehicle impact speed and angle were 62 mi/h and 25 degrees, respectively. Figure 4.36 illustrates different views of the Option B barrier system with the pickup truck.



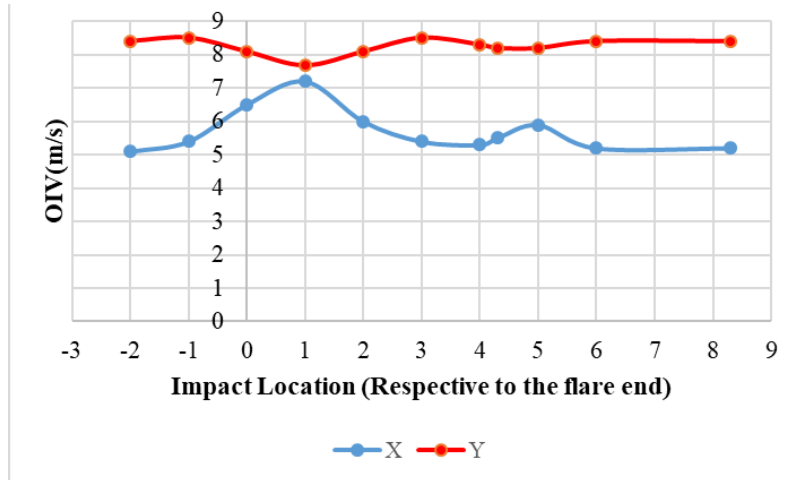
(a) Top View



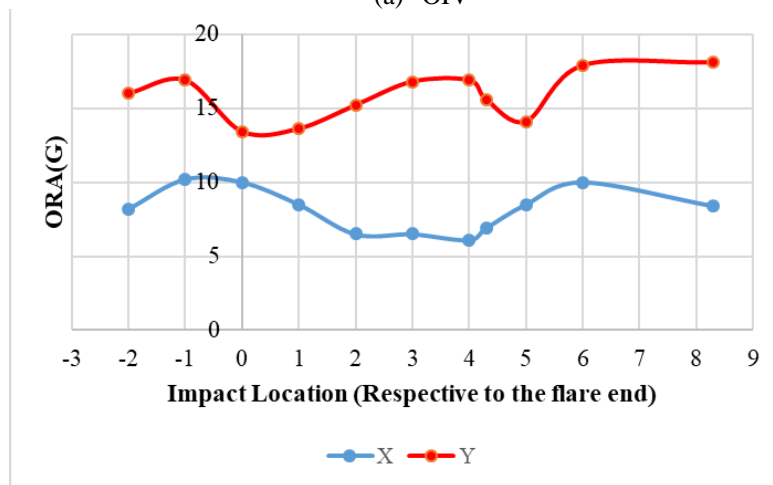
(b) Perspective View

Figure 4.36. Different Views of Computer Simulation Model for Option B with Pickup Truck (with Tire Disengagement).

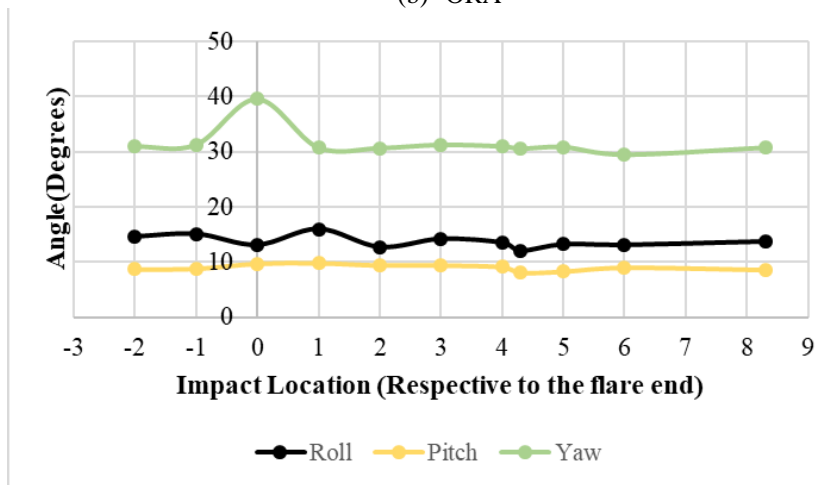
Figure 4.37 shows occupant risk and vehicle stability results from the performed CIP parametric analysis with the pickup truck. Table 4.15 illustrates sequential images of a representative simulation with the pickup truck.



(a) OIV



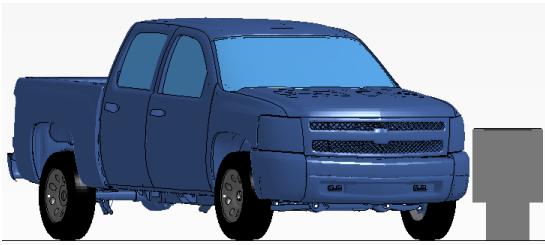
(b) ORA



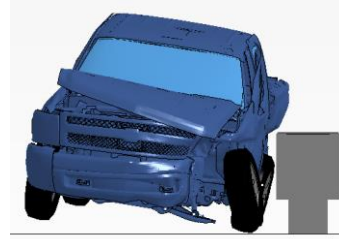
(c) Vehicular Displacement

Figure 4.37. Parametric Analysis Results for Option B with Pickup Truck (with Tire Disengagement).

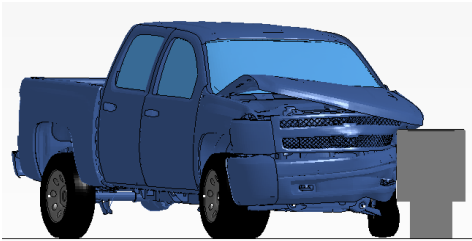
Table 4.15. Sequential Images of the Simulated Computer Model Impact Events for Option B with Pickup Truck (with Tire Disengagement).



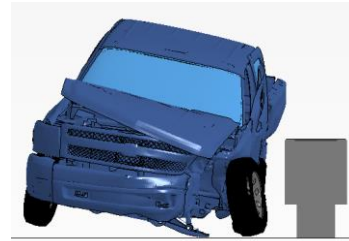
0.00 s



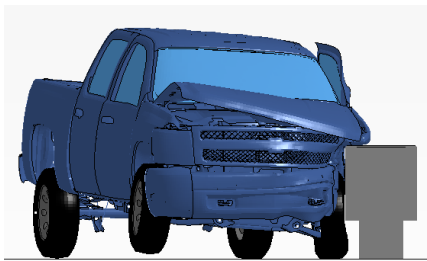
0.25 s



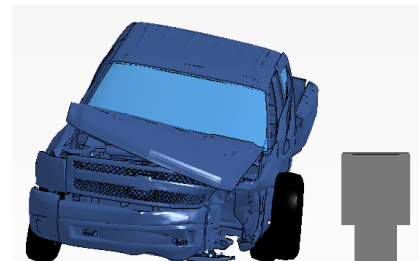
0.05 s



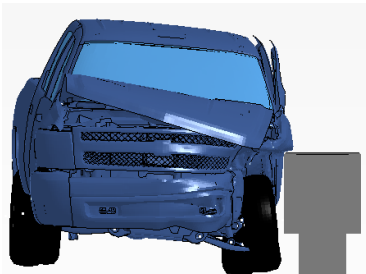
0.30 s



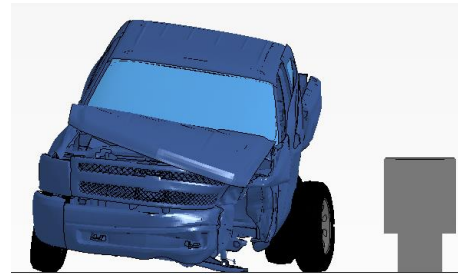
0.10 s



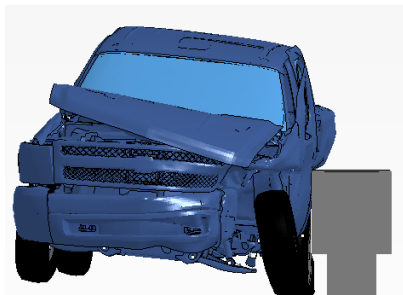
0.40 s



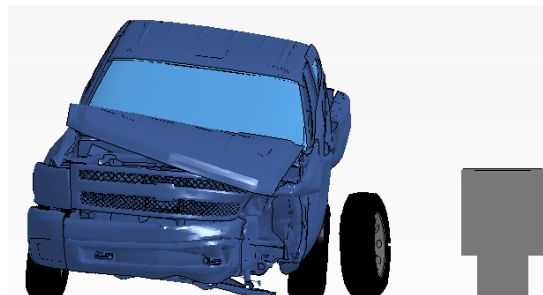
0.15 s



0.5 s



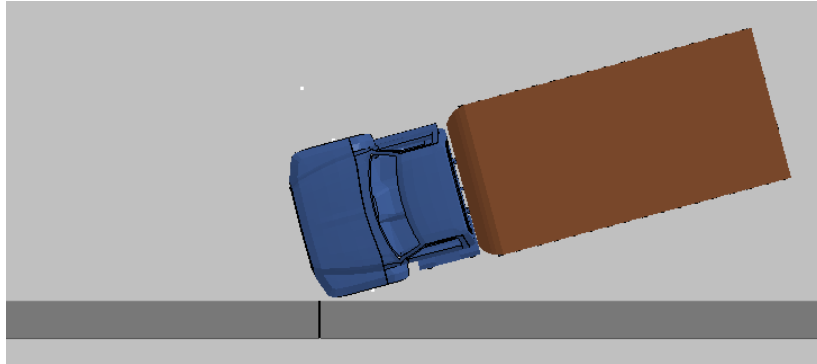
0.20 s



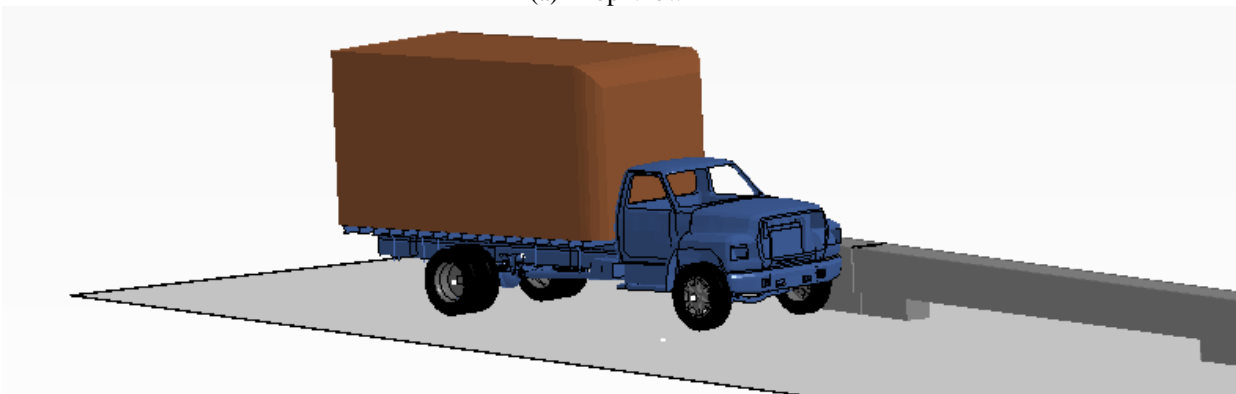
0.6 s

4.4.2.4 T223 TxDOT Post-and-Beam Bridge Rail with Single-Unit Truck

The vehicle impact speed and angle were 56 mi/h and 15 degrees, respectively. Figure 4.38 illustrates different views of the Option B barrier system with the SUT.



(a) Top View

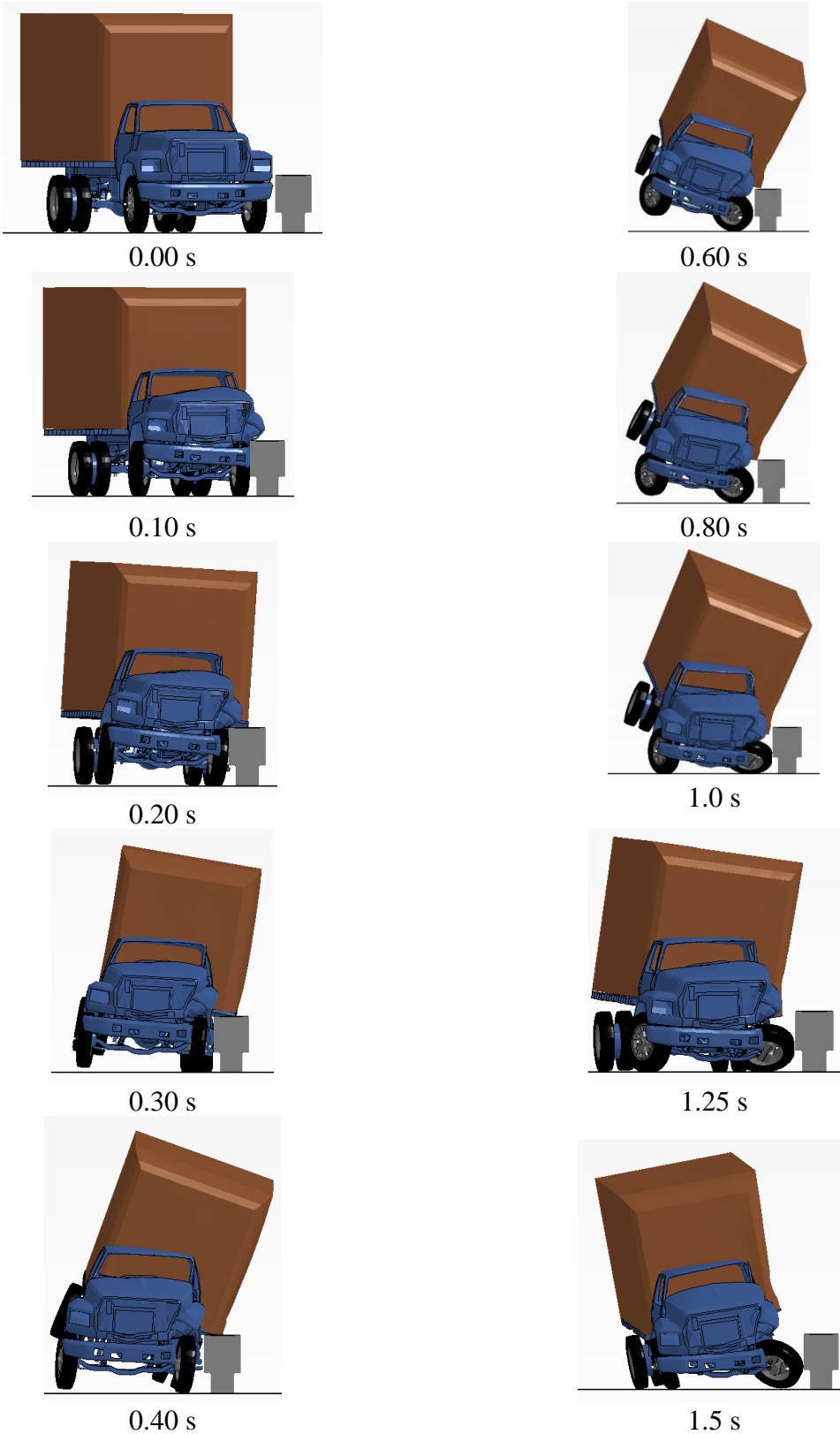


(b) Perspective View

Figure 4.38. Computer Simulation Model for Option B with SUT.

Table 4.16 illustrates sequential images of the simulation results from the performed FEA computer simulations for Option B with the SUT.

Table 4.16. Sequential Images of the Simulated Computer Model Impact Events for Option B with SUT.



4.4.3 Option C: 38-Inch Open Steel Barrier

Figure 4.39 shows the developed computer model for the proposed 38-inch-tall open steel barrier option. Although some dimensions and connections for the proposed option are yet to be detailed, the following simulations are included to illustrate vehicle stability and interaction with the test article during impact. The barrier base plates measure $14\frac{1}{8}$ inches wide and $\frac{7}{8}$ -inch thick. Vertical posts are $11\frac{1}{8}$ inches wide and $\frac{7}{8}$ -inch thick. Three separate longitudinal HSSs are connected to vertical posts with a plate and bolt system. The 5-inch-square HSSs are $\frac{1}{4}$ -inch thick.

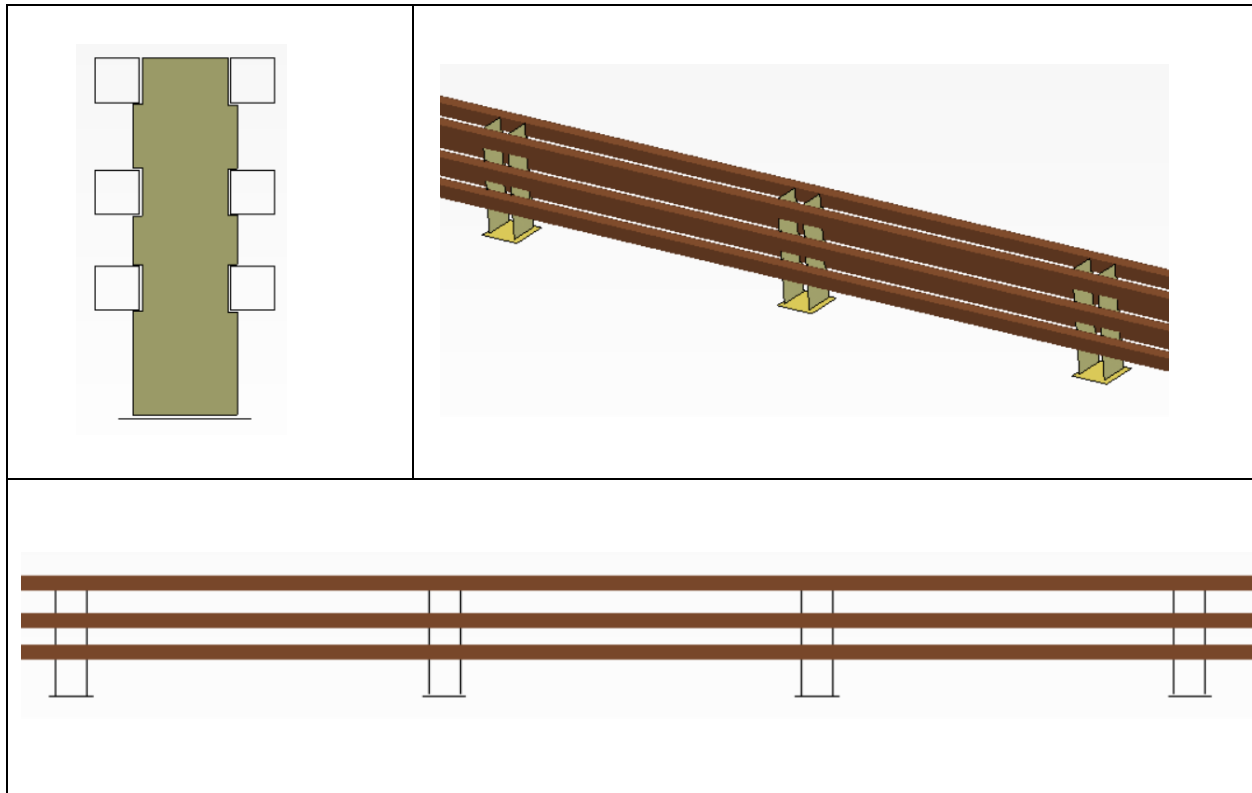


Figure 4.39 Open Steel Barrier Model Developed as Option C.

The analysis was performed with all three vehicles (passenger car, pickup truck, and large SUT truck) (Figure 4.40).

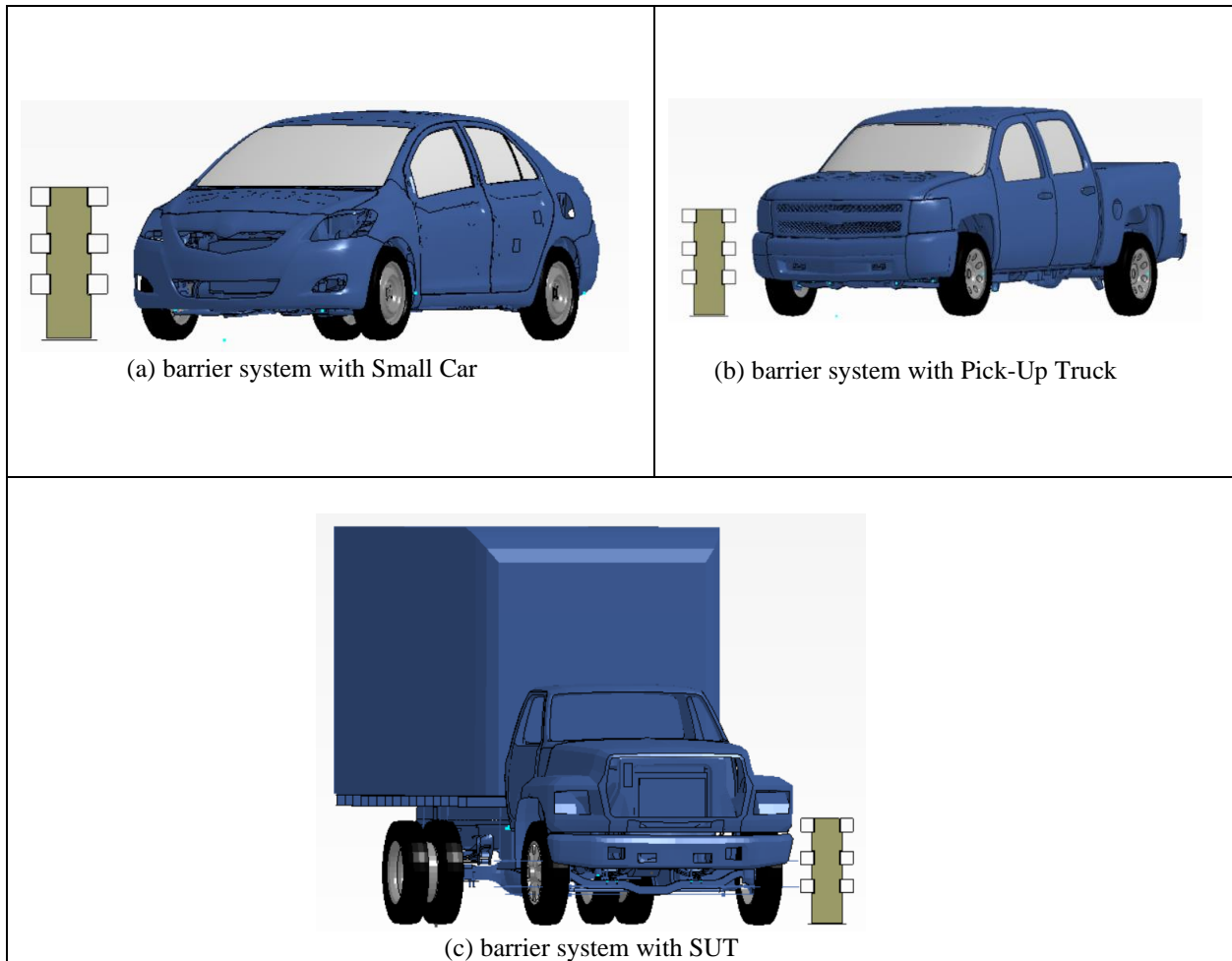


Figure 4.40. Computer Simulation Models for Option C with Different Vehicles.

4.4.3.1 38-Inch Steel Barrier with Passenger Car

The vehicle impact speed and angle were 62 mi/h and 25 degrees, respectively. Figure 4.41 illustrates different views of the Option C barrier system with a passenger car.

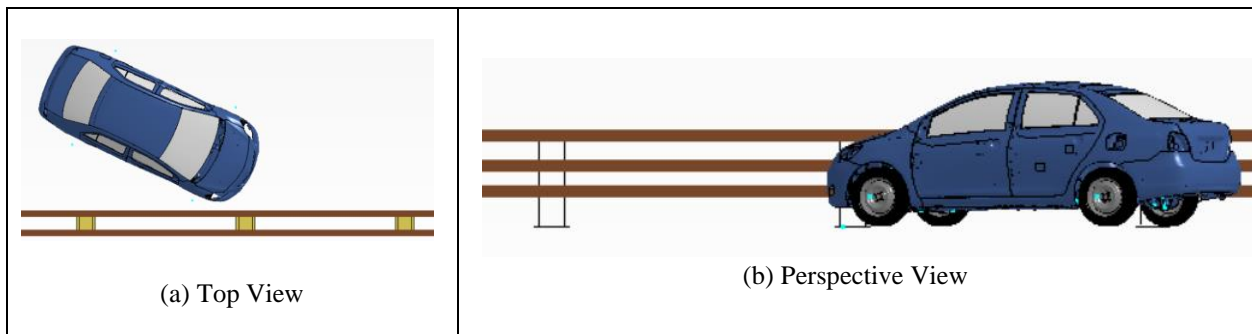


Figure 4.41. Different Views of Computer Simulation Model for Option C with Passenger Car.

Table 4.17 illustrates sequential images of the preliminary simulation results from the performed FEA computer simulations for the passenger car.

Table 4.17. Sequential Images of the Simulated Computer Model Impact Events for Option C with Passenger Car.

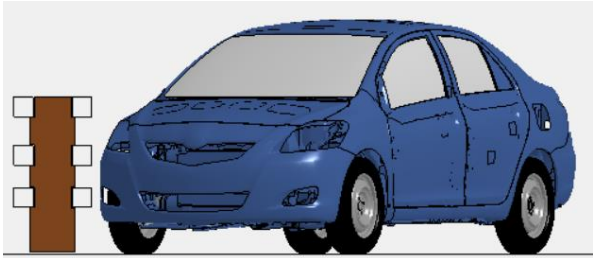
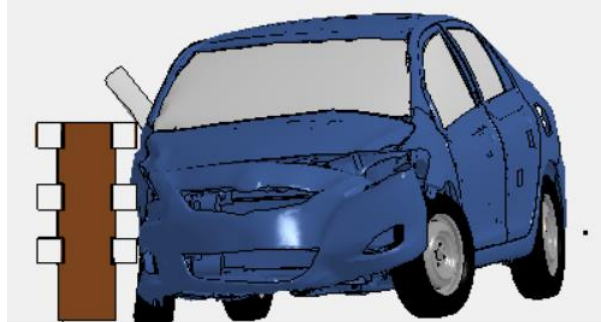
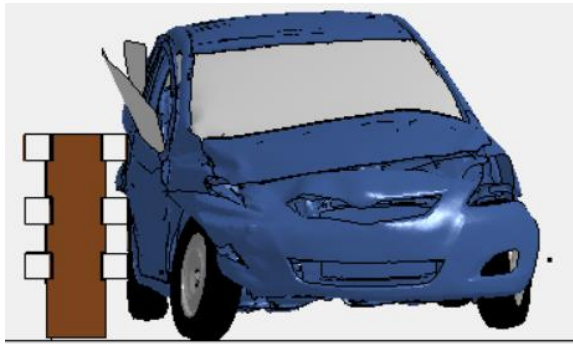
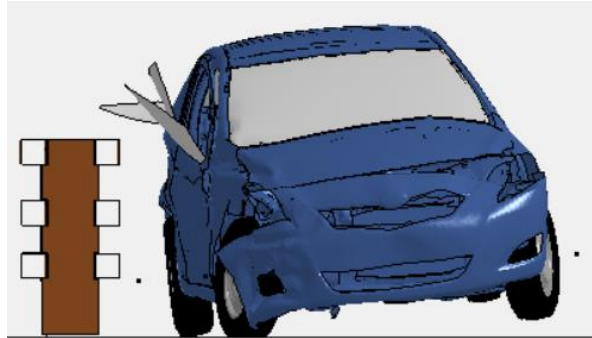
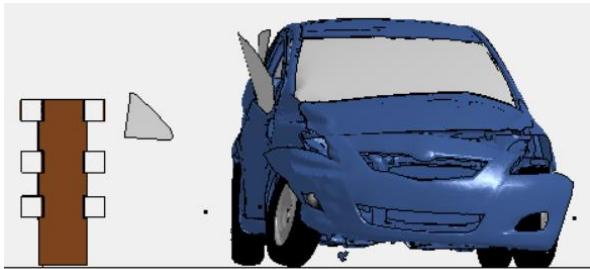
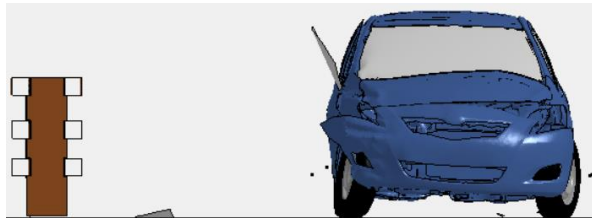
	
0.00 s	0.1 s
	
0.2 s	0.3 s
	
0.5 s	1.0 s

Table 4.18 summarizes occupant risk, vehicle stability information, and system deflection values from the performed FEA simulation for the passenger car. Figure 4.42 illustrates the maximum deformation in the steel barrier from impacting the passenger car.

Table 4.18. Occupant Risk and Vehicle Stability Information for Passenger Car.

	FEA Simulation
Longitudinal OIV	25.25 ft/s
Lateral OIV	-31.48 ft/s
Longitudinal Ridedown	-5.9 g
Lateral Ridedown	21.2 g
THIV	43.7 km/h
PHD	21.3
ASI	2.73
Max 0.050-s Average	
Longitudinal	-15.0 g
Lateral	20.3 g
Vertical	-3.5 g
Maximum Roll	7.3°
Maximum Pitch	4.3°
Maximum Yaw	30.5°
Maximum Barrier Deformation	12.5 mm

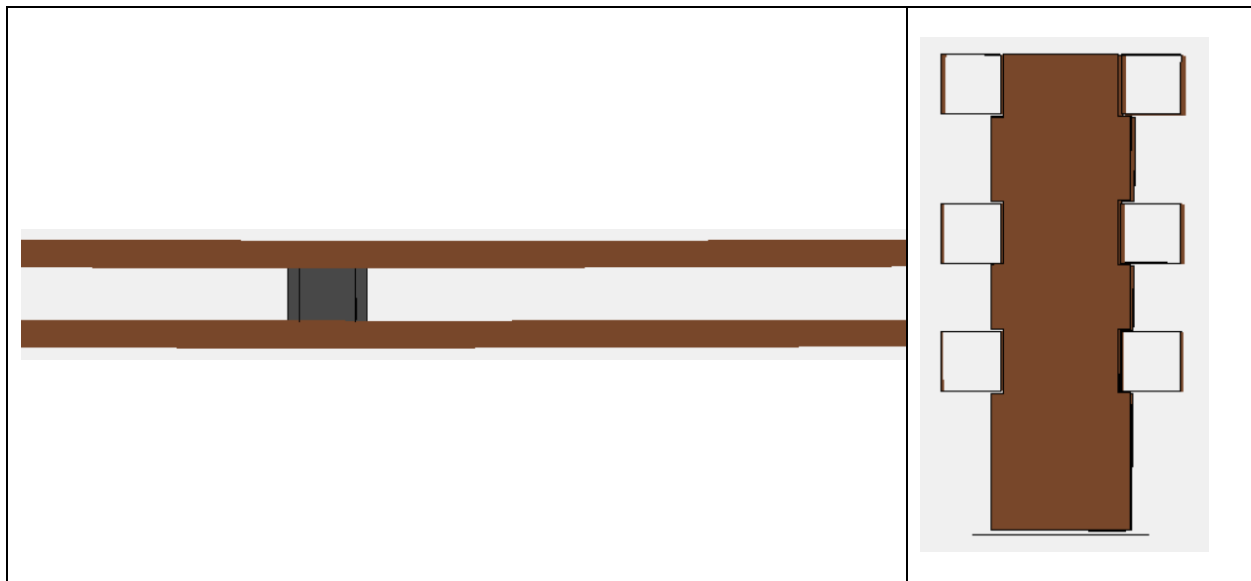


Figure 4.42. Maximum Deformation in Steel Barrier from Passenger Car.

Energy values were evaluated in this detailed FE simulation. The energy distribution history for the passenger car is shown in Figure 4.43.

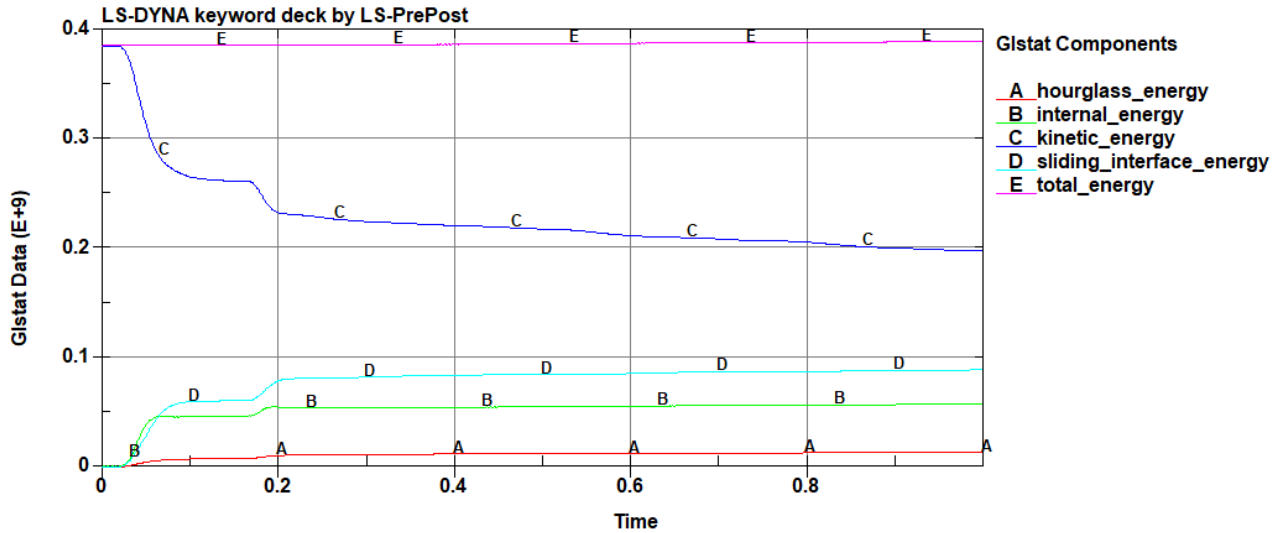


Figure 4.43 Energy Distribution History for Passenger Car.

4.4.3.2 38-Inch Steel Barrier with Pickup Truck

The vehicle impact speed and angle were 62 mi/h and 25 degrees, respectively. F illustrates different views of the Option C barrier system with a pickup truck.

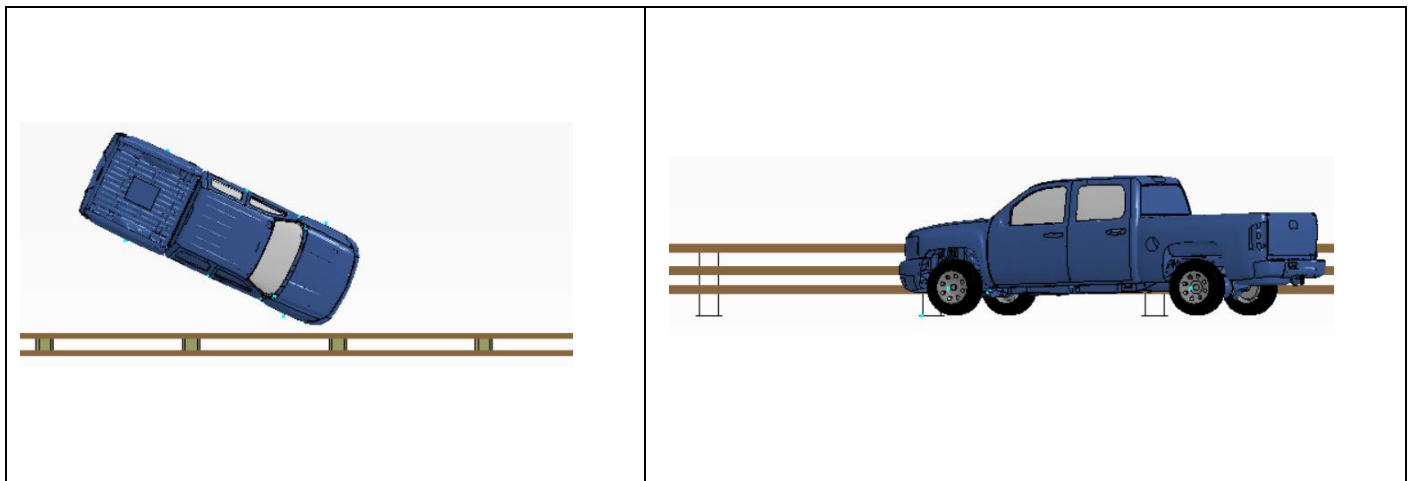


Figure 4.44. Different Views of Computer Simulation Model for Option C with Pickup Truck.

Table 4.19 illustrates sequential images of the preliminary simulation results from the performed FEA computer simulations for Option C with the pickup truck.

Table 4.19. Sequential Images of the Simulated Computer Model Impact Events for Option C with Pickup Truck.

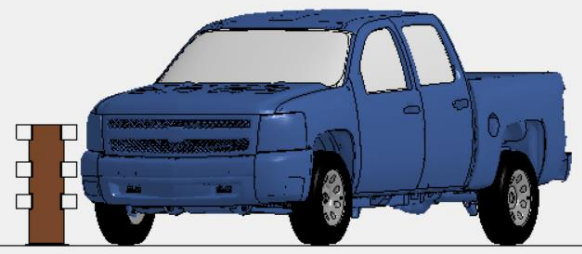
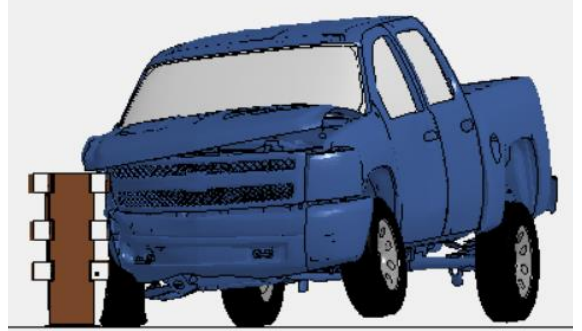
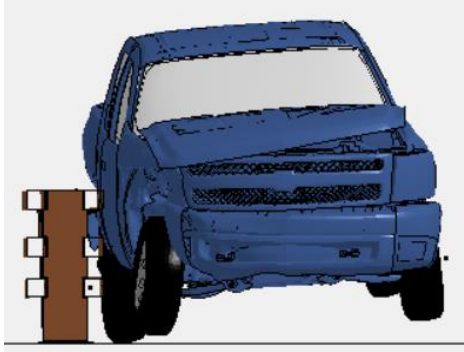
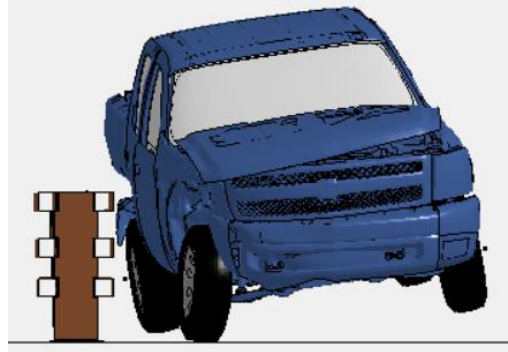
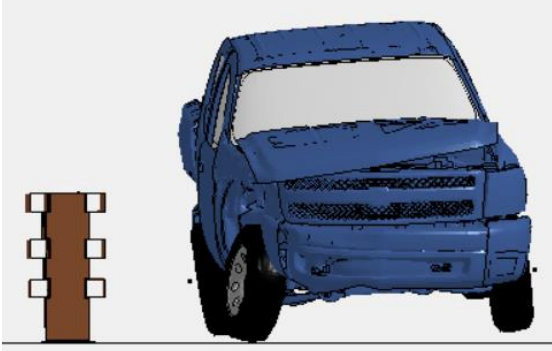
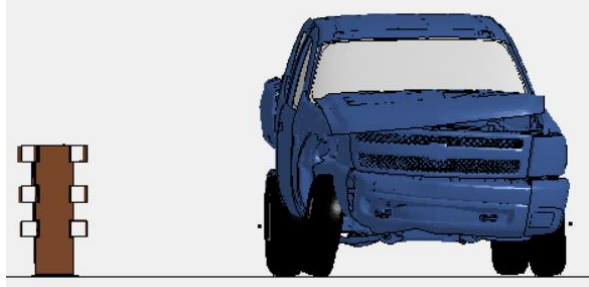
	
0.00 s	0.1 s
	
0.2 s	0.3 s
	
0.5 s	1.0 s

Table 4.20 summarizes occupant risk, vehicle stability information, and system deflection values from the performed FEA simulation for the pickup truck. Figure 4.45 illustrates the maximum deformation in the steel barrier from impacting the pickup truck. The energy distribution history for the pickup truck is shown in Figure 4.46.

Table 4.20. Occupant Risk and Vehicle Stability Information for Pickup Truck.

	FEA Simulation
Longitudinal OIV	21.64 ft/s
Lateral OIV	-26.56 ft/s
Longitudinal Ridedown	-5.2 g
Lateral Ridedown	20.3 g
THIV	37.1 km/h
PHD	20.3
ASI	1.91
Max 0.050-s Average	
Longitudinal	-10.7 g
Lateral	13.9 g
Vertical	-2.7 g
Maximum Roll	10.2°
Maximum Pitch	3.4°
Maximum Yaw	30.8°
Maximum Barrier Deformation	45 mm

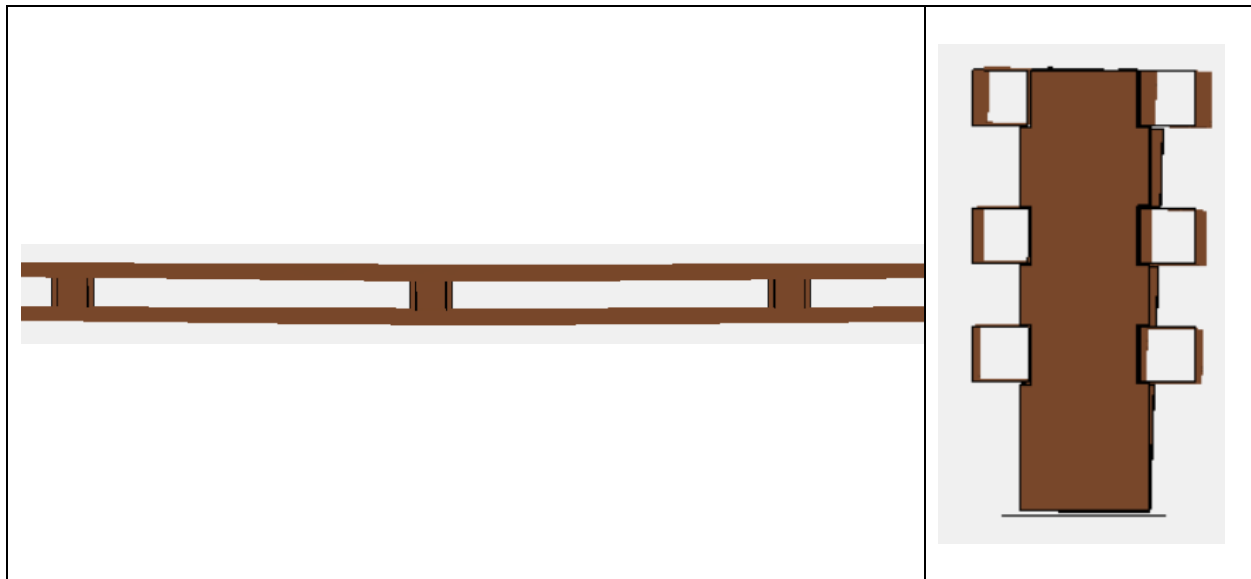


Figure 4.45. Maximum Deformation in Steel Barrier from Pickup Truck.

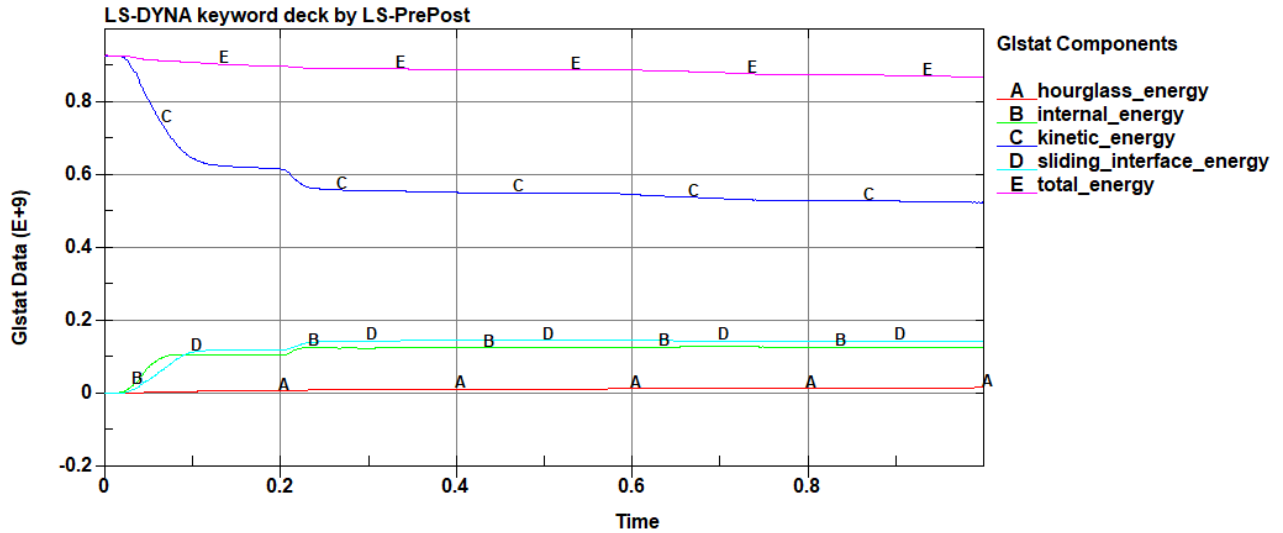


Figure 4.46. Energy Distribution History for Pickup Truck.

4.4.3.3 38-Inch Steel Barrier with SUT

The vehicle impact speed and angle were 56 mi/h and 15 degrees, respectively. Figure 4.47 illustrates different views of the Option C barrier system with the SUT.

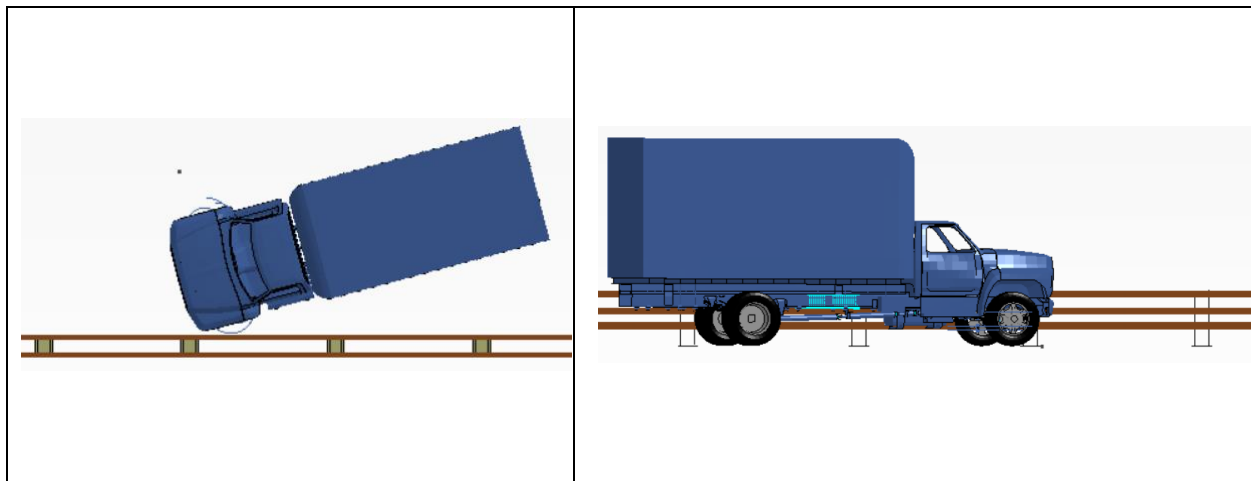


Figure 4.47. Different Views of Computer Simulation Model for Option C with SUT.

Table 4.21 illustrates sequential images of the preliminary simulation results from the performed FEA computer simulations for Option C with the SUT.

Table 4.21. Sequential Images of the Simulated Computer Model Impact Events for Option C with SUT.

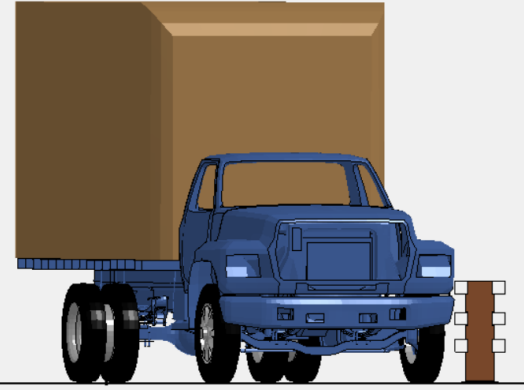



	
<p>0.00 s</p>	<p>0.1 s</p>
	
<p>0.2 s</p>	<p>0.5 s</p>
	
<p>1.0 s</p>	<p>2.0 s</p>

Table 4.22 summarizes occupant risk, vehicle stability information, and system deflection values from the performed FEA simulation for the SUT. Figure 4.48 illustrates the maximum deformation in the steel barrier from impacting the SUT. The energy distribution history for the SUT is shown in Figure 4.49.

Table 4.22. Occupant Risk and Vehicle Stability Information for SUT.

	FEA Simulation
Longitudinal OIV	5.24 ft/s
Lateral OIV	20.33 ft/s
Longitudinal Ridedown	13.3 g
Lateral Ridedown	-10.2 g
THIV	23.0 km/h
PHD	13.3
ASI	1.05
Max 0.050-s Average	
Longitudinal	-3.7 g
Lateral	-9.0 g
Vertical	5.7 g
Maximum Roll	-13.9°
Maximum Pitch	10.1°
Maximum Yaw	-14.9°
Maximum Barrier Deformation	65 mm

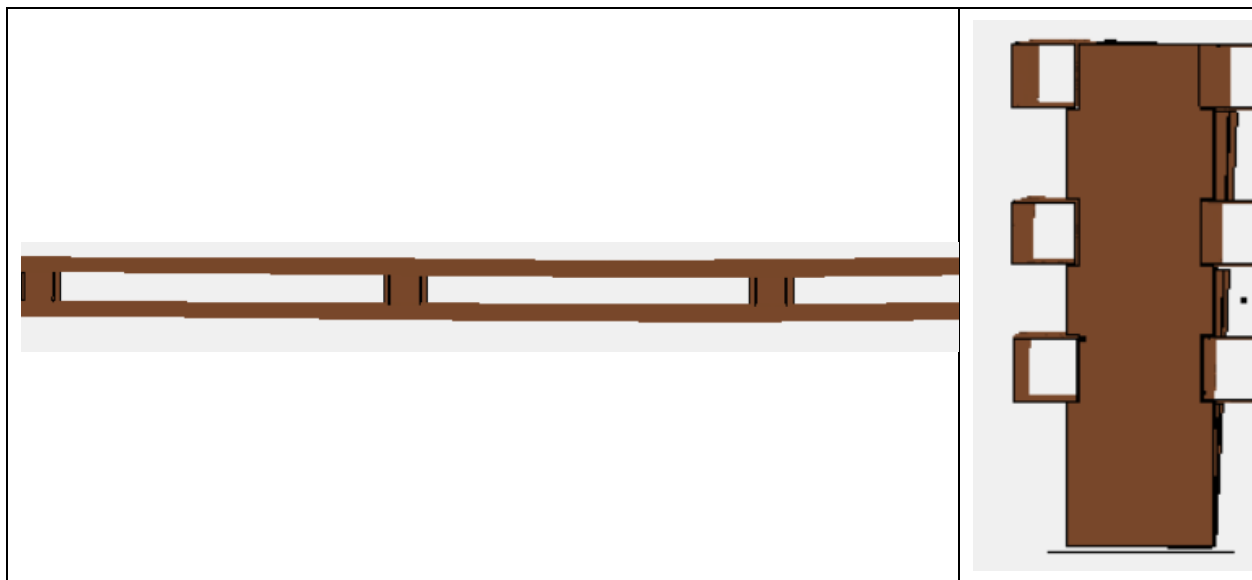


Figure 4.48. Maximum Deformation in Steel Barrier from SUT.

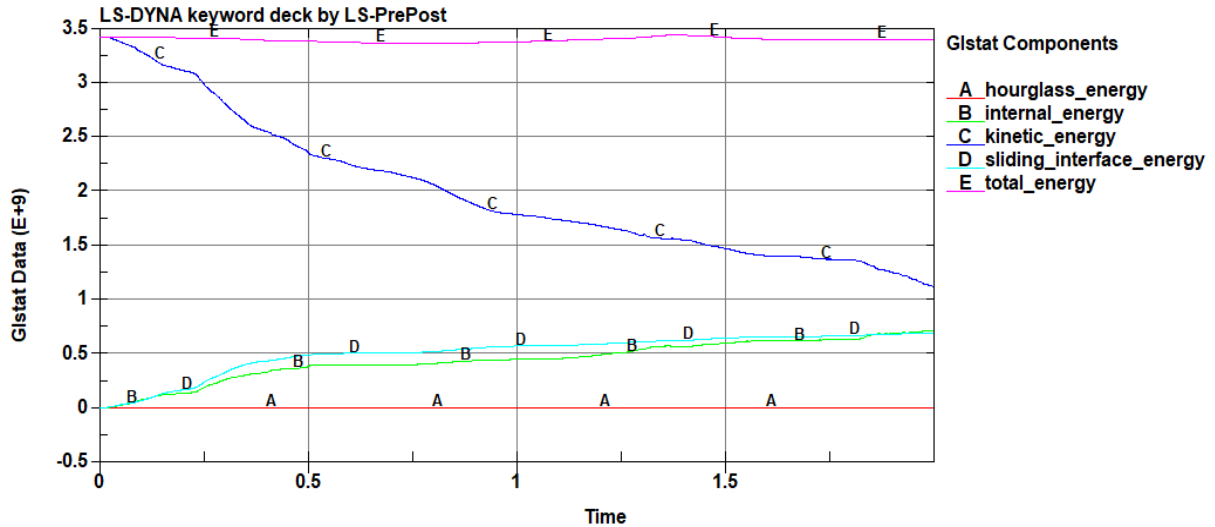


Figure 4.49. Energy Distribution History for SUT.

4.5 CONCLUSIONS

Multiple options were considered for potential development of a rigid median barrier system to be deployed in flood-prone areas to accommodate the passage of floodwater during severe weather events.

Three median barrier options were approved for further investigation through computer simulations:

- Option A: 42-inch-tall single-slope median barrier.
- Option B: 38-inch median version of the T223 TxDOT post-and-beam bridge rail.
- Option C: 38-inch open steel barrier.

It is important to note that the objective of this FE computer simulation study was to specifically investigate the vehicle stability and interaction with the proposed barrier option during a potential impact event, as well as anticipated occupant risk values. Therefore, the strength and structural adequacy of the barrier was not specifically investigated through this FEA. Barrier details, such as steel reinforcement, were detailed in parallel through engineering analysis and through direct communication with the project panel to account for their needs and preferences.

The FEAs conducted on the first two concrete options suggest that both systems' geometrical details have the potential to be deemed crashworthy under *MASH* TL-4 conditions. Parametric analyses conducted with the passenger car, pickup truck, and SUT vehicles seem to indicate that (a) the proposed barrier geometry would be capable of containing and redirecting the impacting vehicle, (b) the vehicle interaction with the test article should not result in any form of severe snagging/pocketing, and (c) the vehicle should maintain its stability throughout the impact event.

CHAPTER 5. LARGE-SCALE HYDRAULIC TESTING*

5.1 INTRODUCTION

The primary objectives for the large-scale testing were to determine the hydraulic performance of each of the proposed median barrier designs by building a rating curve that plots the upstream water depth with respect to increasing flow rates. Rating curves were compared against one another to assess the relative effectiveness of each barrier for mitigating flood effects in flood-prone areas. This investigation leveraged previous research into the hydraulic performance of bridge rails to build a mathematical model for each of the rating curves (18).

5.2 EXPERIMENTAL SETUP

The purpose of this research was to assess the hydraulic efficiency of median barriers with different geometries and compare the results against one another to explore key parameters in hydraulic performance. Model scale barriers were built for each design and installed in a concrete channel for hydraulic testing at the Center for Water and the Environment (CWE) on the J.J. Pickle Research Campus, University of Texas at Austin. Figure 5.1 displays an example of a barrier mid-test.



Figure 5.1. Hydraulic Testing.

* The opinions/interpretations identified/expressed in this chapter are outside the scope of TTI Proving Ground's A2LA Accreditation.

5.2.1 Physical Construction

5.2.1.1 Median Barriers

A total of three barriers were constructed to the dimensions agreed upon by the associated parties. One additional barrier was constructed as a solid weir to serve as a comparison to the barriers with openings. The designs were adapted from existing TxDOT standard barriers with certain adjusted parameters, such as fractional open space, F_o , and edge tapering. In this research, the fractional open space was the primary parameter investigated. Other parameters such as streamlined openings were not explored experimentally since hydraulic response is expected to be limited and constructability constraints outweigh any marginal benefits that streamlined barriers could provide. Initial dimensions were decided among all parties, while specific dimensions such as scupper and support spacing were decided by TTI at the conclusion of crash test numerical simulations. The final vertical dimensions for all barriers were scaled down at a 2:1 ratio. This ratio allowed the barrier to fit within the vertical constraints of the channel while leaving enough space for flow over the barrier crest. The final horizontal dimensions were set at a length of 5 ft to match the width of the test channel. In each case, the scupper length to barrier length ratio was preserved in both the horizontal and vertical directions to conserve F_o . The first three barrier models were constructed entirely from wood, and the final barrier was constructed from steel. Since this experiment involved measuring the hydraulic performance with respect to the barrier geometry, it was not necessary to account for the weight of the barriers, and as such, concrete was not a necessary construction material. All models were anchored to a support base in the channel to ensure stability against hydrodynamic pressure from the flowing water. The edges of the wood models were sealed with silicone caulk, and all exposed faces were coated with multiple layers of a waterproof paint to prevent water infiltration and wood warping/swelling. A general model is included in Figure 5.2 to introduce the parameter notation used throughout the remainder of the report.

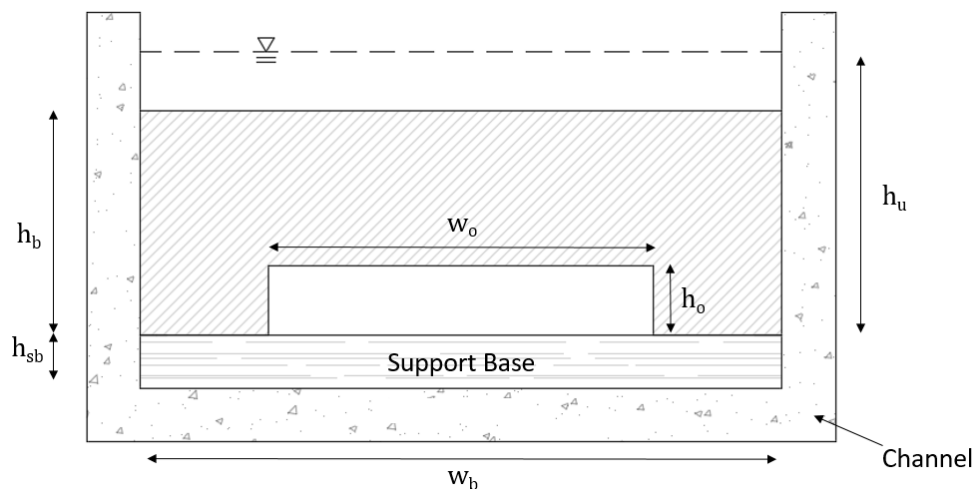


Figure 5.2. Generalized Barrier.

5.2.1.1.1 Weir Barrier

The weir barrier was constructed per the TxDOT SSCB standards. Since there is no drainage, this barrier serves as the worst-case scenario for hydraulic performance where flow overtops the barrier at all flow rates. The weir barrier has a height of 21 inches, bottom width of 12 inches, and top width of 4 inches. After all data were collected, this barrier failed during a redundancy test. Changes were then made in the design of the remaining barriers and the next iteration of the support base. Figure 5.3 displays the barrier installed on the first support base.



Figure 5.3. Weir Barrier.

5.2.1.1.2 SSCB

The SSCB was built to the same overall specifications as the weir barrier with the inclusion of a scupper. The scupper height is 6.5 inches, and the width is 3 ft. Starting at the barrier edge with a width of 1 ft, the barrier support tapers to a width of 4.5 inches at the scupper edge. While tapering the opening is expected to have marginal effects on the hydraulic performance, this design allows the opening height to be increased by an additional inch per structural design standards. This barrier was constructed entirely out of wood and covered in multiple coats of waterproof paint. Figure 5.4 displays the barrier installed in the channel before final seals were applied.



Figure 5.4. SSCB.

5.2.1.1.3 Post-and-Beam Barrier

The post-and-beam barrier has a much greater fractional open space than the SSCB, controlled by an increase in scupper width between the two. The post-and-beam barrier has the simplest geometry of all the barriers, consisting of a rectangular beam supported by rectangular posts. The height of this barrier is 21 inches, the beam width is 1 ft, and the post widths are 4 inches. The scupper height is 6.5 inches, and the scupper length is 4 ft 4 inches. Figure 5.5 displays the barrier installed in the channel with all seals applied.



Figure 5.5. Post-and-Beam Barrier.

5.2.1.1.4 Steel Barrier

The steel barrier has a substantially larger fractional open space than the previous two. This barrier is comprised of three 2.5-inch \times 2.5-inch HSS horizontal beams on each face that span the length of the channel, with 3 inches of vertical spacing between them. The space between the support base and the lowest beam is 5.875 inches. The posts on either side of the channel are each made up of two 19.375-inch \times 7-inch \times 0.5-inch metal plates spaced 2.5 inches apart. Both posts sit on a 16-inch \times 12.5-inch \times 0.5-inch metal base plate with four 0.625-inch diameter holes for connection to the support base with machine screws. All segments are connected through welds, and the barrier base is connected to the support base through eight machine screws. The downstream face of this barrier is displayed in Figure 5.6.



Figure 5.6. Steel Barrier.

The geometries for all four barriers are displayed in Table 5.1. The values for the steel barrier refer to the different sections divided by the horizontal beams and vertical support plates.

Table 5.1. Barrier Dimensions.

	h_b (inches)	h_o (inches)	w_o (inches)	F_o (%)
Weir	21	0	0	0
SSCB	21	6.5	36	18.6
Post and Beam	21	6.5	52	26.8
Steel	19.375	5.875	2.5	60.5
		3	53	
		3	2.5	

5.2.1.2 Support Base

Before construction of the median barriers began, a support base was built in order to anchor the median barriers in place while still allowing its removal when necessary. A total of two bases were constructed. The first base duplicated a successfully tested design by Charbeneau et al. (18), and the second took a new approach to barrier attachment following complications with the original. Both barriers had the same outer dimensions: 57 inches \times 36 inches \times 4.25 inches. Wood planks with attached handles were installed on either side of each base, filling the 5-ft channel span when in place alongside the base and allowing the water to drain completely once removed. The frames of both bases were built from nominal 2-inch \times 4-inch wood planks resting on top of and underneath 0.75-inch plywood sections. Each base was fastened to the channel bed with concrete bolts roughly 90 ft downstream from the pumps.

5.2.1.2.1 Original Design

The support base was built with a combination of wood and concrete. The outer layer of the base was covered in multiple coats of waterproof primer to protect the wood from any swelling. The area within the frame was split into two different sections: the front 1-ft section to house the barrier connection and the rear 2-ft section to counteract the moment created by hydrodynamic pressure on the barrier base system. The front section housed three 3.5-inch-tall wood blocks with 1-inch-diameter holes drilled in their centers, each separated along the channel span by 1 ft 6 inches. The remaining open space in this section was filled with concrete. The hollowed blocks served as the primary point of connection between the barrier and base. Each barrier was to have three $1\frac{5}{16}$ -inch O.D. aluminum pipes extruding from the bottom that fit securely within the vertical slots. The hydrodynamic pressure of the water would then be transferred from the face of the barrier, down through the pipe connection, throughout the support base, and into the channel bed through the bolted connection. The back section was left empty since no extra weight was needed for friction support—simply bolting the rear end of the base to the concrete provided sufficient resistance against the hydrodynamic pressure. The support base design with dimensions included is displayed in Figure 5.7.

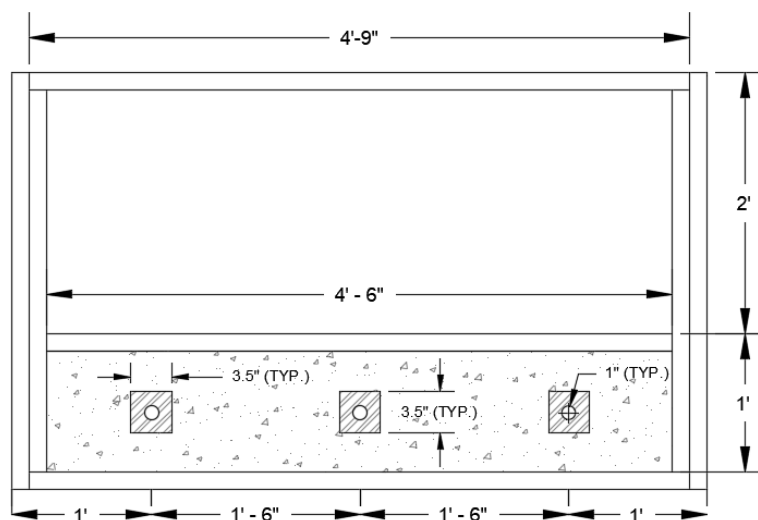


Figure 5.7. Initial Support Base Design.

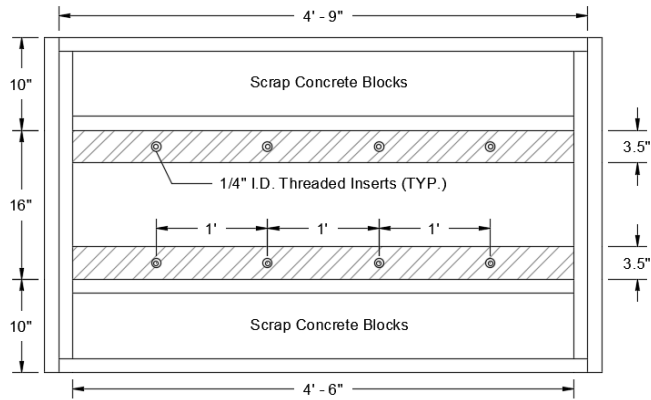
Additional hinged connections were added to the front of the barrier and base following an incident in which the force of the aluminum pipes on the wood blocks and surrounding concrete opened a crack in the center of the concrete itself. This crack opened space between the barrier and base, allowing the flowing water to infiltrate and lift the barrier off the base and carry it downstream. Multiple successful tests were then run with the hinge connection operating properly before the barrier itself gave way. Close inspection revealed a failure of the barrier at the hinge connection, but it was unclear if this was the cause of the accident or if the barrier structure broke first and ripped the connected pieces away from the hinges. In either event, the source of error lies in both a failure to properly seal the barrier and base as well as a hinge location that was too close to the barrier and base edges. Figure 5.8 shows the failed barrier and the failure at the hinged connection. A decision was made at this point to redesign the support base.



Figure 5.8. (a) Weir Barrier Failure; (b) Hinged Connection Failure.

5.2.1.2.2 Final Design

The first change in the new design was to place the barrier in the center of the support base because the previous 2 ft of empty space behind the barrier was determined to be unnecessary for any counter-moment effects. This new barrier location also allowed the addition of another layer of plywood immediately upstream and downstream of the barrier to simulate a pavement overlay on each side of a median barrier. In this new layout, each barrier was connected to a 5 ft \times 1-ft 4-inch section of 0.75-inch plywood that rested on top of two lengths of 3.5-inch \times 3.5-inch wood beams. Four threaded inserts were screwed into each wood beam, and small holes were drilled at corresponding locations in the barrier baseboard. This setup allowed for a total of eight removable machine screws to connect the barrier baseboards to the wood beams in the support base. The center section of the support base as well as the front and back sections were filled with concrete blocks for added weight. To prevent water infiltration into the base, all edges were sealed with silicone caulk, and exposed surfaces were covered in multiple coats of a waterproof paint. Figure 5.9 displays the final support base design and the physical base installed in the channel. Neither the removable boards nor the plywood support base cover are included in Figure 5.9b.



(a)

(b)

Figure 5.9. (a) Final Support Base Design; (b) Installation in Channel Barrier and Support Base Setup in Channel.

The support base was bolted to the concrete channel bed roughly 90 ft from the channel head with a space of 1.5 inches on either side to leave room for the removable boards. The edges between the channel bed and the upstream and downstream support base faces were sealed with silicone caulk. The sides were not sealed because there was not enough space to easily apply a sealant, but this was assumed to be inconsequential since the removable boards would be sealed at their upstream edges to prohibit any leaking through those areas. Once in place, the final support base was not moved for the remainder of testing.

Each median barrier was constructed to be 0.5 inches short of the 5-ft channel width to increase ease of installation. Once in place, narrow wood boards matching the barrier cross-sections were attached via an adhesive to either side on a case-by-case basis to create contact between the barrier and the channel wall. To increase friction support from the barrier-channel interface, wood shims were wedged between the two. The extruding shim pieces were then trimmed with a hand saw. Finally, all edges were sealed with silicone caulk and left to dry for at least a day before testing began.

Hydraulic testing was conducted in an outdoor concrete flume in which water is recirculated by means of an integrated pipe system fed from an on-site reservoir. The flume layout can be seen in Figure 5.10.

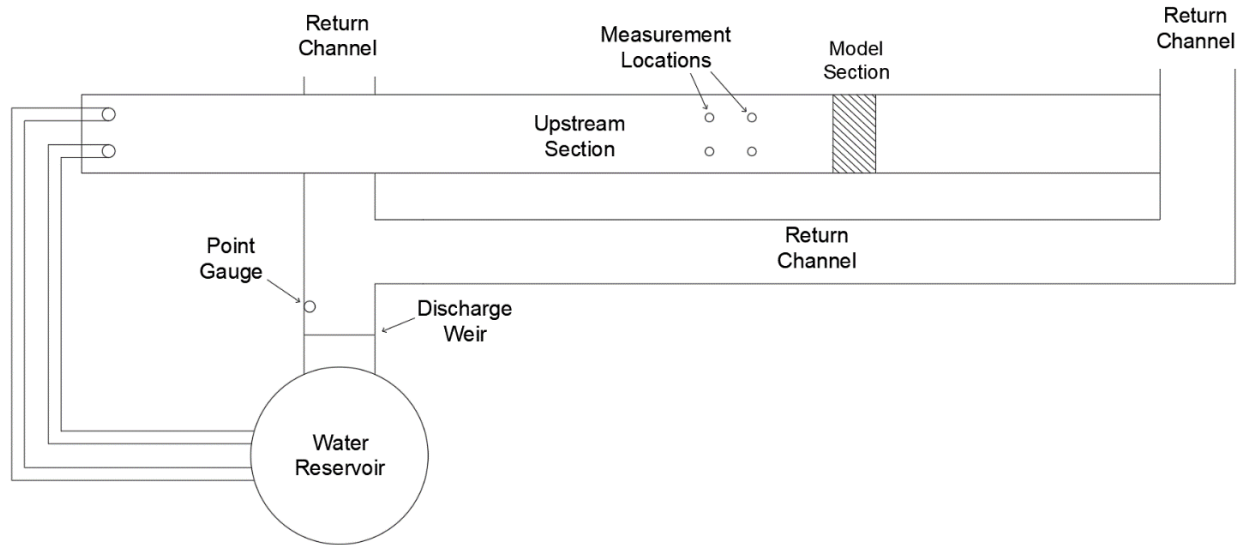


Figure 5.10. Flume Layout.

5.2.2 Reservoir and Pipe Network

The reservoir holds roughly half a million gallons of water, a capacity that is maintained primarily through rainfall. During dry periods when water is lost through evaporation, the reservoir can be refilled by an on-campus water tower. Two pumps are in place to transfer water through the pipe network that runs throughout both the outdoor system and indoor labs. For the purposes of these experiments, the only valves that remained open were those that fed directly into the test channel. Adjusting these two valves controls the pump flow rate into the channel. With all other valves shut, the water is continuously recirculated from the reservoir, through the test channel, and back into the reservoir through a discharge channel. This recirculation allows the system to reach a steady state given a constant flow rate, a necessary condition for these tests.

5.2.3 Test Channel

5.2.3.1 Pump Outlets and Primary Channel

The test channel is a rectangular concrete flume with a width of 5 ft, height of 2 ft 8 inches, and length of about 125 ft. The spanwise and lengthwise channel bed slope is approximately zero, and the walls are all at approximately 90-degree angles with the channel bed. Water enters the channel through the two pipe outlets at the channel's head, as shown in Figure 5.11.



Figure 5.11. Pump Outlets.

5.2.3.2 Return Channel

The water then runs the full length of the channel before spilling into a lower level. There are two return channels on the lower level that feed into the CWE lab building; however, the gates at these channel entrances were closed to ensure recirculation only occurred within the experimental system. Flow continues along the length of the lower channel until it encounters a discharge weir. At a location just upstream, a point gauge is used to measure the head above the weir crest to determine the steady-state flow rate. After spilling over the weir, the water passes through the remainder of the channel and back into the reservoir.

5.2.3.3 Data Collection

The two variables needed to build a rating curve for each barrier are flow rate and upstream water depth. The flow rate is found by measuring the water depth above the discharge weir and using the weir equation introduced in the literature review, while the upstream water depth is measured from ISCO 4230 Bubble Flow Meters that connect to the channel bed through vinyl tubing.

5.2.4 Upstream Water Depth

Four water depth measurements are recorded at locations of 18 ft and 26 ft upstream of the barrier face. For each flow rate, three recordings are taken at all locations to account for small waves in the flow and any small variabilities in instrument measurements. An arithmetic mean is taken from the 12 values to produce a final upstream water depth for that respective flow rate. The measurement locations are displayed in Figure 5.12.

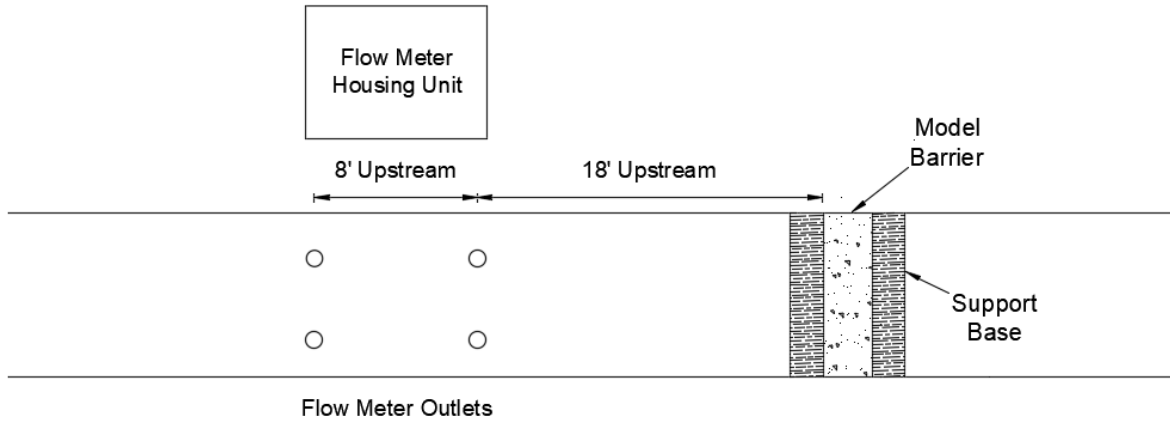


Figure 5.12. Upstream Water Depth Measurement Locations.

5.2.4.1 Bubble Flow Meters

The flow meters reside in a 12V solar-powered housing unit to provide a constant power source and serve as protection from the elements. The solar panel rests on top of the unit and connects to a marine battery that powers all four instruments. A voltage regulator is used as an intermediate in the solar panel–battery circuit. The flow meters record the water depth by measuring the required pressure to send a small air bubble through the length of the 1/8-inch I.D. vinyl tubing. The required pressure is equal to the water pressure at the depth of the tubing outlet, and water depth, h_u , is calculated from the measured pressure, P , water density, ρ_w , and gravitational constant, g :

$$h_u = \frac{P}{\rho_w g} \quad (5.1)$$

Each flow meter was set at a measurement frequency of 1 Hz and a reporting frequency of 0.2 Hz. Under the specified frequency settings, the flow meters report the mean value from five measurements every five seconds. The tubes were positioned along the channel walls and bed, normal to the direction of flow. This orientation negates interference from the fluid velocity at the tube outlet. A waterproof adhesive is applied to the entire length of the tubing that contacts the channel surface, removing any separation of the line from the channel bed where debris could otherwise get caught.

To ensure accurate measurements, moisture is removed from the air bubbles by passing the influent air through a desiccant chamber sitting on top of the flow meter. After about a month of consistent use, the desiccants begin to change color, indicating they are near their saturation point and must be recharged in an oven. The flow meters and housing unit can be seen in Figure 5.13.



(a)



(b)

Figure 5.13. (a) ISCO 4230 Bubble Flow Meter; (b) Solar-Powered Housing Unit.

5.2.4.2 Discharge Weir

The rectangular sharp-crested weir is located in the return channel about 30 ft upstream from the entrance into the reservoir. The weir is a 5-ft \times 2-ft metal plate that has been sealed on all sides to prevent any leaking. The weir is treated as being perfectly rectangular, although there is a small vertical slope across the span of the weir crest. The effects of this slope on the flow rate measurements are considered negligible. At the location of the weir, the return channel walls are 3 ft tall. A 1-ft-tall by 8-inch-wide rectangular orifice located at the weir base allows the channel to drain after testing is complete. During tests, a hinged gate is closed over the orifice and the edges are sealed. A miniscule amount of leakage through the edges of the gate does occur when the channel is full, but any effect on the water depth in the return channel is negligible. A chain is used to pull the gate open for the purposes of draining the channel at the conclusion of testing. The weir and hinged gate are displayed in Figure 5.14. The gate chain serves the secondary purpose of providing a small amount of turbulence as a result of its flow obstruction in the nappe. This turbulence introduces aeration to the nappe, which steadies the upstream flow and allows the weir equation detailed in the literature review to hold true. This equation is repeated below:

$$Q = C_d \frac{2}{3} \sqrt{2g} B H^{3/2} \quad (5.2)$$

The discharge coefficient, C_d , for this specific weir was found to be 0.618 from experiments by Benson (35).



Figure 5.14. Discharge Weir and Gate.

5.2.4.3 Point Gauge

The water depth in the return channel is measured to one thousandth of a foot with a point gauge located 16 ft upstream of the discharge weir. At this location, there are negligible drawdown effects from the weir; however, there are slight variations in the water depth at any given moment due to turbulent effects from a 90-degree bend in the channel 27 ft upstream. To suppress these small waves, the point gauge resides in a 2-inch-diameter plastic stilling well. This setup is displayed in Figure 5.15. A datum is set at the weir crest to measure the water depth over the weir. This datum was measured through a method that began by allowing the return channel to fill completely until water was flowing over the discharge weir. The pumps were then shut off and the weir gate was kept closed, allowing water to only drain to the weir height. Since the weir has a small slope, the datum was set at the location of the intersection between the water surface and the center of the weir span. This measurement was not made in a vertically static condition, as water continued to drain slowly over the lower edge of the slanted weir crest. To increase accuracy, the measurement process was repeated multiple times and averaged. The gauge reading for the weir crest was determined to be 0.958 ft.



Figure 5.15. Point Gauge.

5.3 EXPERIMENTAL PROCEDURE

5.3.1 Start-Up Procedure

Once the barrier was installed in the channel and the seals had been given proper time to set, the start-up process began. The removable boards were set in place on both sides of the base, and the edges on the upstream face were sealed with plumber's putty. This material is ideal for temporary placement and provides a waterproof seal the instant it is applied. Likewise, the gate on the discharge weir was closed and the edges were sealed. As water began to fill the return channel, any leaks around the gate could be identified and sealed with additional putty.

After the proper seals had been applied, the pumps were then turned on to fill the test channel. Once the water level overtopped the support base and flowed through the barrier opening, the pumps were shut off to allow water to drain to the height of the support base. When drained to the support base height, the bubble flow meters were turned on and calibrated by setting the top of the support base as zero. The calibration was accepted when all flow meters read a value of ± 0.002 ft. This datum served the double purpose of ensuring all the flow meters began their measurements from the same point as well as increasing the accuracy of measurements at small flow rates. Note that this calibration method was not possible for the weir barrier because there was no barrier opening for the water to drain through. In this case, the flow meters were calibrated before the barrier was in place. This calibration was saved to the instrument so it would be ready when testing began the following day.

At this point, the pumps were turned back on to begin testing. Once the return channel was filled and water began to spill over the discharge weir, the system was run uninterrupted for

an additional 30 minutes in order to definitively reach a steady state before the first measurements were recorded.

5.3.2 Testing Procedure

For the initial measurements, only one pump was turned on, with the control valve opened at roughly 6.25 percent or $\frac{1}{16}$ the full capacity. A total of three measurements were taken from each individual flow meter as well as the point gauge. Multiple measurements accounted for the presence of waves in the flow, both in the testing and return channels. Upstream water depth measurements were read directly from the flow meter console, and weir depth measurements were read from the point gauge in the return channel, both with a precision of 0.001 ft. All data were manually entered into an Excel file. The two different measurements were recorded intermittently, allowing sufficient time in between each recording to achieve random samples. Additionally, this recording process allowed for steady-state verification; each discharge measurement was tied to the proceeding upstream water depth measurement, and a noticeable trend meant the system was not at steady state. In this case, the process continued until no trend was detected, and the final three rounds of data were then saved. For the upstream water depth, an arithmetic mean was taken for the 12 points to produce one average value. Likewise, for the point gauge measurements, an average was taken over the three recordings. Therefore, from 15 total measurements, a single point representing water depth and flow rate was recorded for each change in flow rate.

After all initial measurements were taken, the second pump was turned on, with its control valve opened at $\frac{1}{16}$ capacity. The recording process then continued, opening one of the pumps by $\frac{1}{16}$ in between each trial. The final trial was limited by either the pumps reaching their maximum flow capacity or the upstream water depth overtopping the channel sides.

5.3.3 Shut-Down Procedure

At the conclusion of testing, both pumps were shut off and both channels drained until they were limited by the support base and discharge weir, respectively. At this point, the removable boards were taken out from the side of the support base and the discharge weir gate was opened to allow all water to return to the reservoir. Any leftover putty was removed and repurposed for a future test.

5.4 TEST CASES

Each barrier was tested for two cases:

1. Performance after installation on a roadway surface (barrier base elevation = top of pavement).
2. Performance after a 2-inch asphalt overlay has been applied to the surface (barrier base elevation = 2 inches below top of pavement).

The 2-inch asphalt overlay was simulated with a 1-inch board on top of the support base immediately upstream and downstream of the model barrier. An example of the overlay case can be seen with the SSCB in Figure 5.16. The datum for both cases was set at the support base height (3.5 inches above the channel bed) when developing the flow rate–water depth rating

curve. The datum was then adjusted to the top of the 1-inch board in post-processing for the purposes of developing the non-dimensional model rating curve. This process is explored further in the following section. All barriers were symmetrical, so there was no need to test their performance against different flow directions.



Figure 5.16. SSCB with Overlay.

5.5 HYDRAULIC TESTING RESULTS AND ANALYSIS

The purpose of this section is to examine the hydraulic rating curves developed from experimental methods detailed in the previous section. These rating curves are then converted to a non-dimensional form and fit to model equations adapted from those presented in Chapter 2 of this report. In this form, the data can be integrated into the software HEC-RAS, a method that is detailed in the following section.

5.5.1 Raw Data Rating Curves

Rating curves were constructed from the upstream water depth values corresponding with each flow rate. Each water depth value was computed from an arithmetic mean of 12 total measurements collected across four locations upstream of the barrier. Likewise, each flow rate value was computed from an arithmetic mean of three point gauge measurements that were then plugged into the weir equation (Equation 5.2). The rating curves for both cases are plotted in Figure 5.17 through Figure 5.19, and a comparison of all six barrier cases and the weir barrier are plotted in Figure 5.20. The weir barrier does not have two different cases because an overlay has no effect on the hydraulic performance of a barrier with no drainage. On each curve, the flow rate is represented along the abscissa, and the upstream water depth is represented along the ordinate.

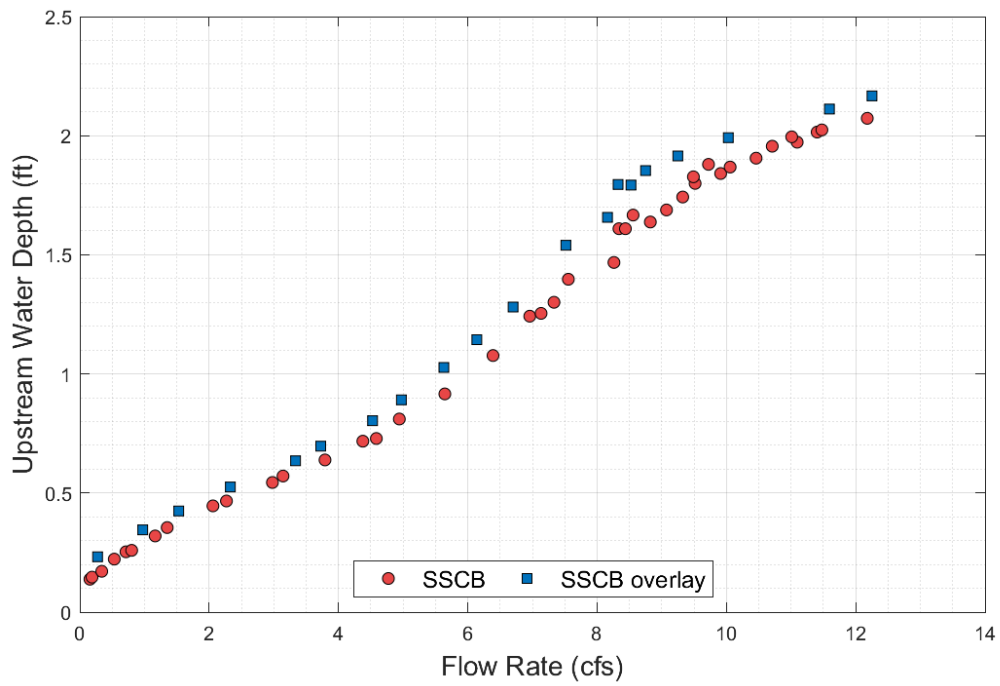


Figure 5.17. SSCB Rating Curves.

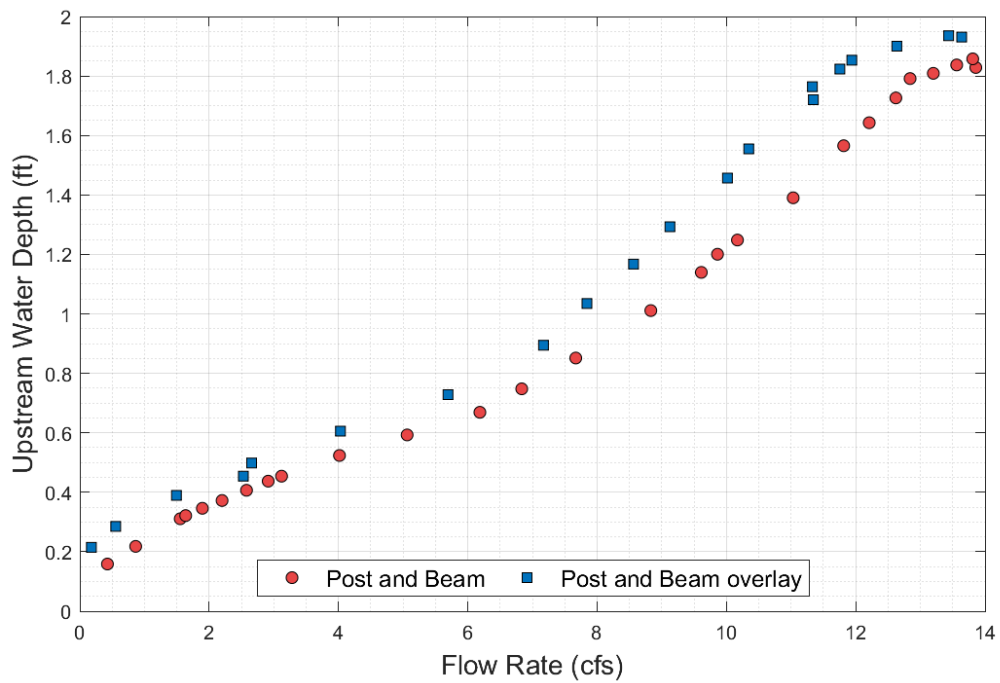


Figure 5.18. Post-and-Beam Rating Curves.

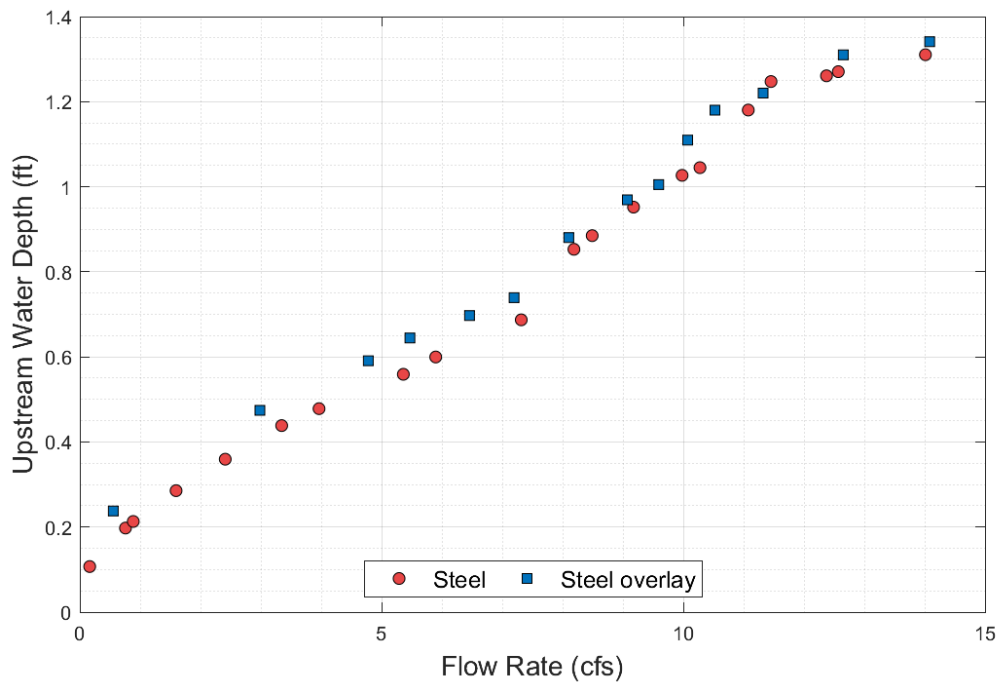


Figure 5.19. Steel Barrier Rating Curves.

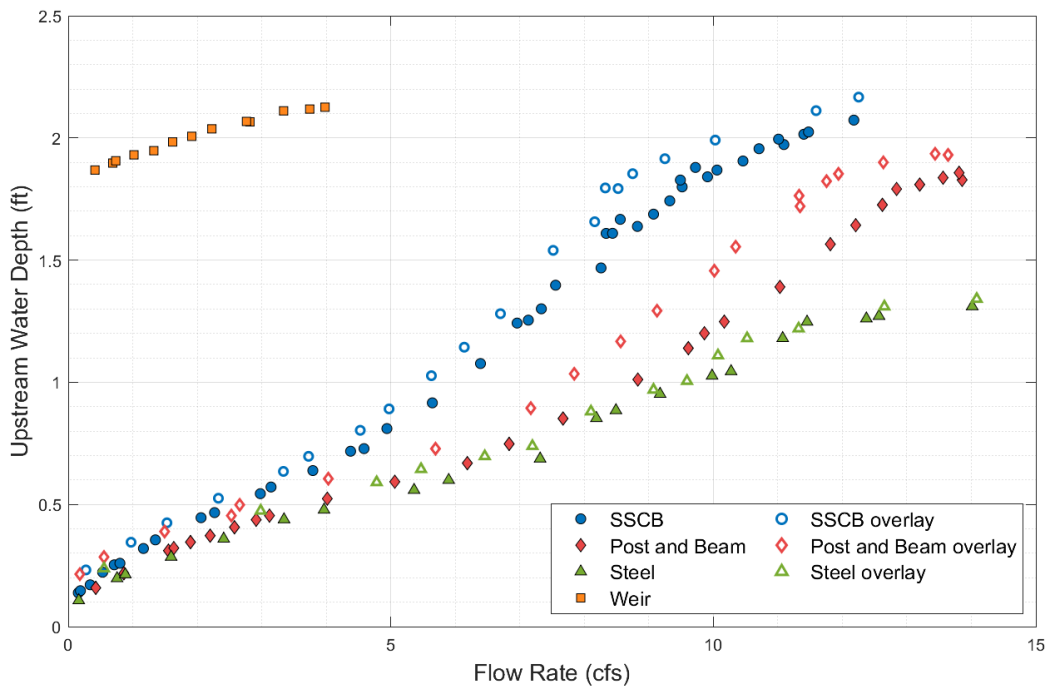


Figure 5.20. Combined Rating Curves.

Hydraulic performance is dictated by the upstream water depth. When comparing two depth values at the same flow rate, the smaller value reflects a greater conveyance through the

barrier opening and, as such, an overall greater hydraulic performance. In Figure 5.20, the weir barrier has the worst performance since the flow is forced to overtop the barrier at all flow rates. This is designated as the worst-case scenario for highway conveyance in an extreme event.

For the three barriers of interest, the steel barrier has the greatest hydraulic performance, followed by the post-and-beam barrier and the SSCB. This order meets the expectation of F_0 as the dominant factor in hydraulic performance. The information on barrier geometries is located in Table 5.1.

5.5.2 Data Accuracy and Limitations

The range of flow rate values was determined by the channel height and pump capacity. For the weir barrier and SSCB, testing was concluded when the upstream water depth was about to overtop the channel walls. For the post-and-beam and steel barriers, testing was concluded when the pumps reached their maximum capacity.

For each data point on the rating curves, 12 measurements were recorded from the flow meters and three were recorded from the point gauge. The standard deviations for flow meter and point gauge measurements are displayed in Table 5.2. Error bars are not displayed in the related previous figures since they are too small to visualize.

One potential source of error within the data collection includes aeration of the barrier nappe. When the upstream water depth is right at the barrier crest, water depth variations increase due to periodic nappe aeration loss and subsequent reaeration. In Figure 5.17, an upstream water depth of 1.75 ft is equal to elevation at the SSCB crest. At this elevation, there is greater variability in the data, an observation reinforced by an increase in standard deviation at the points clustered around point (9.5, 1.75). For all barriers besides the weir barrier, the standard deviation values were greatest at this depth, ranging from ± 0.01 to ± 0.014 . While it might be expected for this phenomenon to be replicated for the weir barrier, variations in the water depth are small at low flow rates.

Table 5.2. Data Standard Deviations.

	Flow Meter Std. Dev. (ft)	Point Gauge Std. Dev. (ft)
SSCB weir	± 0.003	± 0.001
SSCB scupper	± 0.005	± 0.001
SSCB scupper overlay	± 0.004	± 0.001
Post and beam	± 0.007	± 0.002
Post-and-beam overlay	± 0.007	± 0.001
Steel	± 0.005	± 0.001
Steel overlay	± 0.005	± 0.002

5.5.3 Model Fitting

This section discusses the process of converting the data to a non-dimensional form and fitting curves to the new data via three model parameters. Non-dimensionalizing the data serves two purposes. The first purpose is to focus on the hydraulic effects linked to the scupper geometry as opposed to the barrier height. For example, a barrier with a larger fractional open space, F_0 , and larger barrier height may not show a demonstrably greater hydraulic performance than one with a lower F_0 and barrier height. However, by looking at the specific energy instead of upstream water depth, the barriers are normalized by their height and the first barrier will show a clear increase in performance. While it is known that a larger barrier height will increase upstream water depth, this analysis provides insight into how total height can be balanced with scupper geometry to design future median barriers. The second purpose is to produce data that can be integrated into the software HEC-RAS in order to simulate the hydraulic effects of the experimentally tested barriers on actual highways.

5.5.4 Non-dimensional Values

The process of non-dimensionalizing the test data is adapted from Charbeneau et al. (18). To begin, the upstream water depth, h_u , is converted to upstream specific energy, E_u , where Equation 2.2 is rewritten in terms of experimental values:

$$E_u = h_u + \frac{\left(\frac{Q}{h_u w_b}\right)^2}{2g} \quad (5.3)$$

The specific energy is then normalized by the barrier height to produce the non-dimensional form:

$$e_u = \frac{E_u}{h_b} \quad (5.4)$$

Next, the flow rate is non-dimensionalized by the barrier geometry, as in the left-hand side of Equation 2.18, and rewritten in terms of experimental values:

$$\frac{Q}{A\sqrt{gh}} = \frac{Q}{w_b\sqrt{gh_b^3}} \quad (5.5)$$

5.5.5 Model Equations and Coefficients

The model equations first presented in Chapter 2 are rewritten in terms of experimental values. Each equation represents one of the three flow types previously explored.

$$\text{Type 1: } \frac{Q}{w_b\sqrt{gh_b^3}} = C_b F_0 \left(\frac{h_b}{h_o}\right) \left(\frac{2}{3} e_u\right)^{1.5} \quad (5.6)$$

$$\text{Type 2: } \frac{Q}{w_b\sqrt{gh_b^3}} = C_b C_c F_0 \sqrt{2 \left(e_u - C_c \frac{h_o}{h_b}\right)} \quad (5.7)$$

$$\text{Type 3: } \frac{Q}{w_b \sqrt{gh_b^3}} = C_b C_c F_0 \sqrt{2 \left(e_u - C_c \frac{h_o}{h_b} \right) + C_d \left(\frac{2}{3} \right)^{1.5} (e_u - 1)^{1.5}} \quad (5.8)$$

Equations 5.6, 5.7, and 5.8 describe the non-dimensional flow rate as a function of specific energy, barrier geometry, and three dimensionless coefficients, C_b , C_c , and C_d . Each of these three equations models a different range of specific energy values. Equation 5.6 applies to unsubmerged flow through the barrier scupper when $h_u < h_o$, Equation 5.7 applies to fully submerged orifice flow through the scupper when $h_o < h_u < h_b$, and Equation 5.8 applies to the superposition of weir flow over the barrier and orifice flow through the scupper when $h_u > h_b$. Combining the three equations into one piecewise model, the researchers calculated the non-dimensional flow rate for all specific energy values. The standard error was then found between the experimentally measured flow rates and model flow rates:

$$S.E. = \sqrt{\frac{1}{N} \sum_{i=1}^N \left[\left(\frac{Q}{h_b b_c \sqrt{gh_b}} \right)_{exp} - \left(\frac{Q}{h_b b_c \sqrt{gh_b}} \right)_{model} \right]^2} \quad (5.9)$$

Microsoft Excel's Solver was used to fit the three coefficients to the model by minimizing the standard error. The coefficients were subjected to the following constraints:

$$0 < C_b \leq 1.0 \quad (5.10)$$

$$0 < C_c \leq 1.0 \quad (5.11)$$

$$0 < C_d \quad (5.12)$$

These constraints are necessary to create physically meaningful values. Since C_b and C_c are the horizontal and vertical contraction coefficients, respectively, values of 0 would indicate zero conveyance through the barrier openings. Likewise, values above 1.0 would indicate a flow area greater than the size of the opening. Once flow has overtopped the barrier crest, C_d serves as the weir coefficient. This value must be greater than zero to simulate flow; however, there is no upper bound required. The fitted parameters are displayed in Table 5.3.

Table 5.3. Model Parameters.

	C_b	C_c	C_d	Standard Error
SSCB weir	0	0	1.256	0.0049
SSCB scupper	0.774	0.762	0.825	0.0015
SSCB scupper overlay	0.836	0.758	0.738	0.0018
Post and beam	0.752	0.764	0.573	0.0026
Post-and-beam overlay	0.764	0.785	1.455	0.0068
Steel	0.510	0.423	N/A	0.0230
Steel overlay	0.640	0.533	N/A	0.0246

Note: N/A = Not Applicable

5.5.6 Model Rating Curves

Figure 5.21 provides an example of the combination of all three fitted curves to create one piecewise model. The model fitting process outlined above was applied to all seven barrier cases in Figure 5.22 through Figure 5.25. In each figure, non-dimensional flow rate lies on the abscissa and specific energy lies on the ordinate.

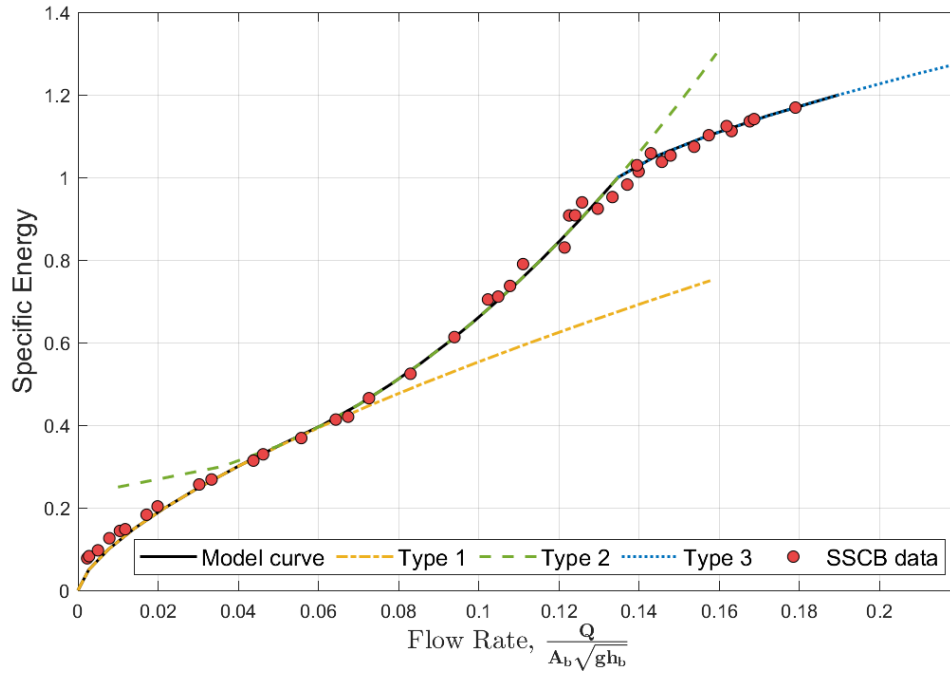


Figure 5.21. Curve Fitting Example.

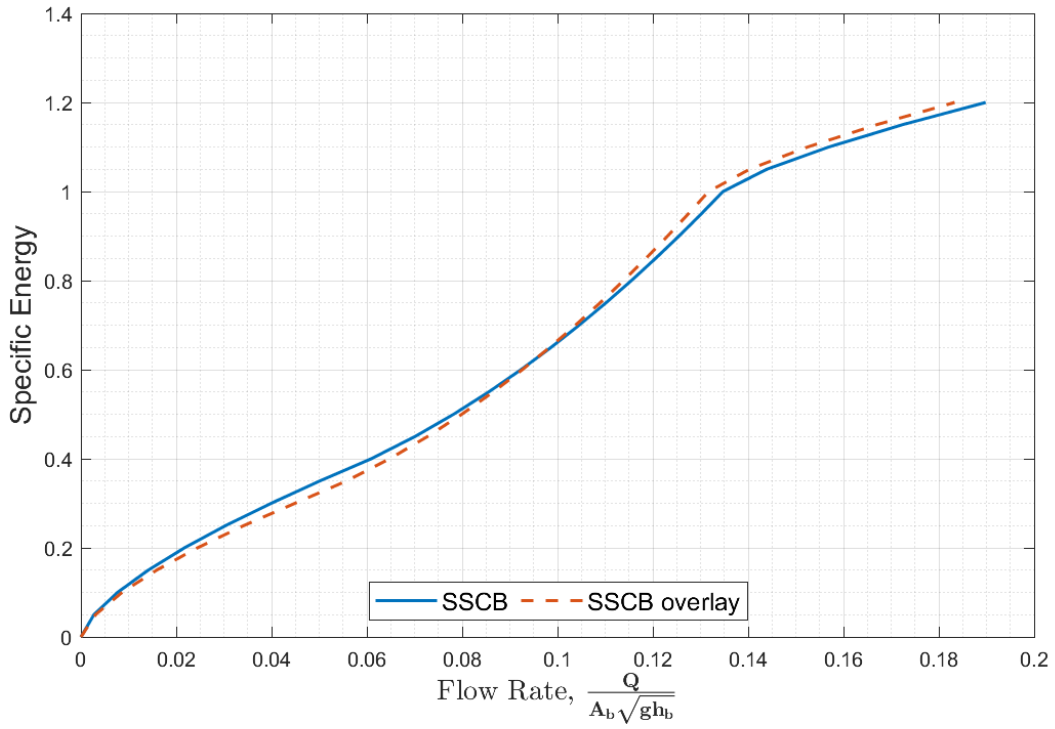


Figure 5.22. SSCB Model Rating Curves.

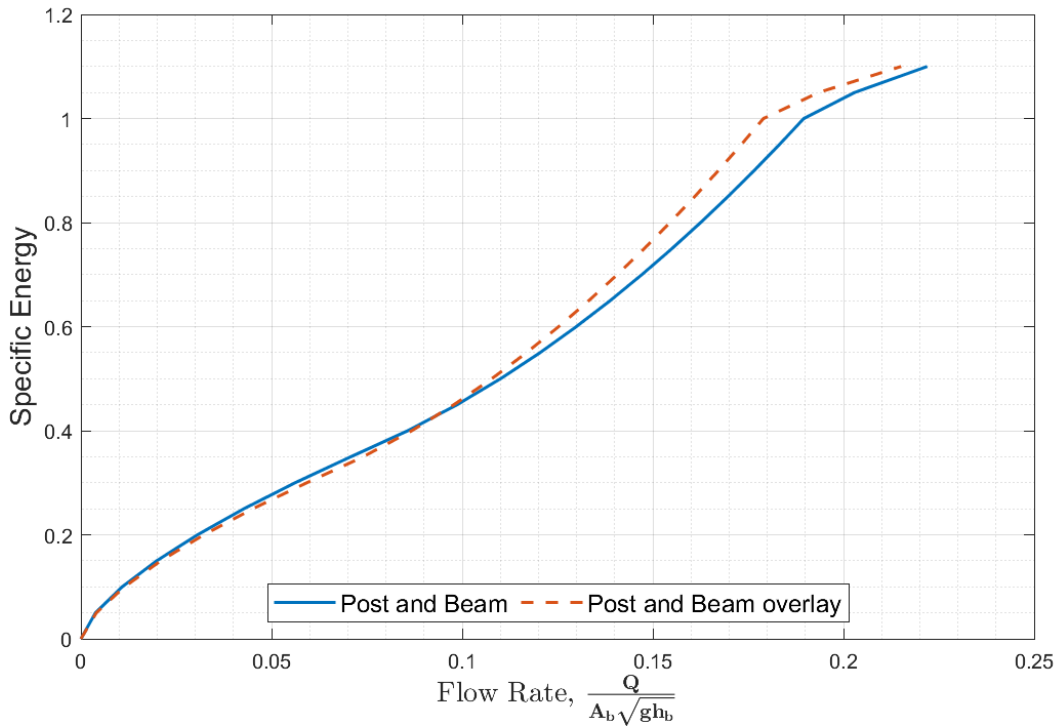


Figure 5.23. Post-and-Beam Model Rating Curves.

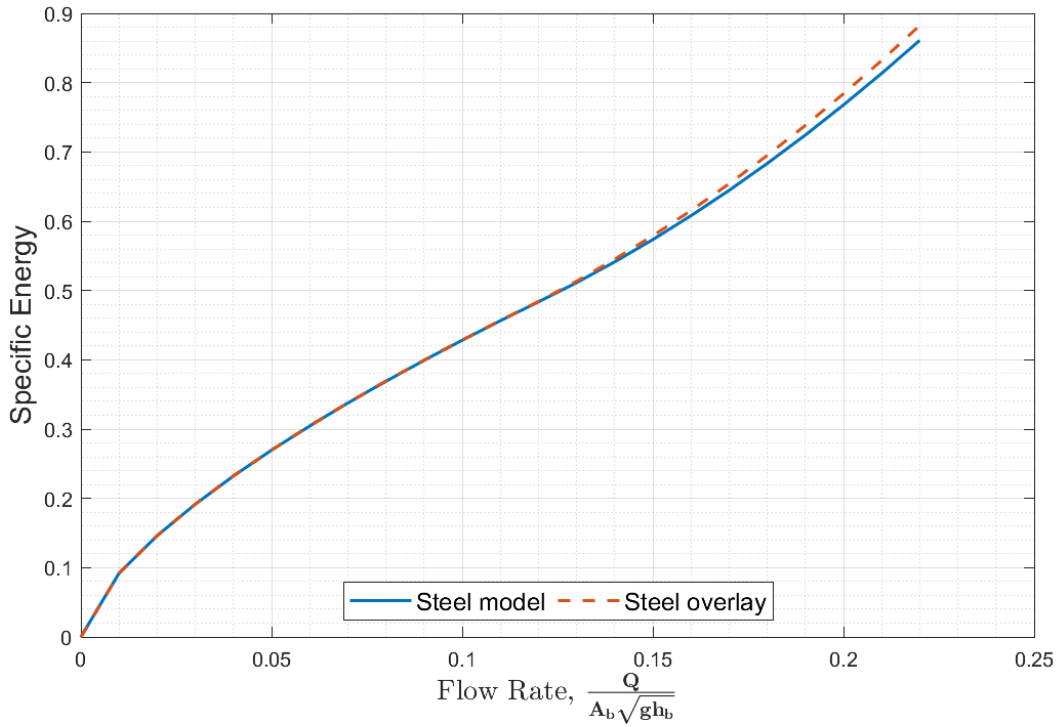


Figure 5.24. Steel Barrier Model Rating Curves.

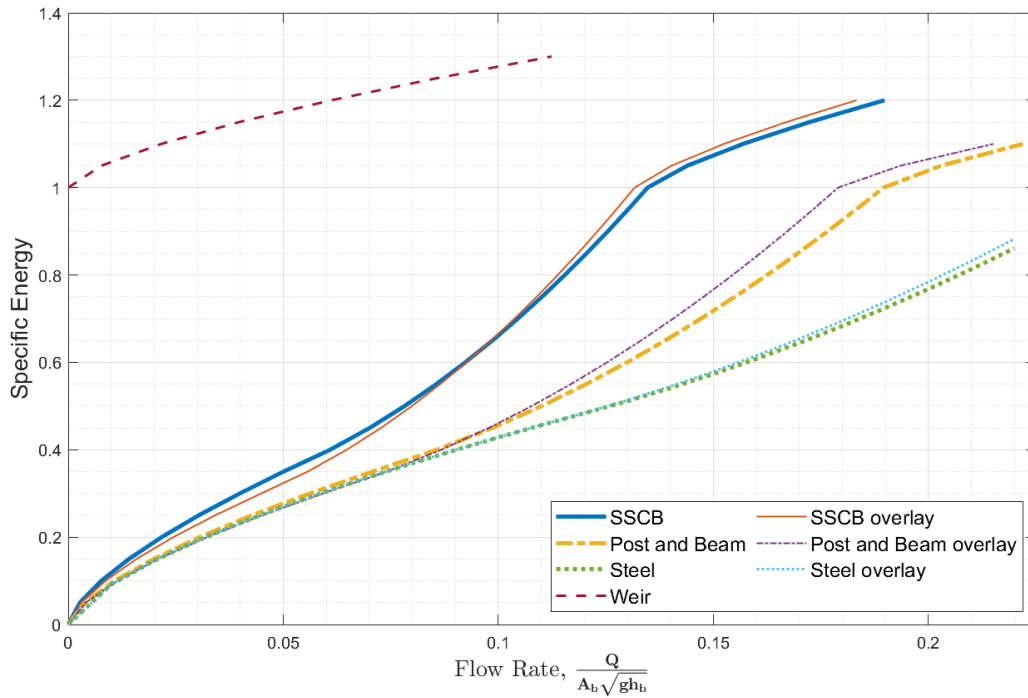


Figure 5.25. Combined Model Rating Curves.

5.5.7 Model Discussion

5.5.7.1 Datum

As mentioned in the previous chapter, the datum for the overlay cases for the model rating curves was set 1 inch above the standard cases. The purpose for changing the datum is to build a non-dimensional rating curve for integration into HEC-RAS where the datum is set at the top of pavement (TOP). For highway cross-sections that have the asphalt overlay elevation set as the TOP, a rating curve built from the original datum would produce inaccurate results. Adjusting the datum changes the effective barrier dimensions by reducing the opening height and barrier height by the same difference in datum elevations. The result is two rating curves with slightly different F_0 values for each barrier, where the overlay cases have a lower hydraulic performance at higher flow rates.

5.5.7.2 Steel Model

Given the large F_0 in the steel barrier, the assumption that flow reaches a critical point as it passes through the obstruction may no longer be valid. This can be seen in a hydraulic jump that is created just downstream of the barrier, resulting in a return to subcritical flow after passing through the steel barrier. In all previous barriers, the critical point assumption is verified by the transition of subcritical flow upstream of the barriers to supercritical flow immediately downstream of the barriers. A comparison of downstream behavior is displayed in Figure 5.26.



(a) Subcritical flow downstream of steel barrier (b) Supercritical flow downstream of weir barrier

Figure 5.26. Downstream Behavior Comparison.

Since the presence of a critical point at the barrier is not clear for the steel barrier, the model equations applied in this case lack a theoretical basis, and as a result, the model curve is not a perfect representation of the physical flow. Additionally, the flow never overtopped the barrier crest due to limited pump capacity, resulting in an incomplete flow description. A comparison between the model and non-dimensional data points is displayed in Figure 5.27.

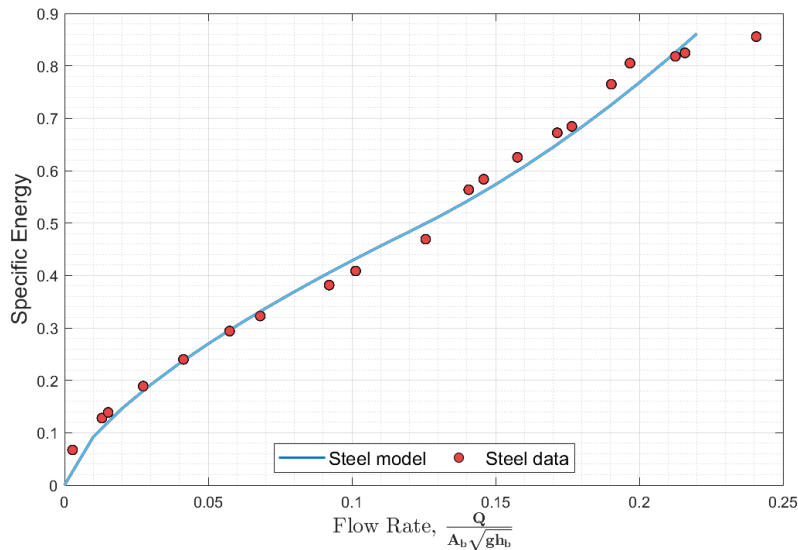


Figure 5.27. Steel Barrier Model Fit Comparison.

As a result of the limitations detailed above, the standard error for the steel barrier is an order of magnitude greater than a majority of the other barriers (Table 5.3). Although the model is not sufficient for a complete characterization of the steel barrier, it is accurate enough to correctly represent an increase in hydraulic performance relative to the SSCB and post-and-beam barriers.

5.5.8 Overlay Comparison

There was a considerable increase in C_d from 0.573 to 1.455 after the overlay was applied for the post-and-beam barrier, as seen in Table 5.3. However, this parameter was fit to a limited number of data points since a more complete characterization of Type 3 flow for the post-and-beam barrier was constrained by the pump capacity. While C_d for both cases could change given new data at larger flow rates, the effect on the model curves is expected to be minimal. For instance, by comparing all post-and-beam parameter values in Table 5.2, C_d is shown to be much more sensitive than C_b or C_c to minor changes in flow behavior displayed in Figure 5.23. In this regard, the increase in C_d is not as physically impactful as the values suggest.

In both the SSCB and post-and-beam barriers, the overlay case performs better at low flow rates when all flow is through the barrier scupper. While the reason for the increased performance is not explicitly known, it could be related to the lack of an overlay paved through the barrier scupper itself. The drop-off from the overlay into the barrier opening might have a subtle drawdown effect in the data. While the addition of an overlay does not show an increase in upstream specific energy at low flow rates, there is still an increase in upstream water depth and, as such, a decrease in overall hydraulic performance, as seen in Figure 5.20.

5.5.9 SSCB Alteration Example

This section provides an example to estimate how changes in barrier geometry affect hydraulic performance. This example uses the SSCB with a scupper width reduced by 10 percent. Two different methods are used to estimate the new rating curve:

1. Adjusting w_o in the model equations and keeping the same fitting parameters from the original SSCB data.
2. Calculating the specific energy value at each flow rate from the SSCB and post-and-beam models using linear extrapolation:

$$e_{new,i} = e_{SSCB,i} + (w_{new} - w_{SSCB}) \left(\frac{e_{SSCB,i} - e_{PB,i}}{w_{SSCB} - w_{PB}} \right)$$

Since the only effective change between the SSCB and post-and-beam models is the decrease in opening width, a relationship can be determined between the specific energy output as a function of opening width only, given that the rest of the parameters remain constant. This method would not be valid for two barriers with significantly different geometries.

A comparison of both methods and the original rating curve is displayed in Figure 5.28.

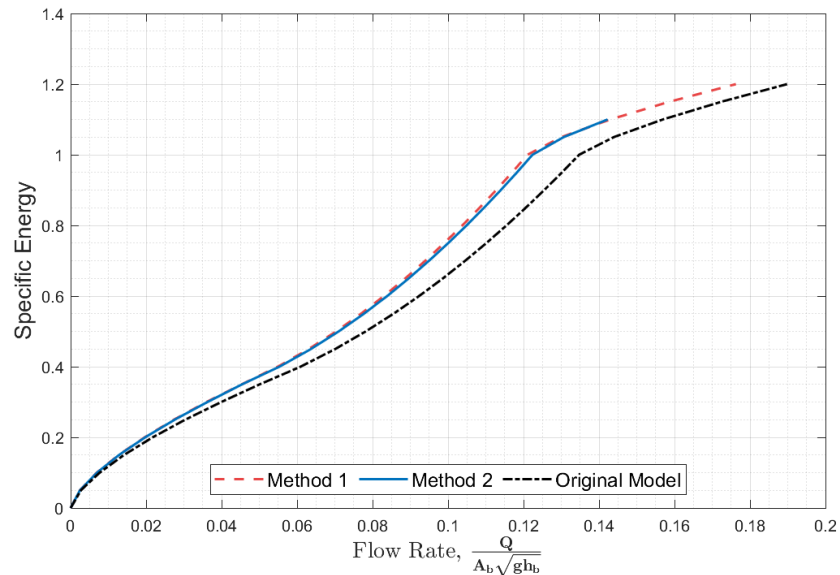


Figure 5.28. SSCB Rating Curve Estimates—10 Percent Opening Reduction.

The new curves fit the expectation since a reduction in fractional open area resulted in decreased hydraulic performance. Both methods produced nearly identical results; however, there was a slight deviation for flow over the barrier crest. This can be explained by the fitting parameter values in Table 5.3, where there is only a small change between the two models for C_b and C_c yet a more significant change for C_d . If there were no change between the parameters, then both methods would be performing the exact same function. While either method would be a sufficient estimate, the rating curve produced by Method 1 should be considered more accurate since the new model parameters are expected to be very similar to the original SSCB model parameters.

5.6 MODELING BARRIERS IN HEC-RAS

5.6.1 Introduction

The purpose of this section is to demonstrate a method for integrating experimental rating curve data into HEC-RAS. This software is used to model the interaction of open-channel flow systems with engineered structures and estimate the water surface level response of the system to a variety of flow conditions. Microsoft Excel was used along with HEC-RAS to provide a method that is applicable to current industry practices. This research employs the most current version at the time of this writing, HEC 5.0.7.

5.6.2 Computation Methods

HEC-RAS uses two methods to determine water depth upstream and downstream of an engineered structure such as a bridge or roadway during a high flow regime: the energy equation and the pressure/weir equations. The energy equation method essentially treats the bridge system as a normal open channel, subtracting the bridge area from the total flow area and adding any edges that come into contact with the water to the overall wetted perimeter. The pressure/weir method separates the flow into pressure flow through an orifice (e.g., a highway culvert or opening under a bridge) and weir flow over the roadway crest, using separate equations for both flow types. In the latter method, the weir flow is controlled by the weir coefficient; the HEC-RAS suggested value of 2.6 reflects a structure with no rails or barriers. As discussed in Charbeneau et al. (18), the pressure/weir method is most effective for modeling barrier additions to the top of the structure. The only necessary modification for the pressure/weir method is altering the weir coefficient, while the energy equation has no such simple adjustments.

5.6.3 Example Details

The pressure/weir method follows closely to previous developments by Klenzendorf et al. (36) and Bin-Shafique et al. (14). However, the method presented in this section was applied to an existing site as opposed to HEC-RAS example problems with simplified geometries. The site selected for this example was FIS Stream W100-00-00, Buffalo Bayou Watershed, Houston, TX—extracted from the Harris County Model and Map Management (M3) System. This river reach was condensed in HEC-RAS to analyze the section between Stations 168169.9 and 162811.9. The presented method used the SSCB scupper model rating curve data with no added overlay, as shown in Figure 5.29.

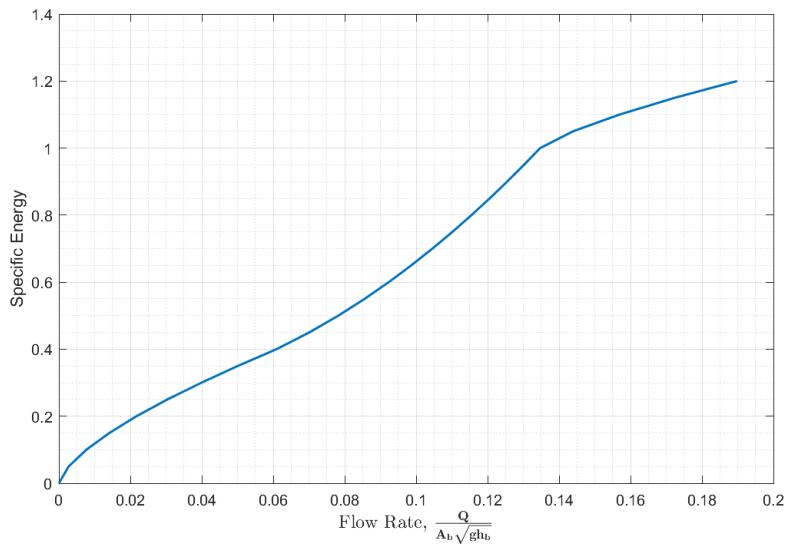


Figure 5.29. SSCB Model Rating Curve.

5.6.4 Site Modifications

Modifications were made to the cross-sections and flow data extracted from the M3 model to illustrate the method more clearly. The first modification was to add a new column of flow rates, labeled TEST FLOWS in Figure 5.30. The existing flows are site-specific estimates for 10-, 50-, and 100-year floods; however, the roadway crest is not overtopped in any of these cases. The new flow rates were calculated by increasing the 100-year flow rates by 30 percent. The second modification was to increase the bridge depth, thereby decreasing the flow area underneath the bridge. The bridge cross-section can be seen in Figure 5.31. In the cross-section, the size of the bridge opening significantly outweighs any flow area differences between the barriers and controls the water surface level behavior as a result. Decreasing the flow area underneath the bridge is not necessary when implementing this method but is done so in this example to help distinguish the effects seen from editing the weir coefficient. Since all sites of interest in the M3 model were bridge crossings with large flow areas underneath the roadway, this modification would be necessary regardless of the selected site. Neither of these modifications affect the methodology, and they exist for the purpose of clarity only.

5.6.5 Data Integration Example

To integrate experimental rating curve data into HEC-RAS, an iterative method can be utilized. The first step in this procedure is to run HEC-RAS with the default weir coefficient of 2.6. This will simulate the flow over the roadway with no barrier present. In the detailed output table (Figure 5.32), the “E.G. US” value is the energy grade line depth, and the “Weir Sta Lft” and “Weir Sta Rgt” values are the horizontal locations where the energy grade line intersects the roadway surface.

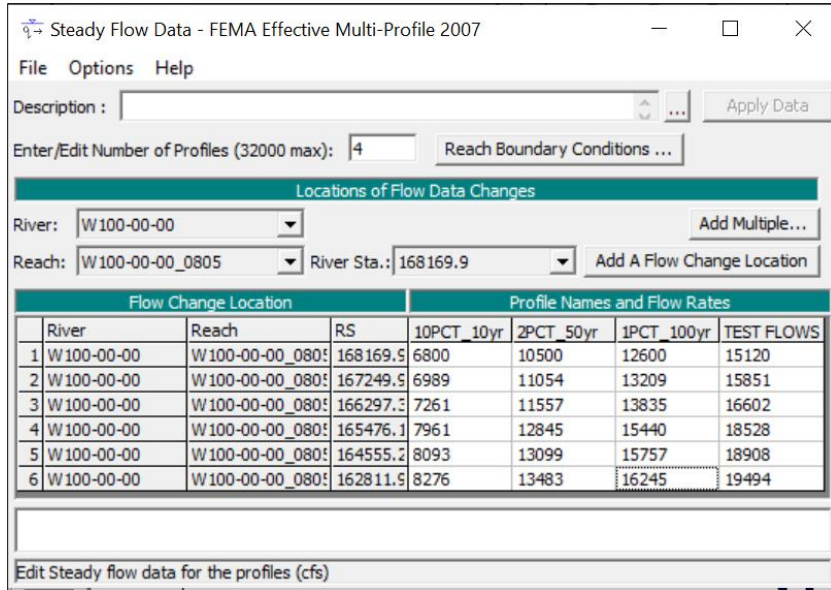


Figure 5.30. Steady-Flow Analysis Modifications.

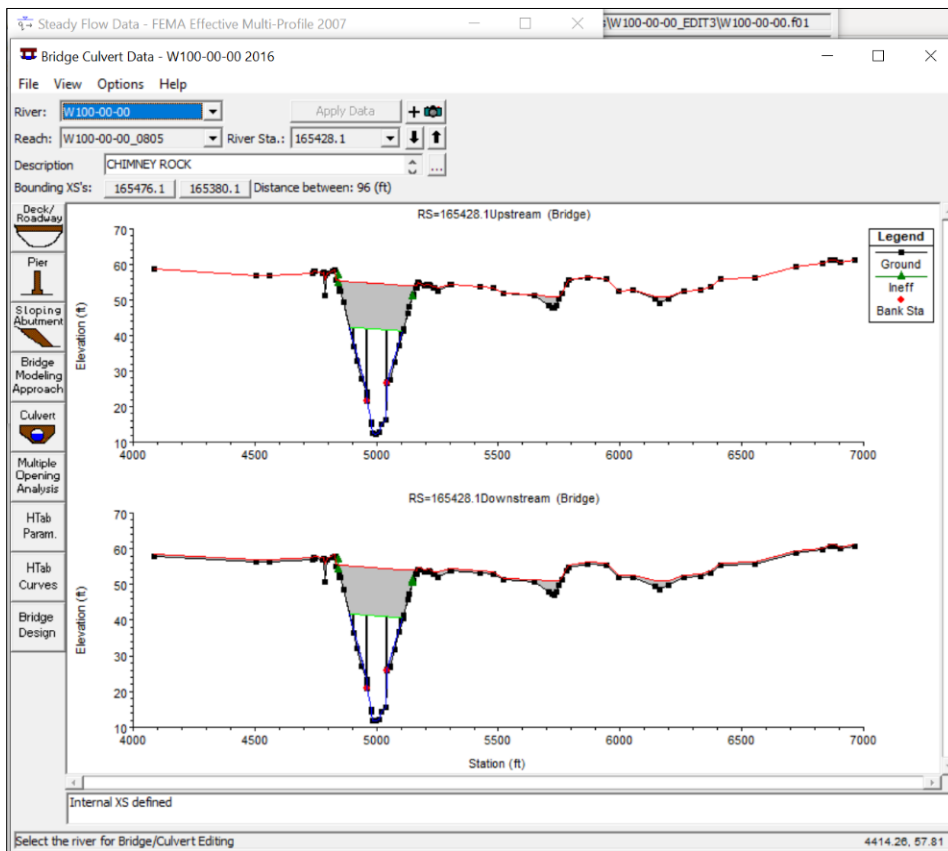


Figure 5.31. HEC-RAS Cross-Section.

Plan: Eff+LOMR MP W100-00-00 W100-00-00_0805 RS: 165428.1 Profile: TEST FLOWS			
E.G. US. (ft)	54.64	Element	Inside BR US
W.S. US. (ft)	54.46	E.G. Elev (ft)	54.64
Q Total (cfs)	18528.00	W.S. Elev (ft)	54.46
Q Bridge (cfs)	10781.35	Crit W.S. (ft)	27.02
Q Weir (cfs)	7746.65	Max Chl Dpth (ft)	42.14
Weir Sta Lft (ft)	5002.07	Vel Total (ft/s)	3.61
Weir Sta Rgt (ft)	6387.74	Flow Area (sq ft)	5137.75
Weir Submerg	0.88	Froude # Chl	0.17
Weir Max Depth (ft)	3.74	Specif Force (cu ft)	81052.30
Min El Weir Flow (ft)	50.91	Hydr Depth (ft)	4.56
Min El Prs (ft)	42.30	W.P. Total (ft)	1647.80
Delta EG (ft)	0.11	Conv. Total (cfs)	
Delta WS (ft)	0.10	Top Width (ft)	1126.11
BR Open Area (sq ft)	3196.18	Frctn Loss (ft)	
BR Open Vel (ft/s)	3.37	C & E Loss (ft)	
BR Sluice Coef		Shear Total (lb/sq ft)	
BR Sel Method	Press/Weir	Power Total (lb/ft s)	

Figure 5.32. HEC-RAS Output Table.

5.6.6 Weir Approximation

To use the pressure/weir method over a non-uniform cross-section, the roadway is segmented into a combination of equal-length horizontal weirs where the right and left weir stations define the domain boundaries. The weir approximation for this bridge cross-section is displayed in Figure 5.33.

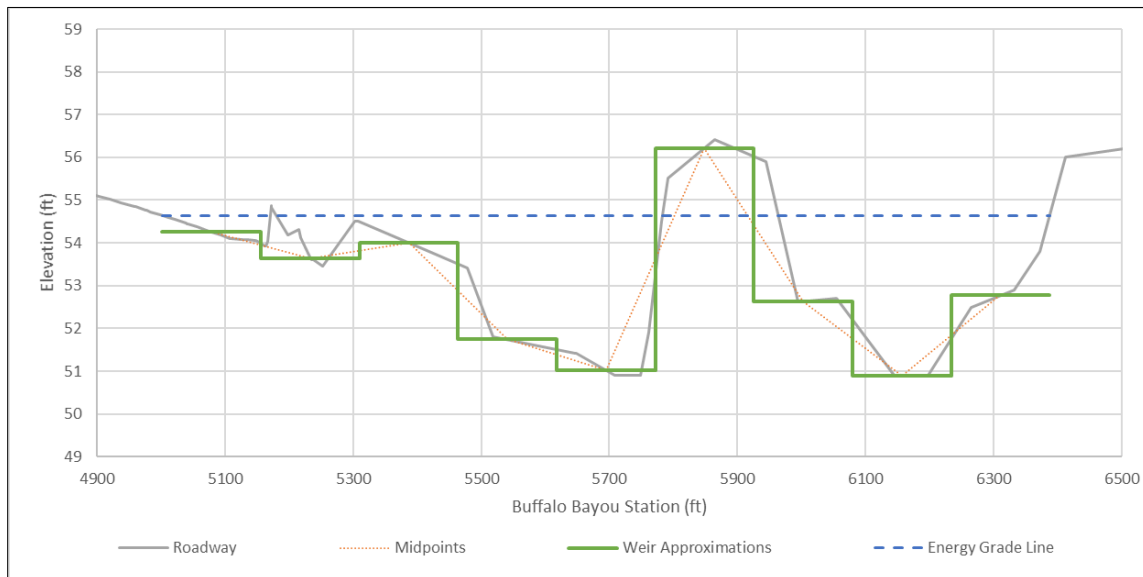


Figure 5.33. Weir Approximation.

The number of weirs depends on shape and resolution of the input roadway geometry. In this example, it was decided that nine weirs were the minimum needed to provide a sufficient

visual fit to the cross-section. The elevation of each section can be interpolated from the roadway cross-section at the midpoint of each weir.

5.6.6.1 Iterative Method

Once this roadway has been discretized into segments, the following steps are computed for each weir:

1. Compute the energy over the i^{th} weir (E_i) by subtracting the weir elevation from the energy grade line.
2. Calculate the specific energy (e_i) by dividing E_i by the barrier height (h_b).
3. Use the specific energy value to find the non-dimensional flow rate by either reading the value directly from the barrier rating curve or plugging the specific energy into the model equations and calculating the non-dimensional flow rate directly.
4. Calculate the actual flow rate over each weir by inverting $Q_{non-dim} = \frac{Q}{L\sqrt{gh_b^3}}$ and solving for Q , where L = weir length and h_b = barrier height:

$$Q = Q_{non-dim} L \sqrt{gh_b^3} \quad (5.13)$$

5. Calculate the weir coefficient by rearranging the weir equation $Q = CLH^{1.5}$ to solve for C where the energy of each weir is substituted for the depth, H :

$$C = \frac{Q}{LE_i^{1.5}} \quad (5.14)$$

6. The final weir coefficient for the roadway section is taken as an average of the weir coefficients for each section. For sections that are not submerged, the coefficient is equal to zero and excluded from the mean calculation.

5.6.6.2 Iteration 1

Excel can be used to build a table with a column for each step above and row for each weir section, as seen in Table 5.4.

For the first iteration, HEC-RAS was run with the standard weir coefficient $C = 2.6$. At this value, the HEC-RAS weir flow rate output was 7747 cfs and the rating curve flow rate was 3703 cfs. From the rating curve, an average weir coefficient $C = 1.122$ was calculated. The steps above could then be repeated with this new coefficient.

Table 5.4. First Iteration.

Weir Section	STA. Left (ft)	STA. Right (ft)	L (ft)	Weir Elev. (ft)	E_i (ft)	e_i (ft/ft)	Q_{RC}	Q (cfs)	C
1	5002.1	5156.0	154.0	54.26	0.38	0.110	0.009	51.0	1.392
2	5156.0	5310.0	154.0	53.65	0.99	0.284	0.037	212.3	1.392
3	5310.0	5464.0	154.0	54.00	0.64	0.182	0.019	108.6	1.392
4	5464.0	5617.9	154.0	51.74	2.90	0.828	0.119	680.7	0.896
5	5617.9	5771.9	154.0	51.02	3.62	1.035	0.141	807.9	0.760
6	5771.9	5925.9	154.0	56.22	-1.58	0.000	0.000	0.0	0.000
7	5925.9	6079.8	154.0	52.62	2.02	0.576	0.090	513.0	1.164
8	6079.8	6233.8	154.0	50.90	3.74	1.069	0.149	850.6	0.764
9	6233.8	6387.7	154.0	52.77	1.87	0.534	0.084	479.1	1.219
								Q_{tot} = 3703.2	
								C_{avg} = 1.122	

5.6.6.3 Iteration 2

The HEC-RAS output table for $C = 1.122$ is displayed in Figure 5.34, and the associated Excel table is displayed in Table 5.5. After the second iteration, the HEC-RAS and rating curve flow rates were 4262 and 3930 cfs, respectively. The method was then continued for two more iterations until the weir coefficient stabilized at 1.107, at which point the HEC-RAS and rating curve flow rates were 4208 and 3947 cfs, respectively.

Plan: Eff+LOMR MP W 100-00-00 W 100-00-00 0805 RS: 165428.1 Profile: TEST FLOWS				
E.G. US. (ft)	54.85	Element	Inside BR US	Inside BR DS
W.S. US. (ft)	54.67	E.G. Elev (ft)	54.85	54.53
Q Total (cfs)	18528.00	W.S. Elev (ft)	54.67	54.36
Q Bridge (cfs)	14266.07	Crit W.S. (ft)	27.02	26.43
Q Weir (cfs)	4261.93	Max Chl Dpth (ft)	42.35	42.63
Weir Sta Lft (ft)	4958.52	Vel Total (ft/s)	3.44	3.68
Weir Sta Rgt (ft)	6391.51	Flow Area (sq ft)	5387.26	5029.01
Weir Submerg	0.80	Froude # Chl	0.16	0.17
Weir Max Depth (ft)	3.95	Specif Force (cu ft)	81933.90	82471.58
Min El Weir Flow (ft)	50.91	Hydr Depth (ft)	4.48	4.66
Min El Prs (ft)	42.30	W.P. Total (ft)	1725.40	1600.22
Delta EG (ft)	0.32	Conv. Total (cfs)		
Delta WS (ft)	0.31	Top Width (ft)	1203.66	1078.55
BR Open Area (sq ft)	3196.18	Frctn Loss (ft)		
BR Open Vel (ft/s)	4.46	C & E Loss (ft)		
BR Sluice Coef		Shear Total (lb/sq ft)		
BR Sel Method	Press/Weir	Power Total (lb/ft s)		

Figure 5.34. HEC-RAS Second Iteration Output.

Table 5.5. Second Iteration.

Weir Section	STA. Left (ft)	STA. Right (ft)	L (ft)	Weir Elev. (ft)	E _i (ft)	e _i (ft/ft)	Q _{rc}	Q (cfs)	C
1	4958.5	5117.8	159.2	54.46	0.39	0.110	0.009	53.0	1.392
2	5117.8	5277.0	159.2	54.19	0.66	0.188	0.020	118.5	1.392
3	5277.0	5436.2	159.2	54.20	0.65	0.186	0.020	116.0	1.392
4	5436.2	5595.4	159.2	51.92	2.93	0.837	0.120	708.9	0.889
5	5595.4	5754.6	159.2	51.19	3.66	1.047	0.144	850.0	0.761
6	5754.6	5913.9	159.2	56.04	-1.19	0.000	0.000	0.0	0.000
7	5913.9	6073.1	159.2	52.69	2.16	0.619	0.095	563.5	1.111
8	6073.1	6232.3	159.2	50.90	3.95	1.129	0.165	977.5	0.782
9	6232.3	6391.5	159.2	52.78	2.07	0.592	0.092	542.9	1.144
								Q_{tot} = 3930.1	
								C_{avg} = 1.108	

5.6.7 Discussion

As seen in Figure 5.33, Weir Section 6 lies above the energy grade line, resulting in no flow through that section of the roadway. This is reflected in Table 5.4 and Table 5.5 where an

if/then statement is used to output zero flow when $E_i < 0$. When $e_i < 1.5C_c \frac{h_o}{h_b}$, flow is through the barrier scupper and the weir coefficient is constant:

$$C = C_b F_o \frac{h_o}{h_b} \left(\frac{2}{3}\right)^{1.5} g^{0.5} \quad (5.15)$$

For the SSCB, $C = 1.392$ for flow through the scupper. This is seen in Weir Sections 1–3 in Table 5. and Table 5.5.

The results for each iteration are displayed in Table 5.6. The percent error calculated between the RAS output and the estimated flow rate stabilized at a value of 6.4 percent. In general, a more acceptable convergence metric of 1 percent error should be pursued if possible, but this will not be feasible for all implementations. One potential method for increasing accuracy is to increase the number of weirs approximated across the cross-section. A weir length of 160 ft was too large to completely characterize the complexities in the cross-section geometry, as seen particularly in the left side of Figure 5.33; however, the number of weirs was limited in this case for the purpose of presentation clarity. Given the computational ease for increasing the number of weirs in Excel, the researchers suggest aiming for a weir length < 50 ft when possible.

Table 5.6. Iterative Method Summary.

Iteration #	C	Q _{RAS}	Q _{RC}	% Error
1	2.6	7747	3703	65.4%
2	1.122	4262	3930	14.0%
3	1.108	4211	3946	6.5%
4	1.107	4208	3947	6.4%

5.7 SUMMARY AND CONCLUSIONS

5.7.1 Summary

The following highlights key components of the experimental approach and critical conclusions that resulted from hydraulic testing of the modeled median barriers.

- A total of three model barriers with openings were tested to determine the hydraulic performance under two test cases: (a) installation directly on a roadway surface, and (b) application of a 2-inch asphalt overlay after the barrier has already been installed. A fourth barrier was used as a worst-case scenario from a hydraulic conveyance perspective in order to serve as a baseline for the designed barriers.
- Rating curves were created to measure the response in upstream water depth to increasing flow rates for all seven barrier cases. Parameters for representing each flow type (unsubmerged, orifice, weir + orifice) were fit to the experimental data to compute non-dimensional rating curve models for each case.
- An example that detailed a method to estimate a new rating curve for a SSCB with a 10 percent reduction in scupper width was provided. This method does not require additional testing.

- The method to apply experimental results in HEC-RAS over non-arbitrary roadway cross-sections was presented. This method consists of dividing the roadway into separate equal-length sections and iteratively computing a new weir coefficient for each section using the non-dimensional model rating curves.

5.7.2 Conclusions

- Hydraulic performance increases with increasing F_0 .
- The inclusion of a pavement overlay decreases hydraulic performance; however, this effect is diminished for barriers with large F_0 , such as the steel barrier.
- The barriers can be ranked by greatest to least hydraulic performance as follows: steel barrier, post-and-beam barrier, SSCB, weir barrier.

CHAPTER 6. BARRIER SYSTEM DETAILS

6.1 TEST ARTICLE AND INSTALLATION DETAILS

The installation consisted of five 30-ft-long scupper barriers spaced at 2 inches apart at the joints, for a total length of 150 ft 8 inches. Each barrier was anchored in place by two fully submerged 72-inch-long × 18-inch-diameter concrete pillars, spaced at 30 inches from the edge of the barrier to the center of the pillar. The barriers were 42 inches tall above grade, had a width on the bottom of 24 inches, and then sloped on both the traffic and field side for a final width of 8 inches at the top. The barriers also had a 13-inch-high scupper at the bottom, starting and ending at 72 inches from each end for an effective scupper length of 18 ft.

Figure 6.1 presents the overall information on the TxDOT large-scupper median barrier (LSMB), and Figure 6.2 provides photographs of the installation. Appendix A provides further details on the TxDOT LSMB. Drawings were provided by the TTI Proving Ground and approved by TxDOT, and construction was performed by Tucker Construction.

6.2 DESIGN MODIFICATIONS DURING TESTS

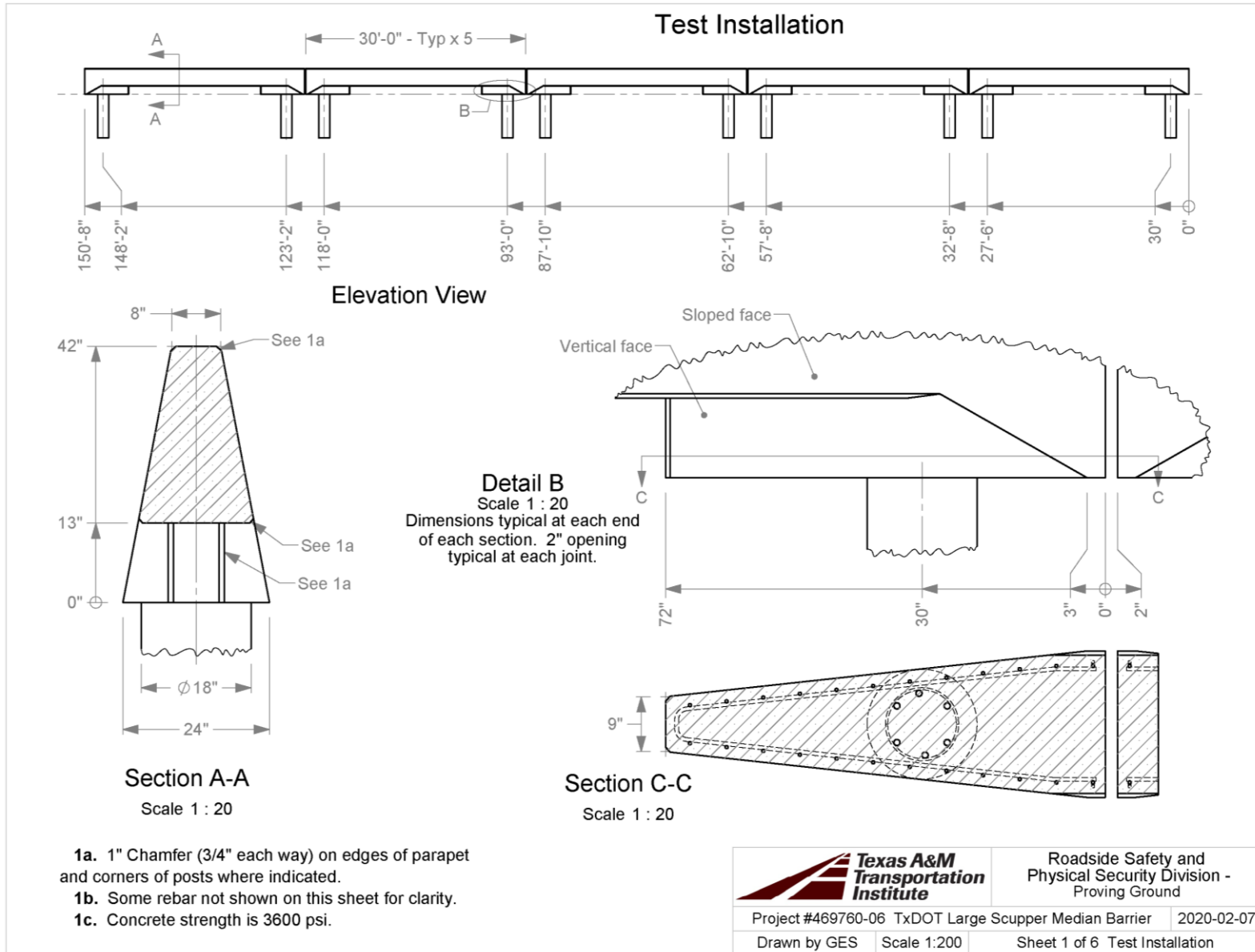
No modification was made to the installation during the testing phase.

6.3 MATERIAL SPECIFICATIONS

The specified compressive strength of the concrete used in the shafts and barrier was 3600 psi. On the day of the first test, June 2, 2020, the average compressive strength of the concrete was as follows:

- Average concrete strength for the shafts: 5243 psi at 63 days of age.
- Average concrete strength for barriers: 4762 psi at 41 days of age.

Appendix B provides material certification documents for the materials used to install/construct the TxDOT LSMB.



Q:\Accreditation-17025-2017\EIR-000 Project Files\469760-06 Median Barrier for Flood-Prone Areas-Dobrovoly\Drafting_469760-06\469760-06 Drawing

Figure 6.1. TxDOT LSMB Details.



Figure 6.2. TxDOT LSMB prior to Testing.

CHAPTER 7. TEST REQUIREMENTS AND EVALUATION CRITERIA

7.1 CRASH TEST PERFORMED/MATRIX

Table 7.1 shows the test conditions and evaluation criteria for *MASH* TL-4 for longitudinal barriers.

Table 7.1. Test Conditions and Evaluation Criteria Specified for *MASH* TL-4 Longitudinal Barriers.

Test Article	Test Designation	Test Vehicle	Impact Conditions		Evaluation Criteria
			Speed	Angle	
Longitudinal Barrier	4-10	1100C	62 mi/h	25°	A, D, F, H, I
	4-11	2270P	62 mi/h	25°	A, D, F, H, I
	4-12	10000S	56 mi/h	15°	A, D, G

The researchers selected CIPs for the *MASH* testing by determining the location that maximizes pocketing and snagging of the vehicle against the tested system (test designations 4-10 and 4-11) and maximizes the potential for failure of the concrete barrier (test designation 4-12). *MASH* provides information for the determination of the CIPs for rigid and temporary barrier tests. Figure 7.1 through Figure 7.3 show the target CIP for *MASH* Tests 4-10, 4-11, and 4-12 on the TxDOT LSMB.

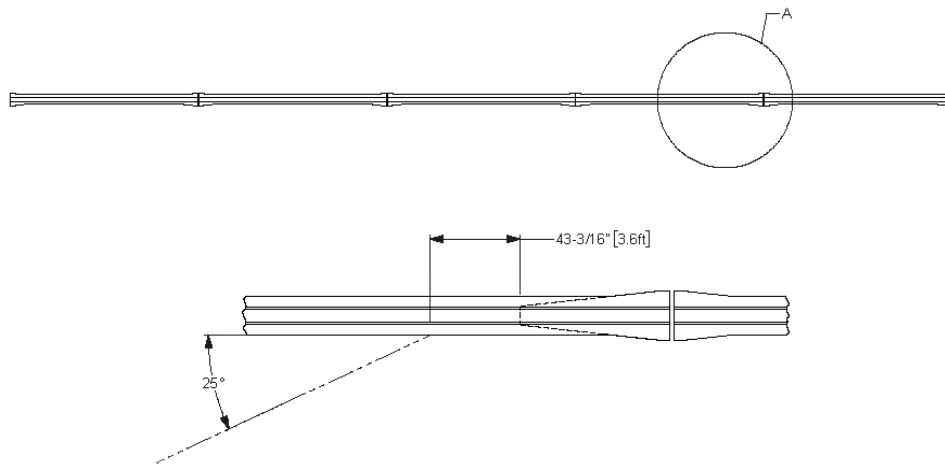


Figure 7.1. Target CIP for *MASH* Test 4-10 on TxDOT LSMB.

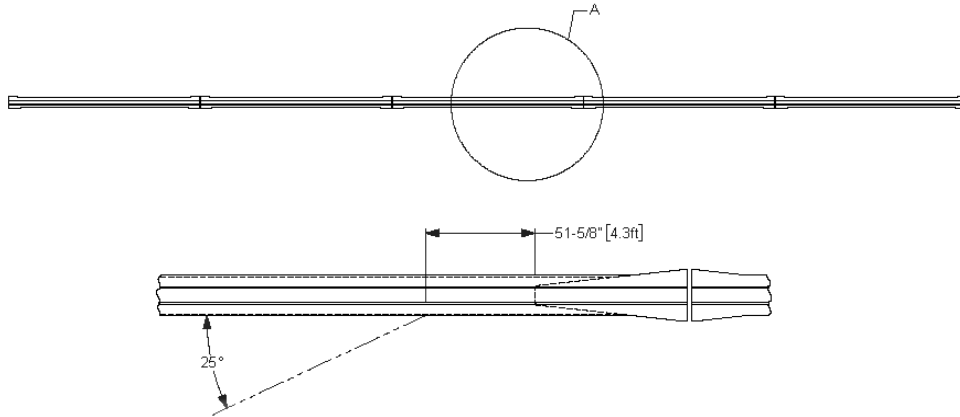


Figure 7.2. Target CIP for MASH Test 4-11 on TxDOT LSMB.

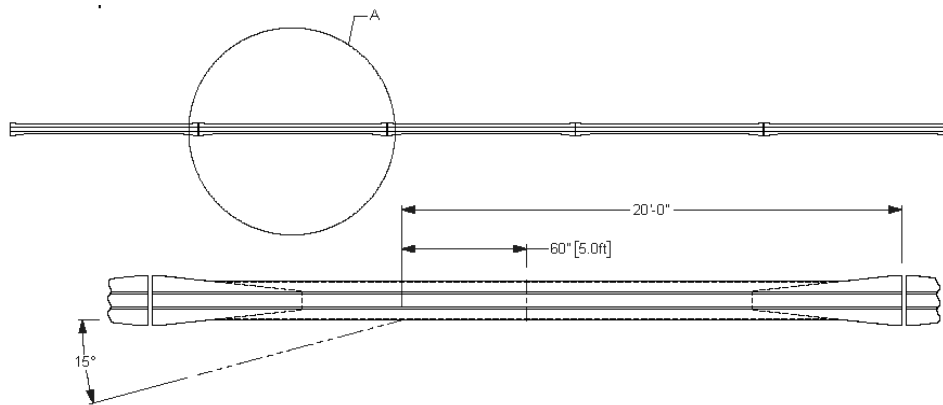


Figure 7.3. Target CIP for MASH Test 4-12 on TxDOT LSMB.

The crash tests and data analysis procedures were in accordance with guidelines presented in *MASH*. Chapter 4 presents brief descriptions of these procedures.

7.2 EVALUATION CRITERIA

The appropriate safety evaluation criteria from Tables 2-2 and 5-1 of *MASH* were used to evaluate the crash tests reported herein. Table 7.1 lists the test conditions and evaluation criteria required for *MASH* TL-4, and Table 7.2 provides detailed information on the evaluation criteria. An evaluation of the crash test results is presented in Chapter 12.

Table 7.2. Evaluation Criteria Required for MASH TL-4 Longitudinal Barriers.

Evaluation Factors	Evaluation Criteria	MASH Test
Structural Adequacy	A. <i>Test article should contain and redirect the vehicle or bring the vehicle to a controlled stop; the vehicle should not penetrate, underide, or override the installation although controlled lateral deflection of the test article is acceptable.</i>	10, 11, 12
Occupant Risk	D. <i>Detached elements, fragments, or other debris from the test article should not penetrate or show potential for penetrating the occupant compartment, or present undue hazard to other traffic, pedestrians, or personnel in a work zone. Deformations of, or intrusions into, the occupant compartment should not exceed limits set forth in Section 5.2.2 and Appendix E of MASH.</i>	10, 11, 12
	F. <i>The vehicle should remain upright during and after collision. The maximum roll and pitch angles are not to exceed 75 degrees.</i>	10, 11
	G. <i>It is preferable, although not essential, that the vehicle remain upright during and after the collision.</i>	12
	H. <i>Occupant impact velocities (OIV) should satisfy the following limits: Preferred value of 30 ft/s, or maximum allowable value of 40 ft/s.</i>	10, 11
	I. <i>The occupant ridedown accelerations should satisfy the following: Preferred value of 15.0 g, or maximum allowable value of 20.49 g.</i>	10, 11

CHAPTER 8. TEST CONDITIONS

8.1 TEST FACILITY

The full-scale crash tests reported herein were performed at the TTI Proving Ground, an International Standards Organization (ISO)/International Electrotechnical Commission (IEC) 17025-accredited laboratory with American Association for Laboratory Accreditation (A2LA) Mechanical Testing Certificate 2821.01. The full-scale crash tests were performed according to TTI Proving Ground quality procedures, as well as *MASH* guidelines and standards.

The test facilities of the TTI Proving Ground are located on The Texas A&M University System RELLIS Campus, which consists of a 2000-acre complex of research and training facilities situated 10 mi northwest of the flagship campus of Texas A&M University. The site, formerly a United States Army Air Corps base, has large expanses of concrete runways and parking aprons well suited for experimental research and testing in the areas of vehicle performance and handling, vehicle-roadway interaction, highway pavement durability and efficacy, and roadside safety hardware and perimeter protective device evaluation. The site selected for construction and testing of the TxDOT LSMB was along the edge of an out-of-service apron. The apron consists of an unreinforced jointed-concrete pavement in 12.5-ft × 15-ft blocks nominally 6 inches deep. The aprons were built in 1942, and the joints have some displacement but are otherwise flat and level.

8.2 VEHICLE TOW AND GUIDANCE SYSTEM

Each vehicle was towed into the test installation using a steel cable guidance and reverse tow system. A steel cable for guiding the test vehicle was tensioned along the path, anchored at each end, and threaded through an attachment to the front wheel of the test vehicle. An additional steel cable was connected to the test vehicle, passed around a pulley near the impact point and through a pulley on the tow vehicle, and then anchored to the ground such that the tow vehicle moved away from the test site. A 2:1 speed ratio between the test and tow vehicle existed with this system. Just prior to impact with the installation, the test vehicle was released and ran unrestrained. The vehicle remained freewheeling (i.e., no steering or braking inputs) until it cleared the immediate area of the test site.

8.3 DATA ACQUISITION SYSTEMS

8.3.1 Vehicle Instrumentation and Data Processing

Each test vehicle was instrumented with a self-contained onboard data acquisition system. The signal conditioning and acquisition system is a 16-channel Tiny Data Acquisition System (TDAS) Pro produced by Diversified Technical Systems Inc. The accelerometers, which measure the x, y, and z axes of vehicle acceleration, are strain gauge type with linear millivolt output proportional to acceleration. Angular rate sensors, measuring vehicle roll, pitch, and yaw rates, are ultra-small, solid-state units designed for crash test service. The TDAS Pro hardware and software conform to the latest SAE J211, Instrumentation for Impact Test. Each of the 16 channels is capable of providing precision amplification, scaling, and filtering based on transducer specifications and calibrations. During the test, data are recorded from each channel at a rate of 10,000 samples per second with a resolution of one part in 65,536. Once data are

recorded, internal batteries back them up inside the unit in case the primary battery cable is severed. Initial contact of the pressure switch on the vehicle bumper provides a time zero mark and initiates the recording process. After each test, the data are downloaded from the TDAS Pro unit into a laptop computer at the test site. The TRAP software then processes the raw data to produce detailed reports of the test results.

Each of the TDAS Pro units is returned to the factory annually for complete recalibration and to ensure that all instrumentation used in the vehicle conforms to the specifications outlined by SAE J211. All accelerometers are calibrated annually by means of an ENDEVCO® 2901 precision primary vibration standard. This standard and its support instruments are checked annually and receive a National Institute of Standards Technology (NIST) traceable calibration. The rate transducers used in the data acquisition system receive calibration via a Genisco Rate-of-Turn table. The subsystems of each data channel are also evaluated annually, using instruments with current NIST traceability, and the results are factored into the accuracy of the total data channel per SAE J211. Calibrations and evaluations are also made anytime data are suspect. Acceleration data are measured with an expanded uncertainty of ± 1.7 percent at a confidence factor of 95 percent ($k = 2$).

TRAP uses the data from the TDAS Pro to compute the occupant/compartiment impact velocities, time of occupant/compartiment impact after vehicle impact, and highest 10-millisecond (ms) average ridedown acceleration. TRAP calculates change in vehicle velocity at the end of a given impulse period. In addition, maximum average accelerations over 50-ms intervals in each of the three directions are computed. For reporting purposes, the data from the vehicle-mounted accelerometers are filtered with an SAE Class 180-Hz low-pass digital filter, and acceleration versus time curves for the longitudinal, lateral, and vertical directions are plotted using TRAP.

TRAP uses the data from the yaw, pitch, and roll rate transducers to compute angular displacement in degrees at 0.0001-s intervals, and then plots yaw, pitch, and roll versus time. These displacements are in reference to the vehicle-fixed coordinate system with the initial position and orientation being initial impact. Rate of rotation data is measured with an expanded uncertainty of ± 0.7 percent at a confidence factor of 95 percent ($k = 2$).

8.3.2 Anthropomorphic Dummy Instrumentation

An Alderson Research Laboratories Hybrid II, 50th percentile male anthropomorphic dummy, restrained with lap and shoulder belts, was placed in the front seat on the impact side of the 1100C vehicle. The dummy was not instrumented.

According to *MASH*, use of a dummy in the 2270P vehicle is optional. However, *MASH* recommends that a dummy be used when testing “any longitudinal barrier with a height greater than or equal to 33 inches.” More specifically, use of the dummy in the 2270P vehicle is recommended for tall rails to evaluate the “potential for an occupant to extend out of the vehicle and come into direct contact with the test article.” Although this information is reported, it is not part of the impact performance evaluation. Since the rail height of the TxDOT LSMB was 42 inches, a dummy was placed in the front seat of the 2270P vehicle on the impact side and restrained with lap and shoulder belts.

MASH does not recommend or require use of a dummy in the 10000S vehicle, and no dummy was placed in the vehicle.

8.3.3 Photographic Instrumentation Data Processing

Photographic coverage of each test included three digital high-speed cameras:

- One overhead with a field of view perpendicular to the ground and directly over the impact point.
- One placed upstream from the installation at an angle to have a field of view of the interaction of the rear of the vehicle with the installation.
- A third placed with a field of view parallel to and aligned with the installation at the downstream end.

A flashbulb on the impacting vehicle was activated by a pressure-sensitive tape switch to indicate the instant of contact with the TxDOT LSMB. The flashbulb was visible from each camera. The video files from these digital high-speed cameras were analyzed to observe phenomena occurring during the collision and to obtain time-event, displacement, and angular data. A digital camera recorded and documented conditions of each test vehicle and the installation before and after the test.

CHAPTER 9. MASH TEST 4-10 (CRASH TEST NO. 469760-06-1)

9.1 TEST DESIGNATION AND ACTUAL IMPACT CONDITIONS

MASH Test 4-10 involves an 1100C vehicle weighing $2420 \text{ lb} \pm 55 \text{ lb}$ impacting the CIP of the longitudinal barrier at an impact speed of $62 \text{ mi/h} \pm 2.5 \text{ mi/h}$ and an angle of $25 \text{ degrees} \pm 1.5 \text{ degrees}$. The CIP for MASH Test 4-10 on the TxDOT LSMB was $3.6 \text{ ft} \pm 1 \text{ ft}$ upstream of the downstream scupper edge of Barrier 4. Figure 7.1 and Figure 9.1 depict the target impact setup (IS).



Figure 9.1. TxDOT LSMB/Test Vehicle Geometrics for Test No. 469760-06-1.

The 1100C vehicle weighed 2449 lb, and the actual impact speed and angle were 64.4 mi/h and 25.0 degrees. The actual impact point was 3.6 ft upstream of the downstream scupper edge of Barrier 4. Minimum target IS was 51 kip-ft, and actual IS was 61 kip-ft.

9.2 WEATHER CONDITIONS

The test was performed on the afternoon of June 8, 2020. Weather conditions at the time of testing were as follows: wind speed: 5 mi/h; wind direction: 227 degrees (vehicle was traveling at a heading of 100 degrees); temperature: 93°F; relative humidity: 56 percent.

9.3 TEST VEHICLE

Figure 9.2 shows the 2015 Nissan Versa used for the crash test. The vehicle's test inertia weight was 2449 lb, and its gross static weight was 2614 lb. The height to the lower edge of the vehicle bumper was 7.0 inches, and the height to the upper edge of the bumper was 22.25 inches. Table C.1 in Appendix C.1 gives additional dimensions and information on the vehicle. The vehicle was directed into the installation using a cable reverse tow and guidance system, and was released to be freewheeling and unrestrained just prior to impact.



Figure 9.2. Test Vehicle before Test No. 469760-06-1.

9.4 TEST DESCRIPTION

Table 9.1 lists events that occurred during Test No. 469760-06-1. Figures C.1 and C.2 in Appendix C.2 present sequential photographs during the test.

Table 9.1. Events during Test No. 469760-06-1.

Time (s)	Events
0.000	Vehicle impacts barrier
0.028	Vehicle begins to redirect
0.082	Right rear tire lifts off pavement
0.161	Right front tire lifts off pavement
0.218	Vehicle travels parallel with barrier
0.262	Rear left corner of vehicle contacts barrier
0.394	Vehicle loses contact with barrier while traveling at 44.4 mi/h, a trajectory of 6.1 degrees, and a heading of 16.4 degrees
0.711	Left rear tire contacts pavement

For longitudinal barriers, it is desirable for the vehicle to redirect and exit the barrier within the exit box criteria (not less than 32.8 ft downstream from loss of contact for cars and pickups). The test vehicle exited within the exit box criteria defined in *MASH*. After loss of contact with the barrier, the vehicle came to rest 156 ft downstream of the point of impact and 44 ft toward traffic lanes.

9.5 DAMAGE TO TEST INSTALLATION

Figure 9.3 shows the damage to the TxDOT LSMB. There was slight gouging in the concrete and paint scuffing on the traffic side of the barrier. There were tire marks 3.5 inches on the upstream face of the downstream barrier scupper post. The soil around the scupper post at the downstream end of Barrier 4 was disturbed. Working width* was 25.2 inches, and height of

* Per *MASH*, “The working width is the maximum dynamic lateral position of any major part of the system or vehicle. These measurements are all relative to the pre-impact traffic face of the test article.” In other words,

working width was at the toe of the barrier. Maximum dynamic deflection during the test was 1.8 inches, and maximum permanent deformation was 0.4 inches.



Figure 9.3. TxDOT LSMB after Test No. 469760-06-1.

9.6 DAMAGE TO TEST VEHICLE

Figure 9.4 shows the damage sustained by the vehicle. The front bumper, hood, left front fender, left front strut and strut tower, left front tire and rim, left front lower control arm, left A-post, left front floor pan, left front door, left rear door, and left rear quarter panel were damaged. The roof was deformed at the B-post, and the windshield was cracked upward and inward of the left A-post. No fuel tank damage was observed. Maximum exterior crush to the vehicle was 11.0 inches in the side plane at the left front corner at bumper height. Maximum occupant compartment deformation was 4.5 inches in the left kick panel area and 1.0 inch in the left front firewall. Figure 9.5 shows the interior of the vehicle. Tables C.2 and C.3 in Appendix C.1 provide exterior crush and occupant compartment measurements.

working width is the total barrier width plus the maximum dynamic intrusion of any portion of the barrier or test vehicle past the field side edge of the barrier.



Figure 9.4. Test Vehicle after Test No. 469760-06-1.



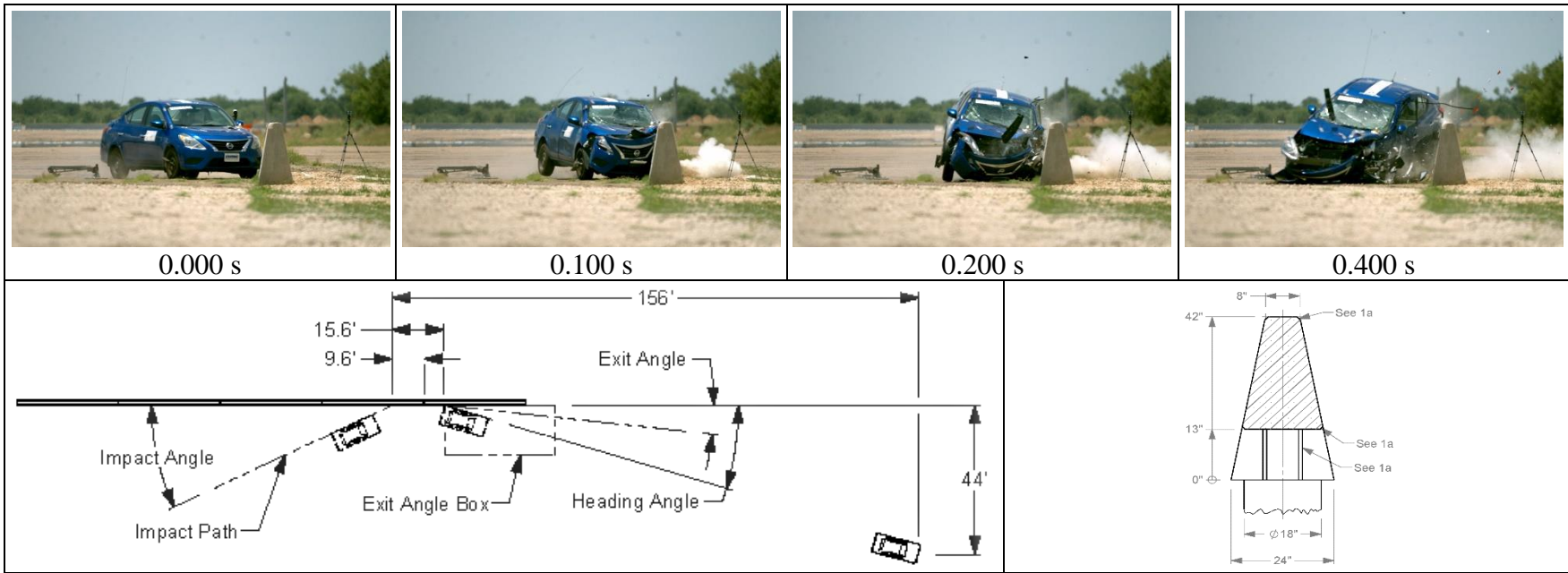
Figure 9.5. Interior of Test Vehicle after Test No. 469760-06-1.

9.7 OCCUPANT RISK FACTORS

Data from the accelerometers were digitized for evaluation of occupant risk, and the results are shown in Table 9.2. Figure C.3 in Appendix C.3 shows the vehicle angular displacements, and Figures C.4 through C.6 in Appendix C.4 show acceleration versus time traces. Figure 9.6 summarizes pertinent information from the test.

Table 9.2. Occupant Risk Factors for Test No. 469760-06-1.

Occupant Risk Factor	Value	Time
OIV		
Longitudinal	27.9 ft/s	at 0.0807 s on left side of interior
Lateral	30.2 ft/s	
Occupant Ridedown Accelerations		
Longitudinal	6.6 g	0.0858–0.0958 s
Lateral	6.0 g	0.0834–0.0934 s
THIV	12.4 m/s	at 0.0790 s on left side of interior
ASI	2.5	0.0500–0.1000 s
Maximum 50-ms Moving Average		
Longitudinal	-16.2 g	0.0276–0.0776 s
Lateral	17.6 g	0.0243–0.0743 s
Vertical	-2.5 g	0.0496–0.0996 s
Maximum Yaw, Pitch, and Roll Angles		
Roll	11°	0.3645 s
Pitch	10°	0.4738 s
Yaw	78°	1.7101 s



General Information

Test Agency Texas A&M Transportation Institute (TTI)
 Test Standard Test No. MASH Test 4-10
 TTI Test No. 469760-06-1
 Test Date 2020-06-08

Test Article

Type Longitudinal Barrier—Median Barrier
 Name TL-4 Barrier for Flood-Prone Areas
 Installation Length 150 ft 8 inches
 Material or Key Elements ... 30-ft-long single-slope concrete barrier with 13-inch x 18-ft scuppers

Soil Type and Condition

Concrete surface, dry

Test Vehicle

Type/Designation 1100C
 Make and Model 2015 Nissan Versa
 Curb 2434 lb
 Test Inertial 2449 lb
 Dummy 165 lb
 Gross Static 2614 lb

Impact Conditions

Speed 64.4 mi/h
 Angle 25.0°
 Location/Orientation 9.6 ft upstream of joint 4–5

Impact Severity

61 kip-ft

Exit Conditions

Speed 44.4 mi/h
 Trajectory/Heading Angle... 6.1°/16.4°

Occupant Risk Values

Longitudinal OIV 27.9 ft/s
 Lateral OIV 30.2 ft/s
 Longitudinal Ridedown 6.6 g
 Lateral Ridedown 6.0 g
 THIV 12.4 m/s
 ASI 2.5

Max. 0.050-s Average

Longitudinal -16.2 g
 Lateral 17.6 g
 Vertical -2.5g

Post-Impact Trajectory

Stopping Distance 156 ft downstream
 44 ft twd traffic lanes

Vehicle Stability

Maximum Roll Angle 11°
 Maximum Pitch Angle 10°
 Maximum Yaw Angle 78°
 Vehicle Snagging No
 Vehicle Pocketing No

Test Article Deflections

Dynamic 1.8 inches
 Permanent 0.4 inches
 Working Width 25.2 inches
 Height of Working Width At toe of barrier

Vehicle Damage

VDS 11LFQ4
 CDC 11FLEW3
 Max. Exterior Deformation 11.0 inches
 OCDI FL0010000
 Max. Occupant Compartment Deformation 4.5 inches

Figure 9.6. Summary of Results for MASH Test 4-10 on TxDOT LSMB.

CHAPTER 10. MASH TEST 4-11 (CRASH TEST NO. 469760-06-2)

10.1 TEST DESIGNATION AND ACTUAL IMPACT CONDITIONS

MASH Test 4-11 involves a 2270P vehicle weighing 5000 lb \pm 110 lb impacting the CIP of the longitudinal barrier at an impact speed of 62 mi/h \pm 2.5 mi/h and an angle of 25 degrees \pm 1.5 degrees. The CIP for MASH Test 4-11 on the TxDOT LSMB was 4.3 ft \pm 1 ft upstream of the downstream edge of the scupper in Barrier 3. Figure 7.1 and Figure 10.1 depict the target impact setup.



Figure 10.1. TxDOT LSMB/Test Vehicle Geometrics for Test No. 469760-06-2.

The 2270P vehicle weighed 5005 lb, and the actual impact speed and angle were 63.4 mi/h and 25.2 degrees. The actual impact point was 4.6 ft upstream of the downstream edge of the scupper in Barrier 3. Minimum target IS was 106 kip-ft, and actual IS was 122 kip-ft.

10.2 WEATHER CONDITIONS

The test was performed on the morning of June 4, 2020. Weather conditions at the time of testing were as follows: wind speed: 8 mi/h; wind direction: 197 degrees (vehicle was traveling at a heading of 100 degrees); temperature: 83°F; relative humidity: 76 percent.

10.3 TEST VEHICLE

Figure 10.2 shows the 2015 RAM 1500 pickup truck used for the crash test. The vehicle's test inertia weight was 5005 lb, and its gross static weight was 5170 lb. The height to the lower edge of the vehicle bumper was 11.75 inches, and height to the upper edge of the bumper was 27.0 inches. The height to the vehicle's center of gravity was 28.25 inches. Tables D.1 and D.2 in Appendix D.1 give additional dimensions and information on the vehicle. The vehicle was directed into the installation using a cable reverse tow and guidance system, and was released to be freewheeling and unrestrained just prior to impact.



Figure 10.2. Test Vehicle before Test No. 469760-06-2.

10.4 TEST DESCRIPTION

Table 10.1 lists events that occurred during Test No. 469760-06-2. Figures D.1 and D.2 in Appendix D.2 present sequential photographs during the test.

Table 10.1. Events during Test No. 469760-06-2.

Time (s)	Events
0.000	Vehicle impacts barrier
0.027	Left front tire lifts off pavement
0.035	Vehicle begins to redirect
0.102	Right front tire lifts off pavement
0.164	Right rear tire lifts off pavement
0.203	Rear left corner of vehicle impacts top rail
0.204	Vehicle travels parallel with barrier
0.449	Vehicle loses contact with barrier while traveling at 45.1 mi/h, with a trajectory of 4.9 degrees and a heading of 9.0 degrees
0.473	Left front tire makes contact with pavement
0.603	Right front tire contacts pavement

For longitudinal barriers, it is desirable for the vehicle to redirect and exit the barrier within the exit box criteria (not less than 32.8 ft downstream from loss of contact for cars and pickups). The test vehicle exited within the exit box criteria defined in *MASH*. After loss of contact with the barrier, the vehicle came to rest 188 ft downstream of the point of impact and 36 ft toward the field side of the barrier.

10.5 DAMAGE TO TEST INSTALLATION

Figure 10.3 shows the damage to the TxDOT LSMB. The soil was disturbed both upstream and downstream at the site of impact. The slab on the downstream end of Barrier 3 was pushed toward the field side 0.5 inches, and 0.25 inches toward the field side on the upstream end of the barrier. Scuffing was present at impact, and the concrete was gouged at the bottom of

Barrier 3. No rebar was exposed during impact. Working width* was 25.8 inches, and height of working width was at the toe of the barrier. Maximum dynamic deflection during the test was 4.4 inches, and maximum permanent deformation was 0.5 inches.



Figure 10.3. TxDOT LSMB after Test No. 469760-06-2.

* Per *MASH*, “The working width is the maximum dynamic lateral position of any major part of the system or vehicle. These measurements are all relative to the pre-impact traffic face of the test article.” In other words, working width is the total barrier width plus the maximum dynamic intrusion of any portion of the barrier or test vehicle past the field side edge of the barrier.

10.6 DAMAGE TO TEST VEHICLE

Figure 10.4 shows the damage sustained by the vehicle. The front bumper, hood, grill, radiator and support, left front fender, left lower control arm, left front tire and rim, left front door and window glass, left front floor pan, left rear door, left rear cab corner, left exterior bed, and rear bumper were damaged. No fuel tank damage was observed. Maximum exterior crush to the vehicle was 14.0 inches in the front and side planes at the left front corner at bumper height. Maximum occupant compartment deformation was 2.0 inches in the left front floor pan and kick panel area. Figure 10.5 shows the interior of the vehicle. Tables D.3 and D.4 in Appendix D.1 provide exterior crush and occupant compartment measurements.



Figure 10.4. Test Vehicle after Test No. 469760-06-2.

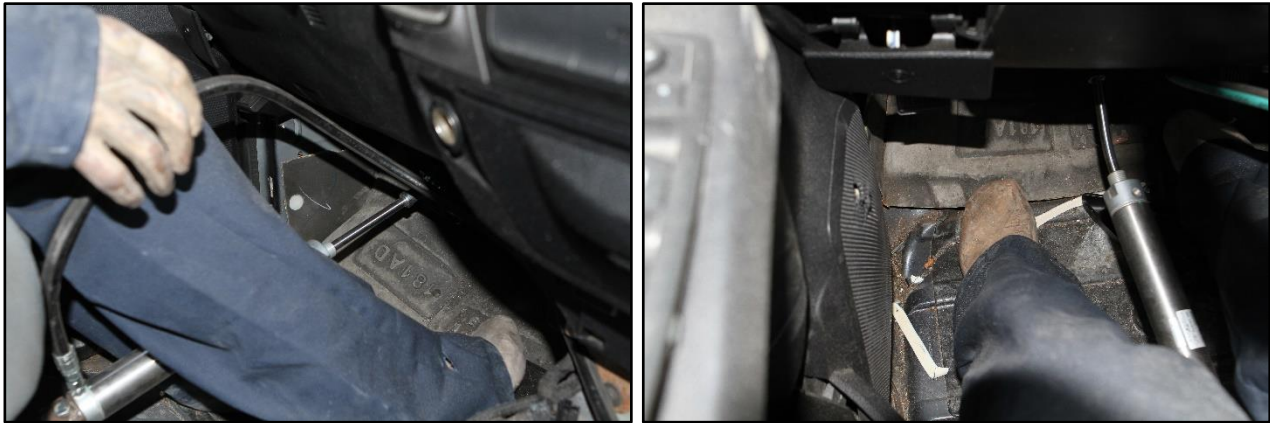


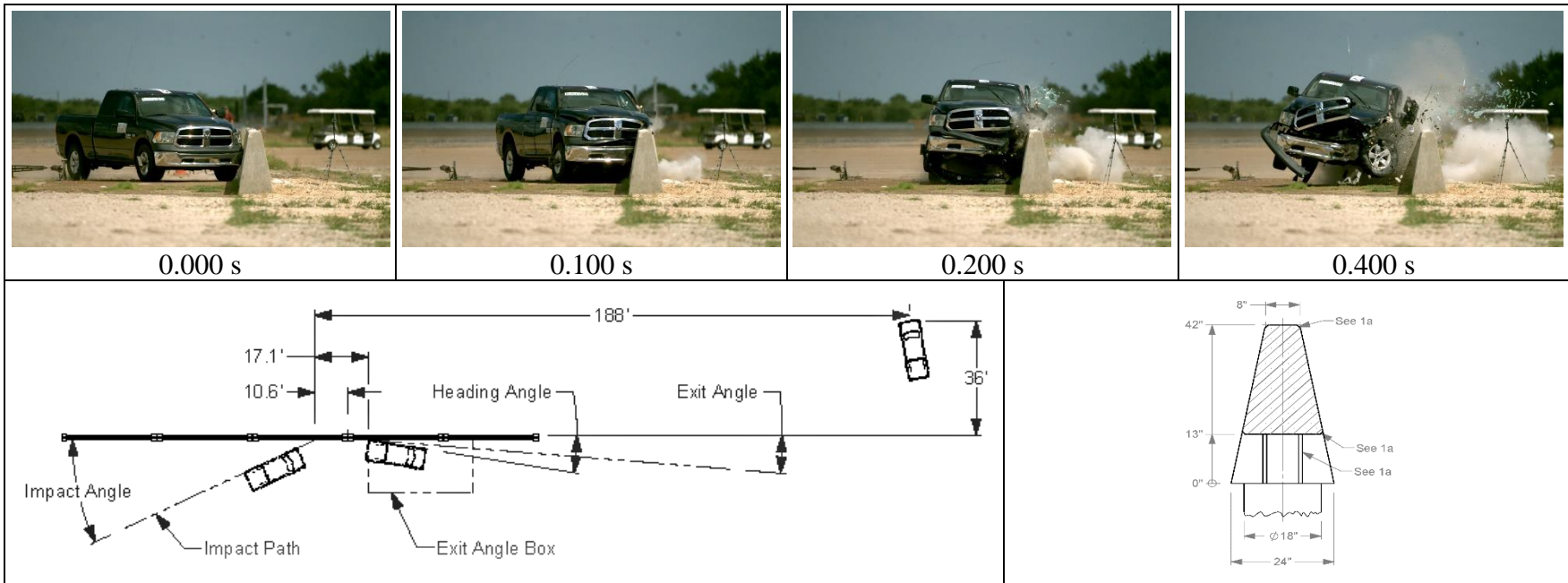
Figure 10.5. Interior of Test Vehicle after Test No. 469760-06-2.

10.7 OCCUPANT RISK FACTORS

Data from the accelerometers were digitized for evaluation of occupant risk, and the results are shown in Table 10.2. Figure D.3 in Appendix D.3 shows the vehicle angular displacements, and Figures D.4 through D.6 in Appendix D.4 show acceleration versus time traces. Figure 10.6 summarizes pertinent information from the test.

Table 10.2. Occupant Risk Factors for Test No. 469760-06-2.

Occupant Risk Factor	Value	Time
OIV		
Longitudinal	18.7 ft/s	at 0.0977 s on left side of interior
Lateral	24.0 ft/s	
Occupant Ridedown Accelerations		
Longitudinal	11.3 g	0.1462–0.1562 s
Lateral	10.7 g	0.2058–0.2158 s
THIV	9.2 m/s	at 0.0948 s on left side of interior
ASI	1.6	0.0525–0.1025 s
Maximum 50-ms Moving Average		
Longitudinal	–8.9 g	0.0196–0.0696 s
Lateral	11.4 g	0.0305–0.0805 s
Vertical	–3.9 g	0.0287–0.0787 s
Maximum Yaw, Pitch, and Roll Angles		
Roll	12°	0.5779 s
Pitch	4°	0.2118 s
Yaw	38°	0.6696 s



General Information

Test Agency..... Texas A&M Transportation Institute (TTI)
 Test Standard Test No. MASH Test 4-11
 TTI Test No. 469760-06-2
 Test Date 2020-06-04

Test Article

Type Longitudinal Barrier—Median Barrier
 Name TL-4 Barrier for Flood-Prone Areas
 Installation Length..... 150 ft 8 inches
 Material or Key Elements ... 30-ft-long single-slope concrete barrier with 13-inch x 18-ft scuppers

Soil Type and Condition

..... Concrete surface, dry

Test Vehicle

Type/Designation 2270P
 Make and Model 2015 RAM 1500 pickup truck
 Curb 4935 lb
 Test Inertial 5005 lb
 Dummy 165 lb
 Gross Static 5170 lb

Impact Conditions

Speed 63.4 mi/h
 Angle 25.2°
 Location/Orientation 10.6 ft upstream of joint 3-4

Impact Severity

..... 122 kip-ft

Exit Conditions

Speed 45.1 mi/h
 Trajectory/Heading Angle... 4.9°/9.0°

Occupant Risk Values

Longitudinal OIV 18.7 ft/s
 Lateral OIV 24.0 ft/s
 Longitudinal Ridedown 11.3 g
 Lateral Ridedown 10.7 g
 THIV 9.2 m/s
 ASI 1.6

Max. 0.050-s Average

Longitudinal -8.9 g
 Lateral 11.4 g
 Vertical -3.9 g

Post-Impact Trajectory

Stopping Distance 188 ft downstream
 36 ft twd field side

Vehicle Stability

Maximum Roll Angle 12°
 Maximum Pitch Angle 4°
 Maximum Yaw Angle 38°
 Vehicle Snagging No
 Vehicle Pocketing No

Test Article Deflections

Dynamic 4.4 inches
 Permanent 0.5 inches
 Working Width 25.8 inches
 Height of Working Width At toe of barrier

Vehicle Damage

VDS 11LFQ4
 CDC 11FLEW3
 Max. Exterior Deformation 14.0 inches
 OCDI FL0010000
 Max. Occupant Compartment Deformation 2.0 inches

Figure 10.6. Summary of Results for MASH Test 4-11 on TxDOT LSMB.

CHAPTER 11. MASH TEST 4-12 (CRASH TEST NO. 469760-06-3)

11.1 TEST DESIGNATION AND ACTUAL IMPACT CONDITIONS

MASH Test 4-12 involves a 10000S vehicle weighing 22,000 lb \pm 660 lb impacting the CIP of the longitudinal barrier at an impact speed of 56 mi/h \pm 2.5 mi/h and an angle of 15 degrees \pm 1.5 degrees. The CIP for *MASH* Test 4-12 on the TxDOT LSMB was 20 ft \pm 1 ft upstream of the center of the joint between Barriers 2 and 3. Figure 7.1 and Figure 11.1 depict the target impact setup.



Figure 11.1. TxDOT LSMB/Test Vehicle Geometrics for Test No. 469760-06-3.

The 10000S vehicle weighed 22,300 lb, and the actual impact speed and angle were 57.6 mi/h and 15.2 degrees. The actual impact point was 20.4 ft upstream of the center of the joint between Barriers 2 and 3. Minimum target IS was 142 kip-ft, and actual IS was 170 kip-ft.

11.2 WEATHER CONDITIONS

The test was performed on the afternoon of June 2, 2020. Weather conditions at the time of testing were as follows: wind speed: 5 mi/h; wind direction: 117 degrees (vehicle was traveling at a heading of 110 degrees); temperature: 90°F; relative humidity: 58 percent.

11.3 TEST VEHICLE

Figure 11.2 shows the 2013 International 4300 SUT used for the crash test. The vehicle's test inertia weight was 22,300 lb, and its gross static weight was 22,300 lb. The height to the lower edge of the vehicle bumper was 18.5 inches, and height to the upper edge of the bumper was 33.5 inches. The height to the center of gravity of the vehicle's ballast was 61.5 inches. Table E.1 in Appendix E.1 gives additional dimensions and information on the vehicle. The vehicle was directed into the installation using a cable reverse tow and guidance system, and was released to be freewheeling and unrestrained just prior to impact.



Figure 11.2. Test Vehicle before Test No. 469760-06-3.

11.4 TEST DESCRIPTION

Table 11.1 lists events that occurred during Test No. 469760-06-3. Figures E.1 and E.2 in Appendix E.2 present sequential photographs during the test.

Table 11.1. Events during Test No. 469760-06-3.

Time (s)	Events
0.000	Vehicle contacts barrier
0.014	Left front tire leaves pavement
0.043	Vehicle begins to redirect
0.104	Front lower right corner of box contacts top barrier
0.128	Right front tire leaves the pavement
0.262	Right lower rear corner of box nicks the top of barrier
0.269	Right rear tire leaves the pavement
0.348	Vehicle travels parallel with barrier
0.707	Right front tire contacts pavement

For longitudinal barriers, it is desirable for the vehicle to redirect and exit the barrier within the exit box criteria (not less than 65.6 ft for heavy vehicles). The test vehicle exited within the exit box criteria defined in *MASH*. Brakes on the vehicle were applied at 2.5 s after impact. After loss of contact with the barrier, the vehicle came to rest 243 ft downstream of the point of impact and 24 ft toward the field side of the median barrier.

11.5 DAMAGE TO TEST INSTALLATION

Figure 11.3 through Figure 11.5 show the damage to the TxDOT LSMB. The base of the barrier on both the upstream and downstream ends of Barrier 2 shifted 1.0 inch toward the field side, and the center of Barrier 2 had a permanent deflection of 3.6 inches. Gouging of the concrete was present along the traffic side of Barrier 2, and there was a stress crack along the field side of the barrier running vertically from the top of the barrier to the bottom. Gouging was also present on the traffic face of the upstream end of Barrier 3 and on Barrier 4 at the top of the traffic-side scupper, deep enough to expose rebar. There was scuffing on Barriers 3, 4, and 5 due

to contact with the vehicle. Working width* was 54.5 inches, and height of working width was 136.1 inches. Maximum dynamic deflection during the test was 9.5 inches, and maximum permanent deformation was 3.6 inches.



Figure 11.3. TxDOT LSMB after Test No. 469760-06-3.

* Per *MASH*, “The working width is the maximum dynamic lateral position of any major part of the system or vehicle. These measurements are all relative to the pre-impact traffic face of the test article.” In other words, working width is the total barrier width plus the maximum dynamic intrusion of any portion of the barrier or test vehicle past the field side edge of the barrier.



Figure 11.4. Movement of Barrier after Test No. 469760-06-3.



Figure 11.5. Field Side of Barrier after Test No. 469760-06-3.

11.6 DAMAGE TO TEST VEHICLE

Figure 11.6 shows the damage sustained by the vehicle. The front bumper, left front spring assembly and U-bolts, left front shock, pitman arm, left front corner of the floor pan, left

front tire and rim, left door, left rear cab corner, left battery box, left side steps and air tank, left lower edge of box, left rear outer tire and rim, and right upper edge of the box were damaged. No damage to the fuel tank was observed. Maximum exterior crush to the vehicle was 16.0 inches in the side plane at the left front corner at bumper height. Maximum occupant compartment deformation was 3.75 inches in the left front corner of the floor pan. Figure 11.7 shows the interior of the vehicle.



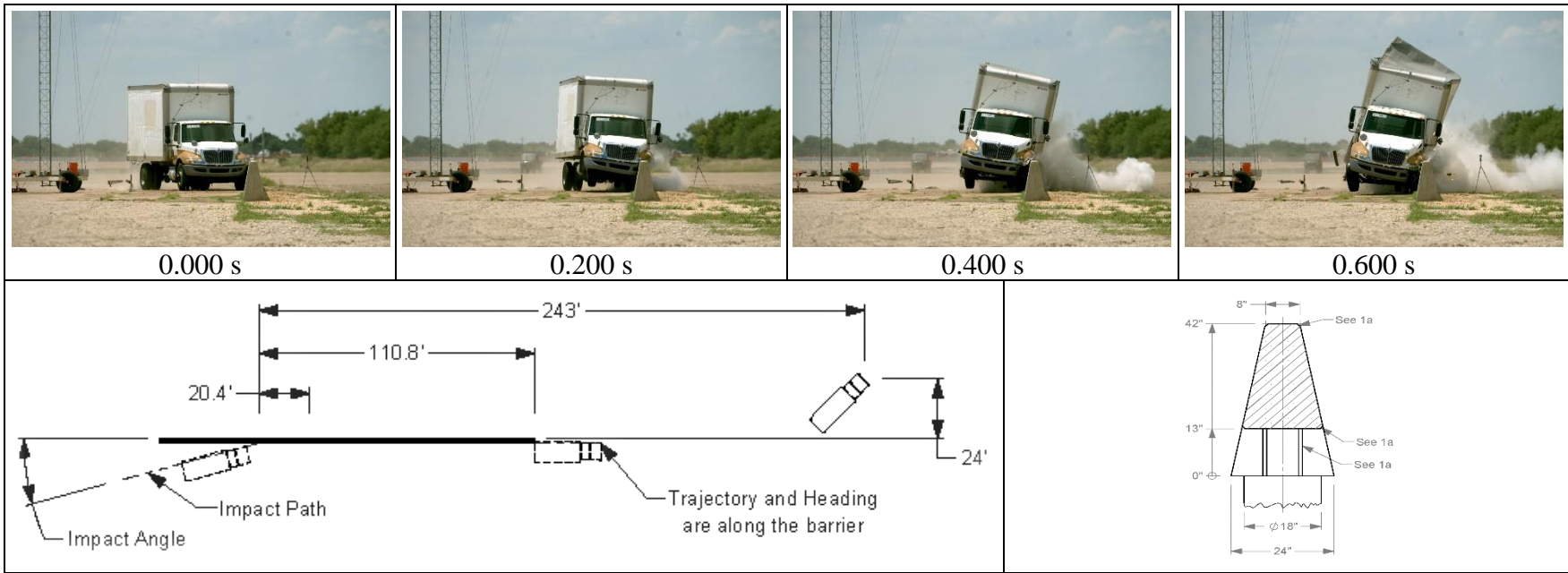
Figure 11.6. Test Vehicle after Test No. 469760-06-3.



Figure 11.7. Interior of Test Vehicle after Test No. 469760-06-3.

11.7 VEHICLE INSTRUMENTATION

Data from the accelerometers were digitized for informational purposes only and are reported in Figure 11.8. Figure E.3 in Appendix E.3 shows the vehicle angular displacements, and Figures E.4 through E.9 in Appendix E.4 show acceleration versus time traces. Figure 11.8 summarizes pertinent information from the test.



General Information

Test Agency Texas A&M Transportation Institute (TTI)
 Test Standard Test No. MASH Test 4-12
 TTI Test No. 469760-06-3
 Test Date 2020-06-02

Test Article

Type Longitudinal Barrier—Median Barrier
 Name TL-4 Barrier for Flood-Prone Areas
 Installation Length 150 ft 8 inches
 Material or Key Elements ... 30-ft-long single-slope concrete barrier with 13-inch x 18-ft scuppers

Soil Type and Condition

Concrete surface, dry

Test Vehicle

Type/Designation 10000S
 Make and Model 2013 International 4300 SUT
 Curb 14,150 lb
 Test Inertial 22,300 lb
 Dummy No Dummy
 Gross Static 22,300 lb

Impact Conditions

Speed 57.6 mi/h
 Angle 15.2°
 Location/Orientation 20.4 ft upstream of joint 2–3

Impact Severity

170 kip-ft

Exit Conditions

Speed Cannot determine
 Trajectory/Heading Angle... Along barrier

Occupant Risk Values

Longitudinal OIV 7.5 ft/s
 Lateral OIV 10.8 ft/s
 Longitudinal Ridedown 2.6 g
 Lateral Ridedown 4.2 g
 THIV 4.0 m/s
 ASI 0.4
 Max. 0.050-s Average
 Longitudinal -1.6 g
 Lateral 2.8 g
 Vertical -2.5 g

Post-Impact Trajectory

Stopping Distance 243 ft downstream
 24 ft twd field side

Vehicle Stability

Maximum Roll Angle 17°
 Maximum Pitch Angle 9°
 Maximum Yaw Angle 18°
 Vehicle Snagging No
 Vehicle Pocketing No

Test Article Deflections

Dynamic 9.5 inches
 Permanent 3.6 inches
 Working Width 54.5 inches
 Height of Working Width 136.1 inches

Vehicle Damage

VDS Not Applicable
 CDC 11FLEW5
 Max. Exterior Deformation 16.0 inches
 OCDI Not Applicable
 Max. Occupant Compartment Deformation 3.75 inches

Figure 11.8. Summary of Results for MASH Test 4-12 on TxDOT LSMB.

CHAPTER 12. SUMMARY AND CONCLUSIONS

12.1 ASSESSMENT OF TEST RESULTS

The crash tests reported herein were performed in accordance with *MASH* TL-4, which involves three tests, on the TxDOT LSMB. Table 12.1 through Table 12.3 provide an assessment of each test based on the applicable safety evaluation criteria for *MASH* TL-4 longitudinal barriers.

12.2 CONCLUSIONS

Table 12.4 shows that the TxDOT LSMB met the performance criteria for *MASH* TL-4 longitudinal barriers.

Table 12.1. Performance Evaluation Summary for MASH Test 4-10 on TxDOT LSMB.

Test Agency: Texas A&M Transportation Institute

Test No.: 469760-06-1

Test Date: 2020-06-08

MASH Test 4-10 Evaluation Criteria	Test Results	Assessment
<p><u>Structural Adequacy</u></p> <p>A. <i>Test article should contain and redirect the vehicle or bring the vehicle to a controlled stop; the vehicle should not penetrate, underride, or override the installation although controlled lateral deflection of the test article is acceptable.</i></p>	The TxDOT LSMB contained and redirected the 1100C vehicle. The vehicle did not penetrate, underride, or override the installation. Maximum dynamic deflection during the test was 1.8 inches.	Pass
<p><u>Occupant Risk</u></p> <p>D. <i>Detached elements, fragments, or other debris from the test article should not penetrate or show potential for penetrating the occupant compartment, or present an undue hazard to other traffic, pedestrians, or personnel in a work zone.</i></p> <p><i>Deformations of, or intrusions into, the occupant compartment should not exceed limits set forth in Section 5.2.2 and Appendix E of MASH.</i></p>	<p>No detached elements, fragments, or other debris from the barrier were present to penetrate or show potential for penetrating the occupant compartment, or present hazard to others in the area.</p> <p>Maximum occupant compartment deformation was 4.5 inches in the left kick panel area and 1.0 inch in the left front firewall.</p>	Pass
<p>F. <i>The vehicle should remain upright during and after collision. The maximum roll and pitch angles are not to exceed 75 degrees.</i></p>	The 1100C vehicle remained upright during and after the collision event. Maximum roll and pitch angles were 11° and 10°.	Pass
<p>H. <i>Occupant impact velocities (OIV) should satisfy the following limits: Preferred value of 30 ft/s, or maximum allowable value of 40 ft/s.</i></p>	Longitudinal OIV was 27.9 ft/s, and lateral OIV was 30.2 ft/s.	Pass
<p>I. <i>The occupant ridedown accelerations should satisfy the following limits: Preferred value of 15.0 g, or maximum allowable value of 20.49 g.</i></p>	Longitudinal occupant ridedown acceleration was 6.6 g, and lateral occupant ridedown acceleration was 6.0 g.	Pass

Table 12.2. Performance Evaluation Summary for MASH Test 4-11 on TxDOT LSMB.

Test Agency: Texas A&M Transportation Institute

Test No.: 469760-06-2

Test Date: 2020-06-04

MASH Test 4-11 Evaluation Criteria	Test Results	Assessment
<u>Structural Adequacy</u>		
A. <i>Test article should contain and redirect the vehicle or bring the vehicle to a controlled stop; the vehicle should not penetrate, underride, or override the installation although controlled lateral deflection of the test article is acceptable.</i>	The TxDOT LSMB contained and redirected the 2270P vehicle. The vehicle did not penetrate, underride, or override the installation. Maximum dynamic deflection during the test was 4.4 inches.	Pass
<u>Occupant Risk</u>		
D. <i>Detached elements, fragments, or other debris from the test article should not penetrate or show potential for penetrating the occupant compartment, or present an undue hazard to other traffic, pedestrians, or personnel in a work zone.</i>	No detached elements, fragments, or other debris from the barrier were present to penetrate or show potential for penetrating the occupant compartment, or present hazard to others in the area.	Pass
<i>Deformations of, or intrusions into, the occupant compartment should not exceed limits set forth in Section 5.2.2 and Appendix E of MASH.</i>	Maximum occupant compartment deformation was 2.0 inches in the left front floor pan.	
F. <i>The vehicle should remain upright during and after collision. The maximum roll and pitch angles are not to exceed 75 degrees.</i>	The 2270P vehicle remained upright during and after the collision event. Maximum roll and pitch angles were 12° and 4°.	Pass
H. <i>Occupant impact velocities (OIV) should satisfy the following limits: Preferred value of 30 ft/s, or maximum allowable value of 40 ft/s.</i>	Longitudinal OIV was 18.7 ft/s, and lateral OIV was 24.0 ft/s.	Pass
I. <i>The occupant ridedown accelerations should satisfy the following limits: Preferred value of 15.0 g, or maximum allowable value of 20.49 g.</i>	Longitudinal occupant ridedown acceleration was 11.3 g, and lateral occupant ridedown acceleration was 10.7 g.	Pass

Table 12.3. Performance Evaluation Summary for MASH Test 4-12 on TxDOT LSMB.

Test Agency: Texas A&M Transportation Institute

Test No.: 469760-06-3

Test Date: 2020-06-02

MASH Test 4-12 Evaluation Criteria	Test Results	Assessment
<p><u>Structural Adequacy</u></p> <p>A. <i>Test article should contain and redirect the vehicle or bring the vehicle to a controlled stop; the vehicle should not penetrate, underride, or override the installation although controlled lateral deflection of the test article is acceptable.</i></p>	The TxDOT LSMB contained and redirected the 10000S vehicle. The vehicle did not penetrate, underride, or override the installation. Maximum dynamic deflection during the test was 9.5 inches.	Pass
<p><u>Occupant Risk</u></p> <p>D. <i>Detached elements, fragments, or other debris from the test article should not penetrate or show potential for penetrating the occupant compartment, or present an undue hazard to other traffic, pedestrians, or personnel in a work zone.</i></p> <p><i>Deformations of, or intrusions into, the occupant compartment should not exceed limits set forth in Section 5.2.2 and Appendix E of MASH.</i></p>	<p>No detached elements, fragments, or other debris from the barrier were present to penetrate or show potential for penetrating the occupant compartment, or present hazard to others in the area.</p> <p>Maximum occupant compartment deformation was 3.75 inches in the left front corner of the floor pan.</p>	Pass
<p>G. <i>It is preferable, although not essential, that the vehicle remain upright during and after collision.</i></p>	The 10000S vehicle remained upright during and after the collision event. Maximum roll and pitch angles were 17° and 9°.	Pass

Table 12.4. Assessment Summary for MASH TL-4 Tests on TxDOT LSMB.

Evaluation Factors	Evaluation Criteria	Test No. 469760-06-1	Test No. 469760-06-2	Test No. 469760-06-3
Structural Adequacy	A	S	S	S
Occupant Risk	D	S	S	S
	F	S	S	N/A
	G	N/A	N/A	S
	H	S	S	N/A
	I	S	S	N/A
	Test No.	<i>MASH Test 4-10</i>	<i>MASH Test 4-11</i>	<i>MASH Test 4-12</i>
	Pass/Fail	Pass	Pass	Pass

Note: S = Satisfactory; N/A = Not Applicable.

CHAPTER 13. IMPLEMENTATION*

The LSMB is a median barrier designed to mitigate roadway flooding while also providing crashworthy cross-median protection. The barrier is a modified version of the TxDOT 42-inch-tall SSCB. The large scuppers located at the bottom of the barrier allow water to traverse across the roadway instead of being dammed on one side as it would by a traditional SSCB. An added benefit is that the large scuppers also allow small wildlife to easily traverse the roadway instead of being blocked by a solid concrete barrier.

The full *MASH* TL-4 matrix was successfully performed on the LSMB. The full-scale crash tests included *MASH* test designations 4-10 (small passenger car), 4-11 (pickup truck), and 4-12 (single-unit truck). Therefore, the LSMB is considered *MASH* TL-4 compliant. Implementation of this median barrier can be achieved by the Design Division through its respective standard sheets.

While the TxDOT LSMB was crash tested with 30-ft-long independent segments, installations with longer segment lengths are considered a *MASH*-compliant alternative. Longer segment lengths may be the more common installation condition, but the shortened 30-ft segment length was viewed as the more critical case for three reasons. First, the 30-ft segment length would maximize barrier movement as opposed to a much longer segment, which would consequently increase the likelihood of vehicle instability. Second, a shorter segment length would increase the possibility of snagging on the joint opening between barriers. Last, the shorter segment lengths would also prevent the contribution of adjoining segment lengths to the structural adequacy of the barrier. In this 30-ft-long condition, the individual impacted segment resisted the full impact load of the tests. If the barrier were installed with longer segment lengths, the adjoining segments would contribute to the structural resistance of the system, and the increased weight would decrease the amount of barrier movement. Consequently, longer segment lengths of the TxDOT LSMB are considered *MASH*-compliant alternatives.

The barrier segments described herein are defined as the length from one joint in the concrete barrier to the subsequent joint. An increase in installation length would equate to a repetition of the 30-ft barrier sections until the desired installation length is achieved or an expansion joint is required. Regardless of the number of sections installed within one segment, the span length from one post to the subsequent post remains the same. The researchers have designed appropriate details for longer segment lengths according to the AASHTO *Load and Resistance Factor Design (LRFD) Bridge Design Specifications (37)*, and they are considered to be *MASH*-compliant alternatives to the tested 30-ft segments. These details can be found in Appendix F.

The TxDOT LSMB was crash tested with 18-inch-diameter, 6-ft-deep drilled shaft foundations anchoring each end of the 30-ft-long barrier segments. The drilled shaft foundations, which are typically used for roadways with flexible pavement, were considered a critical case as opposed to anchoring the barrier to concrete pavement with either cast-in-place or epoxy rebar anchors. The drilled shafts provided only two discrete connections for the barrier anchorage, and the researchers believed the small size of the drilled shafts required evaluation of their structural adequacy through full-scale testing. The cast-in-place or epoxy rebar anchors would provide a

* The opinions/interpretations identified/expressed in this chapter are outside the scope of TTI Proving Ground's A2LA Accreditation.

more continuous connection to the concrete pavement along the “post” sections of the barrier and were, therefore, considered less critical than the drilled shafts. The cast-in-place and epoxy rebar anchor options were designed according to AASHTO *LRFD Bridge Design Specifications (37)* and are considered to be *MASH*-compliant alternatives to the drilled shaft foundations. These details can be found in Appendix F.

In accordance with the scope of TxDOT Project 0-6976, *Development of Concrete Median Barriers for Flood-Prone Areas*, the research teams at TTI and the Center for Transportation Research (CTR) have prepared an estimate for the value of research (VoR) associated with the research products delivered for this project. The benefit areas deemed relevant and identified in the project agreement for the purpose of establishing the VoR encompass both qualitative and economic areas. Information regarding the VoR is contained in Appendix G of this report.

REFERENCES

1. American Association of State Highway and Transportation Officials. *Manual for Assessing Safety Hardware—Second Edition*. AASHTO Subcommittee on Bridges and Structures, Washington, D.C., 2016.
2. Beaumont Enterprise. “An Island. *Flooding cuts off Beaumont, kills city water supply.*” September 1, 2017, accessed at <https://hearstmediasetx.com/print-media>.
3. Kinchen, H. “Median wall caused flooding in Livingston and EBR parishes, cities claim in class-action suit against DOTD.” https://www.theadvocate.com/baton_rouge/news/courts/article_895ea4b6-d38d-11e6-a75e-e70090be9b62.html. Retrieved November 12, 2018.
4. Abc13 Eyewitness News. “Floodwaters wreck concrete median on Texas interstate.” <https://abc13.com/weather/floodwaters-wreck-concrete-median-on-texas-interstate/2359907/>. Retrieved November 12, 2018.
5. “Freeway concrete barrier broke away.” YouTube. <https://www.youtube.com/watch?v=SZ58UxBB88w>. Retrieved November 12, 2018.
6. Personal communication with TxDOT, email, “T223 Barrier,” October 11, 2018.
7. American Association of State Highway and Transportation Officials. *Manual for Assessing Safety Hardware*. AASHTO Subcommittee on Bridges and Structures, Washington, D.C., 2009.
8. Ross, H.E., D.L. Sicking, R.A. Zimmer, and J.D. Michie. *Recommended Procedures for the Safety Performance Evaluation of Highway Features*. NCHRP Report 350, Transportation Research Board, National Research Council, Washington, D.C., 1993.
9. Sheikh, N.M., R.P. Bligh, and W.L. Menges. *Determination of Minimum Height and Lateral Design Load for MASH Test Level 4 Bridge Rails*. Report No. 9-1002-5, Texas A&M Transportation Institute, College Station, TX, 2011.
10. Federal-Aid Policy Guide 23 CFR § 650.105. 1992. <https://www.fhwa.dot.gov/legregs/directives/fapg/cfr0650a.htm>. Retrieved November 27, 2018.
11. Texas Department of Transportation. *Hydraulic Design Manual*. TxDOT, Austin, TX, 2016.
12. Chow, V.T. *Open-Channel Hydraulics*. McGraw-Hill, New York, 1959.
13. Klenzendorf, J.B. *Hydraulic Performance of Bridge Rails Based on Rating Curves and Submergence Effects*. M.S. Thesis in Engineering, The University of Texas at Austin, 2007.
14. Bin-Shafique, S., M. Barrett, H. Sharif, R. Charbeneau, K. Ali, and C. Hudson. *Mitigation Methods for Temporary Concrete Traffic Barrier Effects on Flood Water Flows*. Report No. FHWA/TX-11/0-6094-1, Texas Department of Transportation, Austin, TX, 2011.
15. Mays, L.W. *Water Resources Engineering* (2nd ed.). John Wiley & Sons, Hoboken, NJ, 2011.
16. Crowe, C.T., D.F. Elger, and J.A. Roberson. *Engineering Fluid Mechanics* (8th ed.). John Wiley & Sons, Hoboken, NJ, 2005.

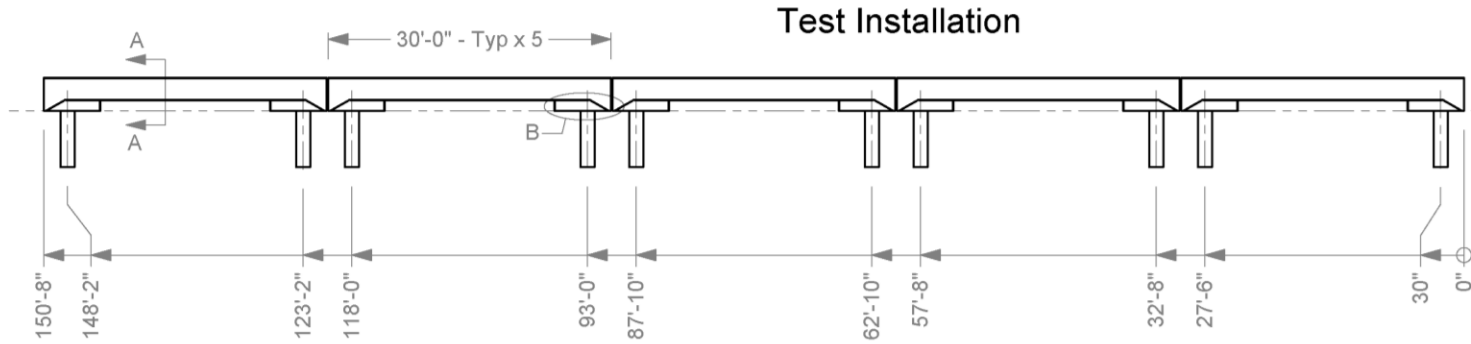
17. Warnock, J.E. “Hydraulic Similitude,” in *Engineering Hydraulics*, H. Rouse (Ed.), John Wiley & Sons, New York, 1950.
18. Charbeneau, R.J., B. Klenzendorf, and M.E. Barrett. *Hydraulic Performance of Bridge Rails*. Report No. FHWA/TX-08/0-5492-1, Texas Department of Transportation, Austin, TX, 2008.
19. Charbeneau, R.J., A.D. Henderson, and L.C. Sherman. “Hydraulic Performance Curves for Highway Culverts.” *Journal of Hydraulic Engineering*, Vol. 132, No. 5, pp. 474–481, 2006.
20. Henderson, F.M. *Open Channel Flow*. Macmillan, New York, 1966.
21. King, H., and E. Brater. *Handbook of Hydraulics* (5th ed.). McGraw-Hill, New York, 1963.
22. Rouse, H. “Engineering Hydraulics.” *Proceedings of the Fourth Hydraulics Conference, Iowa Institute of Hydraulic Research, June 12–15, 1949*. John Wiley & Sons, New York, 1950.
23. Bos, M. *Discharge Measurements Structures*. Publication 20, International Institute for Land Reclamation and Improvement, Wageningen, The Netherlands, 1989.
24. Klenzendorf, J.B., and R.J. Charbeneau. “Bridge Rail Rating Curves and Submergence Characteristics.” *Journal of Hydraulic Engineering*, Vol. 135, No. 2, pp. 88–95, 2009. doi:10.1061/(asce)0733-9429(2009)135:2(88).
25. Akiba, M., S. Morooka, K. Shirakawa, and K. Chuman. Experimental Study on Improvement of Inlet Orifice in BWR Core. *Journal of Nuclear Science and Technology*, Vol. 38, No. 9, pp. 793–798, 2001. doi:10.1080/18811248.2001.9715097.
26. Coduto, D.P. *Foundation Design: Principles and Practices* (2nd ed.). Prentice Hall, New York, 2001.
27. Hibbeler, R.C. *Mechanics of Materials* (7th ed.). Prentice Hall, New York, 2008.
28. Williams, W.F., N. Sheikh, and W.L. Menges. “MASH Test 3-11 of the WsDOT Pin and Loop Concrete Barrier with Drainage Slots.” TM 405160-18-1, Texas A&M Transportation Institute, College Station, TX, 2010.
29. Williams, W.F., and W.L. Menges. “Washington State Department of Transportation Pin and Loop Barrier with Drainage Slots.” TM 405160-30-1, Texas A&M Transportation Institute, College Station, TX, 2012.
30. Williams, W.F., and W.L. Menges. *F-Shape Concrete Barrier with Slotted Drain Holes*. Report No. 405160-19, Texas A&M Transportation Institute, College Station, TX, 2010.
31. Abu-Odeh, A., M.S. Brackin, N.D. Schulz, J.C. Kovar, R.D. Ferron, S. Ahsan, M. Rung, W.L. Menges, and D.L Kuhn. *Development and MASH TL-4 Evaluation of Rubber Mounted Single Slope Barrier*. Report No.468958, Texas A&M Transportation Institute, College Station, TX, 2018.
32. TxDOT. Bridge Standards. <https://www.dot.state.tx.us/insdtdot/orgchart/cmd/cserve/standard/bridge-e.htm>. Retrieved November 10, 2018.
33. TxDOT. Roadway Standards. <https://www.txdot.gov/insdtdot/orgchart/cmd/cserve/standard/rdwylse.htm>. Retrieved November 12, 2018.

34. Dobrovolny, C.S., R.P. Bligh, and W.L. Menges. *MASH Testing and Evaluation of the MassDOT Portable Concrete Barrier*. Report No. 605611-03-F, Texas A&M Transportation Institute, College Station, TX, 2017.
35. Benson, K.S. *Hydraulic Effects of Safety End Treatments on Culvert Performance*. M.S. Thesis in Engineering, The University of Texas at Austin, 2004.
36. Klenzendorf, J.B., M.B. Barrett, and R.J. Charbeneau. Impact of Bridge Rail Geometry on Floodplain Analyses. *Journal of Hydrologic Engineering*. Vol. 15, No. 12, 2010.
37. AASHTO. *LRFD Bridge Design Specifications* (8th ed.). AASHTO, Washington, D.C., 2017.

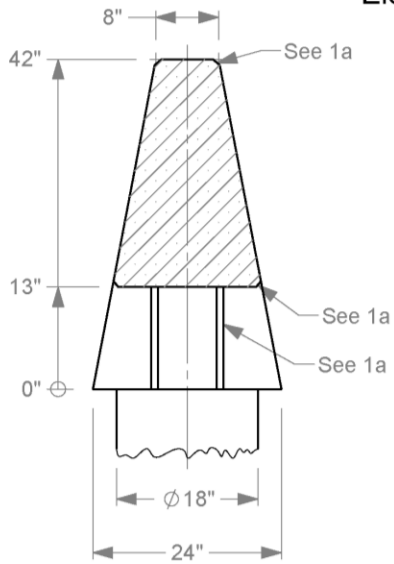
APPENDIX A. DETAILS OF TXDOT LARGE-SCUPPER MEDIAN BARRIER

BARRIER

C:\Accreditation-17025-2017\EIR-000 Project Files\469760-06 Median Barrier for Flood-Prone Areas-Dobrovoly\Drafting_469760-06\469760-06 Drawing



Elevation View

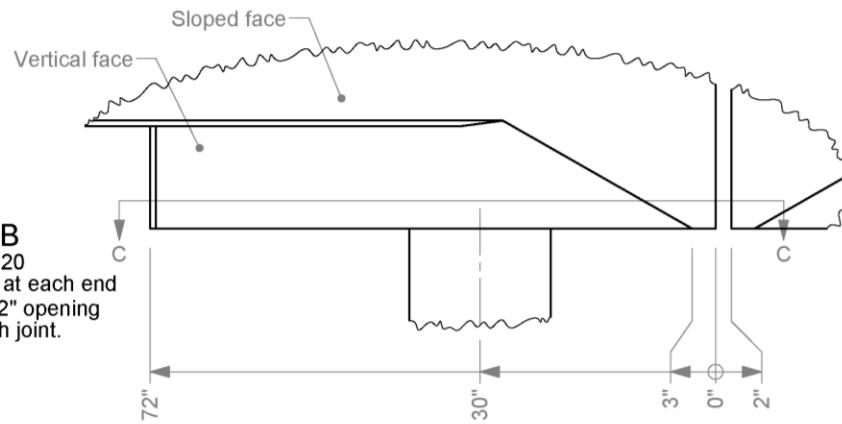


Section A-A

Scale 1 : 20

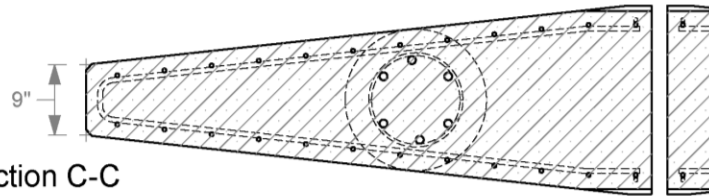
- 1a.** 1" Chamfer (3/4" each way) on edges of parapet and corners of posts where indicated.
- 1b.** Some rebar not shown on this sheet for clarity.
- 1c.** Concrete strength is 3600 psi.

Detail B
Scale 1 : 20
Dimensions typical at each end of each section. 2" opening typical at each joint.



Section C-C

Scale 1 : 20



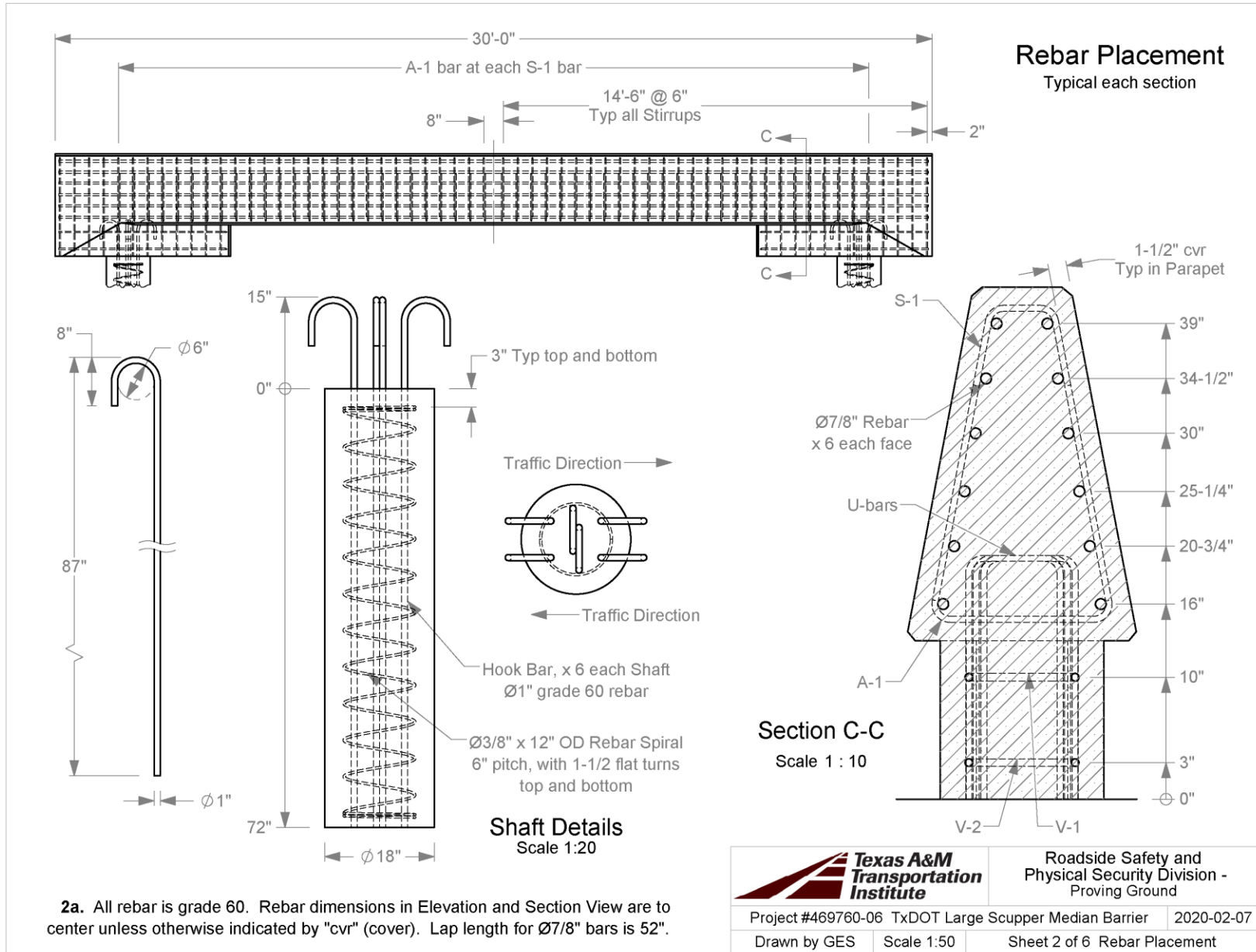
Roadside Safety and Physical Security Division - Proving Ground

Project #469760-06 TxDOT Large Scupper Median Barrier 2020-02-07

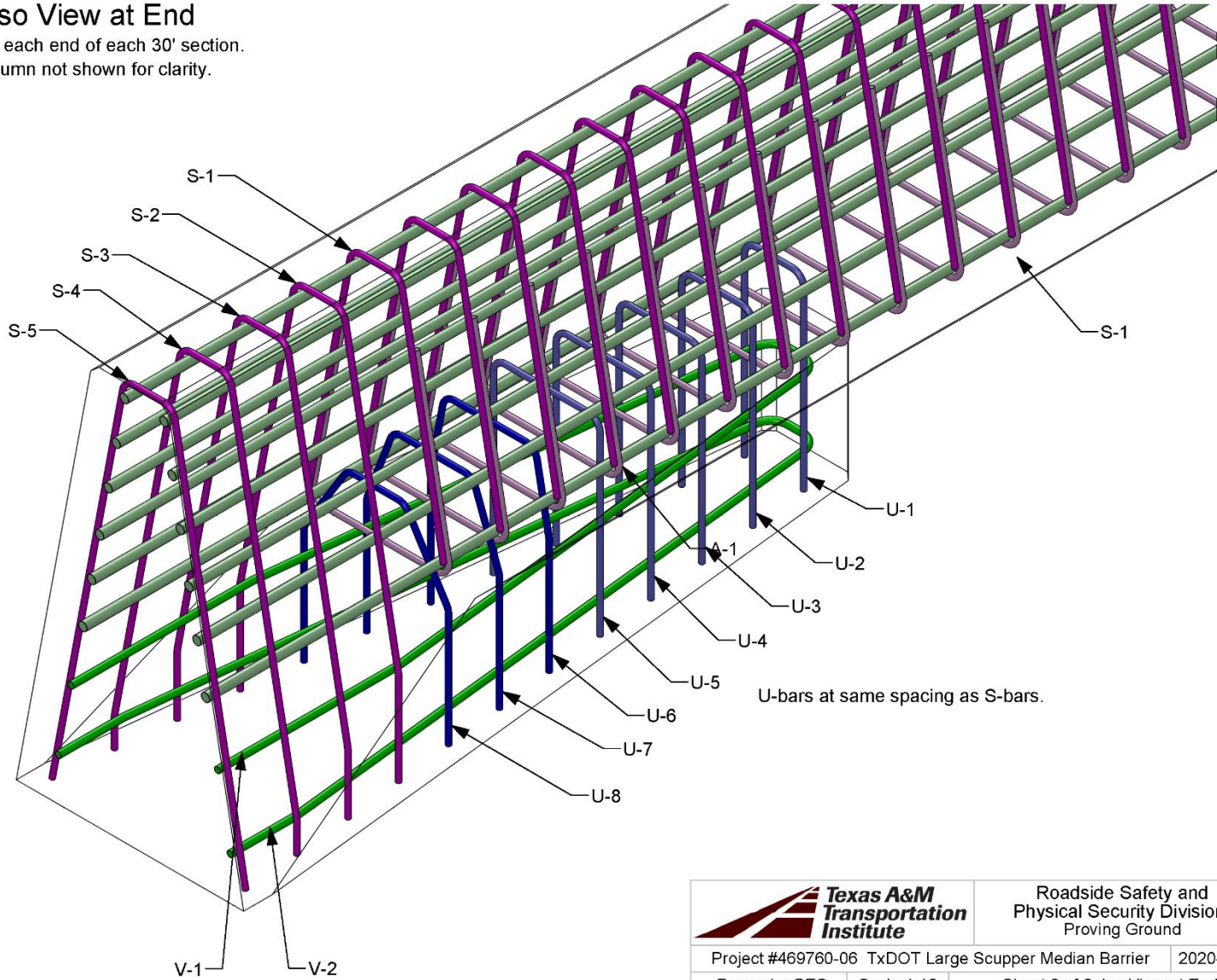
Drawn by GES

Scale 1:200

Sheet 1 of 6 Test Installation

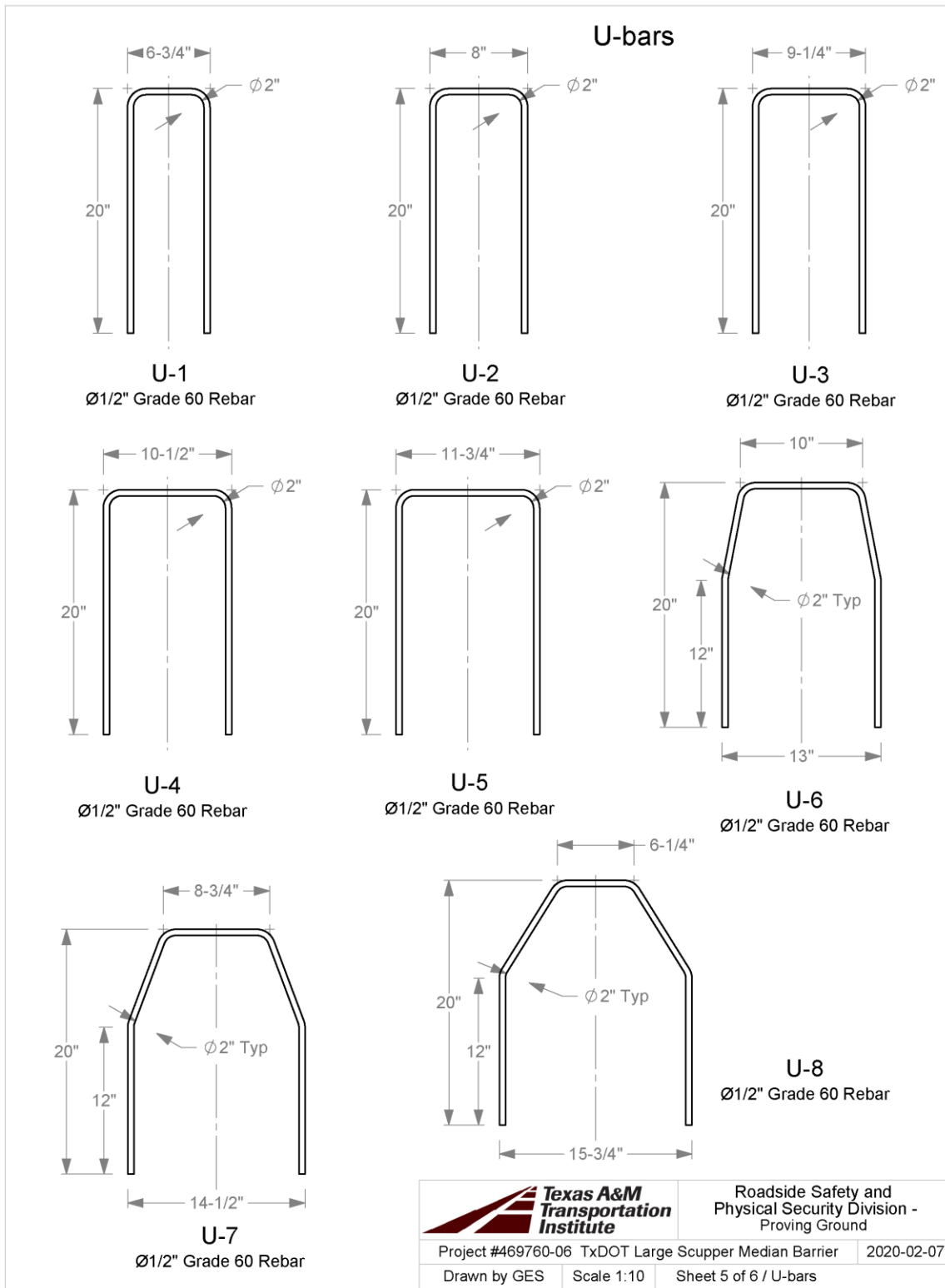


Iso View at End
 Typical each end of each 30' section.
 Column not shown for clarity.



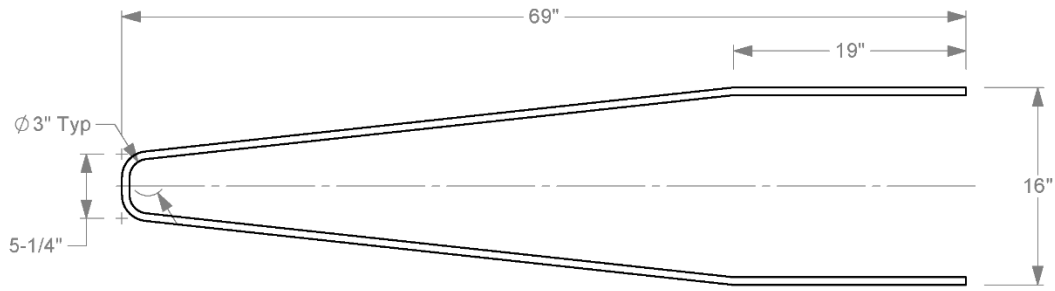
Roadside Safety and
 Physical Security Division -
 Proving Ground

Project #469760-06	TxDOT Large Scupper Median Barrier	2020-02-07
Drawn by GES	Scale 1:10	Sheet 3 of 6 Iso View at End

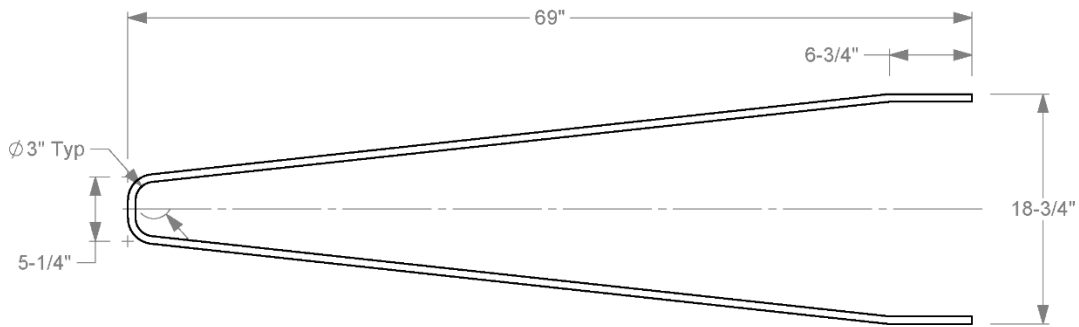


Q:\Accreditation-17025-2017\EIR-000 Project Files\469760-06 Median Barrier for Flood-Prone Areas-Dobrovolya\Drafting_469760-06 Drawing

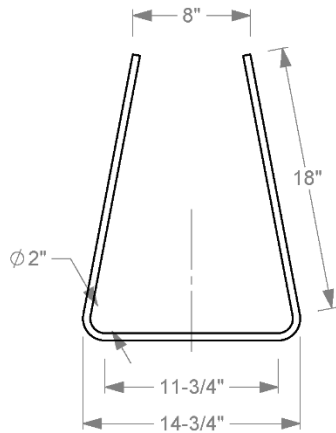
A- and V-bars



V-1
Ø5/8" Grade 60 Rebar



V-2
Ø5/8" Grade 60 Rebar



A-1
Ø1/2" Grade 60 Rebar



Roadside Safety and
Physical Security Division -
Proving Ground

Project #469760-06 TxDOT Large Scupper Median Barrier 2020-02-07

Drawn by GES Scale 1:12 Sheet 6 of 6 / A- and V-bars

Q:\Accreditation-17025-2017\EIR-000 Project Files\469760-06 Median Barrier for Flood-Prone Areas-Dobrovolya\Drafting_469760-06 Drawing

TUCKER CONCRETE

8930 LACY WELL RD CS
878-777-6749 VM1802

Job # TUCKER CONST
MMI

TICKET # 343
START DATE: 03/31/2020 TIME: 12:54:27
STOP DATE: 03/31/2020 TIME: 13:13:26

MIX DESIGN B1400

RAW CEMENT COUNTS ----- 3025
RAW CONVEYOR COUNTS ----- 2254

TOTAL YARDS 4.65

MATERIAL	RATE SETTING	TOTAL
CAPTYPE1	487.4LBPM	2403.0LBS
LRMSAND	6.0 GATE	6347.3LBS
RGBLEND	7.1 GATE	8766.0LBS
WATER	29.2GPM	0.0GAL
SIKA686	1.1GPM	5.6GAL
MAX GPM	23.4	MAX GPY 22.53

NAME -----
NOTES:

CONCRETE COMPRESSIVE STRENGTH TEST REPORT

Report Number: A1171057.0108
 Service Date: 03/31/20
 Report Date: 06/02/20 Revision 1 - Test Date
 Task: PO #469760-06



6198 Imperial Loop
 College Station, TX 77845-5765
 979-846-3767 Reg No: F-3272

Client

Texas Transportation Institute
 Attn: Gary Gerke
 TTI Business Office
 3135 TAMU
 College Station, TX 77843-3135

Project

Riverside Campus
 Riverside Campus
 Bryan, TX

Project Number: A1171057

Material Information

Specified Strength: 4,000 psi @ 28 days

Mix ID: B1400
 Supplier: Tucker
 Batch Time: 1254 Plant:
 Truck No.: VM1802 Ticket No.: 343

Field Test Data

Test	Result	Specification
Slump (in):	5 1/2	Not Specified
Air Content (%):	2.9	Not Specified
Concrete Temp. (F):	78	40 - 95
Ambient Temp. (F):	73	40 - 95
Plastic Unit Wt. (pcf):	146.0	Not Specified
Yield (Cu. Yds.):		

Sample Information

Sample Date: 03/31/20 Sample Time: 1423
 Sampled By: Adam Hill
 Weather Conditions: Partly cloudy, moderate wind
 Accumulative Yards: 4.65/4.65 Batch Size (cy): 4.65
 Placement Method: Direct Discharge
 Water Added Before (gal): 0
 Water Added After (gal): 0
 Sample Location: Furthest south drilled pier (1 out of 10 piers)
 Placement Location: Piers (PO #469760-06)

Laboratory Test Data

Set No.	Specimen ID	Avg Diam. (in)	Area (sq in)	Date Received	Date Tested	Age at Test (days)	Maximum Load (lbs)	Compressive Strength (psi)	Fracture Type	Tested By
1	A	6.01	28.37	04/01/20	06/02/20	63 F	145,940	5,140	5	AWD
1	B	6.01	28.37	04/01/20	06/02/20	63 F	146,260	5,160	3	AWD
1	C	6.01	28.37	04/01/20	06/02/20	63 F	154,180	5,430	3	AWD
1	D			04/01/20		Hold				

Initial Cure: Outside

Final Cure: Field Cured

Comments: F = Field Cured

Samples Made By: Terracon

Services: Obtain samples of fresh concrete at the placement locations (ASTM C 172), perform required field tests and cast, cure, and test compressive strength samples (ASTM C 31, C 39, C 1231).

Terracon Rep.: Adam Hill

Start/Stop: 1315-1500

Reported To: Gary Gerke with TTI

Contractor:

Report Distribution:

- (1) Texas Transportation Institute, Gary Gerke
- (1) Terracon Consultants, Inc., Alex Dunigan, P.E.
- (1) Texas Transportation Institute, Bill Griffith

Reviewed By:

Alexander Dunigan
 Project Manager

Test Methods: ASTM C 31, ASTM C143, ASTM C231, ASTM C1064

The tests were performed in general accordance with applicable ASTM, AASHTO, or DOT test methods. This report is exclusively for the use of the client indicated above and shall not be reproduced except in full without the written consent of our company. Test results transmitted herein are only applicable to the actual samples tested at the location(s) referenced and are not necessarily indicative of the properties of other apparently similar or identical materials.

TUCKER CONCRETE

8830 LACY WELL RD CS
979-777-6749 VM1802

Job # TUCKER
TTI

TICKET # 403
START DATE: 04/22/2020 TIME: 07:49:14
STOP DATE: 04/22/2020 TIME: 08:30:46

MIX DESIGN B1400
RAW CEMENT COUNTS 6586
RAW CONVEYOR COUNTS 4923

TOTAL YARDS 10.09

MATERIAL	RATE SETTING	TOTAL
CAPTYPE1	487.4LBPM	5215.9LBS
LRMSAND	6.0 GATE	13863.2LBS
RGBLEND	7.1 GATE	19145.8LBS
WATER	29.2GPM	0.0GAL
SIKA686	1.1GPM	12.1GAL
MAX GPM	23.4	MAX GPY 22.53

NAME _____
NOTES: _____

TUCKER_concrete

76749

CKER_CONST

TICKET # 820
START DATE: 2020-04-22 TIME: 09:08:31
STOP DATE: 2020-04-22 TIME: 11:14:03

MIX DESIGN: B1400
RAW CEMENT COUNTS: 5744
RAW CONVEYOR COUNTS: 195412
CONVEYOR SPEED: 45
TOTAL YARDS 9.25

MATERIAL	RATE SETTING	TOTAL
CEMENT	8.45924LBS/	4737.076
SAND	5.248304 GA	12486.90
ADJUSTED:	6.848384 GA	17245.13
STONE		219.9316
ADJUSTED:	24.93363GAL	0.00Z
WATER	0.00Z/MIN	978.1854
ADMIX #1	127.62489OZ	0.00Z
ADMIX #2	0.00Z/MIN	
ADMIX #3		

ASTM DATA AVAILABLE UPON REQ

Name _____
NOTES: _____

CONCRETE COMPRESSIVE STRENGTH TEST REPORT

Report Number: A1171057.0111
Service Date: 04/22/20
Report Date: 06/02/20 Revision 2 - Test Date
Task: PO #469760-06

Terracon
6198 Imperial Loop
College Station, TX 77845-5765
979-846-3767 Reg No: F-3272

Client

Texas Transportation Institute
Attn: Gary Gerke
TTI Business Office
3135 TAMU
College Station, TX 77843-3135

Project

Riverside Campus
Riverside Campus
Bryan, TX

Project Number: A1171057

Material Information

Specified Strength: 3,000 psi @ 28 days

Mix ID: B1400
Supplier: Tucker
Batch Time: 0749 Plant:
Truck No.: VM 1802 Ticket No.: 403

Field Test Data

Test	Result	Specification
Slump (in):	5 3/4	Not Specified
Air Content (%):	2.3	Not Specified
Concrete Temp. (F):	80	40 - 95
Ambient Temp. (F):	74	40 - 95
Plastic Unit Wt. (pcf):	147.8	Not Specified
Yield (Cu. Yds.):		

Sample Information

Sample Date: 04/22/20 Sample Time: 0907
Sampled By: Randolph E. Rohrbach
Weather Conditions: Cloudy, moderate wind
Accumulative Yards: 10/20 Batch Size (cy): 10
Placement Method: Direct Discharge
Water Added Before (gal): 0
Water Added After (gal): 0
Sample Location: South end 14" form top
Placement Location: Scupper barricade

Laboratory Test Data

Set No.	Specimen ID	Avg Diam. (in)	Area (sq in)	Date Received	Date Tested	Age at Test (days)	Maximum Load (lbs)	Compressive Strength (psi)	Fracture Type	Tested By
1	A	6.01	28.37	04/24/20	06/02/20	41 F	131,120	4,620	6	AWD
1	B	6.01	28.37	04/24/20	06/02/20	41 F	130,520	4,600	6	AWD
1	C	6.01	28.37	04/24/20	06/02/20	41 F	143,660	5,060	3	AWD
1	D			04/24/20		Hold				

Initial Cure: Outside

Final Cure: Field Cured

Comments: F = Field Cured

Samples Made By: Terracon

Services: Obtain samples of fresh concrete at the placement locations (ASTM C 172), perform required field tests and cast, cure, and test compressive strength samples (ASTM C 31, C 39, C 1231).

Terracon Rep.: Randolph E. Rohrbach

Start/Stop: 0830-1215

Reported To:

Contractor:

Report Distribution:

(1) Texas Transportation Institute, Gary Gerke (1) Terracon Consultants, Inc., Alex Dumigan, P.E.
(1) Texas Transportation Institute, Bill Griffith

Test Methods: ASTM C 31, ASTM C143, ASTM C231, ASTM C1064

The tests were performed in general accordance with applicable ASTM, AASHTO, or DOT test methods. This report is exclusively for the use of the client indicated above and shall not be reproduced except in full without the written consent of our company. Test results transmitted herein are only applicable to the actual samples tested at the location(s) referenced and are not necessarily indicative of the properties of other apparently similar or identical materials.

CONCRETE COMPRESSIVE STRENGTH TEST REPORT

Report Number: A1171057.0111
Service Date: 04/22/20
Report Date: 06/02/20 Revision 2 - Test Date
Task: PO #469760-06

Terracon

6198 Imperial Loop
College Station, TX 77845-5765
979-846-3767 Reg No: F-3272

Client

Texas Transportation Institute
Attn: Gary Gerke
TTI Business Office
3135 TAMU
College Station, TX 77843-3135

Project

Riverside Campus
Riverside Campus
Bryan, TX

Project Number: A1171057

Material Information

Specified Strength: 3,000 psi @ 28 days

Mix ID: B1400
Supplier: Tucker
Batch Time: 0908 Plant:
Truck No.: VM 1701 Ticket No.: 820

Sample Information

Sample Date: 04/22/20 Sample Time: 0820
Sampled By: Randolph E. Rohrbach
Weather Conditions: Cloudy, moderate wind
Accumulative Yards: 20/20 Batch Size (cy): 10
Placement Method: Direct Discharge
Water Added Before (gal): 0
Water Added After (gal): 0
Sample Location: North end 14" from top
Placement Location: Scupper barricade

Field Test Data

Test	Result	Specification
Slump (in):	8	Not Specified
Air Content (%):	1.8	Not Specified
Concrete Temp. (F):	81	40 - 95
Ambient Temp. (F):	74	40 - 95
Plastic Unit Wt. (pcf):	146.2	Not Specified
Yield (Cu. Yds.):		

Laboratory Test Data

Set No.	Specimen ID	Avg Diam. (in)	Area (sq in)	Date Received	Date Tested	Age at Test (days)	Maximum Load (lbs)	Compressive Strength (psi)	Fracture Type	Tested By
2	A	6.01	28.37	04/24/20	06/02/20	41 F	142,560	5,030	3	AWD
2	B	6.01	28.37	04/24/20	06/02/20	41 F	133,020	4,690	6	AWD
2	C	6.01	28.37	04/24/20	06/02/20	41 F	129,630	4,570	6	AWD
2	D			04/24/20		Hold				

Initial Cure: Outside

Final Cure: Field Cured

Comments: F = Field Cured

Samples Made By: Terracon

Services: Obtain samples of fresh concrete at the placement locations (ASTM C 172), perform required field tests and cast, cure, and test compressive strength samples (ASTM C 31, C 39, C 1231).

Terracon Rep.: Randolph E. Rohrbach

Start/Stop: 0830-1215

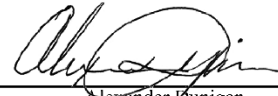
Reported To:

Contractor:

Report Distribution:

(1) Texas Transportation Institute, Gary Gerke (1) Terracon Consultants, Inc., Alex Dunigan, P.E.
(1) Texas Transportation Institute, Bill Griffith

Reviewed By:



Alexander Dunigan
Project Manager

Test Methods: ASTM C 31, ASTM C143, ASTM C231, ASTM C1064

The tests were performed in general accordance with applicable ASTM, AASHTO, or DOT test methods. This report is exclusively for the use of the client indicated above and shall not be reproduced except in full without the written consent of our company. Test results transmitted herein are only applicable to the actual samples tested at the location(s) referenced and are not necessarily indicative of the properties of other apparently similar or identical materials.



CMC STEEL FLORIDA
16770 Rebar Road
Baldwin FL 32234-4100

CERTIFIED MILL TEST REPORT
For additional copies call
904-266-1468

We hereby certify that the test results presented here
are accurate and conform to the reported grade specification

Alex Renosto
Quality Assurance Manager

HEAT NO.:5006591 SECTION: WIRE ROD 3/8" 420/60 GRADE: ASTM A615-18e1 Grade 420 (60) ROLL DATE: MELT DATE: 02/10/2020 Cert. No.: / 006591K231		S O L D T O	S H I P T O	Delivery#: BOL#: CUST PO#: CUST P/N: DLVRY LBS / HEAT: 0.000 LB DLVRY PCS / HEAT:	
Characteristic	Value	Characteristic	Value	Characteristic	Value
C	0.31%	Bend Test 1	Passed	The Following is true of the material represented by this MTR: *Material is fully killed *100% melted and rolled in the USA *EN10204:2004 3.1 compliant *Contains no weld repair *Contains no Mercury contamination *Manufactured in accordance with the latest version of the plant quality manual *Meets the "Buy America" requirements of 23 CFR635.410, 49 CFR 661 *Warning: This product can expose you to chemicals which are known to the State of California to cause cancer, birth defects or other reproductive harm. For more information go to www.P65Warnings.ca.gov	
Mn	0.95%				
P	0.014%				
S	0.030%				
Si	0.18%				
Cu	0.31%				
Cr	0.10%				
Ni	0.14%				
Mo	0.023%				
V	0.035%				
Cb	0.003%				
Sn	0.013%				
Yield Strength test 1	71.9ksi				
Yield Strength test 1 (metri)	495MPa				
Tensile Strength test 1	103.1ksi				
Tensile Strength 1 (metric)	711MPa				
Elongation test 1	14%				
Elongation Gage Lgth test 1	8IN				
Tensile to Yield ratio test1	1.44				
Elongation Gage Lgth 1(metri)	200mm				
REMARKS :					



CMC STEEL TEXAS
1 STEEL MILL DRIVE
SEGUIN TX 78155-7510

CERTIFIED MILL TEST REPORT
For additional copies call
830-372-8771

We hereby certify that the test results presented here
are accurate and conform to the reported grade specification

Rolando A Davila
Rolando A Davila

Quality Assurance Manager

HEAT NO.:3094958 SECTION: REBAR 13MM (#4) 40'0" 420/60 GRADE: ASTM A615-18e1 Gr 420/60 ROLL DATE: 02/25/2020 MELT DATE: 02/16/2020 Cert. No.: 83003292 / 094958A371		S O L D T O	CMC Construction Svcs College Stati 10650 State Hwy 30 College Station TX US 77845-7950 979 774 5900	S H I P T O	CMC Construction Svcs College Stati 10650 State Hwy 30 College Station TX US 77845-7950 979 774 5900	Delivery#: 83003292 BOL#: 73447157 CUST PO#: 842514 CUST P/N: DLVRY LBS / HEAT: 19881.000 LB DLVRY PCS / HEAT: 744 EA
Characteristic	Value	Characteristic	Value	Characteristic	Value	
C	0.44%	Bend Test Diameter	1.750IN	The Following is true of the material represented by this MTR: *Material is fully killed *100% melted and rolled in the USA *EN10204:2004 3.1 compliant *Contains no weld repair *Contains no Mercury contamination *Manufactured in accordance with the latest version of the plant quality manual *Meets the "Buy America" requirements of 23 CFR635.410, 49 CFR 661 *Warning: This product can expose you to chemicals which are known to the State of California to cause cancer, birth defects or other reproductive harm. For more information go to www.P65Warnings.ca.gov		
Mn	0.85%					
P	0.008%					
S	0.046%					
Si	0.17%					
Cu	0.33%					
Cr	0.10%					
Ni	0.19%					
Mo	0.074%					
V	0.000%					
Cb	0.001%					
Sn	0.020%					
Al	0.000%					
Yield Strength test 1	68.2ksi					
Tensile Strength test 1	106.1ksi					
Elongation test 1	14%					
Elongation Gage Lgth test 1	8IN					
Tensile to Yield ratio test1	1.56					
Bend Test 1	Passed					

REMARKS :



CMC STEEL TEXAS
1 STEEL MILL DRIVE
SEGUIN TX 78155-7510

CERTIFIED MILL TEST REPORT
For additional copies call
830-372-8771

We hereby certify that the test results presented here
are accurate and conform to the reported grade specification

Rolando A Devila
Quality Assurance Manager

HEAT NO.:3094648 SECTION: REBAR 16MM (#5) 40"0" 420/60 GRADE: ASTM A615-18e1 Gr 420/60 ROLL DATE: 02/14/2020 MELT DATE: 02/04/2020 Cert. No.: 83003290 / 094648A765		S O L D T O	CMC Construction Svcs College Stati 10650 State Hwy 30 College Station TX US 77845-7950 979 774 5900	S H I P T O	CMC Construction Svcs College Stati 10650 State Hwy 30 College Station TX US 77845-7950 979 774 5900	Delivery#: 83003290 BOL#: 73447155 CUST PO#: 842512 CUST P/N: DLVRY LBS / HEAT: 24030.000 LB DLVRY PCS / HEAT: 576 EA
Characteristic	Value	Characteristic	Value	Characteristic	Value	
C	0.42%	Bend Test Diameter	2.188IN	The Following is true of the material represented by this MTR: *Material is fully killed *100% melted and rolled in the USA *EN10204:2004 3.1 compliant *Contains no weld repair *Contains no Mercury contamination *Manufactured in accordance with the latest version of the plant quality manual *Meets the "Buy America" requirements of 23 CFR635.410, 49 CFR 661 *Warning: This product can expose you to chemicals which are known to the State of California to cause cancer, birth defects or other reproductive harm. For more information go to www.P65Warnings.ca.gov		
Mn	0.93%					
P	0.010%					
S	0.047%					
Si	0.18%					
Cu	0.28%					
Cr	0.12%					
Ni	0.20%					
Mo	0.075%					
V	0.000%					
Cb	0.001%					
Sn	0.027%					
Al	0.000%					
Yield Strength test 1	65.7ksi					
Tensile Strength test 1	104.6ksi					
Elongation test 1	14%					
Elongation Gage Lgth test 1	8IN					
Tensile to Yield ratio test1	1.59					
Bend Test 1	Passed					

REMARKS :



CMC STEEL TEXAS
1 STEEL MILL DRIVE
SEGUIN TX 78155-7510

CERTIFIED MILL TEST REPORT
For additional copies call
830-372-8771

We hereby certify that the test results presented here
are accurate and conform to the reported grade specification

Rolando A Devila

Quality Assurance Manager

HEAT NO.:3094268 SECTION: REBAR 22MM (#7) 40'0" 420/60 GRADE: ASTM A615-18e1 Gr 420/60 ROLL DATE: 01/21/2020 MELT DATE: 01/19/2020 Cert. No.: 82989276 / 094268A055		S O L D T O CMC Construction Svcs College Stati 10650 State Hwy 30 College Station TX US 77845-7950 979 774 5900		S H I P T O CMC Construction Svcs College Stati 10650 State Hwy 30 College Station TX US 77845-7950 979 774 5900		Delivery#: 82989276 BOL#: 73426865 CUST PO#: 841311 CUST P/N: DLVRY LBS / HEAT: 7849.000 LB DLVRY PCS / HEAT: 96 EA	
Characteristic	Value	Characteristic	Value	Characteristic	Value		
C	0.43%	Bend Test Diameter	4.375IN	The Following is true of the material represented by this MTR: *Material is fully killed *100% melted and rolled in the USA *EN10204:2004 3.1 compliant *Contains no weld repair *Contains no Mercury contamination *Manufactured in accordance with the latest version of the plant quality manual *Meets the "Buy America" requirements of 23 CFR635.410, 49 CFR 661 *Warning: This product can expose you to chemicals which are known to the State of California to cause cancer, birth defects or other reproductive harm. For more information go to www.P65Warnings.ca.gov			
Mn	1.03%						
P	0.010%						
S	0.045%						
Si	0.21%						
Cu	0.30%						
Cr	0.11%						
Ni	0.18%						
Mo	0.062%						
V	0.000%						
Cb	0.002%						
Sn	0.010%						
Al	0.001%						
Yield Strength test 1	63.5ksi						
Tensile Strength test 1	104.0ksi						
Elongation test 1	15%						
Elongation Gage Lgth test 1	8IN						
Tensile to Yield ratio test1	1.64						
Bend Test 1	Passed						

REMARKS :



CMC STEEL TEXAS
1 STEEL MILL DRIVE
SEGUIN TX 78155-7510

CERTIFIED MILL TEST REPORT
For additional copies call
830-372-8771

We hereby certify that the test results presented here
are accurate and conform to the reported grade specification

Rolando A Devila
Quality Assurance Manager

HEAT NO.:3091896 SECTION: REBAR 25MM (#8) 40"0" 420/60 GRADE: ASTM A615-18e1 Gr 420/60 ROLL DATE: 10/19/2019 MELT DATE: 10/14/2019 Cert. No.: 82948892 / 091896A060	S O L D T O	CMC Construction Svcs College Stati 10650 State Hwy 30 College Station TX US 77845-7950 979 774 5900	S H I P T O	CMC Construction Svcs College Stati 10650 State Hwy 30 College Station TX US 77845-7950 979 774 5900	Delivery#: 82948892 BOL#: 73369400 CUST PO#: 837935 CUST P/N: DLVRY LBS / HEAT: 7903.000 LB DLVRY PCS / HEAT: 74 EA
------------------------------------------------------------------------------------------------------------------------------------------------------------------------------------	----------------------------	------------------------------------------------------------------------------------------------------------------	----------------------------	------------------------------------------------------------------------------------------------------------------	------------------------------------------------------------------------------------------------------------------------------------

Characteristic	Value	Characteristic	Value	Characteristic	Value
C	0.42%	Bend Test Diameter	5.000IN		
Mn	1.08%				
P	0.013%				
S	0.037%				
Si	0.20%				
Cu	0.32%				
Cr	0.17%				
Ni	0.20%				
Mo	0.072%				
V	0.000%				
Cb	0.001%				
Sn	0.009%				
Al	0.000%				
Yield Strength test 1	65.3ksi				
Tensile Strength test 1	105.8ksi				
Elongation test 1	15%				
Elongation Gage Lgth test 1	8IN				
Tensile to Yield ratio test1	1.62				
Bend Test 1	Passed				
				The Following is true of the material represented by this MTR: *Material is fully killed *100% melted and rolled in the USA *EN10204:2004 3.1 compliant *Contains no weld repair *Contains no Mercury contamination *Manufactured in accordance with the latest version of the plant quality manual *Meets the "Buy America" requirements of 23 CFR635.410, 49 CFR 661 *Warning: This product can expose you to chemicals which are known to the State of California to cause cancer, birth defects or other reproductive harm. For more information go to www.P65Warnings.ca.gov	

REMARKS :

APPENDIX C. MASH TEST 4-10 (CRASH TEST NO. 469760-06-1)

C.1 VEHICLE PROPERTIES AND INFORMATION

Table C.1. Vehicle Properties for Test No. 469760-06-1.

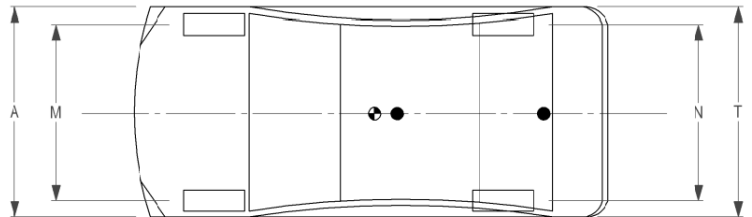
Date: 2020-06-08 Test No.: 469760-6-1 VIN No.: 3N1CN7AP1FL814580
 Year: 2015 Make: NISSAN Model: VERSA
 Tire Inflation Pressure: 36 PSI Odometer: 62832 Tire Size: P185/65R15

Describe any damage to the vehicle prior to test: None

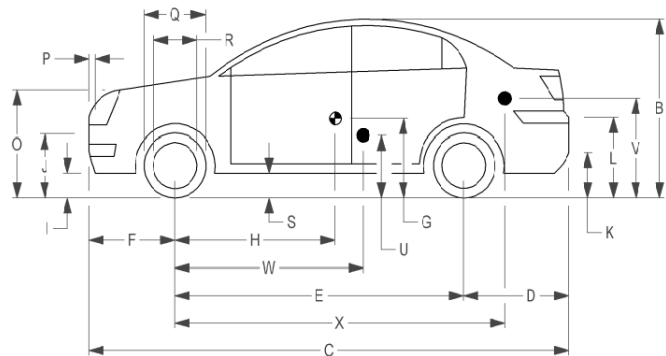
- Denotes accelerometer location.

NOTES: None

Engine Type: 4 CYL
 Engine CID: 1.6 L
 Transmission Type:
 Auto or Manual
 FWD RWD 4WD
 Optional Equipment:
None



Dummy Data:
 Type: 50th Percentile Male
 Mass: 165 lb
 Seat Position: IMPACT SIDE



Geometry: inches

A <u>66.70</u>	F <u>32.50</u>	K <u>12.50</u>	P <u>4.50</u>	U <u>15.50</u>
B <u>59.60</u>	G _____	L <u>26.00</u>	Q <u>24.00</u>	V <u>21.00</u>
C <u>175.40</u>	H <u>40.05</u>	M <u>58.30</u>	R <u>16.25</u>	W <u>40.00</u>
D <u>40.50</u>	I <u>7.00</u>	N <u>58.50</u>	S <u>7.50</u>	X <u>79.00</u>
E <u>102.40</u>	J <u>22.25</u>	O <u>30.50</u>	T <u>64.50</u>	
Wheel Center Ht Front <u>11.50</u>		Wheel Center Ht Rear <u>11.50</u>		W-H <u>-0.05</u>

RANGE LIMIT: A = 65 ±3 inches; C = 169 ±8 inches; E = 98 ±5 inches; F = 35 ±4 inches; H = 39 ±4 inches; O (Top of Radiator Support) = 28 ±4 inches
 (M+N)/2 = 59 ±2 inches; W-H < 2 inches or use MASH Paragraph A4.3.2

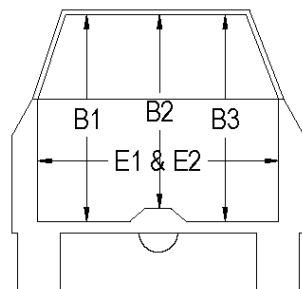
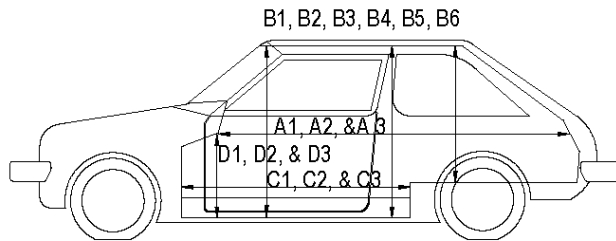
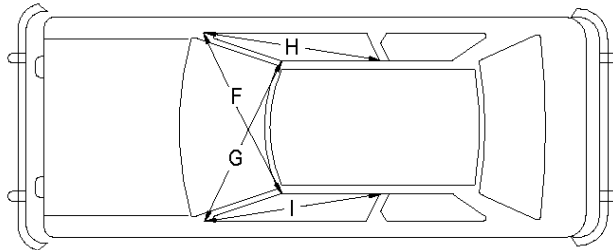
GVWR Ratings:	Mass: lb	Curb	Test Inertial	Gross Static
Front <u>1750</u>	M _{front} <u>1463</u>	<u>1463</u>	<u>1491</u>	<u>1576</u>
Back <u>1687</u>	M _{rear} <u>971</u>	<u>971</u>	<u>958</u>	<u>1038</u>
Total <u>3389</u>	M _{Total} <u>2434</u>	<u>2434</u>	<u>2449</u>	<u>2614</u>

Allowable TIM = 2420 lb ±55 lb | Allowable GSM = 2585 lb ± 55 lb

Mass Distribution:
 lb LF: 768 RF: 723 LR: 458 RR: 500

Table C.3. Occupant Compartment Measurements for Test No. 469760-06-1.

Date: 2020-6-8 Test No.: 469760-6-1 VIN No.: 3N1CN7AP1FL814580
 Year: 2015 Make: NISSAN Model: VERSA



OCCUPANT COMPARTMENT DEFORMATION MEASUREMENT

	Before	After (inches)	Differ.
A1	75.00	75.00	0.00
A2	74.00	74.00	0.00
A3	74.00	74.00	0.00
B1	43.00	43.00	0.00
B2	37.00	37.00	0.00
B3	43.00	43.00	0.00
B4	46.50	46.50	0.00
B5	42.50	42.50	0.00
B6	46.50	46.50	0.00
C1	26.00	25.00	-1.00
C2	0.00	0.00	0.00
C3	26.00	26.00	0.00
D1	12.50	13.50	1.00
D2	0.00	0.00	0.00
D3	10.00	10.00	0.00
E1	45.00	47.00	2.00
E2	48.75	50.75	2.00
F	47.50	47.50	0.00
G	47.50	46.00	-1.50
H	39.00	38.50	-0.50
I	39.00	39.00	-0.50
J*	48.50	44.00	-4.50

*Lateral area across the cab from driver's side kick panel to passenger's side kick panel.

C.2 SEQUENTIAL PHOTOGRAPHS

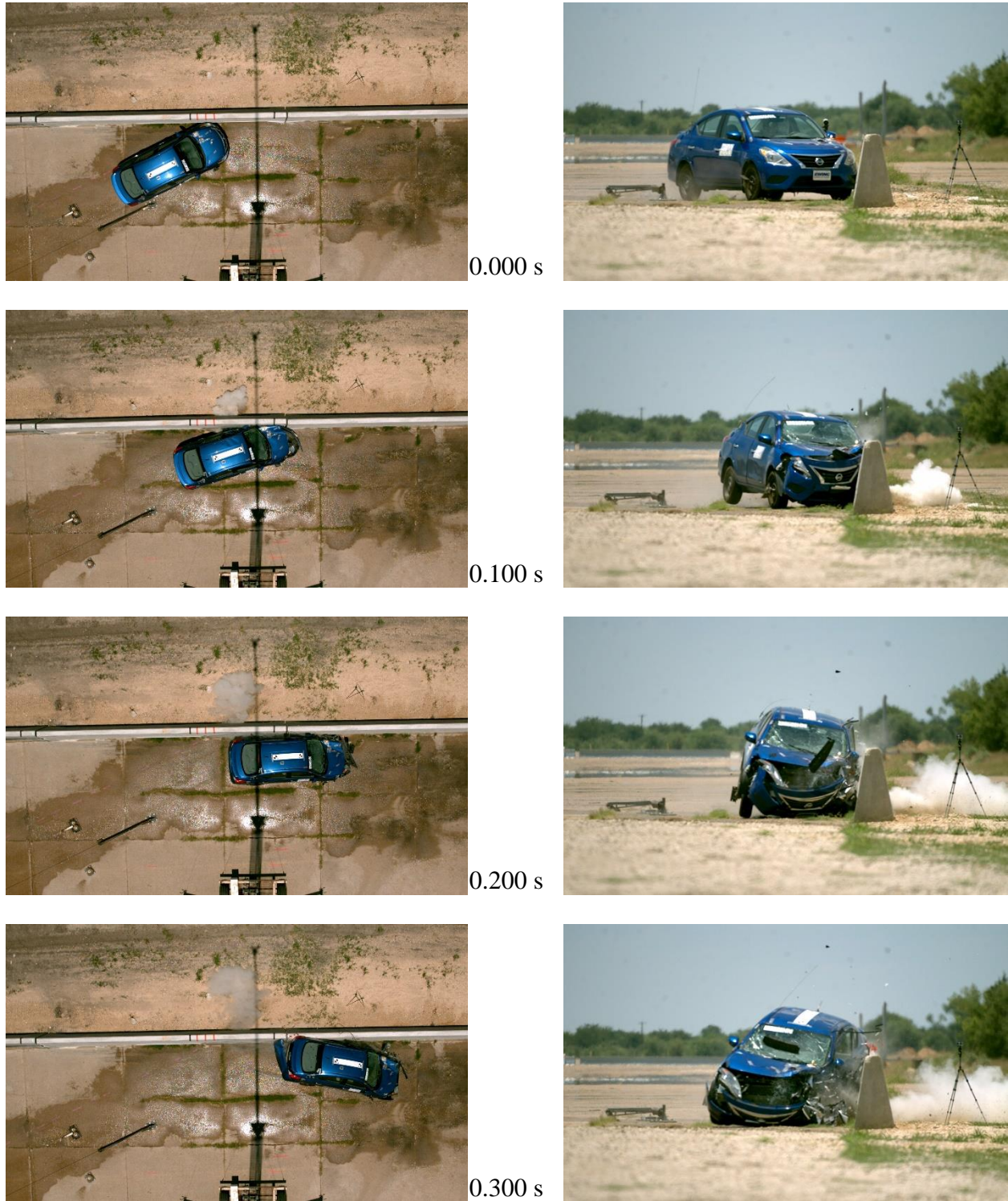


Figure C.1. Sequential Photographs for Test No. 469760-06-1 (Overhead and Frontal Views).



0.400 s



0.500 s



0.600 s



0.700 s



Figure C.1. Sequential Photographs for Test No. 469760-06-1 (Overhead and Frontal Views) (Continued).



0.000 s



0.400 s



0.100 s



0.500 s



0.200 s



0.600 s



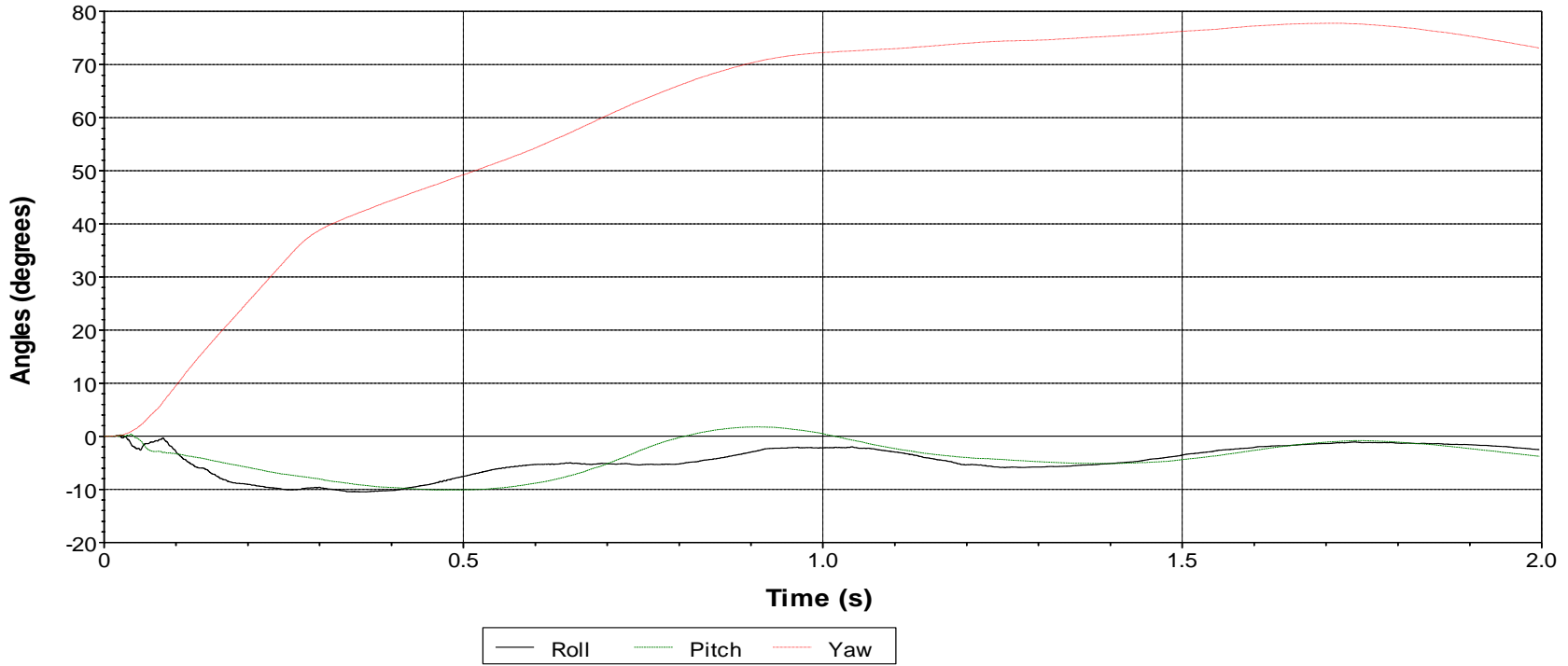
0.300 s



0.700 s

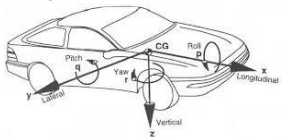
Figure C.2. Sequential Photographs for Test No. 469760-06-1 (Rear View).

Roll, Pitch, and Yaw Angles



Axes are vehicle-fixed.
Sequence for determining orientation:

1. Yaw.
2. Pitch.
3. Roll.



Test Number: 469760-06-1
 Test Standard Test Number: *MASH* Test 4-10
 Test Article: TxDOT Large-Scupper Median Barrier
 Test Vehicle: 2015 Nissan Versa
 Inertial Mass: 2449 lb
 Gross Mass: 2614 lb
 Impact Speed: 64.4 mi/h
 Impact Angle: 25.0°

Figure C.3. Vehicle Angular Displacements for Test No. 469760-06-1.

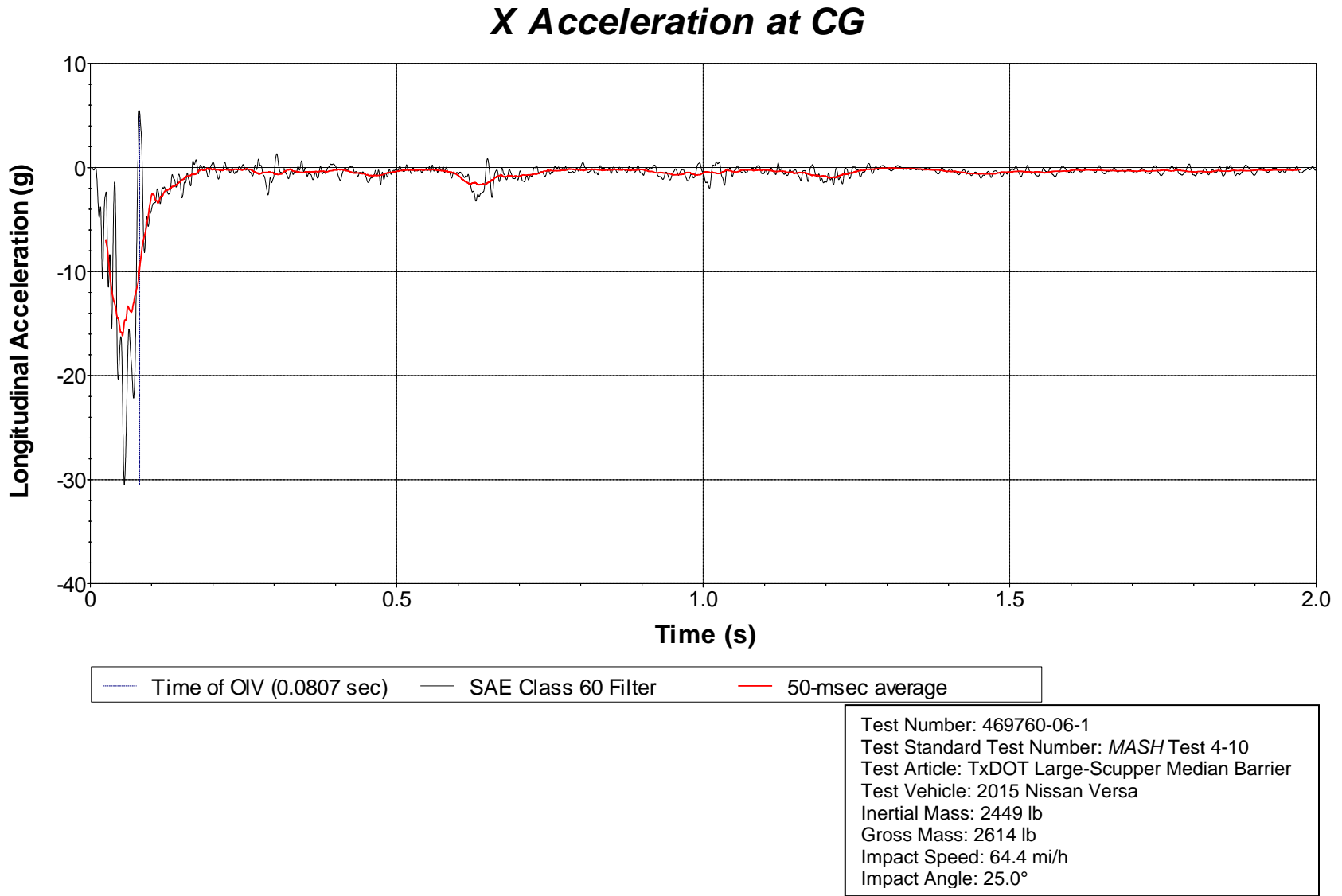
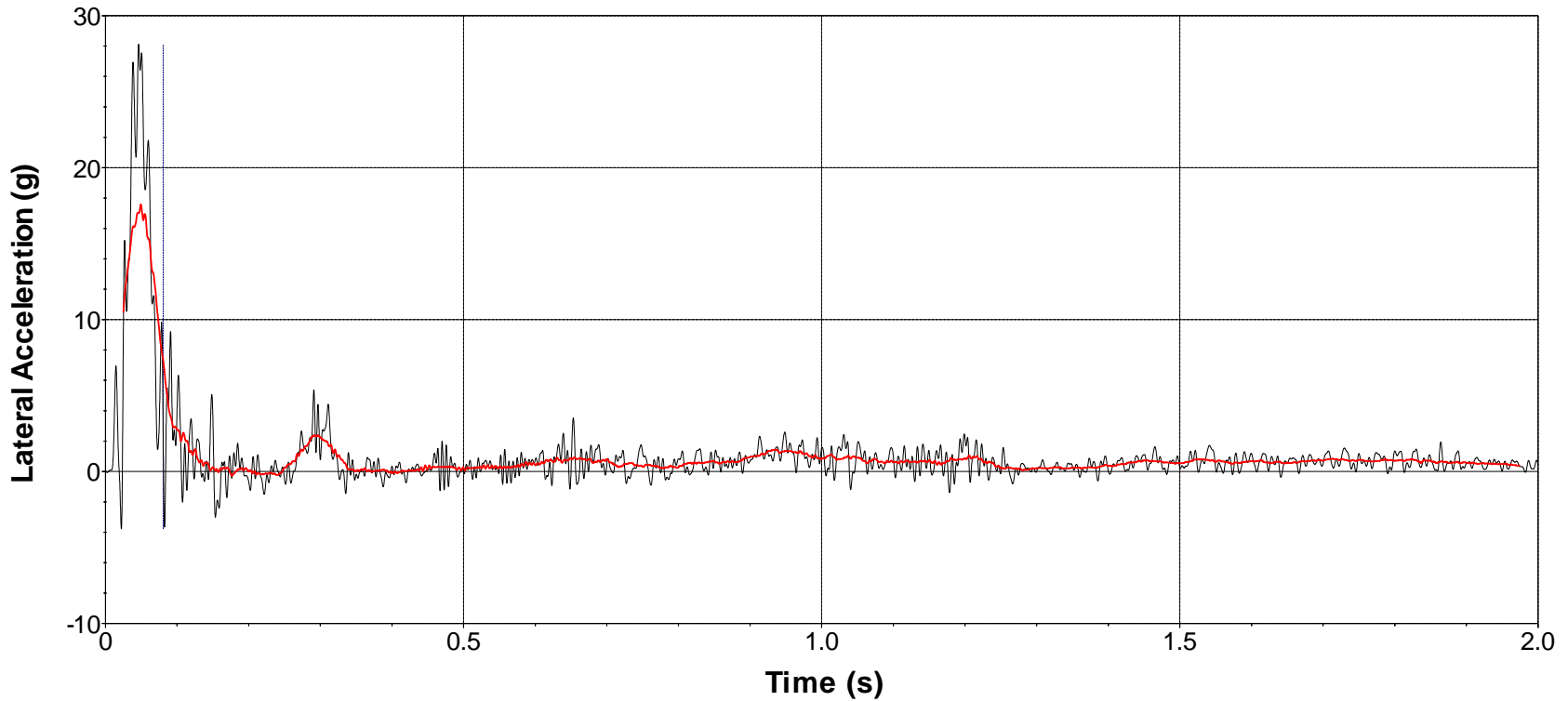


Figure C.4. Vehicle Longitudinal Accelerometer Trace for Test No. 469760-06-1 (Accelerometer Located at Center of Gravity).

Y Acceleration at CG

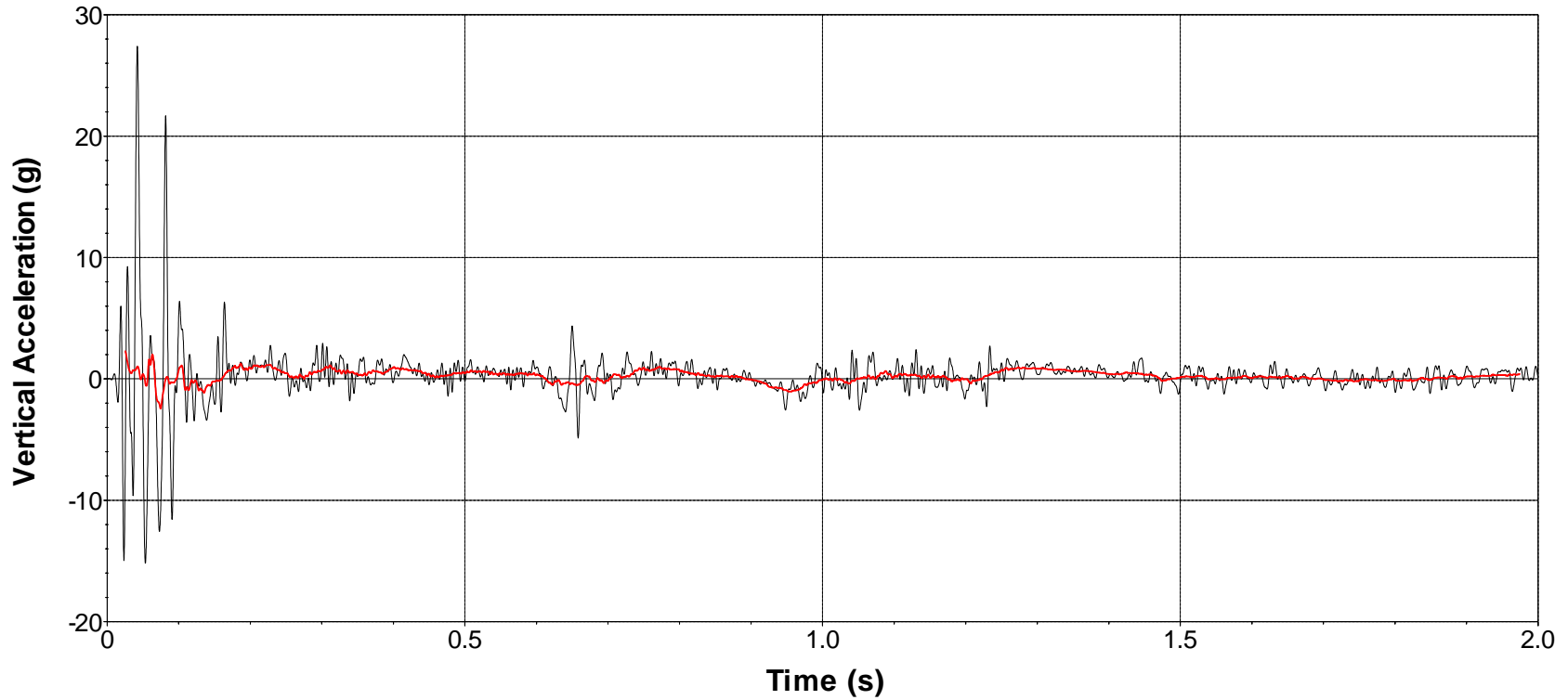


Time of OIV (0.0807 sec) SAE Class 60 Filter 50-msec average

Test Number: 469760-06-1
Test Standard Test Number: MASH Test 4-10
Test Article: TxDOT Large-Scupper Median Barrier
Test Vehicle: 2015 Nissan Versa
Inertial Mass: 2449 lb
Gross Mass: 2614 lb
Impact Speed: 64.4 mi/h
Impact Angle: 25.0°

Figure C.5. Vehicle Lateral Accelerometer Trace for Test No. 469760-06-1 (Accelerometer Located at Center of Gravity).

Z Acceleration at CG



— SAE Class 60 Filter	— 50-msec average
Test Number: 469760-06-1	
Test Standard Test Number: <i>MASH</i> Test 4-10	
Test Article: TxDOT Large-Scupper Median Barrier	
Test Vehicle: 2015 Nissan Versa	
Inertial Mass: 2449 lb	
Gross Mass: 2614 lb	
Impact Speed: 64.4 mi/h	
Impact Angle: 25.0°	

Figure C.6. Vehicle Vertical Accelerometer Trace for Test No. 469760-06-1 (Accelerometer Located at Center of Gravity).

APPENDIX D. MASH TEST 4-11 (CRASH TEST NO. 469760-06-2)

D.1 VEHICLE PROPERTIES AND INFORMATION

Table D.1. Vehicle Properties for Test No. 469760-06-2.

Date: 2020-6-4 Test No.: 469760-6-2 VIN No.: 1C6RR6FT3FS505939
 Year: 2015 Make: RAM Model: 1500
 Tire Size: 265/70 R 17 Tire Inflation Pressure: 35 psi
 Tread Type: Highway Odometer: 116212
 Note any damage to the vehicle prior to test: None

• Denotes accelerometer location.

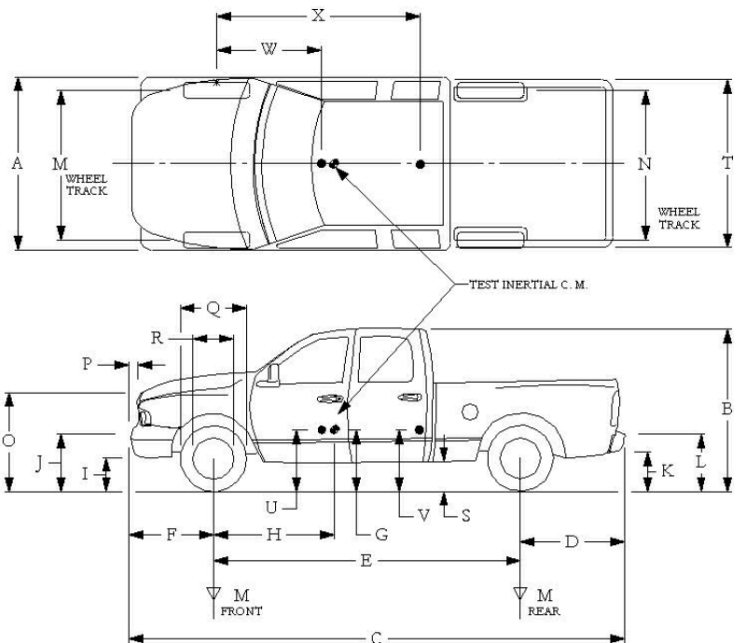
NOTES: None

Engine Type: V-8
 Engine CID: 5.7L

Transmission Type:
 Auto or Manual
 FWD RWD 4WD

Optional Equipment:
None

Dummy Data:
 Type: 50th Percentile male
 Mass: 165 lb
 Seat Position: IMPACT SIDE



Geometry: inches

A	<u>78.50</u>	F	<u>40.00</u>	K	<u>20.00</u>	P	<u>3.00</u>	U	<u>26.75</u>
B	<u>74.00</u>	G	<u>28.25</u>	L	<u>30.00</u>	Q	<u>30.50</u>	V	<u>30.25</u>
C	<u>227.50</u>	H	<u>61.28</u>	M	<u>68.50</u>	R	<u>18.00</u>	W	<u>61.25</u>
D	<u>44.00</u>	I	<u>11.75</u>	N	<u>68.00</u>	S	<u>13.00</u>	X	<u>79.00</u>
E	<u>140.50</u>	J	<u>27.00</u>	O	<u>46.00</u>	T	<u>77.00</u>		
Wheel Center Height Front	<u>14.75</u>	Wheel Well Clearance (Front)	<u>6.00</u>	Bottom Frame Height - Front	<u>12.50</u>				
Wheel Center Height Rear	<u>14.75</u>	Wheel Well Clearance (Rear)	<u>9.25</u>	Bottom Frame Height - Rear	<u>22.50</u>				

RANGE LIMIT: A=78 ±2 inches; C=237 ±13 inches; E=148 ±12 inches; F=39 ±3 inches; G = > 28 inches; H = 63 ±4 inches; O=43 ±4 inches; (M+N)/2=67 ±1.5 inches

GVWR Ratings:	Mass: lb	Curb	Test Inertial	Gross Static
Front <u>3700</u>	M _{front}	<u>2895</u>	<u>2822</u>	<u>2907</u>
Back <u>3900</u>	M _{rear}	<u>2040</u>	<u>2183</u>	<u>2263</u>
Total <u>6700</u>	M _{Total}	<u>4935</u>	<u>5005</u>	<u>5170</u>

(Allowable Range for TIM and GSM = 5000 lb ±110 lb)

Mass Distribution:
 lb LF: 1420 RF: 1402 LR: 1098 RR: 1085

**Table D.2. Measurements of Vehicle Vertical Center of Gravity for
Test No. 469760-06-2.**

Date: 2020-6-4 Test No.: 469760-6-2 VIN: 1C6RR6FT3FS505939
 Year: 2015 Make: RAM Model: 1500
 Body Style: Quad Cab Mileage: 116212
 Engine: 5.7L V-8 Transmission: Automatic
 Fuel Level: Empty Ballast: 140 (440 lb max)
 Tire Pressure: Front: 35 psi Rear: 35 psi Size: 265/70 R 17

Measured Vehicle Weights: (lb)							
LF:	1420		RF:	1402		Front Axle:	2822
LR:	1098		RR:	1085		Rear Axle:	2183
Left:	2518		Right:	2487		Total:	5005
							5000 ±110 lb allowed
Wheel Base:	140.50	inches	Track: F:	68.50	inches	R:	68.00 inches
148 ±12 inches allowed			Track = (F+R)/2 = 67 ±1.5 inches allowed				
Center of Gravity, SAE J874 Suspension Method							
X:	61.28	inches	Rear of Front Axle	(63 ±4 inches allowed)			
Y:	-0.21	inches	Left - Right +	of Vehicle Centerline			
Z:	28.25	inches	Above Ground	(mininum 28.0 inches allowed)			

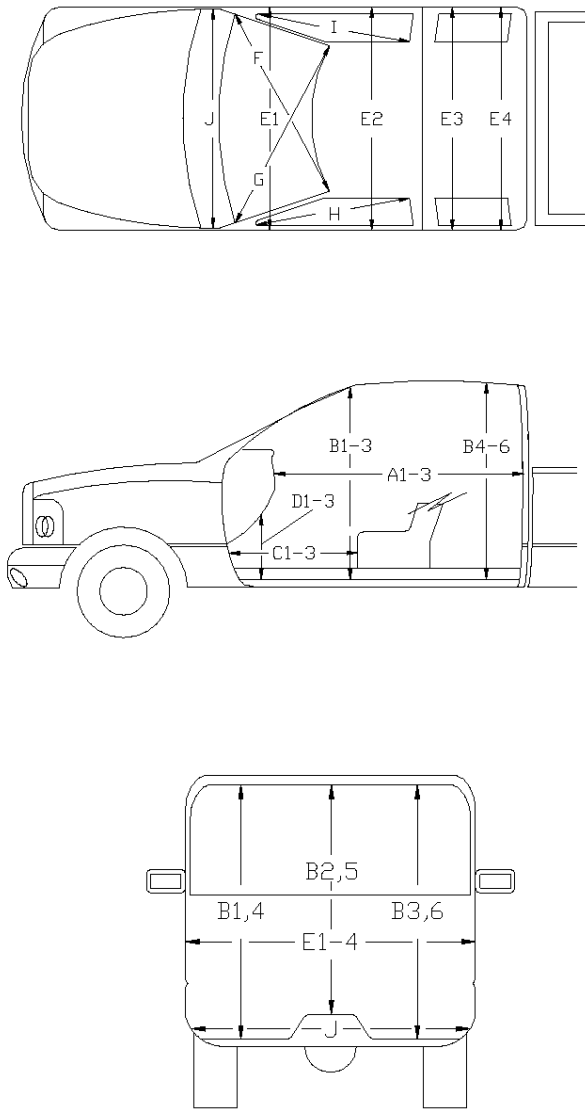
Hood Height: 46.00 inches Front Bumper Height: 27.00 inches
 43 ±4 inches allowed

Front Overhang: 40.00 inches Rear Bumper Height: 30.00 inches
 39 ±3 inches allowed

Overall Length: 227.50 inches
 237 ±13 inches allowed

Table D.4. Occupant Compartment Measurements for Test No. 469760-06-2.

Date: 2020-6-4 Test No.: 469760-6-2 VIN No.: 1C6RR6FT3FS505939
 Year: 2015 Make: RAM Model: 1500



OCCUPANT COMPARTMENT DEFORMATION MEASUREMENT

	Before	After (inches)	Differ.
A1	65.00	65.00	0.00
A2	63.00	63.00	0.00
A3	65.50	65.50	0.00
B1	45.00	45.00	0.00
B2	38.00	38.00	0.00
B3	45.00	45.00	0.00
B4	39.50	39.50	0.00
B5	43.00	43.00	0.00
B6	39.50	39.50	0.00
C1	26.00	24.00	-2.00
C2	0.00	0.00	0.00
C3	26.00	26.00	0.00
D1	11.00	11.00	0.00
D2	0.00	0.00	0.00
D3	11.50	11.50	0.00
E1	58.50	59.00	0.50
E2	63.50	64.5	1.00
E3	63.50	63.50	0.00
E4	63.50	63.50	0.00
F	59.00	59.00	0.00
G	59.00	59.00	0.00
H	37.50	37.50	0.00
I	37.50	37.50	0.00
J*	25.00	23.00	-2.00

*Lateral area across the cab from driver's side kickpanel to passenger's side kickpanel.

D.2 SEQUENTIAL PHOTOGRAPHS

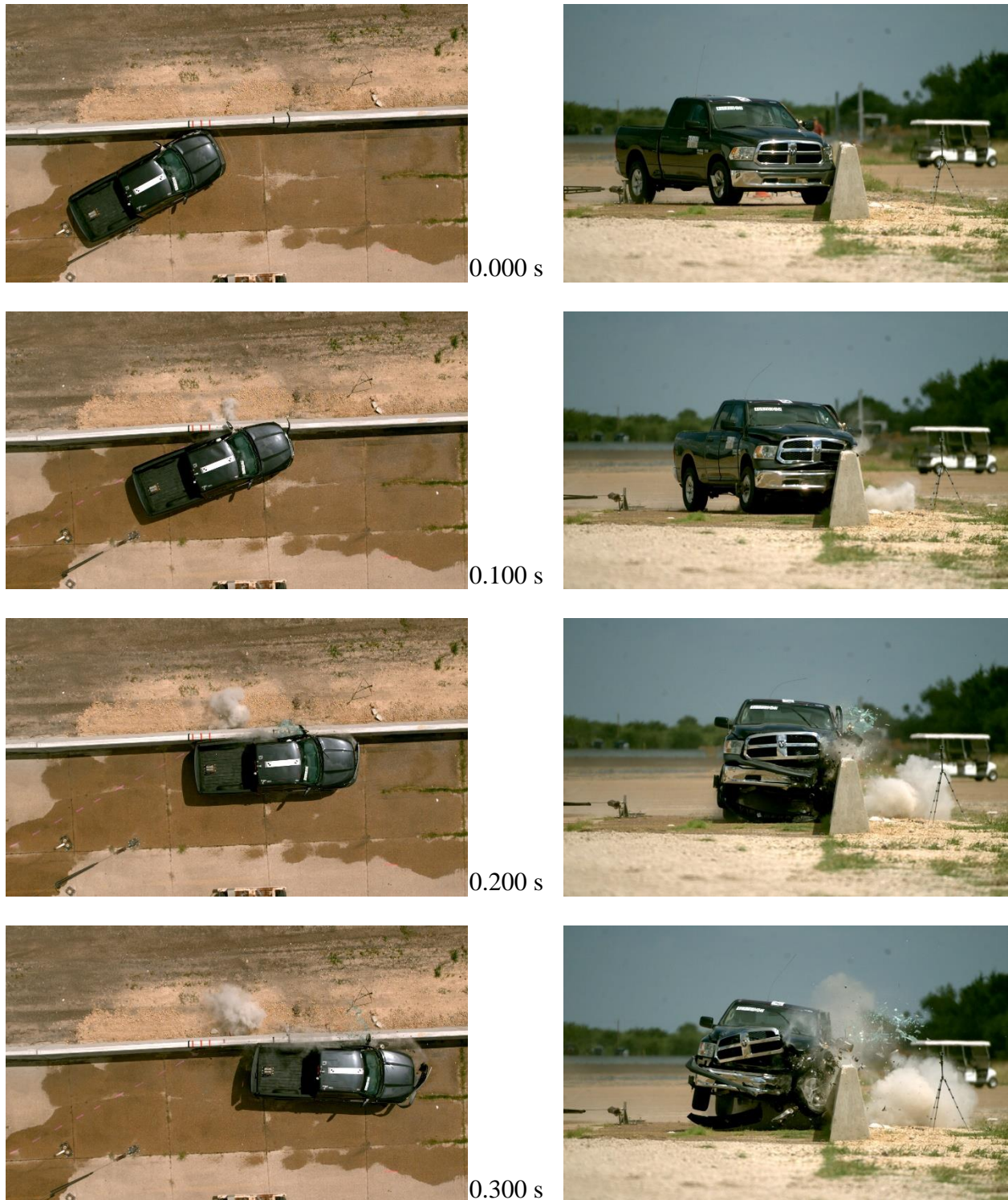


Figure D.1. Sequential Photographs for Test No. 469760-06-2 (Overhead and Frontal Views).



0.400 s



0.500 s



0.600 s



0.700 s



Figure D.1. Sequential Photographs for Test No. 469760-06-2 (Overhead and Frontal Views) (Continued).



0.000 s



0.400 s



0.100 s



0.500 s



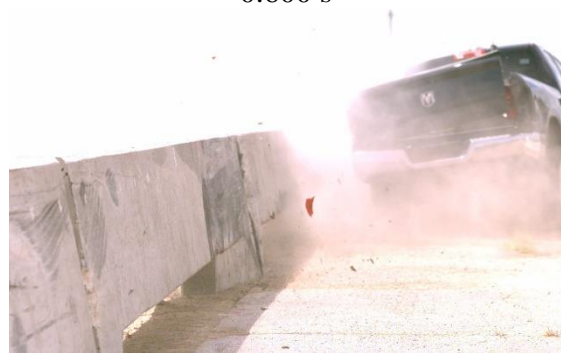
0.200 s



0.600 s

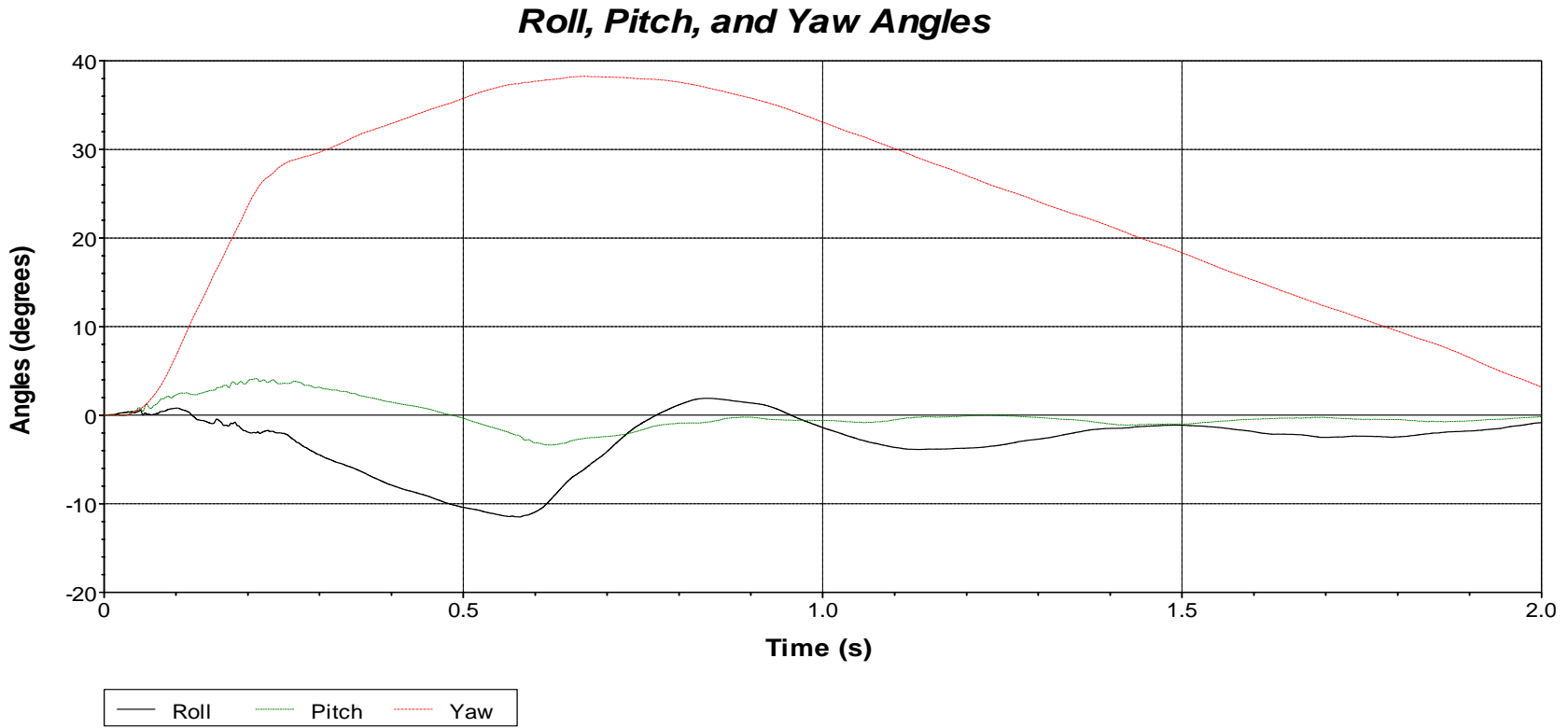


0.300 s



0.700 s

Figure D.2. Sequential Photographs for Test No. 469760-06-2 (Rear View).



Axes are vehicle-fixed.
Sequence for determining orientation:

1. Yaw.
2. Pitch.
3. Roll.

Test Number: 469760-06-2
 Test Standard Test Number: *MASH* Test 4-11
 Test Article: TxDOT Large-Scupper Median Barrier
 Test Vehicle: 2015 RAM 1500 Pickup
 Inertial Mass: 5005 lb
 Gross Mass: 5170 lb
 Impact Speed: 63.4 mi/h
 Impact Angle: 25.2°

Figure D.3. Vehicle Angular Displacements for Test No. 469760-06-2.

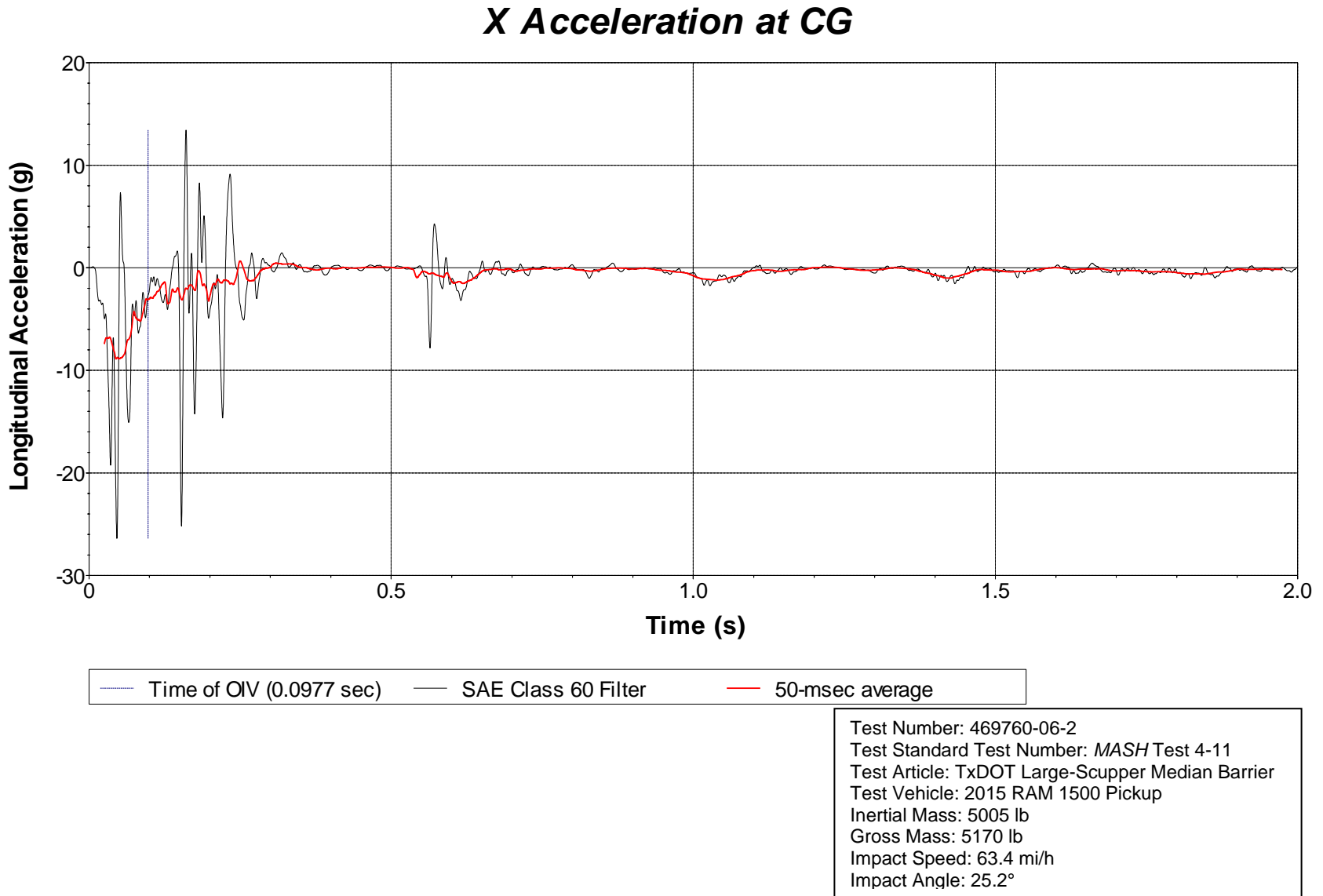
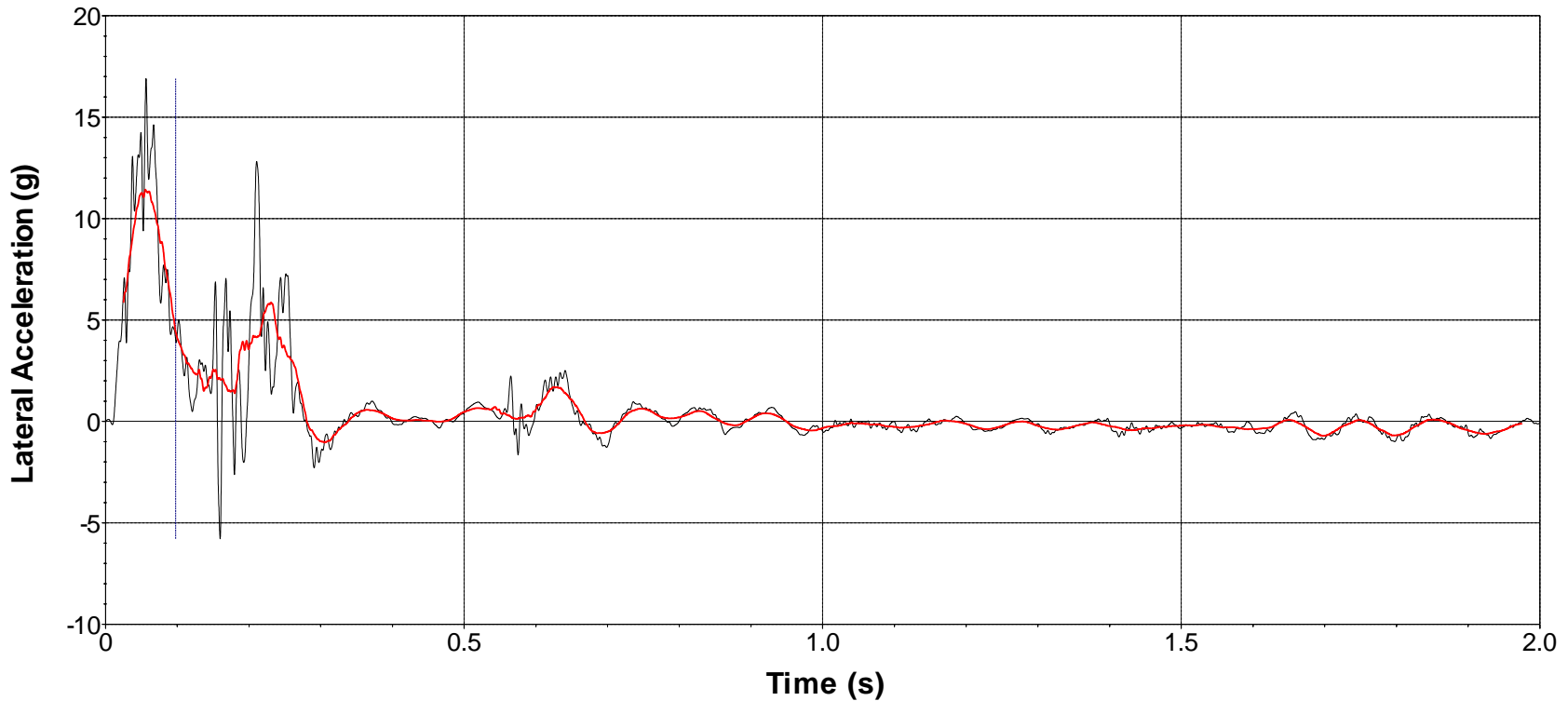


Figure D.4. Vehicle Longitudinal Accelerometer Trace for Test No. 469760-06-2 (Accelerometer Located at Center of Gravity).

Y Acceleration at CG

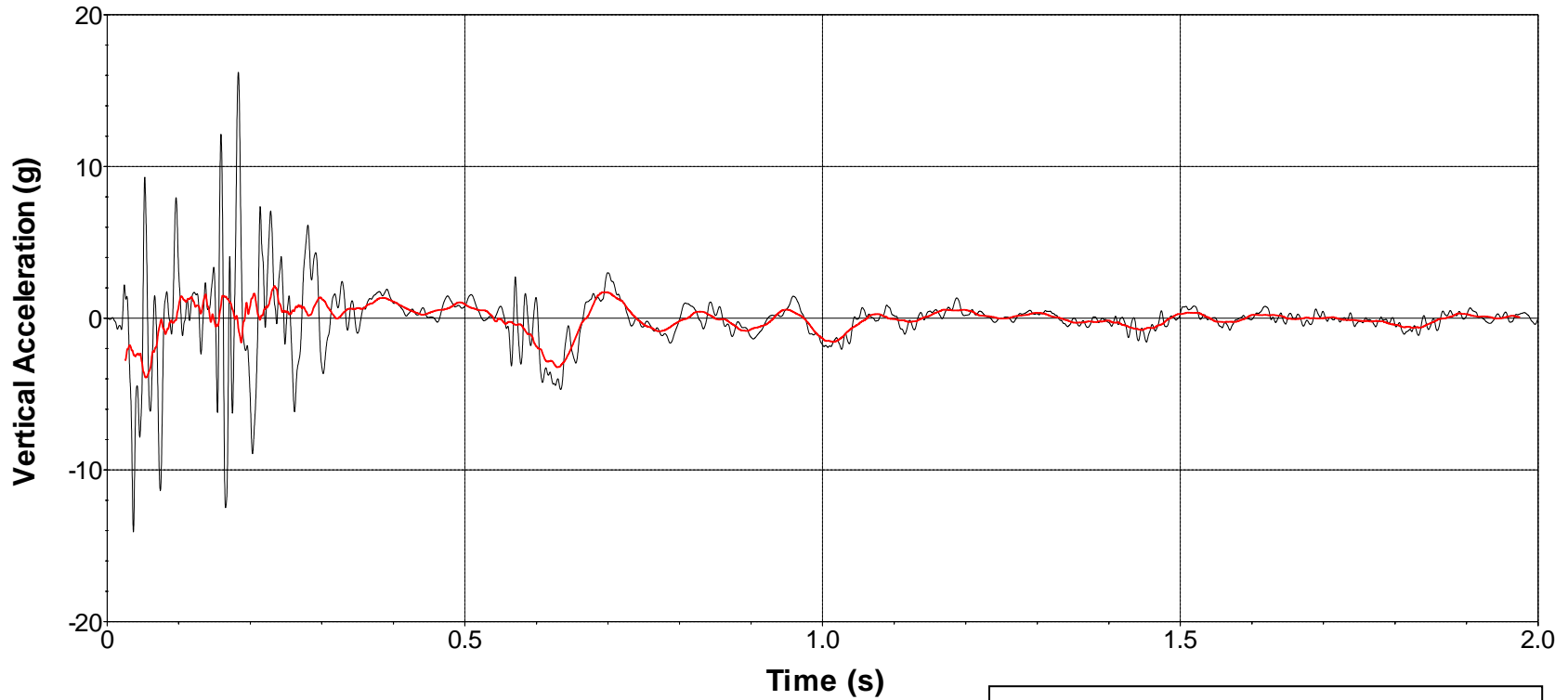


Time of OIV (0.0977 sec) SAE Class 60 Filter 50-msec average

Test Number: 469760-06-2
Test Standard Test Number: MASH Test 4-11
Test Article: TxDOT Large-Scupper Median Barrier
Test Vehicle: 2015 RAM 1500 Pickup
Inertial Mass: 5005 lb
Gross Mass: 5170 lb
Impact Speed: 63.4 mi/h
Impact Angle: 25.2°

Figure D.5. Vehicle Lateral Accelerometer Trace for Test No. 469760-06-2 (Accelerometer Located at Center of Gravity).

Z Acceleration at CG



— SAE Class 60 Filter — 50-msec average

Test Number: 469760-06-2
Test Standard Test Number: *MASH* Test 4-11
Test Article: TxDOT Large-Scupper Median Barrier
Test Vehicle: 2015 RAM 1500 Pickup
Inertial Mass: 5005 lb
Gross Mass: 5170 lb
Impact Speed: 63.4 mi/h
Impact Angle: 25.2°

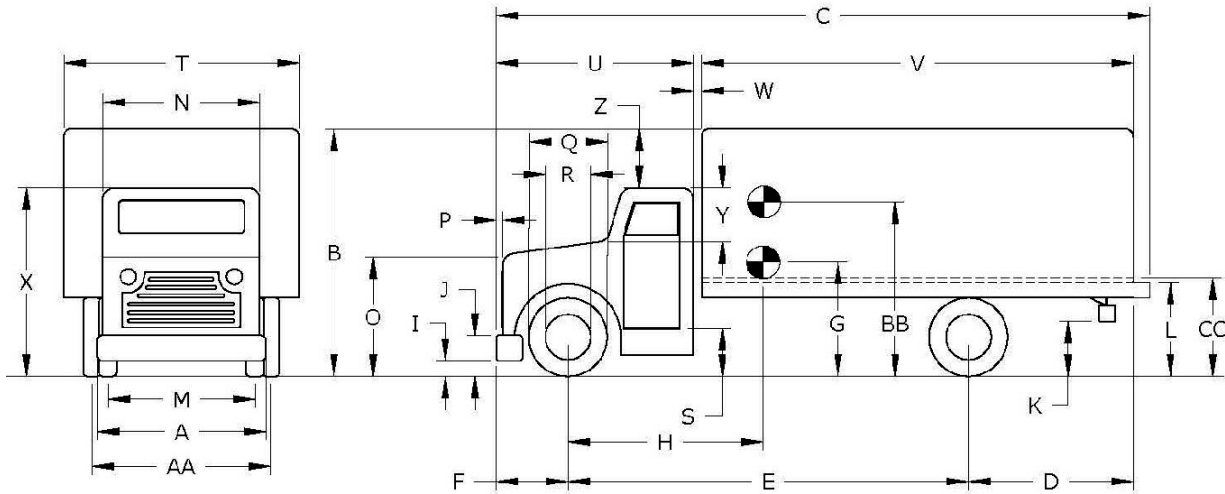
**Figure D.6. Vehicle Vertical Accelerometer Trace for Test No. 469760-06-2
(Accelerometer Located at Center of Gravity).**

APPENDIX E. MASH TEST 4-12 (CRASH TEST NO. 469760-06-3)

E.1 VEHICLE PROPERTIES AND INFORMATION

Table E.1. Vehicle Properties for Test No. 469760-06-3.

Date:	2020-6-2	Test No.:	469760-6-3	VIN No.:	3HAMMAANODL179005
Year:	2013	Make:	INTERNATIONAL	Model:	4300
Odometer:	140773	Tire Size Front:	275/80R22.5	Tire Size Rear:	275/80R22.5



Vehicle Geometry:		<input checked="" type="checkbox"/> inches	or	<input type="checkbox"/> mm		
A	Front Bumper Width:	92.50		K	Rear Bumper Bottom:	
B	Overall Height:	150.00		L	Rear Frame Top:	37.00
C	Overall Length:	330.10		M	Front Track Width:	80.00
D	Rear Overhang:	84.00		N	Roof Width:	71.00
E	Wheel Base:	206.60		O	Hood Height:	59.00
F	Front Overhang:	39.50		P	Bumper Extension:	
G	C.G. Height:			Q	Front Tire Width:	39.00
H	C.G. Horizontal Dist. w/Ballast:	128.10		R	Front Wheel Width:	23.50
I	Front Bumper Bottom:	18.50		S	Bottom Door Height:	37.50
J	Front Bumper Top:	33.50		T	Overall Width:	101.75
				U	Cab Length:	106.00
				V	Trailer/Box Length:	221.50
				W	Gap Width:	2.00
				X	Overall Front Height:	98.50
				Y	Roof-Hood Distance:	30.00
				Z	Roof-Box Height Difference:	51.50
				AA	Rear Track Width:	73.00
				BB	Ballast Center of Mass:	61.50
				CC	Cargo Bed Height:	49.00
Allowable Range: C = 394 inches max.; E = 240 inches max.; CC = 49 ±2 inches; BB = 63 ±2 inches above ground;						
	Wheel Center Height Front	19.00			Wheel Well Clearance (Front)	9.00
	Wheel Center Height Rear	19.00			Wheel Well Clearance (Rear)	2.50
					Bottom Frame Height (Front)	25.50
					Bottom Frame Height (Rear)	27.50

More information needed on next page →

Table E.1. Vehicle Properties for Test No. 469760-06-3 (Continued).

Date: 2020-6-2 Test No.: 469760-6-3 VIN No.: 3HAMMAANODL179005
 Year: 2013 Make: INTERNATIONAL Model: 4300

WEIGHTS

(lb or kg)

	CURB	TEST INERTIAL
$W_{\text{front axle}}$	<u>7230</u>	<u>8470</u>
$W_{\text{rear axle}}$	<u>6920</u>	<u>13830</u>
W_{TOTAL}	<u>14150</u>	<u>22300</u>

Allowable Range for CURB = 13,200 ±2200 lb | Allowable Range for TIM = 22,046 ±660 lb

Ballast: 8150 (lb or kg) (as-needed)
(See MASH Section 4.2.1.2 for recommended ballasting)

Mass Distribution

(lb or kg):

LF: 4370 **RF:** 4100 **LR:** 7080 **RR:** 6750

Engine Type: DT Accelerometer Locations (inches or mm)
 Engine Size: 466 **x¹** **y** **z²**

Transmission Type: **Front:** _____
 Auto or Manual **Center:** 128.00 0.00 48.50
 FWD RWD 4WD **Rear:** 228.00 0.00 48.50

Describe any damage to the vehicle prior to test: None

Other notes to include ballast type, dimensions, mass, location, center of mass, and method of attachment:

Two blocks: 30 inches high x 60 inches wide x 30 inches long
Centered in middle of bed
61.5 inches from center of block to ground
Tied down with four 5/16-inch cables per block

Performed by: SCD Date: 2020-06-02

¹ Referenced to the front axle

² Above ground

E.2 SEQUENTIAL PHOTOGRAPHS



0.000 s



0.100 s



0.200 s



0.300 s



Figure E.1. Sequential Photographs for Test No. 469760-06-3 (Overhead and Frontal Views).



0.400 s



0.500 s



0.600 s



0.700 s



Figure E.1. Sequential Photographs for Test No. 469760-06-3 (Overhead and Frontal Views) (Continued).



0.000 s



0.400 s



0.100 s



0.500 s



0.200 s



0.600 s

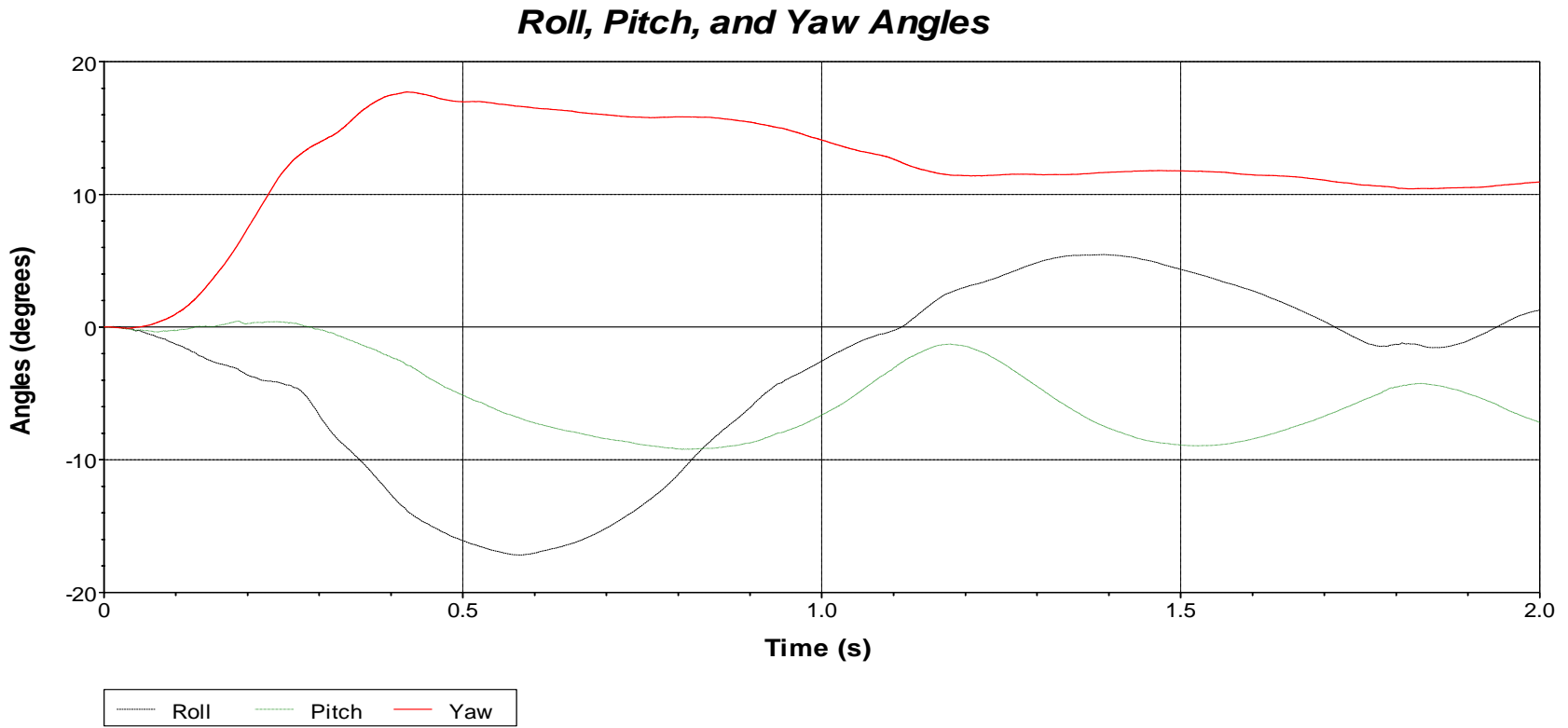


0.300 s



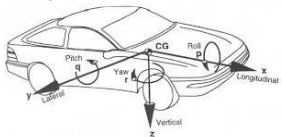
0.700 s

Figure E.2. Sequential Photographs for Test No. 469760-06-3 (Rear View).



Axes are vehicle-fixed.
 Sequence for determining orientation:

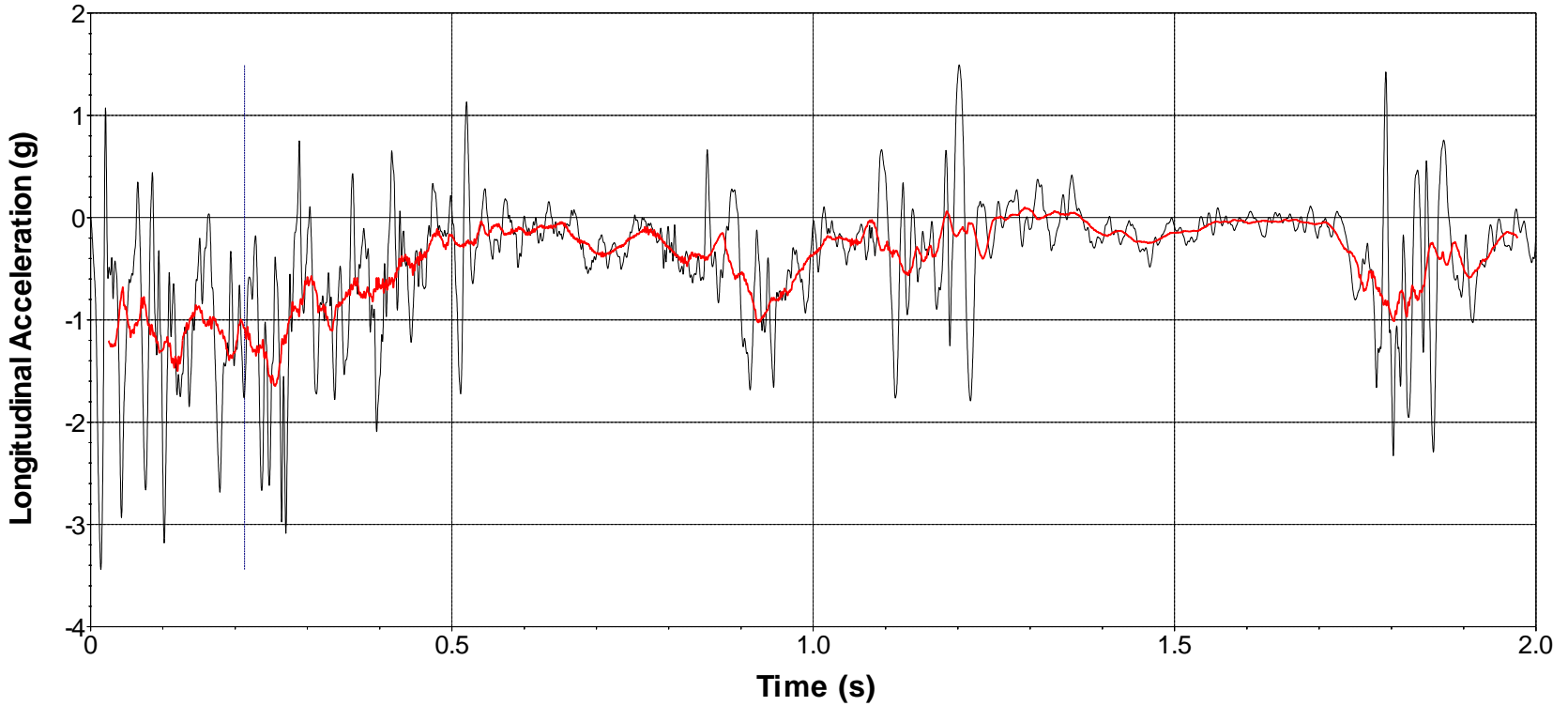
1. Yaw.
2. Pitch.
3. Roll.



Test Number: 469760-06-3
 Test Standard Test Number: *MASH* Test 4-12
 Test Article: TxDOT Large-Scupper Median Barrier
 Test Vehicle: 2013 International 4300 PUT
 Inertial Mass: 22,300 lb
 Gross Mass: 22,300 lb
 Impact Speed: 57.6 mi/h
 Impact Angle: 15.2°

Figure E.3. Vehicle Angular Displacements for Test No. 469760-06-3.

X Acceleration at CG

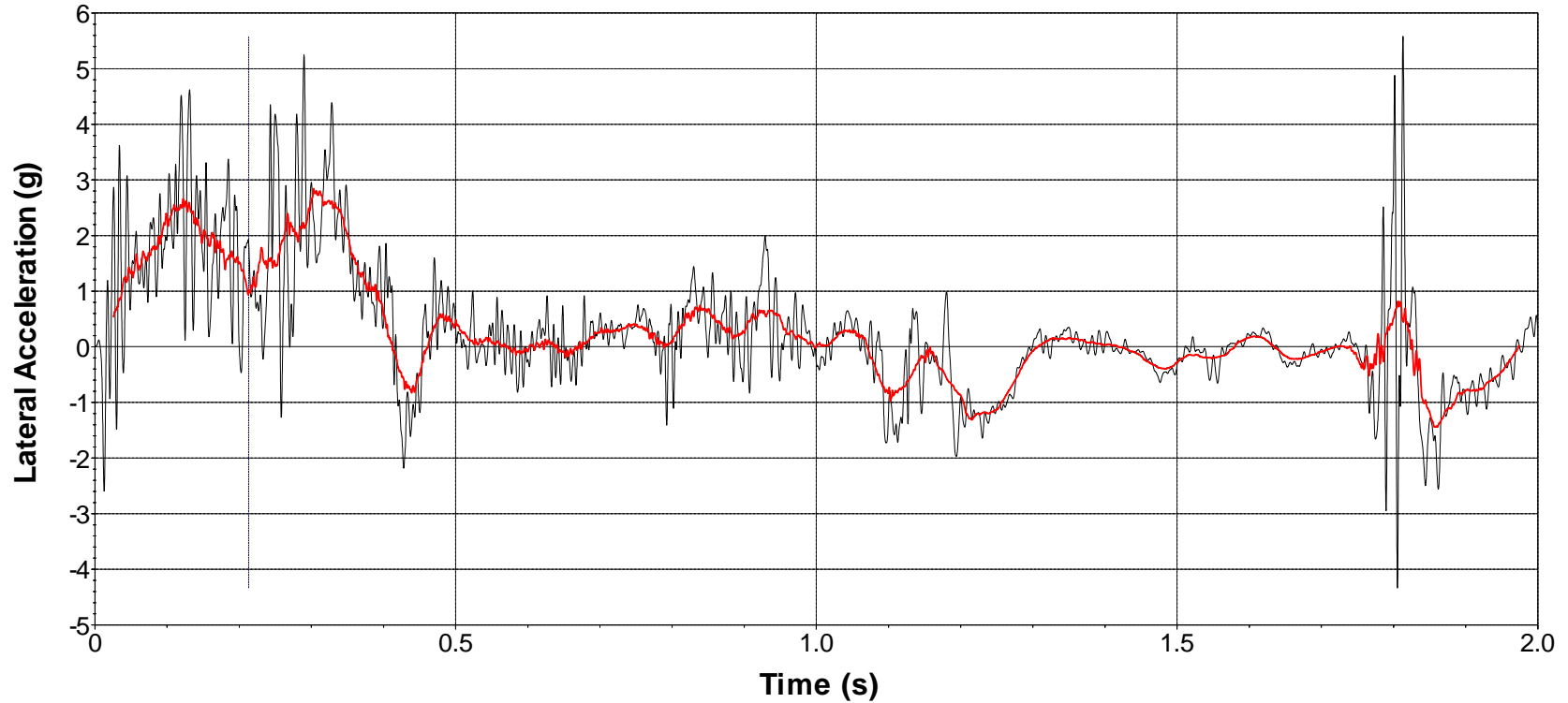


— Time of OIV (0.2131 sec) — SAE Class 60 Filter — 50-msec average

Test Number: 469760-06-3
Test Standard Test Number: MASH Test 4-12
Test Article: TxDOT Large-Scupper Median Barrier
Test Vehicle: 2013 International 4300 PUT
Inertial Mass: 22,300 lb
Gross Mass: 22,300 lb
Impact Speed: 57.6 mi/h
Impact Angle: 15.2°

Figure E.4. Vehicle Longitudinal Accelerometer Trace for Test No. 469760-06-3 (Accelerometer Located at Center of Gravity).

Y Acceleration at CG

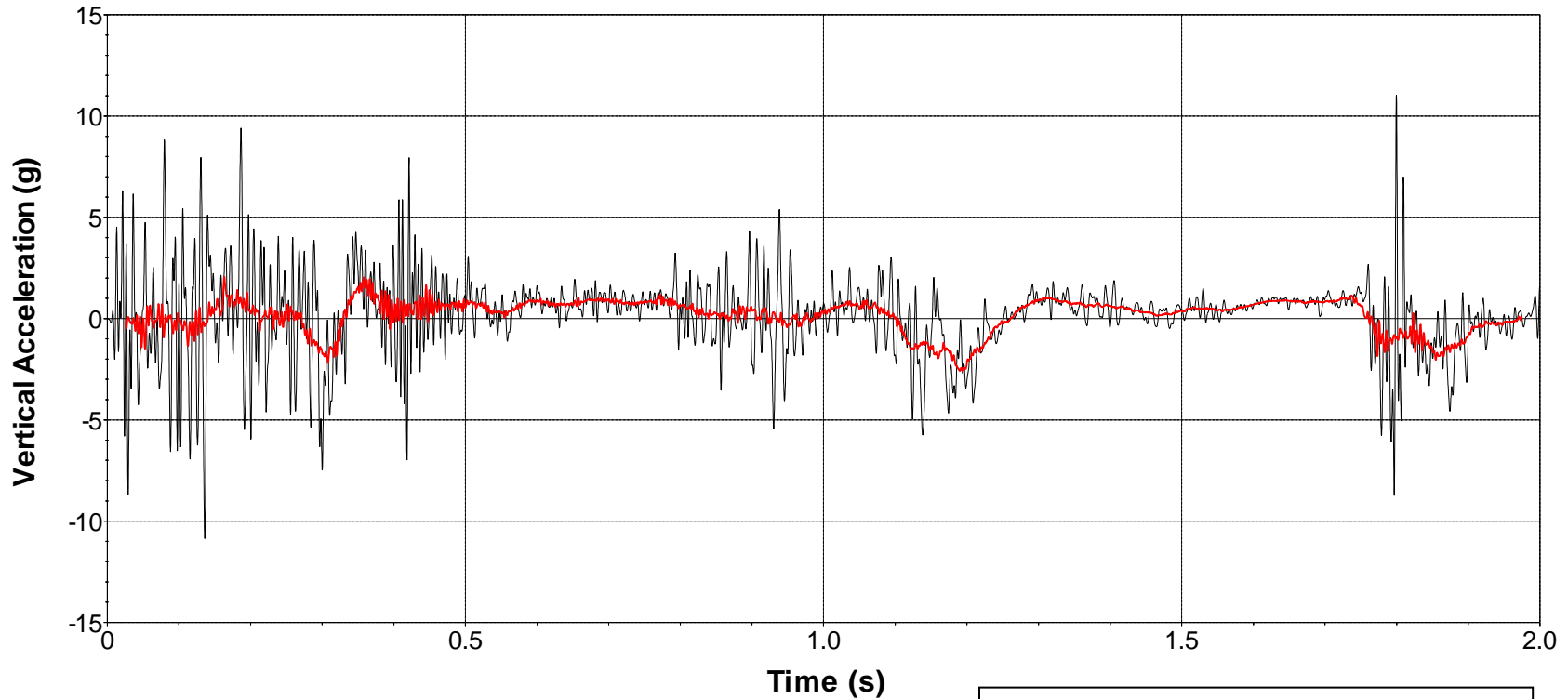


— Time of OIV (0.2131 sec) — SAE Class 60 Filter — 50-msec average

Test Number: 469760-06-3
Test Standard Test Number: *MASH* Test 4-12
Test Article: TxDOT Large-Scupper Median Barrier
Test Vehicle: 2013 International 4300 PUT
Inertial Mass: 22,300 lb
Gross Mass: 22,300 lb
Impact Speed: 57.6 mi/h
Impact Angle: 15.2°

Figure E.5. Vehicle Lateral Accelerometer Trace for Test No. 469760-06-3 (Accelerometer Located at Center of Gravity).

Z Acceleration at CG

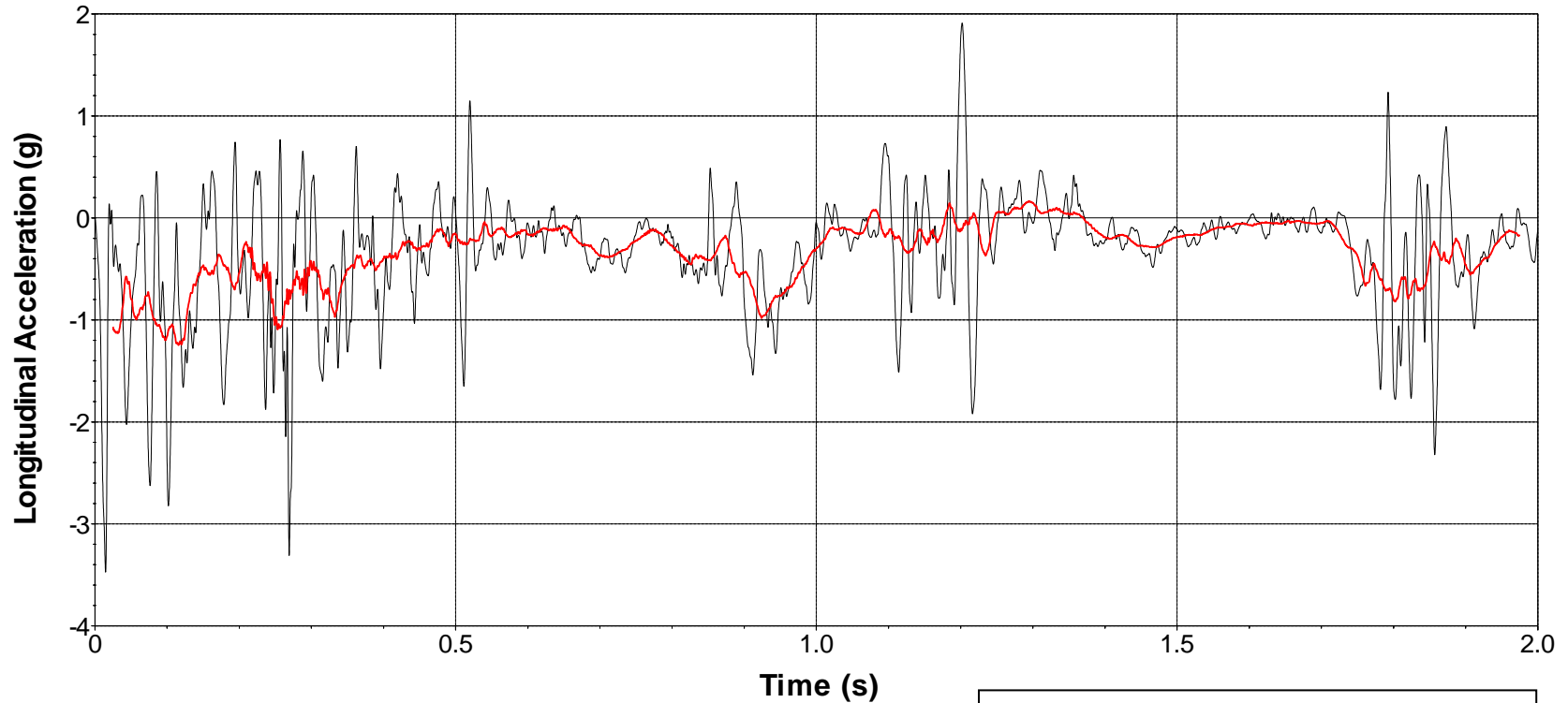


— SAE Class 60 Filter — 50-msec average

Test Number: 469760-06-3
Test Standard Test Number: *MASH* Test 4-12
Test Article: TxDOT Large-Scupper Median Barrier
Test Vehicle: 2013 International 4300 PUT
Inertial Mass: 22,300 lb
Gross Mass: 22,300 lb
Impact Speed: 57.6 mi/h
Impact Angle: 15.2°

**Figure E.6. Vehicle Vertical Accelerometer Trace for Test No. 469760-06-3
(Accelerometer Located at Center of Gravity).**

X Acceleration at Rear of Vehicle

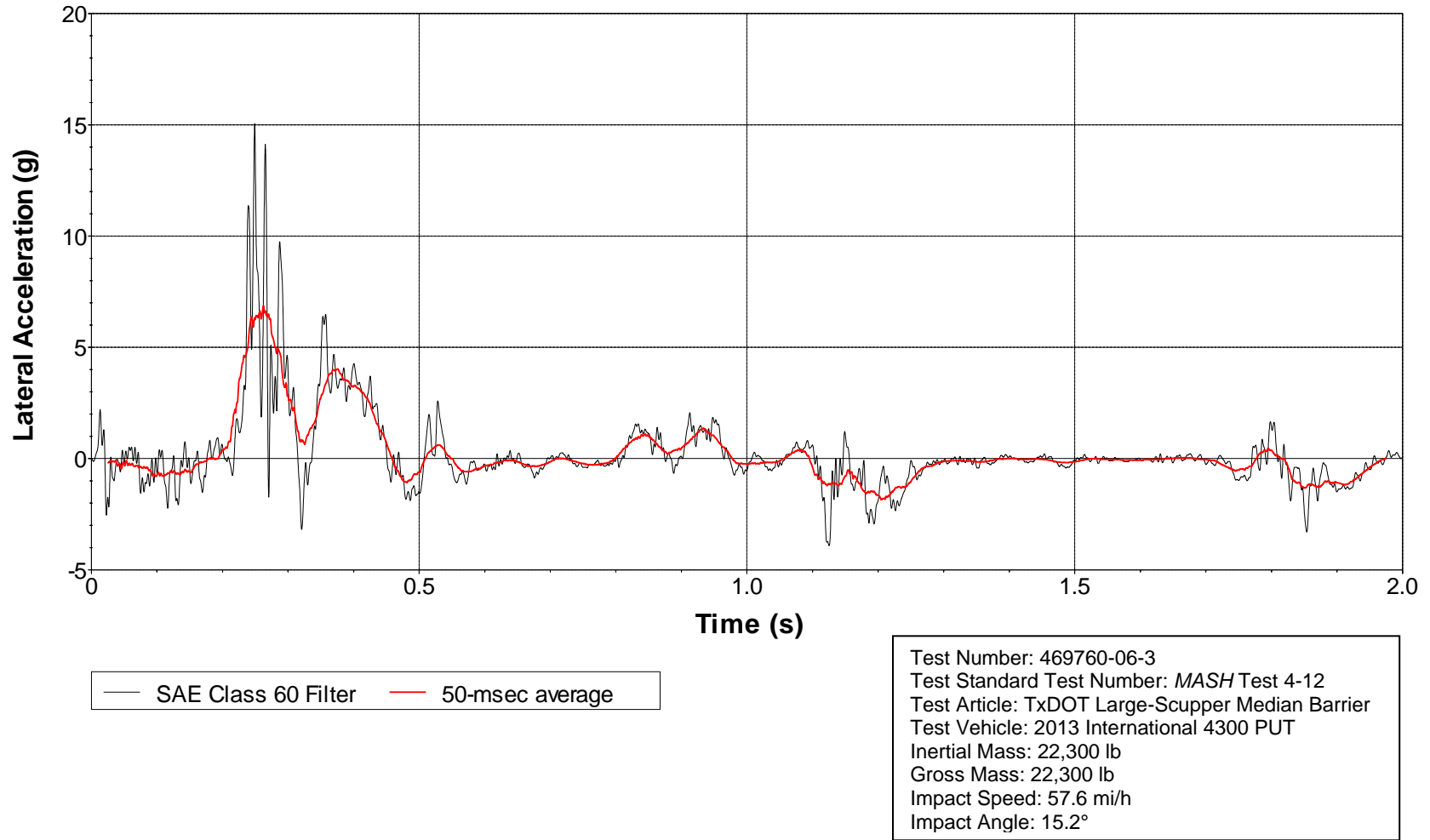


— SAE Class 60 Filter — 50-msec average

Test Number: 469760-06-3
 Test Standard Test Number: *MASH* Test 4-12
 Test Article: TxDOT Large-Scupper Median Barrier
 Test Vehicle: 2013 International 4300 PUT
 Inertial Mass: 22,300 lb
 Gross Mass: 22,300 lb
 Impact Speed: 57.6 mi/h
 Impact Angle: 15.2°

Figure E.7. Vehicle Longitudinal Accelerometer Trace for Test No. 469760-06-3 (Accelerometer Located at Rear of Vehicle).

Y Acceleration at Rear of Vehicle



**Figure E.8. Vehicle Lateral Accelerometer Trace for Test No. 469760-06-3
(Accelerometer Located at Rear of Vehicle).**

Z Acceleration at Rear of Vehicle

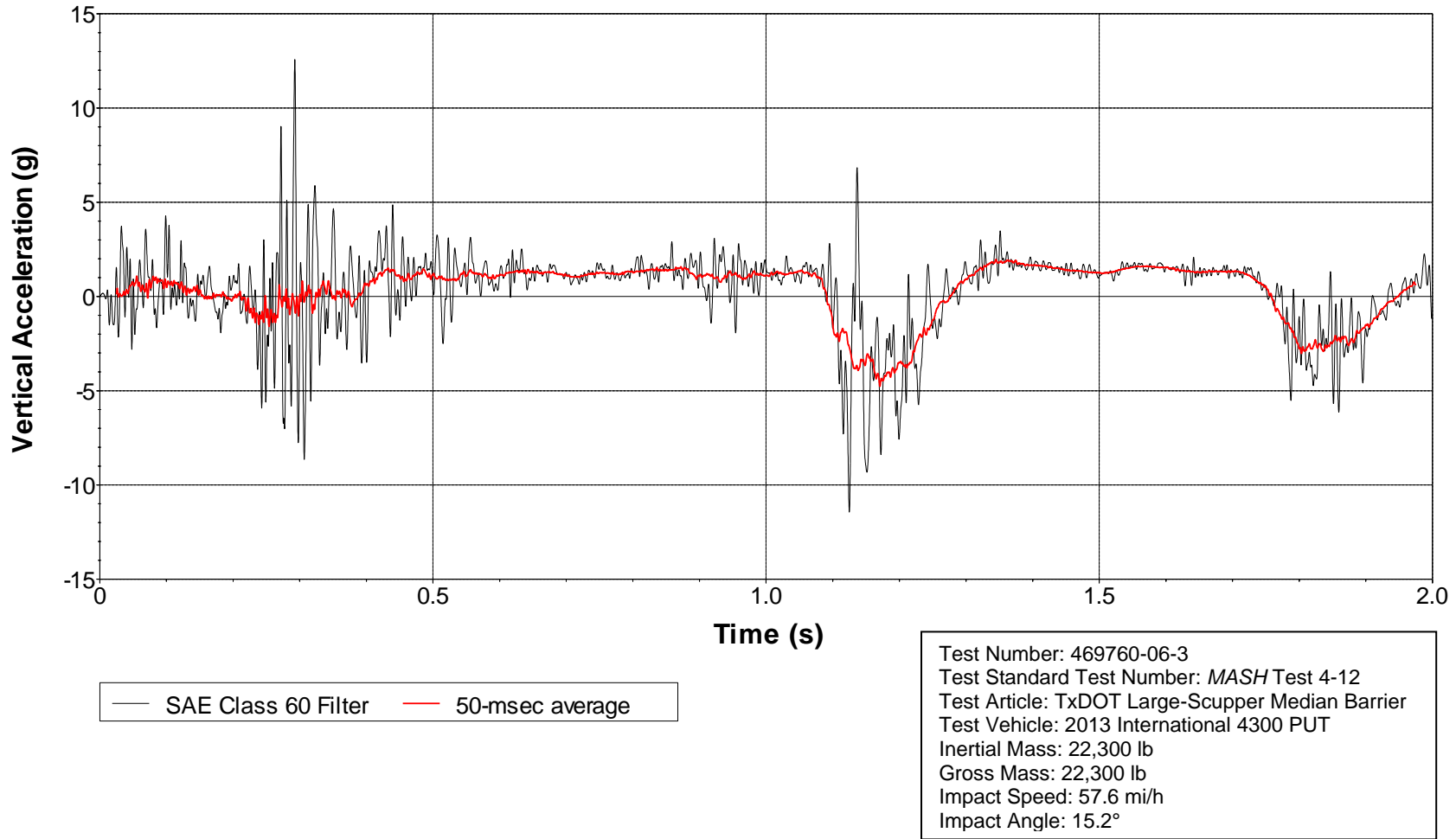
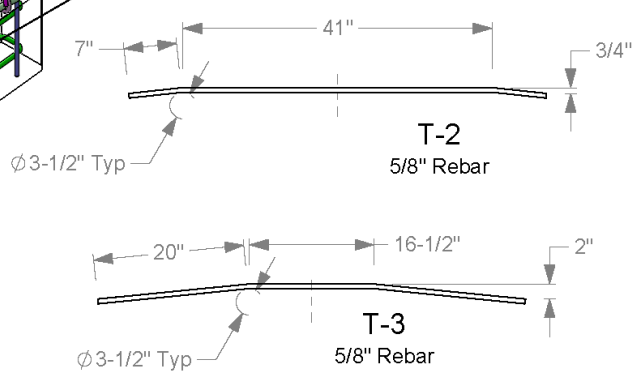
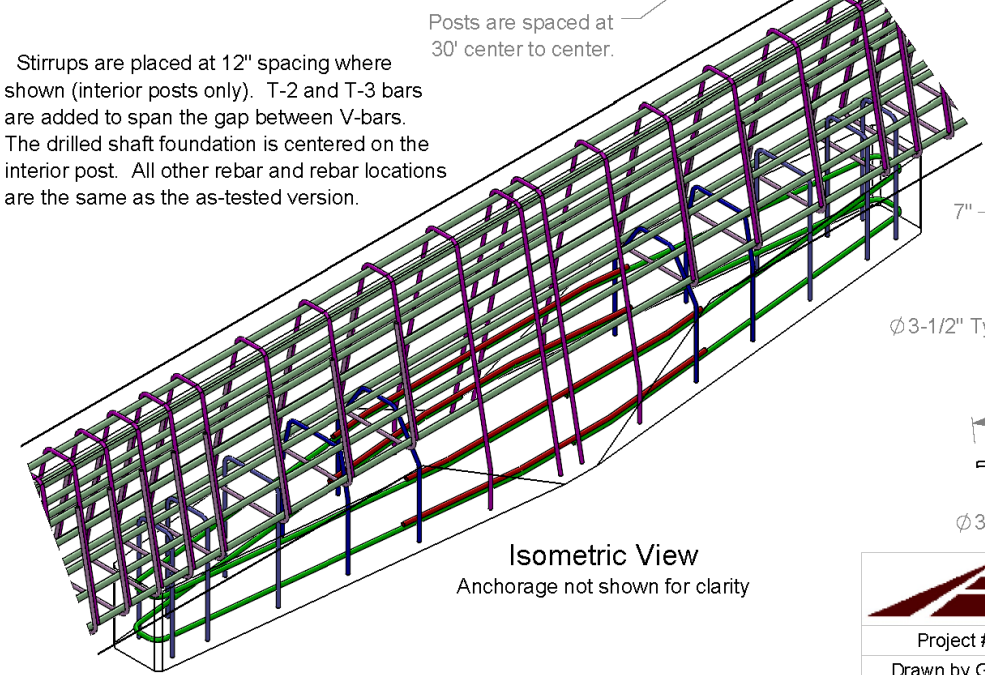
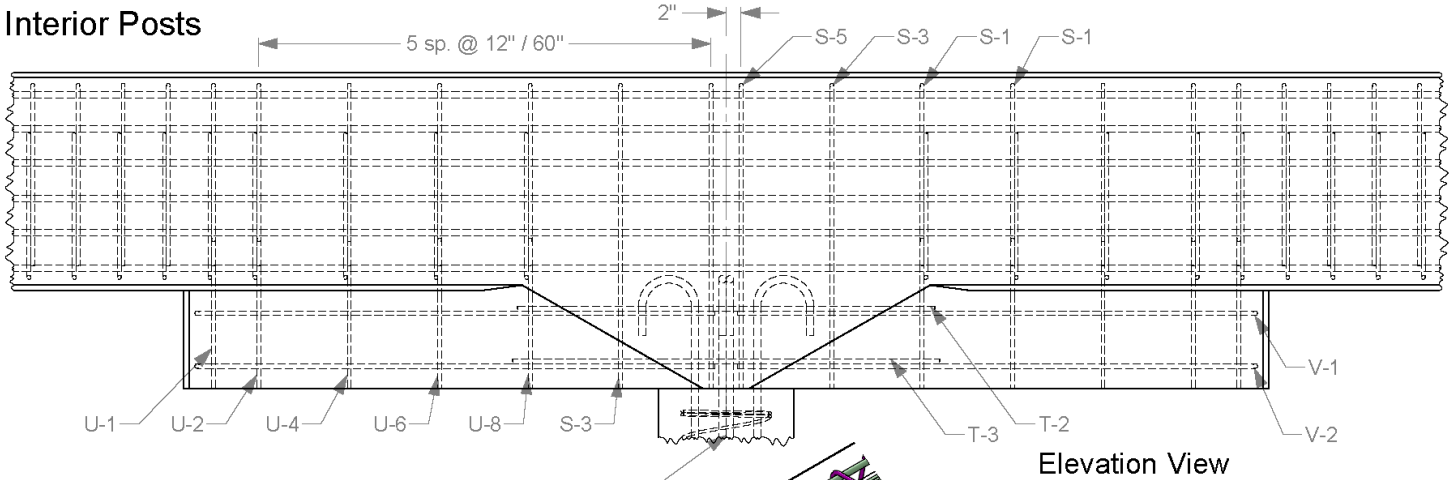
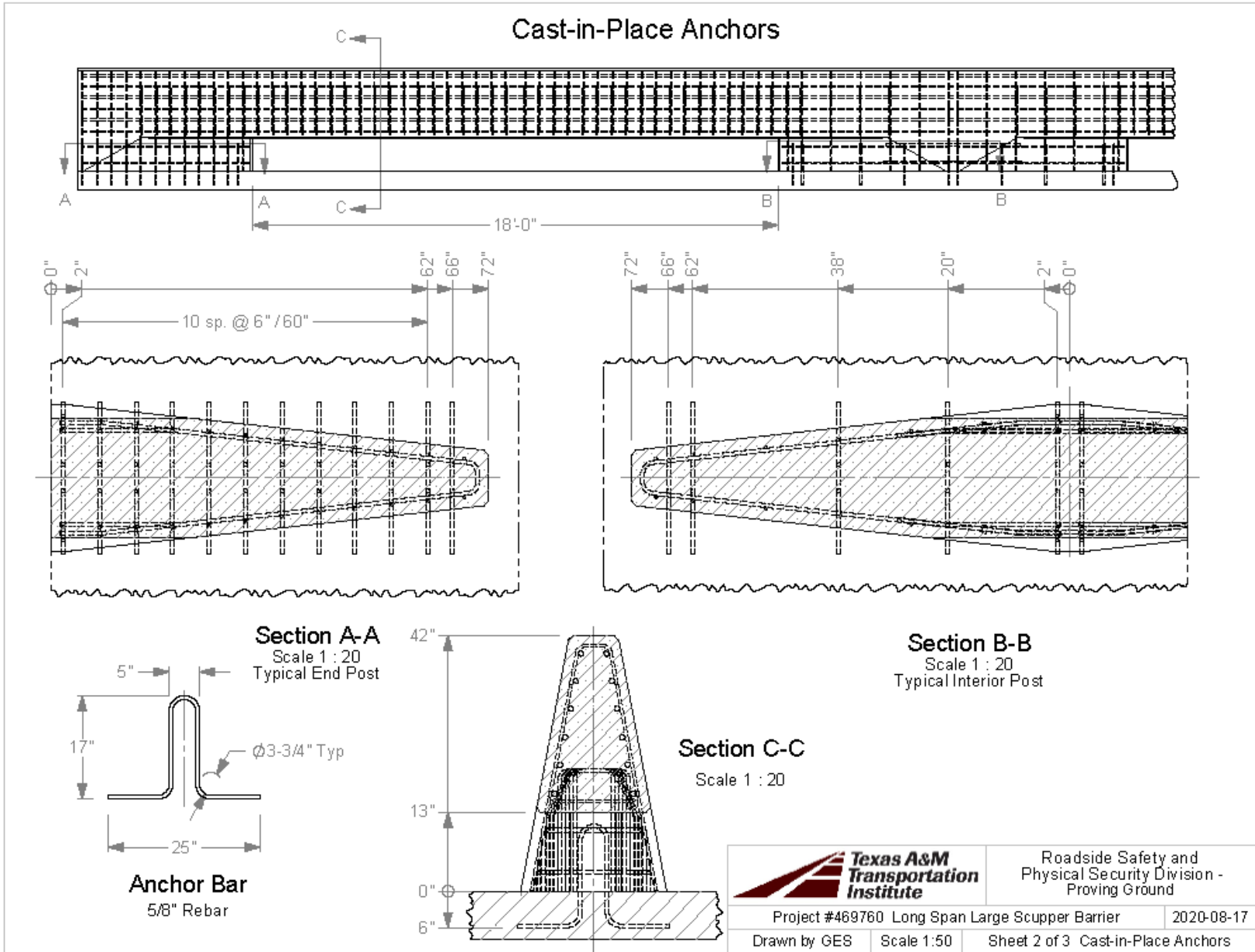


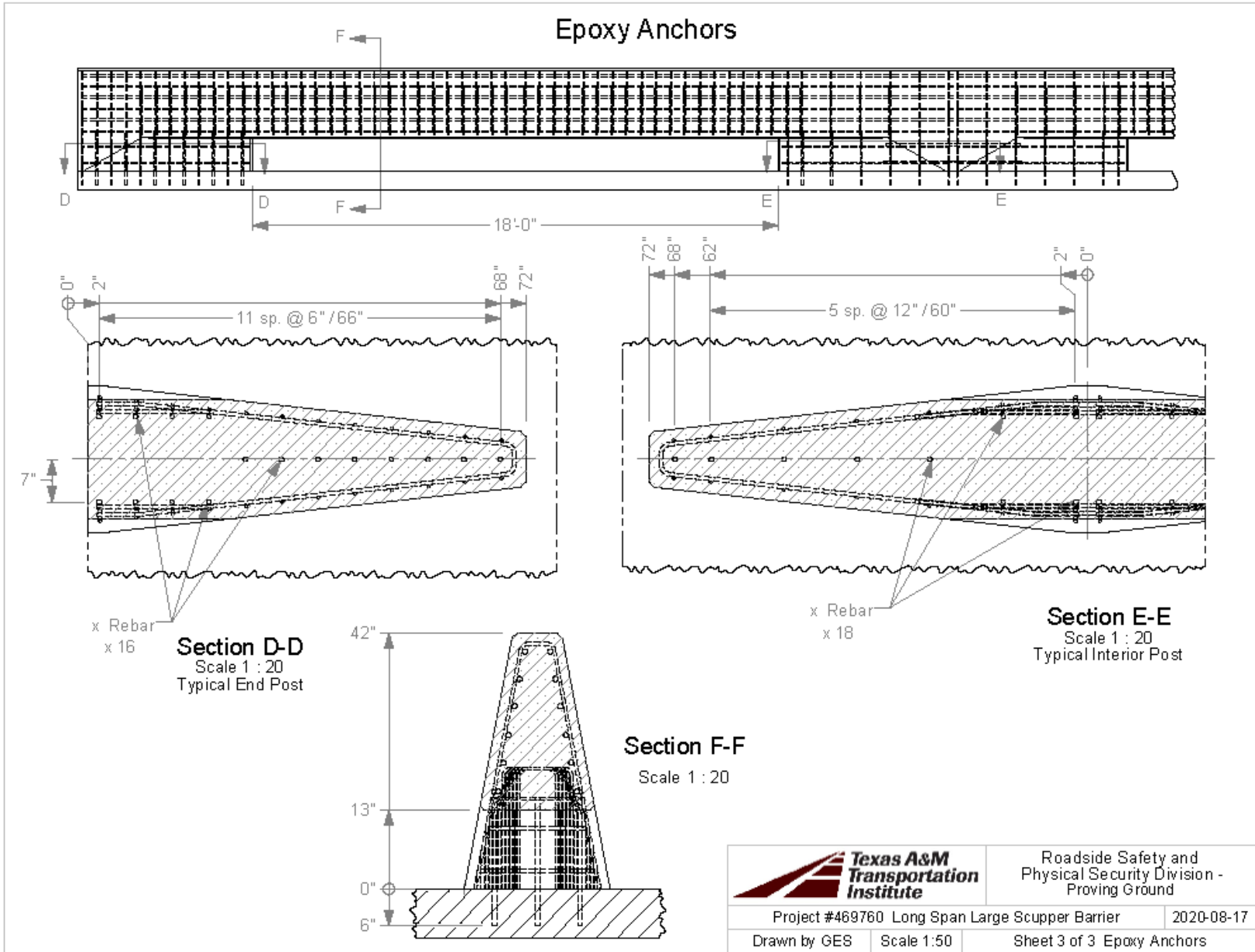
Figure E.9. Vehicle Vertical Accelerometer Trace for Test No. 469760-06-3 (Accelerometer Located at Rear of Vehicle).

**APPENDIX F. DETAILS FOR LONGER SEGMENT LENGTHS AND
CAST-IN-PLACE AND EPOXY REBAR ANCHOR OPTIONS FOR
TXDOT L5MB**



		Roadside Safety and Physical Security Division - Proving Ground	
		Project #469760 Long Span Large Scupper Barrier	2020-08-17
Drawn by GES	Scale 1:20	Sheet 1 of 3 Interior Posts	





Roadside Safety and Physical Security Division - Proving Ground

Project #469760 Long Span Large Scupper Barrier		2020-08-17
Drawn by GES	Scale 1:50	Sheet 3 of 3 Epoxy Anchors

APPENDIX G. VALUE OF RESEARCH ESTIMATE

G.1 INTRODUCTION

In accordance with the scope of TxDOT Project 0-6976, *Development of Concrete Median Barriers for Flood-Prone Areas*, the research teams at TTI and CTR have prepared an estimate for the VoR associated with the research products delivered for this project.

The benefit areas deemed relevant and identified in the project agreement for the purpose of establishing the VoR encompass both qualitative and economic areas. The benefit areas identified for this project are summarized in Table G.1.

Table G.1. Selected Benefit Areas for Project 0-6976.

Selected	Benefit Area	Qual	Econ	Both	TxDOT	State	Both
	Level of Knowledge	X			X		
	Management and Policy	X			X		
	Quality of Life	X			X		
	Customer Satisfaction	X			X		
	Environmental Sustainability	X				X	
X	System Reliability		X		X		
	Increased Service Life		X		X		
	Improved Productivity and Work Efficiency		X		X		
	Expedited Project Delivery		X		X		
	Reduced Administrative Costs		X		X		
	Traffic and Congestion Reduction		X			X	
	Reduced User Cost		X			X	
	Reduced Construction, Operations, and Maintenance Cost		X			X	
	Materials and Pavements		X			X	
X	Infrastructure Condition		X				X
	Freight Movement and Economic Vitality		X				X
	Intelligent Transportation Systems		X				X
X	Engineering Design Improvement			X			X
X	Safety			X			X

G.2 QUALITATIVE BENEFIT AREAS

G.2.1 Engineering Design Development/Improvement

One of the primary outcomes to Project 0-6976 was to provide rating curves highlighting the relative hydraulic efficiency of a novel concrete median barrier designed uniquely for this

project to reduce highway flooding in comparison to existing barrier designs with openings already used by TxDOT in various applications. These rating curves need to be determined experimentally on a case-by-case basis. The testing of several barrier types, with and without model overlays indicative of future highway maintenance, allows researchers to use these rating curves as a reference for implementation of these barriers without need for further experimental testing.

G.2.2 Safety

Flooded highways negatively affect safety for road users in Texas. At best, traffic may be diverted to alternate and unfamiliar routes. Drivers attempting to navigate flooded highways are at an increased likelihood of being involved in a crash, causing possible harm or injury to themselves and to others, including property and infrastructure damage that may have longstanding consequences.

G.3 ECONOMIC BENEFITS

Economic analysis pertaining to four functional areas relevant to the performance of this project and identified in the project agreement was requested.

- System Reliability.
- Infrastructure Condition.
- Engineering Design Improvement.
- Safety.

For analyzing these functional areas, the research team generated Figure G.1. The considerations that went into the computation of the VoR (explained in greater detail below) can be summarized as follows.

If a road is flooded, it cannot be used. This reduces commercial transport of goods and services. This problem is exacerbated when (a) significant distances of highway are closed, (b) segments are closed for substantial amounts of time, or (c) some combination thereof. Personal travel is also impacted, which can range from mere inconveniences and delays to more substantial health outcomes.

A significant flooding event can result in many detrimental effects to the highway condition. For example, there is an increased risk of potholes, washouts, or other damage to the highway surface that require repair or replacement. In coastal regions, there may be affects associated with saline or brackish water intruding inland during an extreme storm event. There is also risk of debris accumulating on roadways, which requires manual or machine-assisted removal. Further, as in the case of Hurricane Harvey, when explosives were used to remove a portion of the median barriers that were contributing to upstream flooding, follow-up repair may be required to return the highway to its normal functioning condition.

In addition to concerns associated with the roadway itself, upstream flooding exacerbated by the damming effect of highway median barriers can persist through commercial and residential zones adjacent to the highway. The cost to such regions can be significant and is highly variable by region, depending on topography (i.e., likelihood to flood) and level of development (commercial, residential, medical, industrial, etc.).

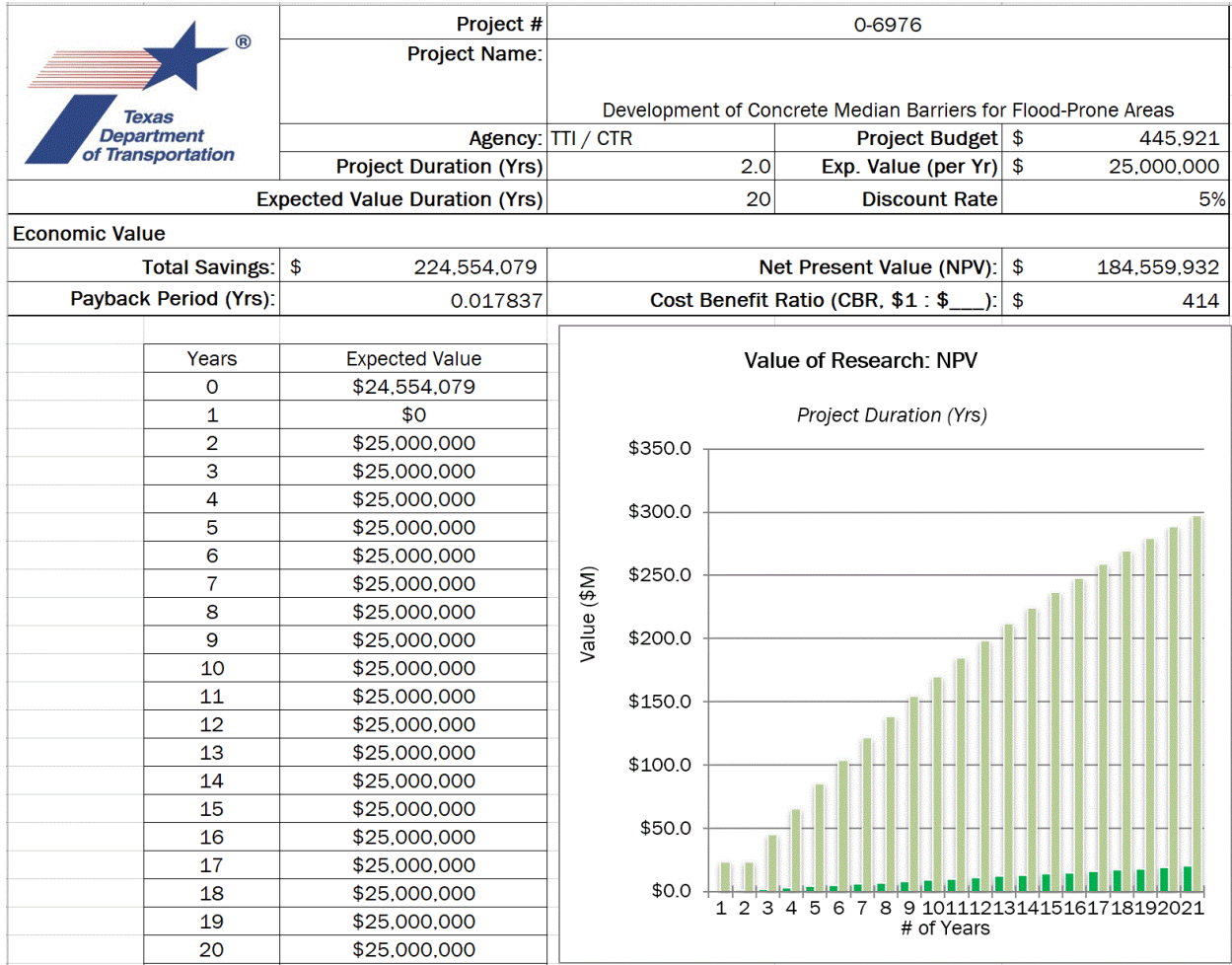


Figure G.1. Summary of VoR Calculations for Project 0-6976.

G.4 COMPUTED VOR

The values assigned in Figure G.1 are attributed to two primary sources:

- The costs attributed to reduction in accidents in suboptimal (i.e., wet or submerged) roadway conditions leading to personal injury or fatality.
- The economic cost resulting from loss of commerce, transit, and so forth due to highway closures during sustained flooding caused by damming effects of a traditional solid concrete median barrier.

These two factors were identified as the leading drivers of quantifiable cost savings, and they are detailed below. Also potentially very significant, but difficult to quantify, are the costs to businesses and residences due to upstream flooding in the vicinity of the highway.

According to the Texas Crash Records Information System (CRIS) data for the City of Houston from 2018 and 2019, approximately 14 percent of reported vehicular crashes occurred on roads that were either wet or contained standing water. Of these reported crashes in either wet or standing water conditions, approximately 2 percent of accidents sustained either fatal (type K) or severe personal injury (type A), while 7 percent were of type B (non-incapacitating injury).

The 2020 *Highway Safety Improvement Program Guidelines* assign the cost associated with either a type K or A event to be \$3.6 million, while the cost associated with a B event is equal to \$500,000. Using these values, the total cost associated with the total number of reported crashes with type K, A, and B injuries occurring in either wet or standing water conditions was equal to \$996 million for 2018 and \$934 million for 2019.

While wet roadway conditions are inevitable during and immediately following rainfall, sustained wet roads or roads with standing water can be mitigated by improving drainage of roads. The installation of median barriers with openings will be limited to highways. However, these barriers will improve conditions of standing water on not only the highways on which they are implemented but also the other roads upstream that remain submerged when traditional concrete median barriers result in damming and backwater effects. Supposing the installation of the new median barriers will provide just a 2 percent reduction in overall accidents attributed to either wet or standing water road surface conditions by reducing the likelihood of having sustained wet or standing water conditions on highways or surface roads, there would be a savings incurred of approximately **\$20 million/year**. Note that this cost savings is representative of Houston crash data, but other coastal or low-lying metropolitan areas could see similar benefits.

Data provided by CTR to the TxDOT Austin District estimating incremental user delay cost for highway closure for one direction of IH 35 through Austin was used to estimate a similar effect for a highway in Houston, approximating similar overall usage and cost to users, given the proximity of these two metropolitan regions. Given the greater population and quantity of economic activity in Houston, it seems likely that a road closure for a highway in Houston would impede a larger volume of traffic than a similar incident on IH 35 in Austin, and so actual costs may be higher than estimated.

Assuming a value of lost time of \$23 per hour per user for the year 2020, the following can be calculated for the heaviest usage periods in a typical single day. CTR determined that during the morning peak, the volume of users affected in Austin in 2016 equated to 7,641 person-hours. In the evening, the corresponding value was 5,064 person-hours, and during the early morning period (midnight to 6:00 a.m.), the number was 1,910 person-hours. Assuming a closure of 3 hours during each of these periods, multiplied by the number of person-hours lost and the value of time per user, a total cost of lost time of **\$2 million per day** is obtained for a single highway closure. In the aftermath of Hurricane Harvey, flooding was not limited to a single highway. Several major highways and dozens if not hundreds of local surface roads were closed due to standing water, some for one month or more. IH 10 and US 90 had significant multiday closures. IH 10 was closed in many locations, and closures were also required on IH 45, IH 69, and other important arterial highways through the Houston area. IH 10 in Beaumont and other highways in Beaumont and neighboring cities were closed for significant periods of time due to both flooding during and after the storm and clearing of debris and obstructions after the floodwater subsided.

Given the widespread geographical region of the storm, the number of highways affected, the multiday length of the closures, and the significance of these facilities for interstate commerce, the cost incurred from a single event of the magnitude of Hurricane Harvey will easily exceed \$50 million (assuming on average five roads closed for 5 days). This estimate only encompasses delays to users specifically on these highways, and not the complete economic loss

to industries that rely on reliable transport of goods, which could extend orders of magnitude above this estimate.

A hurricane of this magnitude does not occur annually, yet smaller hurricanes (e.g., Hurricane Imelda in 2019) have also caused closure of parts of the IH 10 corridor in Texas due to standing water and transport of debris in floodwaters that requires clearing. Additionally, significant rainstorms commonly close highway underpasses and access roads, thereby impacting highway traffic. Given the wide range of flood-related events that can result in highway closures, a conservative estimate of **\$5 million/year** is used in the VoR calculations.

Finally, the life cycle of the new median barrier had to be estimated for use in the economic cost estimate calculations. The typical lifespan of a concrete median barrier is estimated to be about 30–50 years. Because vehicle interaction with the edge along the top of the opening may reduce its lifespan with respect to a solid concrete median barrier, the life of the new median barrier with openings for passage of floodwater is conservatively estimated to be 20 years. A discount rate of 5 percent was selected as an estimate for future values.

G.5 DISCUSSION

This VoR estimate was developed by the research team based on its understanding of the functional areas and assessment of the relative importance of various factors. This estimate likely includes incomplete information and several assumptions. The research team believes this VoR estimate is conservative because there are many factors that could not be accounted for due to lack of data. For example, the CRIS database only includes reported crashes and does not provide data on all incidents. Further, the cost of flooding due to damming and backwater effects in areas surrounding the flooded highways was not included.

